Karlsruher Institut für Technologie

ETP-KA/2022-07

NOISE AND DETECTION EFFICIENCY STUDIES ON FULL-SIZE 2S MODULE PROTOTYPES FOR THE PHASE-2 UPGRADE OF THE CMS EXPERIMENT

Zur Erlangung des akademischen Grades eines

Doktors der Naturwissenschaften (Dr. rer. nat.)

von der KIT-Fakultät für Physik des
Karlsruher Instituts für Technologie (KIT)

angenommene

DISSERTATION

von

M.Sc. Roland Koppenhöfer
aus Karlsruhe

Tag der mündlichen Prüfung: 08.07.2022

Referent:	Prof. Dr. Ulrich Husemann	Institut für Experimentelle Teilchenphysik
Korreferent:	Prof. Dr. Thomas Müller	Institut für Experimentelle Teilchenphysik

Roland Koppenhöfer:
Noise and Detection Efficiency Studies on Full-Size 2S Module Prototypes
for the Phase-2 Upgrade of the CMS Experiment
July 2022

Contents

Part I.

Introduction and Basics

1

Introduction

At the *European Organization for Nuclear Research* (CERN) in Geneva, Switzerland, the most powerful particle accelerator today is operated: The *Large Hadron Collider* (LHC) can accelerate protons or heavy ions in a circular storage ring with a circumference of approximately 27 km. Two particle beams are accelerated counter-rotating within two beam pipes. At dedicated points along the storage ring, the two beams can be brought to collision. By studying the properties of newly created particles emerging from these collisions with specialised detectors, physicists can investigate the properties of already known particles and search for evidence of new physics.

The performance of a particle collider can be characterized by its center-of-mass energy and its luminosity. The LHC reaches center-of-mass energies up to 14 TeV when operated with protons and is designed to operate at a luminosity of $1 \cdot 10^{34}\,\mathrm{cm}^{-2}\,\mathrm{s}^{-1}$. However, it was possible to reach luminosities of more than $2 \cdot 10^{34}\,\mathrm{cm}^{-2}\,\mathrm{s}^{-1}$ in 2017 by optimizing the operating parameters [Pra17]. To keep the chance for new discoveries high and guarantee high data quality, the LHC luminosity is planned to be increased significantly for the data taking runs starting in 2029. This phase is called *High-Luminosity LHC* (HL-LHC) during which luminosities of up to $7.5 \cdot 10^{34}\,\mathrm{cm}^{-2}\,\mathrm{s}^{-1}$ can be reached [Apo+17]. During the minimum planned HL-LHC operation time of ten years, this allows to significantly increase the data set size for physics analysis. Increased luminosities correlate with higher particle rates that the accelerator components and experiments at the LHC have to endure. To compensate for the induced radiation damage and to minimize the risk of failures during accelerator operation, the hardware components need to be repaired, exchanged and upgraded. This repair and upgrade work is performed during scheduled shutdown times.

The *Compact Muon Solenoid* (CMS) experiment is one of the four large experiments at the LHC. The CMS detector is designed as multi-purpose detector and built cylindrically around the beam pipe at one of the LHC interaction points. The subdetectors are seen from the inside out: a silicon tracker, an electromagnetic and hadronic calorimeter and muon chambers. While tracker and both calorimeters are located inside a superconducting solenoid, the muon chambers are embedded outside the solenoid into an iron return yoke. A more detailed description of the CMS detector is given in Chapter 2 after a short summary of the LHC accelerator complex.

In preparation for the HL-LHC, the CMS detector will be substantially upgraded before 2029 in the scope of the *Phase-2 Upgrade*. This thesis deals with a topic from the Phase-2 Upgrade of the CMS Outer Tracker. The new design of the outer part of the tracker is mainly driven by the goal to increase radiation hardness of the detector modules and maintain the hit occupancy of the currently installed tracker by increasing the density of readout channels. To improve the performance of the CMS trigger system, tracking information will be included at the LHC bunch crossing rate of 40 MHz. Bandwidth limitations do not allow to read out all hits per event. Therefore, modules with on-module transverse momentum discrimination are developed. Two different type of detector modules made of two parallel silicon sensor layers will be installed in the outer tracker. Particles crossing these modules deposit charge in both sensor layers, which is read out by the same set of readout chips. Through the CMS magnetic field, the trajectories of charged particles are bent in the detector volume. Particles with low transverse momenta p_T follow trajectories with a higher curvature compared to particles with high p_T. This results in a varying spatial distance of the detected hits in the two module sensor layers depending on the particles' p_T. By monitoring this distance, the modules can identify trajectories from particles above a programmable p_T threshold. Each combination of hits from top and bottom sensor is called *stub*. Only valid stubs fulfilling the spatial requirements of a high p_T trajectory are sent out by the modules to the CMS trigger system [CMS17c]. Details about the HL-LHC and the Phase-2 Upgrade of the CMS Outer Tracker including a discussion of all 2S module components is given in Chapter 3. To understand the physics of particle detection with silicon detectors, different interaction mechanisms of particles with matter are summarized in Chapter 4. Additionally, the working principle of silicon strip detectors and the consequences of radiation damage for the performance of silicon detectors are explained.

The *Institute of Experimental Particle Physics* (ETP) at *Karlsruhe Institute of Technology* (KIT) is one of the 2S module assembly centers within the CMS community. Between 2023 and 2025, it is planned to assemble between 1300 and 2000 modules. This requires a suitable production line with precise assembly techniques and mechanics in order to meet the alignment requirements for 2S modules to guarantee efficient stub logic performance. At the end of the module assembly process, the modules need to be checked for their full functionality. Within this thesis, a test station has been developed to provide the necessary hardware for a test of the full module readout chain. Besides offering shielding against light and electromagnetic radiation from the outside, the station can be flushed with dry air. Air temperature and relative humidity are monitored. An easy and safe module fixation mechanism is used to minimize the risk of damaging the modules during handling. Additionally, the station houses a custom designed LED array to illuminate the two 2S sensors. This LED array is called *Karlsruhe Infrared Array* (KIRA) and has been produced and tested within this thesis. Details about the test station design and the performance of the KIRA system are given in Chapter 5.

To validate the 2S module design at an early stage, several module prototypes are built prior to the start of module production. These prototypes help to qualify the combined performance and interplay of all module components well before the final components are available. The latest 2S module prototype versions available between 2019 and 2022 have been subject to several functional tests within this thesis. The two main parameters to qualify 2S module performance are the channel noise level and the detection efficiency for hits and stubs. Detailed studies of the noise contributions of the latest 2S module prototypes are conducted. Additionally, the module detection efficiency is measured within a beam test setup at *Deutsches Elektronen-Synchrotron* in Hamburg, Germany. 2S modules are exposed to an electron beam with energies up to 6 GeV. The DESY beam test facility provides beam telescopes to reconstruct particle tracks. By placing 2S modules inside the telescope, their detection efficiency can be quantified. To study the 2S module performance at the beginning and end of lifetime of the CMS detector, the module performance of unirradiated modules and modules assembled with irradiated silicon sensors are compared. By rotating the module with respect to the particle beam, bent particle trajectories can be emulated and the stub detection efficiency is measured. The results of channel noise measurements and beam test studies are summarized in Chapter 6.

2

The Large Hadron Collider and the Compact Muon Solenoid Experiment

In order to understand the fundamental properties of matter in the universe, particle physicists use accelerators to study the interaction of already known particles and search for new phenomena. The most powerful particle accelerator today is the *Large Hadron Collider* (LHC) at the *European Organization for Nuclear Research* (CERN) in Geneva, Switzerland. An overview about the LHC accelerator complex is given in Section 2.1. The *Compact Muon Solenoid* (CMS) experiment is one of the large LHC experiments and is introduced in Section 2.2.

2.1. The Large Hadron Collider

The Large Hadron Collider can accelerate protons or heavy ions in a circular storage ring of about 27 km circumference. The storage ring is made of two beam pipes to circulate two particle beams in opposite directions. At dedicated interaction points the two beams can be brought to collision. Within the storage ring, the two beams are simultaneously accelerated to a maximum energy of 7 TeV in case of protons and 2.76 TeV per nucleon for heavy ions [EB08]. Before protons and heavy ions can be injected into the LHC, they need to be accelerated to energies of 450 GeV and 177 GeV per nucleon, respectively. This is achieved via several preceding accelerator stages on the CERN site.

A schematic view of the LHC accelerator complex is shown in Figure 2.1. Until 2020, protons for the LHC were extracted from hydrogen atoms by separating electrons and protons using an electric field. These protons were subsequently accelerated by the *Linear Accelerator 2* in groups of particles, called *bunches*. After reaching energies of 50 MeV, they were injected into the *Proton Synchrotron Booster* (BOOSTER). In 2020, the Linear Accelerator 2 was replaced by the *Linear Accelerator 4* (LINAC 4) which accelerates hydrogen anions to energies of 160 MeV before stripping the electrons from the anions and, thus, injecting protons into the BOOSTER [Arn+06]. The BOOSTER accelerates the protons further and transfers them to the *Proton Synchrotron* (PS) at an energy of 1.4 GeV. Inside the PS, protons reach energies of 25 GeV before they are injected into the *Super Proton Synchrotron*, which accelerates them to the LHC injection energy of 450 GeV. In order to inject heavy ions into the LHC, only the first two acceleration stages differ: *Linear Accelerator 3* and the *Low Energy Ion Ring* provide the ions with enough energy to inject them into the Proton Synchrotron [Ben+04].

To accelerate particles in the LHC, 16 superconducting radio frequency cavities are used. A resonantly oscillating electric field at a frequency of 400 MHz exerts an overall force onto passing charged particles. This leads to gradual acceleration of these particles. Simultaneously, the oscillating field keeps the particles together in bunches of the same energy. At nominal operation, 2808 bunches with about 10^{11} protons each are circulating in the LHC [EB08]. To guide the two particle beams inside the storage ring, the LHC uses a superconducting magnet system combining dipole, quadrupole and higher order magnets. The magnets are made of niobium-titanium (Nb-Ti) and are cooled down to a temperature of 1.9 K using superfluid

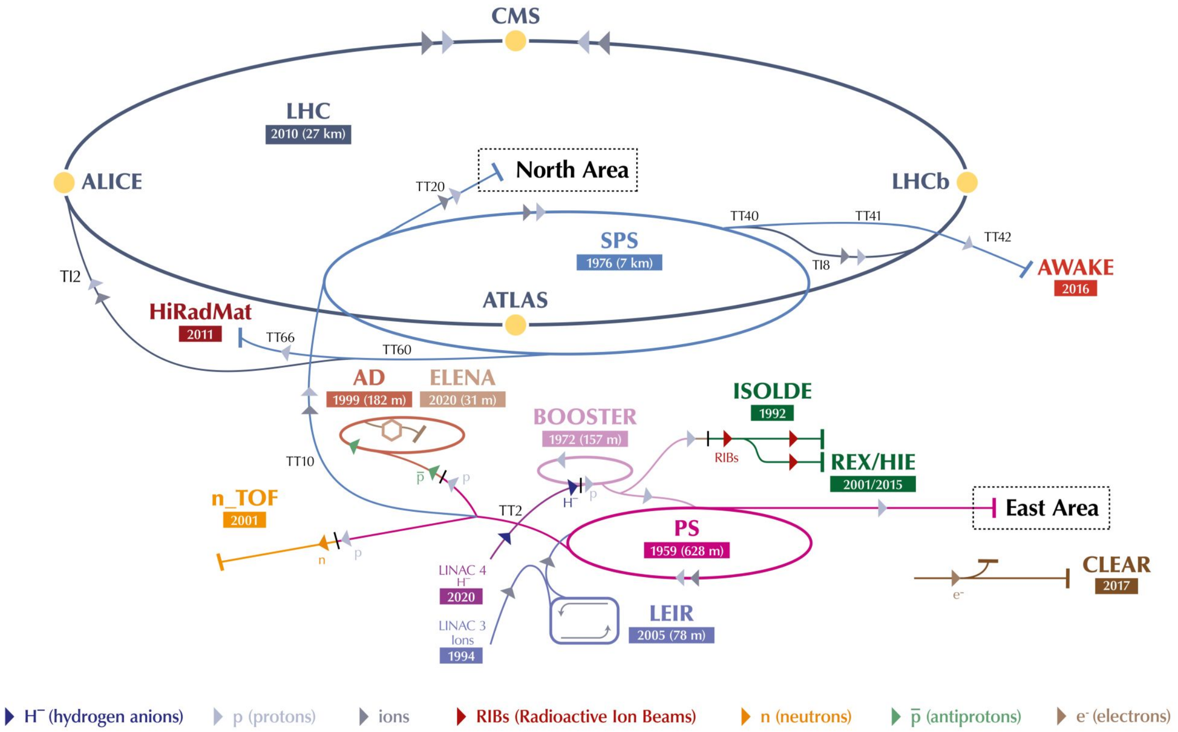

Figure 2.1.: The CERN accelerator complex: Protons for the LHC storage ring are accelerated successively by a linear accelerator (LINAC 4) and three circular accelerators (BOOSTER, PS and SPS), before finally being passed into the LHC in two opposite directions. The two beams can be brought to collision at four interaction points where the experiments ALICE, ATLAS, CMS and LHCb are located. [Mob19]

helium. The 1232 dipole magnets provide a magnetic field of 8.33 T in nominal operational condition and bend the particles on a nearly circular trajectory via the Lorentz force. The quadrupole and higher order magnets are necessary to focus the particle beams [Ros03; EB08].

There are four interaction points along the ring where particles from the two beam pipes can be brought to collision. Around these interaction points, the four large experiments of the LHC (ALICE, ATLAS, CMS and LHCb) are located to detect secondary particles emerging from the primary particle collisions. Each experiment uses specialized detector systems to investigate dedicated physics objectives.

Besides the center-of-mass energy (up to 14 TeV for proton-proton collisions in the LHC), the *luminosity* $\mathcal{L}$ is another crucial parameter to characterize the performance of a particle collider. The luminosity is defined as the constant of proportionality between the production cross section σ_i for a specific particle process i and its appearance rate $\mathrm{d}N_i/\mathrm{d}t$,

$$\frac{\mathrm{d}N_i}{\mathrm{d}t} = \mathcal{L} \cdot \sigma_i \ . \tag{2.1}$$

Thus, a high luminosity corresponds to a large number of particle interactions per second at the interaction point. The luminosity of two colliding beams can be calculated to

$$\mathcal{L} = \frac{n_1 n_2 f N_b}{A} \tag{2.2}$$

where n_1 and n_2 indicate the number of particles per bunch in the two beams, N_b the number of bunches, f the beam circulation frequency in the collider and A the overlapping cross section of both beam profiles [HM06].

The LHC was designed to operate at a luminosity of $1 \cdot 10^{34}\,\mathrm{cm}^{-2}\,\mathrm{s}^{-1}$. By optimizing the operating parameters, it was possible to significantly exceed the design luminosity and reach a luminosity of more than $2 \cdot 10^{34}\,\mathrm{cm}^{-2}\,\mathrm{s}^{-1}$ in 2017 [Pra17].

To calculate the number of observable events of a process N_i with known cross section for a given luminosity and measurement time T, the *integrated luminosity* $\mathcal{L}_{\mathrm{int}}$ is used

$$N_i = \sigma_i \cdot \int_0^T \mathcal{L}(t)\,\mathrm{d}t = \sigma_i \cdot \mathcal{L}_{\mathrm{int}} \ . \tag{2.3}$$

Thus, the integrated luminosity scales with the data set size for physics analyses. It is measured in inverse femtobarn (fb^{-1}) [HM06]. Until 2021, the LHC has produced data equivalent to $193\,\mathrm{fb}^{-1}$ with proton collisions [CMS17b].

2.2. The Compact Muon Solenoid Detector

The CMS Experiment is one of the four large experiments at the LHC and is designed as a general-purpose detector to study the Standard Model of particle physics as well as to search for new physic beyond it. To fully exploit the potential for new discoveries, the CMS detector design aims to provide the best possible event reconstruction by measuring and identifying all possible decay products. Figure 2.2 illustrates the structure of the CMS detector. It consists of several subdetectors located cylindrically around the beam pipe. Each subdetector measures a dedicated physical property of particular particle types. *Endcap detectors* are instrumenting the flat areas of the cylinder. This geometry provides nearly perfect coverage with active detector area across the entire 4π solid angle. CMS has a length of approximately 29 m and is 15 m in diameter, making it the second largest experiment at the LHC.

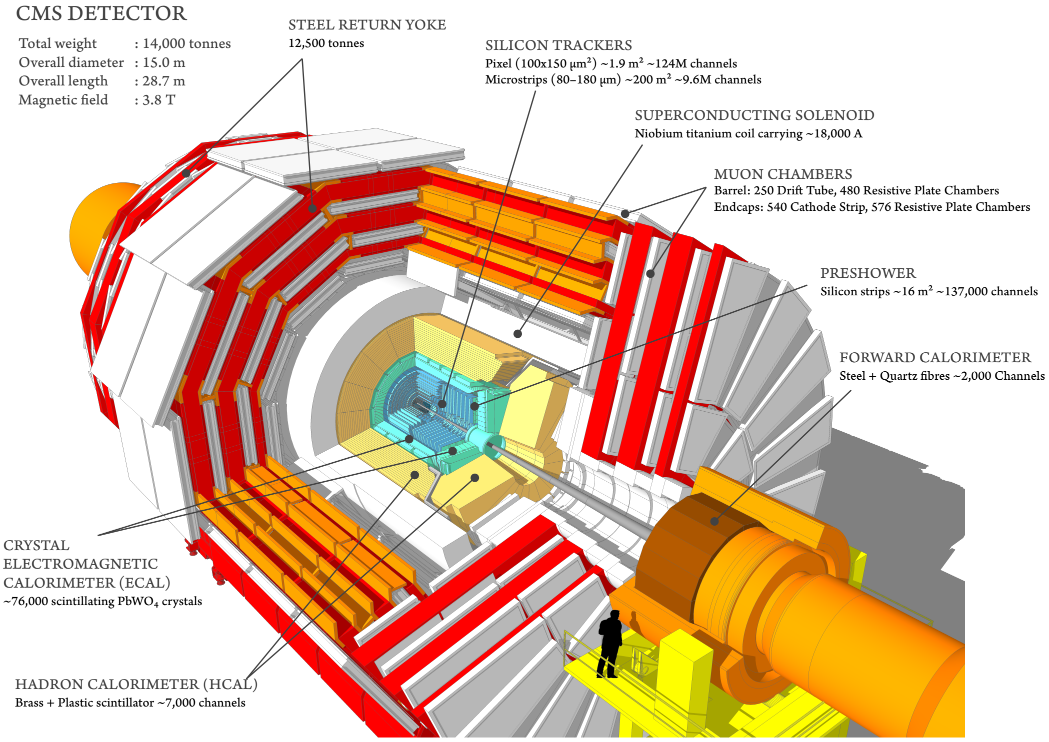

Figure 2.2.: Sectional view of the CMS detector: the subdetectors are from inside out: silicon tracker, electromagnetic calorimeter, hadronic calorimeter, solenoid and muon chamber inside the steel return yoke. [Sak19].

2.2.1. Subdetectors

One key feature of the CMS design is the **superconducting solenoid** made of niobium-titanium, providing a homogeneous magnetic field of 3.8 T in its inside. With a length of 12.5 m and an inner diameter of 6 m, it is large enough to enclose the tracker as well as the electromagnetic and hadronic calorimeters. The magnetic field bends the trajectories of charged particles passing through the detector due to the Lorentz force. This effect is crucial for particle identification and strongly increases the performance of tracker and both calorimeters. To close the magnetic field lines outside the solenoid, a steel return yoke is used. [CMS08]

The innermost layers in the CMS experiment are formed by the **silicon tracker**. The tracker is designed to precisely measure trajectories of charged particles in the CMS magnetic field and reconstruct secondary vertices as best as possible. At LHC luminosities of up to $2 \cdot 10^{34}\,\mathrm{cm}^{-2}\,\mathrm{s}^{-1}$, the number of simultaneously occurring proton-proton collisions each 25 ns (called *pile-up*) is 50 and more. With respect to these particle rates, it has been decided to construct the whole tracker from silicon sensor modules. These modules provide fast detector response and the possibility to reach a high readout channel granularity. Thus, the tracker occupancy is kept at an adequate level. [CMS12]

The CMS tracker consists of a barrel part and two endcaps. Currently, the barrel part is equipped with pixel modules on the inside and strip modules on the outside. Pixel modules are arranged in four layers at radii between 3 cm and 16 cm around the beam axis. Strip modules are distributed over ten layers at radii up to 1.1 m. Each endcap is instrumented with three layers of pixel modules and nine layers of strip modules. The silicon sensors in the pixel modules are segmented into 66 560 pixels with a pixel size of $100\,\mu\mathrm{m} \times 150\,\mu\mathrm{m}$. The silicon strip sensors vary in their geometry depending on the position in the tracker and have strip pitches between

80 µm and 205 µm. In total the tracker provides an active area of about 200 m^2 of silicon, which makes it the largest silicon tracker to date. [CMS08; CMS12]

The CMS tracker achieves spatial resolutions down to 10 µm for the vertex reconstruction of high transverse momentum particles along the beam pipe. Multiple scattering effects in the detector layers degrade the resolution for particles with low transverse momenta. By combining the hit information provided by the tracker, it is possible to reconstruct the curvature of particle trajectories. This allows to measure transverse momenta of charged particles. Thus, a transverse momentum resolution of one to two percent is achievable for high momentum tracks. Analogous to the spatial resolution, the transverse momentum resolution degrades for lower momenta due to multiple scattering. [CMS08]

The homogeneous **electromagnetic calorimeter** (ECAL) surrounds the CMS tracker and is used to measure the energy of electromagnetically interacting particles. It is made of about 76 000 lead tungstate scintillating crystals which are used to detect the energy deposition via electromagnetic showers. The energy deposition creates scintillation light, which is measured by avalanche photodiodes in the barrel detector and by vacuum phototriodes in the endcaps. The usage of lead tungstate crystals allows to build a calorimeter with high granularity, fast response and good energy resolution. As lead tungstate features a small Molière radius of 2.19 cm and a small radiation length of 0.85 cm, it was possible to build a compact electromagnetic calorimeter inside the solenoid with a total depth of nearly 26 radiation lengths. More detailed information about the ECAL can be found in [CMS97b] and [CMS08].

Adjacent to the ECAL, the **hadronic calorimeter** (HCAL) is located. It is built as a sampling calorimeter with alternating layers made of steel or copper alloy and 4 mm thick plastic scintillator tiles. Thus, the hadronic interactions take place in the steel and copper alloy layers generating hadronic showers. Fragments thereof interact with the scintillator material. The created light is wavelength shifted and guided to photomultiplier tubes and silicon photomultipliers for detection. With a total depth of 79 cm, the HCAL calorimeter provides a thickness of about five to ten nuclear interaction lengths to incoming particles, depending on their incidence angle [Bai+07]. Further information about the HCAL can be found in [CMS97a] and [CMS08].

The outermost subdetector of CMS is the **muon system** integrated in the return yoke. Its main goals are the identification of muons, the muon momentum measurement and the generation of fast input to the trigger system including transverse momentum information. To achieve that, three different types of gaseous detectors are used. While the barrel detector is equipped with drift tube chambers and resistive plate chambers, the endcap uses cathode strip chambers together with resistive plate chambers. Independently, the muon system provides a transverse momentum resolution between nine and 40 percent depending on the muon energy and incidence angle. It is, however, possible to improve the muon momentum resolution significantly by combining tracking information from muon system and tracker [CMS08]. A description of the muon system performance can be found in [Lay97] and [CMS08].

By combining the information of all these subdetectors, it is possible to efficiently reconstruct the primary vertices and to identify the particle reactions based on the signatures of the detected particles. A detailed explanation of the applied algorithms can be found in [CMS17a].

2.2.2. Trigger System

At the LHC design luminosity the CMS detector generates about 1 MB of zero suppressed data every 25 ns resulting at a data rate of 40 TB/s generated by the detector frontends. It is impossible to handle and store this amount of data on currently available storage devices. Thus, a dedicated trigger system is needed to reduce this data amount efficiently without losing the potential to study new physics.

The CMS trigger system consists of two stages. In the first stage, called *Level-1 Trigger*, a trigger decision has to be taken and sent back to the detector frontends within 3.2 µs. This decision is based on the information gathered from the calorimeters and the muon system. Criteria to send out a Level-1 trigger signal are the detection of specific particle signatures and cuts on the measured transverse energy and missing transverse energy in each event. This trigger stage results in a data rate reduction to 100 kHz [CMS00].

When the detector frontends receive a Level-1 trigger signal, they send out the corresponding event information stored in their internal buffer. This event information is passed to the second trigger stage which is called *High-Level Trigger*. The High-Level Trigger is an entirely software-based system with access to the complete event data set. It further reduces the data rates to an average of 400 Hz which allows offline storage for further analysis [Kha+17].

3

The Phase-2 Upgrade of the CMS Outer Tracker

The Large Hadron Collider (LHC) at CERN is the currently most powerful particle accelerator in the world. To guarantee high data quality and to keep the probability for discoveries of new physics high, the accelerator and its detectors need to be upgraded continuously during their runtime. From 2029 on, the LHC shall deliver an instantaneous luminosity of factors of five to seven higher than the original design luminosity of $1 \cdot 10^{34}\,\mathrm{cm}^{-2}\,\mathrm{s}^{-1}$. This phase is called *High-Luminosity LHC* and will be introduced in Section 3.1. The necessary changes to prepare the CMS detector to the High-Luminosity LHC are summarized under the name *Phase-2 Upgrade*. An overview of the changes to the CMS Tracker is given in Section 3.2.

3.1. The High-Luminosity LHC

The LHC has delivered an integrated luminosity of about $200\,\mathrm{fb}^{-1}$ since the start of data taking in 2010 up to the beginning of the long shutdown 2 starting end of 2018. From 2021 to 2025, it is planned to collect another $230\,\mathrm{fb}^{-1}$ of data at luminosities of approximately $2 \cdot 10^{34}\,\mathrm{cm}^{-2}\,\mathrm{s}^{-1}$. A further increase in luminosity is needed to guarantee scientific progress and efficient data taking. Thus, the High-Luminosity LHC (HL-LHC) will start its operation in 2029 at a nominal luminosity of $5 \cdot 10^{34}\,\mathrm{cm}^{-2}\,\mathrm{s}^{-1}$ allowing to collect about $3000\,\mathrm{fb}^{-1}$ within ten years of operation. Considering the safety margins of all HL-LHC accelerator components, the machine and its experiments can handle luminosities of up to $7.5 \cdot 10^{34}\,\mathrm{cm}^{-2}\,\mathrm{s}^{-1}$. This allows to extend the HL-LHC runtime further within the *ultimate scenario* leading to integrated luminosities of up to $4000\,\mathrm{fb}^{-1}$ [Apo+17]. Figure 3.1 sketches the current schedule for the physics program and upgrades of the LHC and HL-LHC.

Higher luminosities and, thus, higher particle rates imply increased radiation damage to the accelerator components. Therefore, several systems need to be upgraded before the start of the HL-LHC. Regarding the quadrupole and higher order magnets in the LHC storage ring, the probability for sudden failures will increase drastically beyond $400\,\mathrm{fb}^{-1}$. To prevent time consuming repairs that would stop the complete accelerator operation, the collimating system and beam injection system will be upgraded before 2029. The new system will provide better beam focusing.

A drastic increase in luminosity can be achieved by installing crab radiofrequency cavities next to the interaction points (IPs). As the two colliding beams cross each other under an angle at the IPs, the luminosity can be calculated via Equation (2.2) using for the beam cross section area A the overlapping cross section of both beams. The crab cavities will introduce a time-dependent transverse rotation to the bunch profiles, minimizing A. A detailed overview of the measures to prepare the accelerator for the HL-LHC phase can be found in [Apo+17].

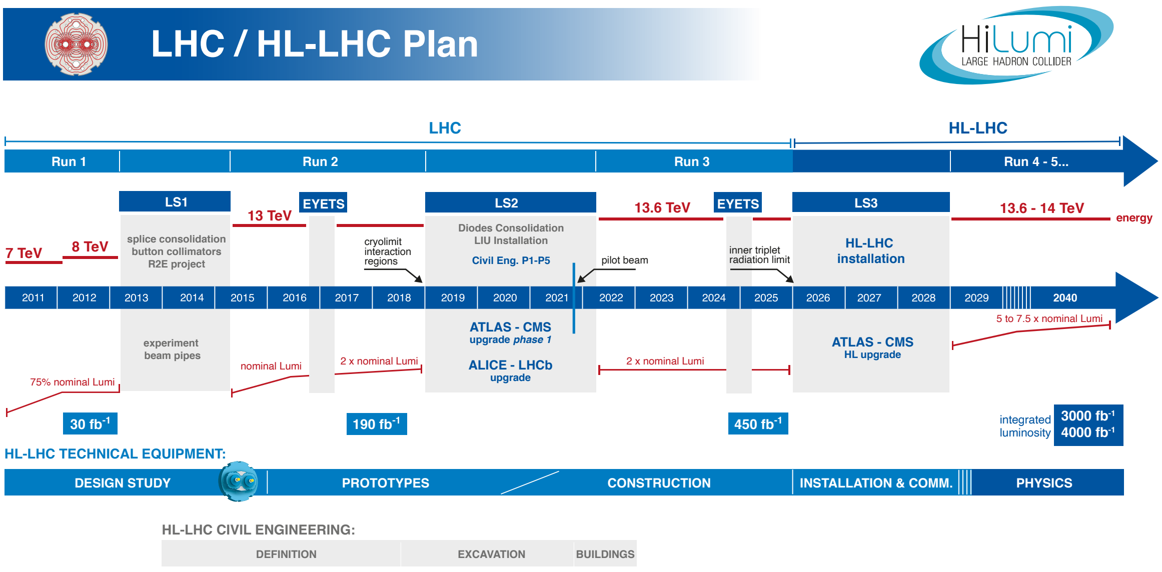

Figure 3.1.: Schedule of the LHC and HL-LHC Upgrade and Physics Program. The main upgrades to prepare for the HL-LHC phase will be performed during the long shutdown 3 between 2025 and 2029. Starting from 2029, the HL-LHC will deliver an unprecedented amount of data with expected integrated luminosities of up to 4000 fb^{-1}. [CER22b]

3.2. The Phase-2 Upgrade of the CMS Tracker

The increased luminosities during the HL-LHC impose new demands upon the whole CMS detector. Due to its proximity to the interaction point, the CMS tracker suffers most from radiation damage. Performance studies have shown that the currently installed silicon tracker will develop unacceptable degradation at integrated luminosities larger than 1000 fb^{-1}. For this reason, a complete new tracker will be built in the scope of the Phase-2 Upgrade and installed during Long Shutdown 3.

The design of the new tracking system was mainly driven by the need to provide a high radiation tolerance, as well as the goals to increase the density of readout channels called *granularity*, to increase the two-track separation, and to contribute to the *Level-1 Trigger* decision [CMS17c]. The following sections will present the resulting design choices.

3.2.1. Tracker Layout

Figure 3.2 shows a sketch of a slice of one quarter of the Phase-2 tracker with the beam pipe situated along the z-axis. The new tracker is made of a cylindrical barrel section centered around the beam pipe, with endcap discs on both sides of the barrel.

The *Inner Tracker* directly surrounds the beam pipe and is equipped with silicon pixel modules marked in green and orange. The usage of 100 µm to 150 µm thin silicon sensors with pixel sizes of 25 µm × 100 µm and 50 µm × 50 µm offers the desired radiation hardness together with high spatial resolution and low occupancy levels. The sensors are read out by a 65 nm CMOS chip developed within the RD53 collaboration [CG13]. By equipping the endcaps with pixel detectors, the upgraded CMS tracker will increase its geometrical coverage in the

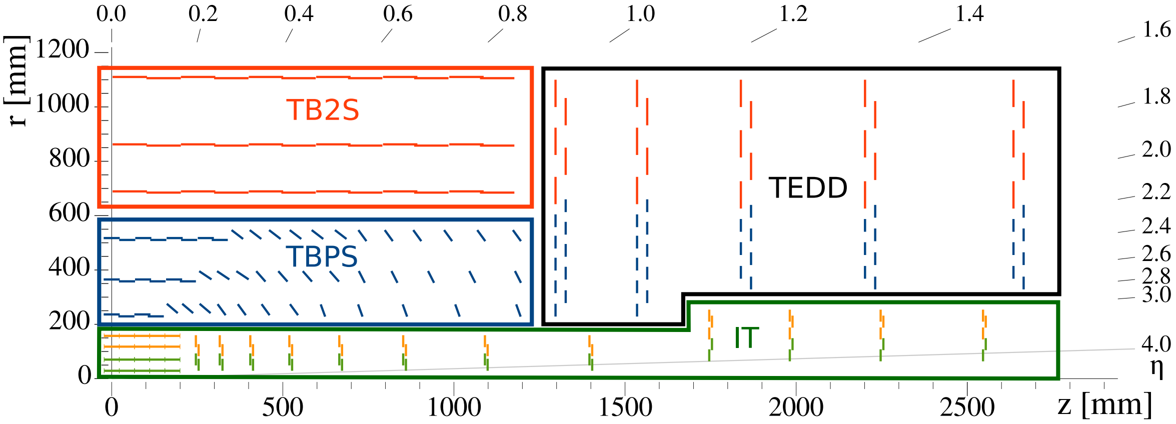

Figure 3.2.: Sketch of one quarter of the CMS Phase-2 Tracker layout. The beam pipe is orientated along the z-axis. The Inner Tracker (IT) is made of two types of silicon pixel modules represented in green and orange while the Outer Tracker consists of modules combining silicon macropixel sensors and silicon strip sensors called PS and 2S modules marked in blue and red, respectively. To quantify the geometrical coverage of the tracker as a function of the particle's track angle ϑ with respect to beam axis, the pseudorapidity η is used. It is defined as $\eta = -\ln\left[\tan\left(\frac{\vartheta}{2}\right)\right]$. The Phase-2 tracker provides a coverage up to $\eta = 4$. Adapted from [CMS17c].

forward direction compared to the currently installed tracker. The design of the Inner Tracker additionally allows to extract the modules and services in case a replacement is needed during the HL-LHC runtime. [CMS17c]

The *Outer Tracker* (OT) encloses the Inner Tracker. It is equipped with two different types of detector modules providing two parallel silicon sensor layers. The *Pixel Strip* (PS) modules consist of one macro-pixel sensor and one strip sensor while the *Strip Strip* (2S) modules are built of two strip sensors. Further details about these modules can be found in Section 3.2.3. The PS modules are placed in the layers nearest to the interaction point because of their higher granularity compared with the 2S modules. Thus, it is possible to distinguish between three detector regions in the Outer Tracker: the *Tracker Barrel equipped with PS and 2S modules* called TBPS and TB2S, respectively, and the *Tracker Endcap Double-Discs* (TEDD). [CMS17c]

TBPS and TB2S both consist of three layers of support structures which are instrumented on both sides with detector modules. The modules are mounted in such a way that the active sensor areas overlap within the structures. These structures additionally house cooling pipes and are routing the module connection cables and fibers. Figure 3.3a depicts a 3D rendering of the structures used in the TB2S called *ladders*. In the TBPS, the PS modules are mounted under an angle towards the beam axis for larger z coordinates. This more complex arrangement allows to minimize the tracker material budget while keeping the full geometrical coverage. [CMS17c]

The endcaps are made of double-discs in order to achieve hermetic layers with fully overlapping silicon sensor areas using the rectangular shaped 2S and PS modules. Part of a double disc is shown in Figure 3.3b. In total there are five double discs on each side of the barrel detector.

To operate the detector modules during the HL-LHC, it is essential to efficiently remove the heat generated by the electronics and sensor leakage currents from the detector volume. Additionally, the silicon sensors have to be operated at low temperatures to keep their thermal power under control. A new two-phase CO_2 cooling system will be installed during the Phase-2 upgrade. It will be able to handle the expected power dissipation of 150 kW in the complete tracker. The nominal coolant operating temperature is $-35°C$, resulting in a temperature of

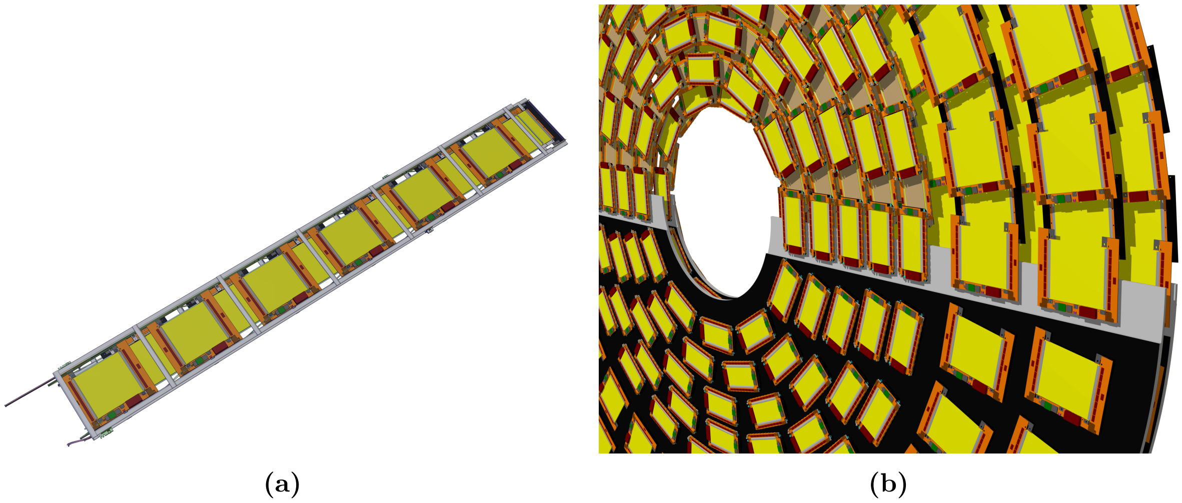

Figure 3.3.: 3D rendering of a TB2S ladder (a) and part of a TEDD double disc (b). The 2S and PS modules are mounted back to back on the mechanical structures to achieve full coverage with active sensor area. [CMS17c]

−33°C at the warmest point along the cooling loop. This configuration allows to operate the silicon sensors at temperatures around −20°C. [CMS17c]

3.2.2. Radiation Environment

During the design of the Phase-2 Upgrade, detailed studies of the expected dose rate and particle fluences in the upgraded detector have been made. Based on the results, the radiation hardness requirements for each tracker module type was formulated. These studies have been performed by the CMS *Beam Radiation Instrumentation and Luminosity* (BRIL) project and their results are illustrated in Figure 3.4. The figure shows the expected integrated particle fluence expressed in 1 MeV neutron equivalent ($\mathrm{n_{eq}}$) per $\mathrm{cm^2}$ (see Section 4.3). For an integrated luminosity of $3000\,\mathrm{fb^{-1}}$, the first layer of the Inner Tracker has to withstand the maximum fluence of $3.1 \cdot 10^{16}\,\mathrm{n_{eq}\,cm^{-2}}$. With increasing distance of the modules to the beam pipe, the fluence levels drop significantly. For the PS and 2S modules in the Outer Tracker, maximum fluences of $1.05 \cdot 10^{15}\,\mathrm{n_{eq}\,cm^{-2}}$ and $3.7 \cdot 10^{14}\,\mathrm{n_{eq}\,cm^{-2}}$, respectively, are expected [CMS21a]. These values increase by a factor of 1.33 for the ultimate scenario with an integrated luminosity of $4000\,\mathrm{fb^{-1}}$. Based on these results, the module and silicon sensor designs were optimized for all CMS tracker modules. The studies included detailed thermal simulations of the module performance for different irradiation scenarios.

3.2.3. Outer Tracker Modules

As shown in Section 3.2.1, the CMS Outer Tracker is equipped with Pixel Strip (PS) modules and Strip Strip (2S) modules. Both module types consist of two closely spaced parallel silicon sensors that are read out by a common set of chips. This allows to correlate the signal of both sensor layers at the bunch crossing rate of 40 MHz and extract information about the transverse momentum of charged particles. Figure 3.5 illustrates this principle. Due to the Lorentz force in the CMS magnetic field of 3.8 T, the trajectory bending radii of particles with a high transverse momentum p_T are smaller than for particles with a low p_T. Thus, the spatial displacement between the clusters detected in the two sensor layers per module depends on the particle p_T. The readout chips of the 2S and PS modules search for cluster pairs in the two

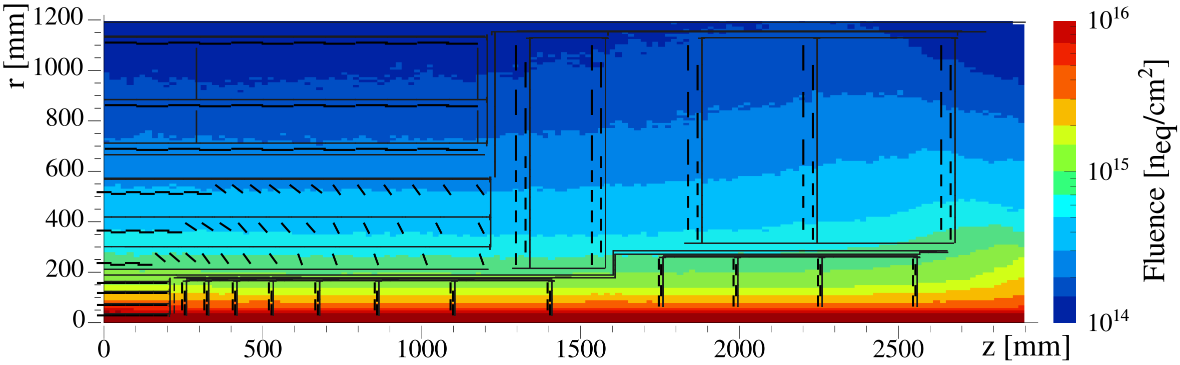

Figure 3.4.: Map of the expected integrated particle fluence in 1 MeV neutron equivalent per cm^2 in the CMS Phase-2 tracker. Data are shown for an integrated luminosity of $3000\,fb^{-1}$ with proton-proton collisions at a center-of-mass energy of 14 TeV and a total cross section of $\sigma_{pp} = 80\,mb$. [CMS17c]

sensor layers which are called *stubs*. The sensor located closer to the interaction points acts as *seed layer*, defining the primary position of a search window in the *correlation layer*. If a cluster in the correlation sensor is detected within the search window, the stub is valid and the stub information is sent out to serve as input for the Level-1 Trigger system. Each valid stub is characterized by the stub position given by the cluster center in the seed sensor and the stub bend given by the offset between correlation and seed cluster. By programming different search window sizes, it is possible to select particle trajectories above different p_T thresholds.

3D renderings of a PS and a 2S module are shown in Figure 3.6. The PS module is made of a macro-pixel sensor (PS-p sensor) as bottom sensor and a strip sensor (PS-s sensor) as top sensor. The PS-p sensor provides 32 rows of 960 1.5 mm long macro-pixel implants on an active area of approximately 5 cm × 10 cm. The PS-s sensor features the same active area as a PS-p sensor but is made of two rows of 960 2.5 mm long strip implants. The silicon strip sensors used in 2S modules have an active area of approximately 10 cm × 10 cm providing two rows of 1016 strips each. Therefore, PS modules provide a higher granularity than 2S modules. The PS sensors have a separation of 100 µm between neighbouring strips (also called *pitch*). The pitch of 2S sensors is 90 µm. Both PS and 2S sensors are made of float zone silicon with a physical thickness of 320 µm and an active thickness of 290 µm. The sensor implants are made of n-doped silicon while the sensor bulk is made of p-doped silicon. This sensor material and design choice was identified to yield the best sensor performance for the complete range of expected fluences for the CMS Outer Tracker modules. More details about the five-year qualification campaign performed by the CMS community can be found in [Ada+20] and [Ada+21a]. An overview about the working principle of silicon particle detectors is given in Chapter 4. [CMS17c]

Depending on their position in the CMS tracker, modules with different sensor distances are used. This is necessary to compensate for the lower particle incidence angles for modules nearer to the interaction point. By increasing the sensor distance for the innermost modules, it is possible to keep the p_T discrimination mechanism at a comparable level within the whole outer tracker. Thus, there are PS module variants with 1.6 mm, 2.6 mm and 4 mm sensor distances. The 2S modules are assembled with two different sensor distances of 1.8 mm and 4 mm. As all studies within this thesis are made with this module type, 2S modules are discussed in more detail in the following section. [CMS17c]

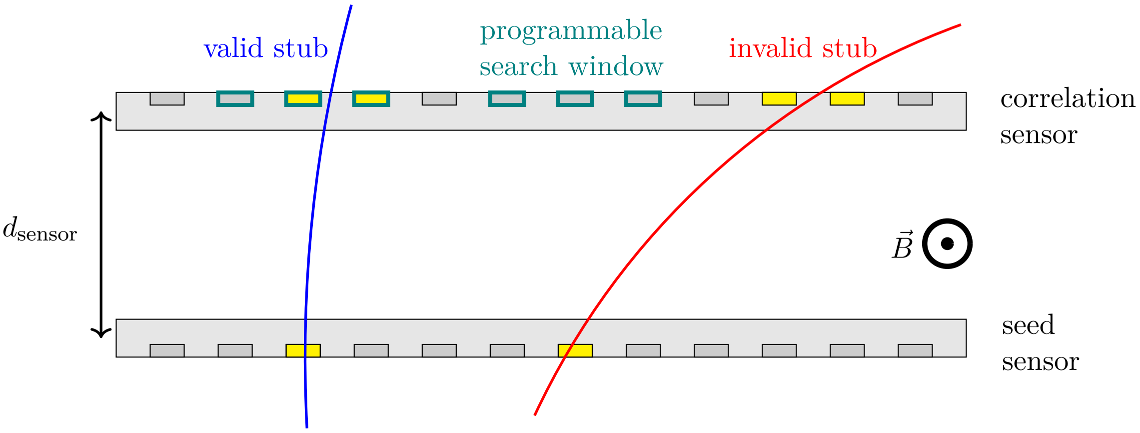

Figure 3.5.: Sketch of the p_T discrimination concept in the CMS Outer Tracker modules. Trajectories crossing the two silicon sensors generate clusters in the readout channels marked in yellow. These cluster combinations are called stubs. Due to the magnetic field within CMS, the trajectories of charged particles are bent depending on their transverse momentum p_T. Thus, it is possible to select trajectories above different p_T values by defining a search window (marked in green) in the correlation sensor. If the correlation sensor cluster lies within the correlation window, the stub is called valid. Depending on the module position in the outer tracker, different sensor distances d_{sensor} are used.

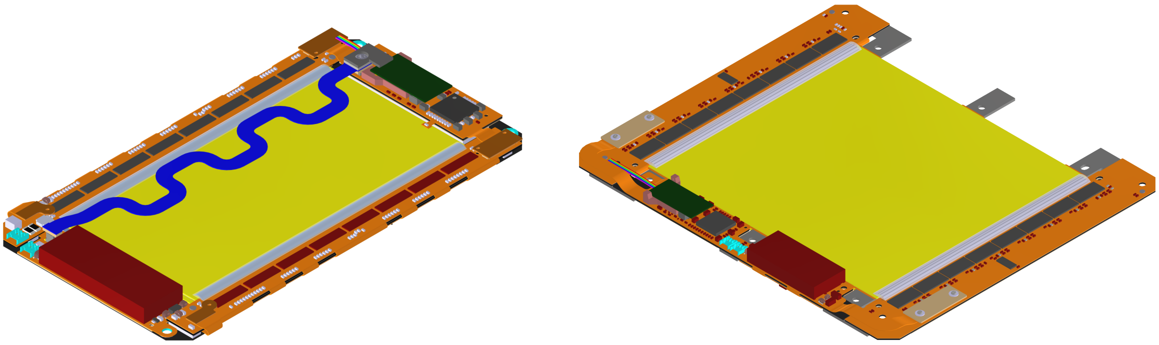

(a) **(b)**

Figure 3.6.: 3D renderings of a PS module (a) and a 2S module (b). The PS module consists of a macro-pixel sensor and a strip sensor and is made in three different sensor spacing variants with 1.6 mm, 2.6 mm and 4 mm spacing. The 2S module uses two silicon strip sensors mounted within a distance of 1.8 mm or 4 mm to each other. Updated from [CMS17c].

3.2.4. 2S Module Mechanics and Electronics

Figure 3.7 shows an exploded view of a 2S module. The silicon sensors are marked in yellow. To achieve the two sensor spacings of 1.8 mm and 4 mm, the silicon sensors are glued onto spacers made of carbon fiber reinforced aluminium (Al-CF), called *bridges*. Using holes in the bridges, it is possible to mount the modules on support structures. All electronic components of a 2S module are located on electronic circuit boards called *hybrids* which are glued onto dedicated fixation points on the bridges. Thus, the heat produced by the silicon sensors and module electronics is conducted via the bridges to the module mounting points which are directly connected to the cooling system of the CMS tracker. Based on the results of recent thermal simulations, all 2S modules in the Tracker Endcap Double-Discs as well as all first modules in the TB2S ladders and all modules in the innermost TB2S ladder are equipped with two long bridges and two short *stump* bridges (as depicted in Figure 3.6b and Figure 3.7). These modules are exposed to the highest fluences of all 2S modules and, thus, produce the highest thermal power. For all remaining 2S modules, it is possible to remove the second stump bridge on the hybrid free module side, reducing the tracker material budget. [CMS17c]

The Bare Module

The two silicon sensors are glued with their backsides onto the Al-CF bridges. As the sensor backsides are on high voltage potential and the bridges are connected to the detector support structures on ground potential, 25 µm thin polyimide strips are used for electrical isolation. High voltage tails are glued and bonded to the sensor backsides to provide the bias potential. Additionally, a thermistor is placed on the top sensor high voltage tail to allow measuring the sensor temperature of every module. The resulting object is called *bare module*. While gluing the sensors to the bridges it is important to achieve a precise alignment of the sensor strips between top and bottom sensor in order to guarantee efficient operation of the module stub logic. The maximum allowed relative strip rotation is set to less than 400 µrad. [CMS17c]

The Frontend Hybrids

The two frontend hybrids (FEHs) per module consist of a flexible electronic circuit folded around a carbon-fiber-reinforced polymer stiffener. Thus, it is possible to position wire bonding pads on the top and bottom side of each hybrid, allowing to connect both sensor strips via bonds to the FEHs. The signal of the bottom sensor is routed via the fold-over to the top side where the readout chips are located. By adjusting the thickness of the stiffener, it is possible to align the bonding pads at the same level as the sensor surfaces for both 2S module spacings. [Gad+18]

Eight *CMS Binary Chips* (CBCs) [Uch+18] are bump bonded onto each FEH to read out the signal coming from the sensor strips. Each CBC provides 254 input channels which are alternatingly connected to bottom and top sensor strips to correlate the sensor hits and perform the transverse momentum discrimination described in Section 3.2.3. To avoid inefficiencies in the stub finding logic, neighbouring CBCs can exchange hit information. The functionality of the CBC is discussed in the following paragraphs on the basis of the latest chip version called CBC3.1.

Signal seen by the AC coupled sensor strips is processed by the analogue frontend of each channel depicted in Figure 3.8a. The charge is amplified in two stages called pre-amplifier and post-amplifier. Before the resulting pulse is compared to a chip-wide programmable threshold measured in the internal DAC unit V_{cth}, it is possible to shift the signal level of each channel frontend using an 8-bit offset register. The comparator stage produces a binary output that is further processed by the digital back-end. The analogue frontend was designed to produce

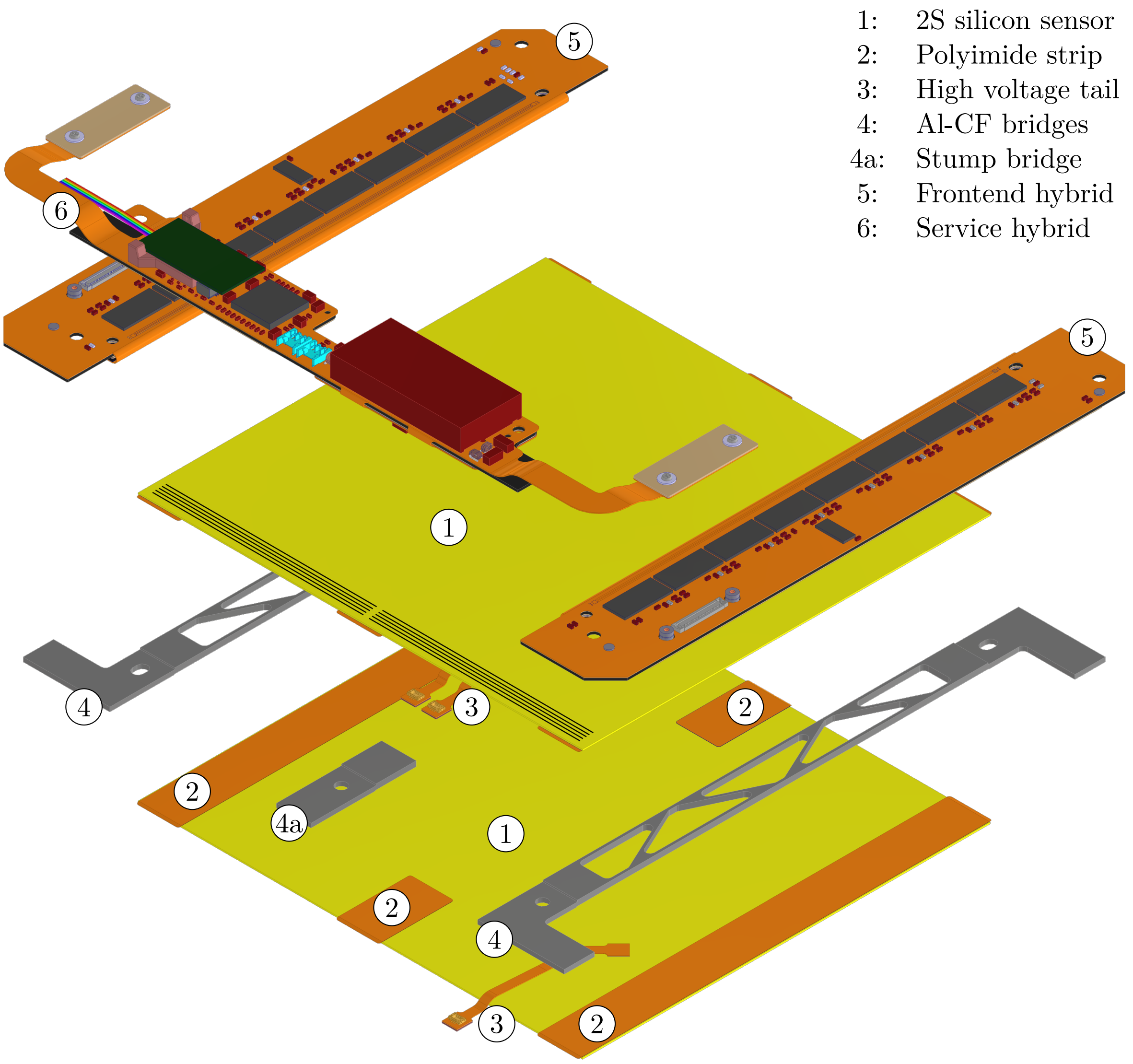

Figure 3.7.: Exploded view of a 2S module. The silicon strip sensors are marked in yellow. The first strips of the two rows of 1016 strips per 2S sensor are shown schematically using black lines. The carbon fiber reinforced aluminium bridges are marked in gray. This module houses two stump bridges from which only one is visible in this view. The sensor backsides are electrically isolated to the bridges via polyimide strips. The two frontend hybrids and the service hybrid are glued onto extensions of the bridges and house the module electronics. Updated from [CMS17c].

a channel noise of less than 1000 electrons when connected to the 2S sensor strips [Pry19]. To measure the channel response to a known signal, it is possible to inject test pulses with programmable amplitude into the frontend amplifier using on-chip capacitors.

Figure 3.8b illustrates the main circuit blocks processing the signal within the CBC. The binary signal leaving the analogue frontend is transferred to the digital back-end and passed to the *Hit Detect* block. Four different outputs are generated from the input signal that can be independently routed to the stub logic unit and hit pipeline. The default operation mode samples the comparator output using a 40 MHz clock. When the comparator output is high at a rising edge of the clock, the hit logic stays high until the comparator output returned to zero at a following rising edge of the clock. The output of the Hit Detect block for each channel is stored within the hit pipeline static random-access memory for 512 clock cycles corresponding to 12.8 µs. This defines the time available for the CMS trigger system to decide about reading out complete hit information from the modules.

In parallel the output of the Hit Detect block is processed within the stub logic. Hits within neighboring sensor channels within the same event form a cluster. Due to the exchange in hit information between CBCs clusters are also detected within neighboring chips. In the first stub logic block, the detected cluster widths are compared to a programmable variable and rejected if their widths exceed the set value. The maximum programmable value is a cluster width of four. As a next step, the matching of seed layer clusters with correlation layer clusters is performed to find suitable combinations fulfilling the logic explained in Section 3.2.3. For valid cluster combinations the stub position and stub bend information is kept. While the stub position is kept with half strip resolution, the stub bend is converted from a 5-bit to a 4-bit value using a programmable lookup table to reduce the stub data output.

While all the logic blocks described previously operate with a 40 MHz clock, a second clock domain at 320 MHz is used for the data assembly logic. The information about stub position and bend is serialized and sent out continuously via five scalable low-voltage signaling (SLVS) lines operating at 320 Mbps. A sixth SLVS line is used to send out the hit information after a trigger signal was detected.

Each frontend hybrid houses one *Concentrator Integrated Circuit* (CIC) [Ber+19] that receives all data sent out by the eight CBCs. Each of the incoming SLVS lines is first phase and word aligned using configurable delays to compensate for the different routing lengths between the chips on the hybrid. Stub and hit information are processed separately. The incoming stub data of eight consecutive bunch crossings are stored within the CIC and are sorted by the stub bend. Low bends corresponding to high p_T particle tracks are prioritized in case the CIC buffer size reaches its limit for high stub occupancies. After a serialization step, the stub data are sent out via five output lines. [CMS17c]

In case of a Level-1 trigger signal, the hit information of all CBCs of the corresponding bunch crossing is read-out and stored in the CIC. The data amount is reduced by searching for hits in neighboring strips forming clusters. Only information about the cluster position and cluster width is serialized and sent out by the CIC. Similar to the stub data, the cluster information is given with a resolution of half a strip pitch. This data reduction allows to reach the expected mean trigger rates of 750 kHz. However, it is possible to configure the CIC to send out the raw hit information without zero-suppression for debugging purposes. This limits the trigger rate to 100 kHz. [Nod+18; CMS17c]

The Service Hybrid

The service hybrid (SEH) connects to the two frontend hybrids (FEHs) via two fine-pitch connectors on flexible L-shaped tails. As the FEHs, it is made of a flexible electronic circuit board glued onto a carbon-fiber-reinforced polymer stiffener and partially folded around the

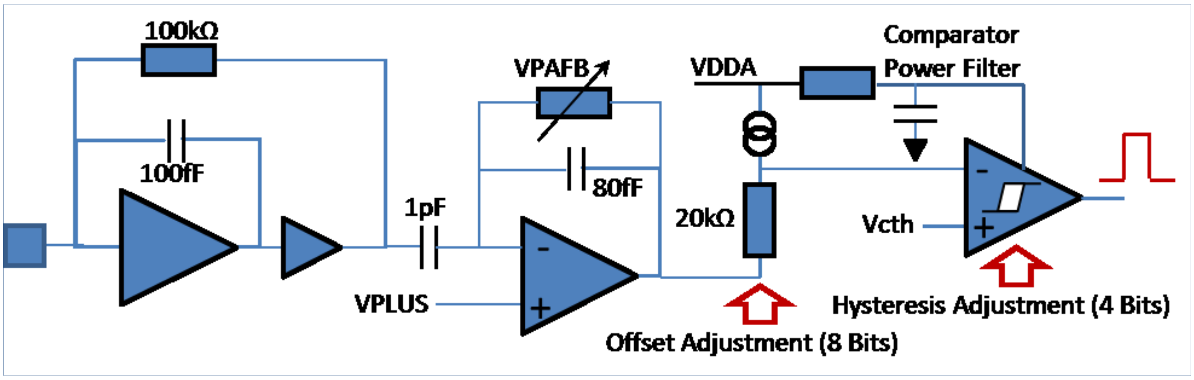

(a)

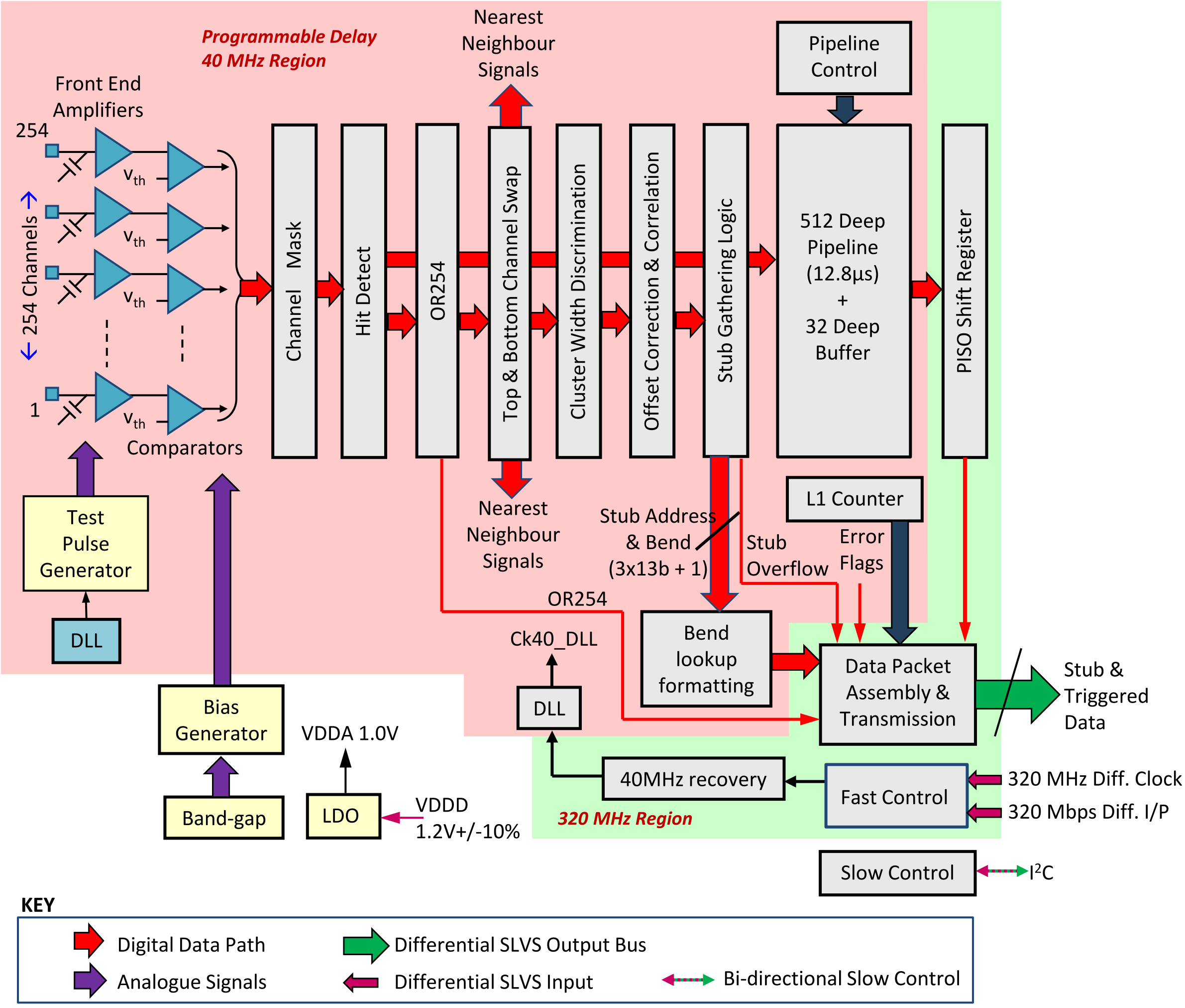

(b)

Figure 3.8.: (a) The analogue frontend of a CBC channel is formed by a pre-amplifier, a post-amplifier and a comparator creating a digital output from the analogue sensor signal. (b) The block diagram illustrates the main circuit blocks processing the analogue and digital signals within the CBC3.1 chip. [Pry19]

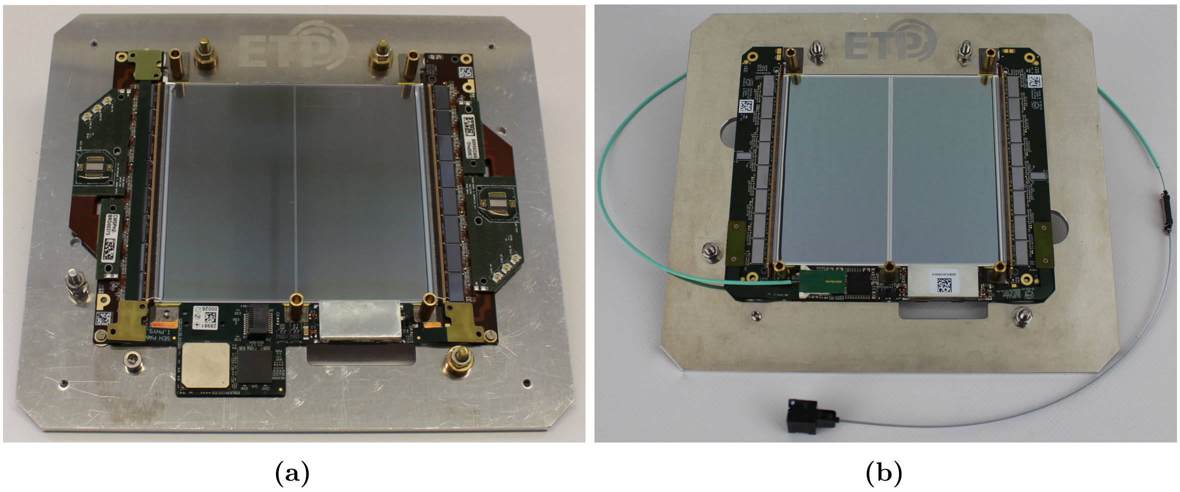
(a) (b)

Figure 3.9.: The latest 2S module prototype versions. (a) The 8CBC3 modules houses a service hybrid of the version V3.1 with a FEAST2 chip, a GBTX and a VTRx chip. The CIC2 chips are placed on separate circuit boards connected to the frontend hybrids. (b) The latest 2S prototypes use a bPOL chip, the lpGBT and the VTRx+ module on the SEH. The CIC chips are bump bonded directly to the frontend hybrids.

stiffener. It houses a *Low Power Gigabit Transceiver* (LpGBT) that receives the output of the CICs on both FEHs, serializes the data and sends them to the *Versatile Transceiver Plus* (VTRx+) module for opto-electrical conversion. The VTRx+ module is connected via optical fibers to the off-module electronics. The LpGBT additionally configures and monitors the frontend chips via I^2C. [Fel+18]

All electronic chips on the 2S modules are powered by two sequential DC-DC converters mounted on the SEH. The bPOL12V converts the module input voltage of about 11 V to an output voltage of 2.55 V which is fed to the VTRx+ module. Additionally, this voltage is used as input for the bPOL2V5 creating a voltage of 1.25 V which is fed to all other chips. This conversion scheme reduces drastically the electrical power losses in the cables to the modules. To shield the module from electromagnetic influence created in the DC-DC stages, the converters are covered with an aluminium shield. The high voltage tails attached to the silicon sensors are connected on the bottom side of the SEH to the high voltage circuit. [Fel+18]

3.2.5. 2S Module Prototyping

To study and validate the performance of all 2S module components, several module prototype iterations have been produced prior to the order of the final module parts for the production. Within this thesis, two versions of 2S module prototypes have been investigated. The *8CBC3 modules* were the first 2S module prototypes read out fully via the optical chain. A photo of an 8CBC3 module can be seen in Figure 3.9a. Each frontend hybrid houses eight readout chips of the latest version CBC3.1 [Pry19]. The CIC chips are mounted on separate circuit boards and can be connected to the frontend hybrids via dedicated connectors. The results presented in this thesis are taken with the chip version CIC2 [Ber+19]. Service hybrids of the version V3.1 are assembled in the 8CBC3 modules. These hybrids house a FEAST2 chip [CER16] as DC-DC converter, a GBTX chip [MCW21] together with a VTRx module [Vas+17] for optical data transmission.

The latest *2S prototypes* use frontend hybrids onto which the CIC chips have been bump bonded. Major changes have been made to the service hybrids. As DC-DC converters, bPOL chips [CER22a; CER21] are used. The GBTX chip is replaced by the lpGBT chip of the version v0 [lpG21]. The VTRx+ module [Ola+20] replaces the VTRx. As these newest chip versions are smaller as their predecessors, the latest 2S prototypes are the first 2S modules matching the final outer dimensions of 2S modules.

3.2.6. Outer Tracker Module Readout

To optically read out the presented 2S module prototypes, an *FC7 evaluation board* [PV15] is used. The FC7 board is an *Advanced Mezzanine Card* offering a flexible FPGA based hardware for multi-gigabit transceiver operation. The optical fibres leaving the module prototypes are connected to an *FPGA Mezzanine Card* (FMC) housing optical transceivers. Up to two FMCs can be connected to an FC7 board. Within this thesis, FMCs are used for the optical module readout and as external trigger interface. Dedicated firmware versions can be uploaded to the FC7 board to configure and read out different module prototypes.

The *Phase-2 Acquisition and Control Framework* (Ph2_ACF) [CMS22] is a readout software framework developed within the CMS community to coordinate the CMS Outer Tracker module readout. By communicating via ethernet with the FC7 board, the software framework sends commands to the modules and receives data streams which are analysed or stored locally. Besides basic routines like e.g. electrical calibration of the readout chips, the software is being continuously extended to perform dedicated tests on modules.

Each 2S module prototype needs to be electrically calibrated before being used for data taking. After aligning the timing of all data streams of the chips in the 2S readout chain during the *phase alignment*, the steps presented in the following are performed. During all steps, no external charge is injected into the 2S module.

1. An offset calibration is needed to achieve a uniform response of all module channels by adjusting the offset registers. By performing threshold scans for each channel, the hit occupancy is measured. The threshold at which the hit occupancy reaches 50% is called pedestal. By tuning the offset registers, it is possible to move the channel pedestals to the same external threshold setting. Thus, it is possible to choose a global threshold relative to the common pedestal value for data taking.

2. The module noise is a crucial property of 2S modules. The origins of noise in silicon detectors are discussed in Section 4.2.3. As the CBC is a binary chip, noise is measured by performing threshold scans for every module channel. The resulting distributions are shown in Figure 3.10. At high physical thresholds (corresponding to low chip threshold settings) the channel occpuancies are zero. While decreasing the physical threshold, the occupancies rise to 1. Assuming purely Gaussian distributed noise, this rise is described by the error function

$$f(x) = \frac{1}{2}\mathrm{erf}\left(\frac{x-\mu}{\sqrt{2}\sigma}\right) \tag{3.1}$$

   with the pedestal μ and the width σ. The width σ is used to quantify the channel noise.

After performing an offset calibration and measuring the module noise, it is possible to define a threshold for data taking. This threshold is chosen relatively to the pedestal position. Depending on the trigger source, a latency scan needs to be performed first. The latency is the time delay between the time when charge is detected by the readout chips and the arrival of a trigger signal in the FC7. As the hit and stub information is sent out via independent

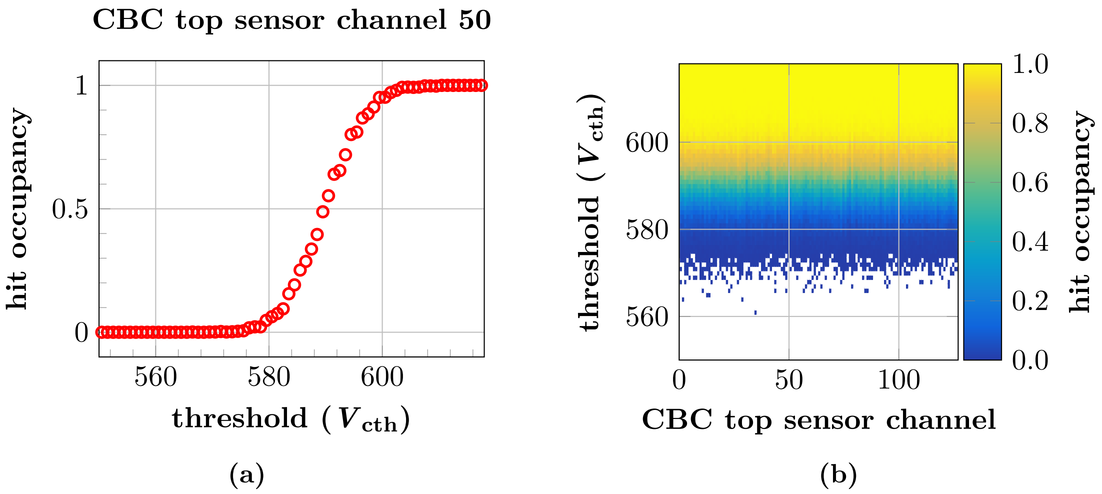

(a) (b)

Figure 3.10.: The 2S module channel noise is determined by measuring the hit occupancy as a function of the threshold for every channel without external charge injection. (a) The digital frontend returns an S-shaped curve in response to Gaussian distributed noise. Low threshold set values correspond to high physical thresholds. (b) After a successful offset calibration, the noise curves of all module channels are leveled to the same pedestal.

lines, separate latency scans for hit and stub data have to be performed. For 2S modules, the latency can be set in steps of 25 ns (corresponding to one CBC clock cycle).

3.2.7. Naming Conventions

Within this thesis, the following naming conventions are used:

- The operation voltage for 2S sensors is applied between the sensor backplane and the bias ring on the sensor surface. While the bias ring is connected with electrical ground, a negative potential is applied to the sensor backside. Thus, negative voltages have to be applied at the high voltage supplies to operate 2S modules. To simplify reading, only absolute voltage values will be used to quantify the sensor bias voltage.

- The 2S module components are numbered as shown in Figure 3.11. Looking onto a 2S module from above with the service hybrid showing to the lower side, the right frontend hybrid is assigned the identification number (id) zero, and the left hybrid is assigned the id one. The eight CBCs per frontend hybrid are numbered from zero to seven with CBC 0 being adjacent to the service hybrid. CBC channels connected to bottom and top sensor strips are treated separately. For both hybrids, channel zero indicates the channel nearest to the service hybrid. The following channel numbers are incremented reaching channel 1015 on the hybrid free module side, as indicated in Figure 3.11. Thus, the spatial distribution of hits seen by both hybrids correlates with the channel number.

- As introduced in the previous section, the physically applied CBC threshold is given by the difference between the pedestal value and the chosen threshold setting in V_{cth} units. High physical thresholds correspond to low V_{cth} values. To simplify understanding, the *relative threshold* is introduced as

$$\text{relative threshold} = \text{pedestal value} - \text{threshold setting} .$$

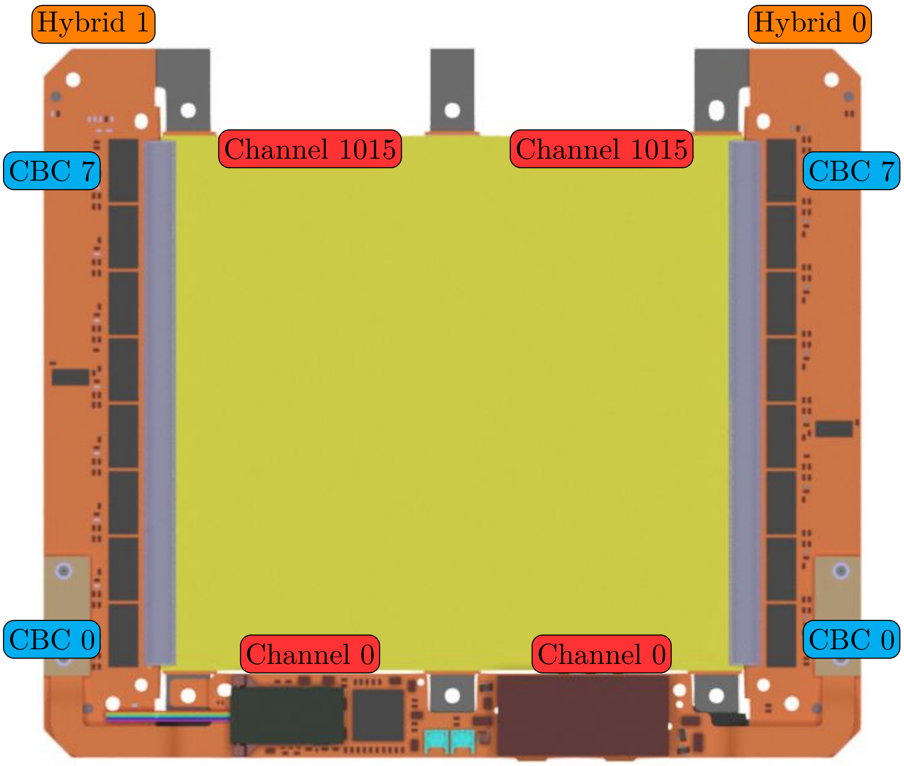

Figure 3.11.: 3D rendering of a 2S module seen from above. In this orientation, the right frontend hybrid is assigned the id zero and the left frontend hybrid the id one. The eight CBCs per frontend hybrid are numbered from zero to seven. Within this thesis, CBC 0 is on both hybrids the chip nearest to the service hybrid. The channels per hybrid are numbered from zero to 1015 per silicon sensor as indicated in the sketch. Channel zero indicates the strip nearest to the service hybrid for top and bottom sensor.

To convert V_{cth} units into an electron equivalent charge, the conversion $1\ V_{\mathrm{cth}} = 156\,\mathrm{e}^-$ is used [Mai19].

- The hit occupancy is defined as the average number of hits detected per module channel and event within a data set taken at constant threshold. When performing hit occupancy measurements without any external charge generation in the module, the intrinsic noise level of 2S modules is measured. In these cases, the hit occupancy is called *noise occupancy*.

4

Silicon Particle Detectors

Experiments in particle physics use specialized detector systems to measure particle properties and search for new physics. To optimize the detector performance, it is crucial to understand the interaction of particles with different materials. A brief overview of the interaction mechanisms of particles with matter is given in Section 4.1. It has been found that silicon is a suitable material to be used in modern tracking detectors as, e.g., in the CMS experiment. The design and functionality of silicon particle detectors are discussed in Section 4.2. The property changes of silicon with irradiation are introduced in Section 4.3.

4.1. Interaction of Particles with Matter

Particles interact with matter via different mechanisms depending on their own properties like charge, mass, and energy, or the properties of the interaction material. As there are fundamental differences in the interaction mechanisms for charged particles and photons with matter, these cases will be treated separately in Section 4.1.1 and Section 4.1.2.

4.1.1. Charged Particles

Heavy Particles

Charged particles with masses significantly larger than the electron mass (e.g. muons and hadrons) interact mainly via collisions with the shell electrons in a material. Depending on the energy transfer, this results in excitation or ionization of the material's atoms. The mean energy loss per unit length is given by the mass stopping power $\left\langle -\frac{\mathrm{d}E}{\mathrm{d}x} \right\rangle$ described by the *Bethe equation*

$$\left\langle -\frac{\mathrm{d}E}{\mathrm{d}x} \right\rangle = 4\pi N_A r_e^2 m_e c^2 z^2 \frac{Z}{A} \frac{1}{\beta^2} \left[\frac{1}{2} \ln \left(\frac{2 m_e c^2 \beta^2 \gamma^2 W_{\max}}{I^2} \right) - \beta^2 - \frac{\delta(\beta\gamma)}{2} \right] \tag{4.1}$$

with the Avogadro constant N_A, the electron radius r_e, the electron mass m_e, the speed of light c, the atomic number Z and atomic mass A of the interaction material, the relative speed of the particle in relation to the speed of light β, the Lorentz factor γ, the maximum energy transfer to an electron during a collision $W_{\max}$, the mean excitation energy I and the density effect correction $\delta(\beta\gamma)$. The Bethe equation applies to particle velocities with $0.1 \leq \beta\gamma \leq 1000$. Figure 4.1 depicts the mass stopping power of muons in copper. The distribution shows a distinct minimum for particles with $\beta\gamma \approx 3$ at an approximate stopping power of $2\,\mathrm{MeV\,cm^{-2}\,g^{-1}}$. These particles are called *minimum ionizing particles* (MIPs) and are used as a measure of the sensitivity of a particle detector. An example of MIPs are cosmic muons. [Zyl+20]

Radiative effects become significant with increasing particle energies. The dominant interaction processes are pair production, bremsstrahlung, and photonuclear interactions resulting in electromagnetic and hadronic showers. At low particle energies atomic bindings have to be considered in addition to Equation (4.1). Additionally, phenomenological fits to observed data

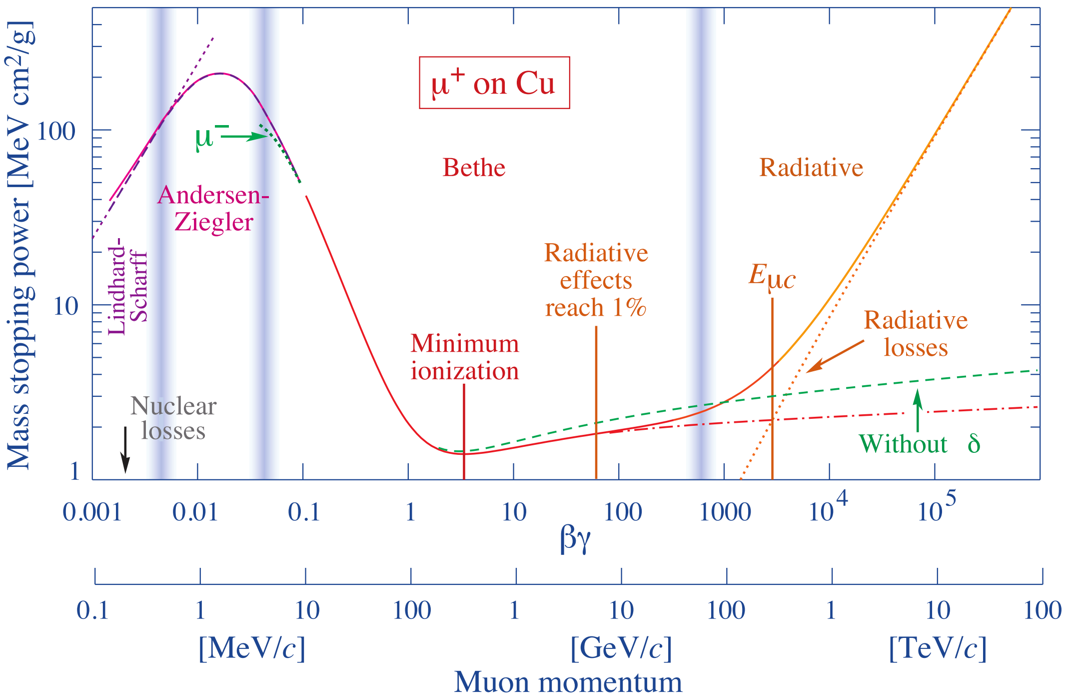

Figure 4.1.: Mean energy loss per unit length of muons in copper as a function of $\beta\gamma$. For $0.1 \leq \beta\gamma \leq 1000$ the energy loss is described by the Bethe equation. At higher particle energies radiative effects become significant. For lower energies nuclear interactions have to be considered. [Zyl+20]

are used to calculate the energy loss. More details about the different energy loss contributions can be found in [Zyl+20].

Electrons and Positrons

For electrons and positrons, additional factors like spin and charge lead to a different energy loss distribution compared to heavy charged particles. For incoming electrons, interactions with the atomic electrons are interactions of identical particles which has to be taken into account additionally. At high energies, electrons and positrons mainly lose energy via bremsstrahlung. At low energies, energy loss by ionization is dominant but also electron-electron scattering (*Møller scattering*) and electron-positron scattering (*Bhabha scattering*) has to be taken into account. The different contributions to the fractional energy loss of electrons and positrons in lead are shown in Figure 4.2a. The transition from ionization dominated energy loss to radiation dominated processes can be quantified with the *critical energy* E_c. For silicon, E_c is approximately 40 MeV. The minimum mean energy loss per unit length in silicon is $1.5\,\mathrm{MeV\,cm^2\,g^{-1}}$, which is comparable to the energy loss of MIPs. Within the scope of this thesis electrons sent out by the radioactive decay of the isotope ^{90}Sr are used to characterize silicon sensor modules. These electrons deposit a similar energy in silicon as cosmic muons [Dro21]. [Zyl+20]

Energy Loss Fluctuations

While the mean energy loss of heavy charged particles in matter is given by the Bethe equation, the energy loss per particle crossing is a stochastic process and can vary significantly. The energy deposition distribution for a fixed $\beta\gamma$ depends on the thickness of the detector material. For

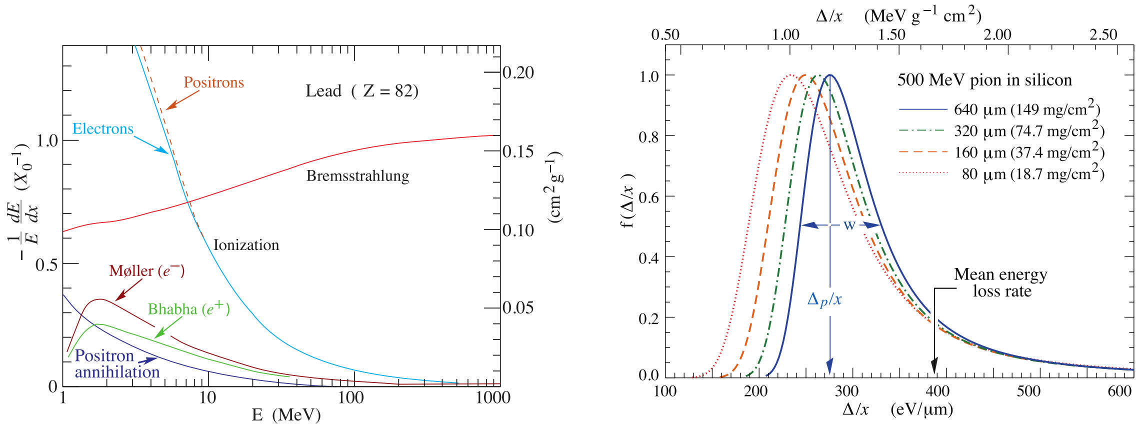

(a) (b)

Figure 4.2.: (a) Fractional energy loss of electrons and positrons in lead. The critical energy E_c is defined as the energy at which the losses through ionization and radiation are the same. (b) The energy deposition Δ per unit length for 500 MeV pions in silicon with different thicknesses. The distributions are normalised to the most probable value. [Zyl+20]

thin detectors (in the case of silicon given by thicknesses in the order of a few millimeters), the distribution can be described by a Landau distribution characterized by the *most probable value* (MPV) and the *full width at half maximum*. Due to single collisions with a large energy deposit resulting in e.g. δ electrons, the distribution shows an asymmetric tail towards high energy depositions. However, the Landau distribution fails to describe the energy loss for the typical thicknesses of modern silicon tracking detectors with thicknesses of a few hundred micrometers at maximum. While the most probable energy deposition value can still be evaluated using the Landau distribution, single collisions with a large energy transfer lead to a significant increase of the observed distribution width. Figure 4.2b depicts the energy deposition of pions with an energy of 500 MeV for different silicon detector thicknesses. [Zyl+20]

4.1.2. Photons

Photon interactions with matter are based on four major processes relevant at different energies. The dominant interaction process at small photon energies below approximately a few 10 keV (depending on the detector material) is the *photoelectric effect*. If the photon energy is larger than the binding energy of atomic shell electrons, the photon can be absorbed and an electron is released from the atom. A second interaction process at small photon energies is *Rayleigh scattering*. In this process, the photon is elastically scattered at bound electrons. As no energy transfer is taking place, this process is of small importance for the detection of photons in experiments for high energy physics. Inelastic photon scattering processes are called *Compton scattering*. Photons transfer parts of their energy to atomic electrons and are scattered into a new direction. This process is dominant for photon energies in the MeV range. For photon energies larger than 1.022 MeV, a photon can produce an electron-positron pair in the field of atomic nuclei transferring all its energy to the two particles. This process is called *pair production* and gets dominant at photon energies of a few tens of MeV (also depending on the detector material). [Lec18]

For most of the discussed processes, the incoming photons are absorbed or transfer a large part of their energy to electrons. Thus, the photon flux I follows an exponential decrease while traveling a distance x inside a material with density ρ

$$I(x) = I_0 \exp\left(-\frac{\mu}{\rho}x\right) \ . \tag{4.2}$$

The mass attenuation coefficient μ/ρ is material specific and depends on the photon energy. [Fle+21]

In this thesis, infrared light at a wavelength of 950 nm is used to generate charge carriers in a silicon detector. At this wavelength, photons have an energy of 1.29 eV and cannot excite electrons from the valence band directly via the 3.6 eV wide direct bandgap into the conduction band (see Section 4.2). However, electrons can be excited via the indirect band gap of 1.1 eV at room temperature including a momentum transfer to phonons. Photons with a wavelength of 950 nm have a mass attenuation coefficient $\mu/\rho = 156\,\mathrm{cm}^{-1}$ in silicon at room temperature [Gre08]. Thus, the photon flux is reduced to a factor of $1/e$ at a depth of $x = 64\,\mu\mathrm{m}$.

4.2. Silicon Sensor Properties

4.2.1. Basic Properties of Silicon and the p-n Junction

Several years of research have shown that silicon is a well suited material for specialized detectors in particle physics. Being a semiconductor, the electronic energy states of silicon can be described by the band model. Intrinsic crystalline silicon at low temperatures is characterized by a full valence band and an empty conduction band separated by the band gap of energetically forbidden states. The band gap has a width of 1.1 eV at room temperature. However, the minimum of the conduction band and the maximum of the valence band in the first Brillouin zone do not coincide at the same wavevector. Thus, an electronic excitation is only possible indirectly via an additional momentum transfer to phonons. This suppresses this transition strongly. The smallest direct band transition has a band gap of 3.6 eV at room temperature.

The conductivity of silicon can be influenced by replacing some silicon atoms in the cristalline lattice with atoms of elements from neighboring groups in the periodic table. This process is called *doping* and inserts additional energy states in the band gap. With silicon being a group IV element, it can be *n-doped* by adding group V elements. Having five instead of four valence electrons, an additional (electron) *donor* state is created close to the conduction band, drastically reducing the energy needed for electron excitation into the conduction band. A typical element to perform n-doping is phosphorus. Analogously, *p-doped* silicon can be obtained by inserting atoms of a group III element, e.g. boron. An additional *acceptor* energy state close to the valence band is created reducing the energy needed for hole excitations.

Bringing in contact p-doped and n-doped silicon, a *p-n junction* is created. As the p-doped area is characterized by an excess of holes as free charge carriers and the n-doped area by an excess of electrons, a gradient in charge carrier concentration emerges at the junction. This gradient leads to a drift of the free charge carriers through the junction into the neighboring area where they recombine with their opposite charge carriers. By this recombination, the remaining dopant atoms (formerly neutral) in the crystalline lattice get ionized and an electric field forms. This field slows down the charge carrier drift until an equilibrium state is reached. In this equilibrium the area around the pn-junction is electrically charged and the number of free charge carriers is largely reduced. Thus, this area is called *space charge region.*

By applying a voltage to a p-n junction, it is possible to reduce or enlarge the area of the space charge region. Connecting the p-doped area to a negative electric potential and the n-doped area to a positive potential withdraws the respective free charge carriers from the doped areas and, thus, increases the size of the space charge region. No large electric current can flow through the p-n junction. This configuration is called *reverse bias* and is the standard operation mode for silicon sensors in high energy physics. Industrially processed semiconductors always have impurities in their lattice structure resulting in additional energy levels in the band gap. This allows to excite electrons e.g. by thermal energy and leads to a small (temperature dependent) current flowing through p-n junctions operated in reverse bias. This current is called *leakage current*. Its temperature dependence is given by

$$I(T) \propto T^2 \cdot \exp\left(\frac{E_a}{2k_BT}\right) \tag{4.3}$$

with E_a being the *activation energy*, k_B the Boltzmann constant and T the absolute temperature [Chi13]. For silicon, $E_a = 1.21\,\mathrm{eV}$.

By connecting the positive electric potential to the p doped area and the negative potential to the n doped area, the p-n junction is operated in *forward bias*. For this configuration the width of the space charge region is decreased by the electric field until the p-n junction gets conductive.

4.2.2. Position Sensitive Silicon Sensors as Particle Detectors

The tracker of the CMS experiment uses position sensitive silicon sensors to reconstruct the tracks of charged particles emerging from the collisions in the interaction point. This chapter concentrates on the functionality of silicon strip sensors, as these sensors are part of the modules investigated within this thesis.

Silicon strip sensors are made of p-n junctions operated in reverse bias. A common p-doped bulk with a thickness of several tens of micrometers to several hundreds of micrometers is processed with highly n-doped (n^+) strip implants on the topside. These implants have typical lengths in the order of a few centimeters and repeat on the sensor surface with a pitch of some tens of micrometers. This sensor configuration is called *n-in-p* sensor and is illustrated in Figure 4.3a. The space charge region in the bulk is growing from the bulk topside by applying a voltage between implants and bulk backside. At the *depletion voltage*, the space charge region is extended over the full bulk. The bulk backside is often made of a thin, highly p-doped (p^{++}) layer to achieve a good ohmic contact with low resistivity to provide the sensor operation voltage. Additionally, the backside is covered by a layer of aluminium. [Har17]

Electron-hole pairs generated by the energy deposition of a traversing particle are separated by the electric field inside the bulk. The electrons drift towards the strips on the topside while the holes are collected on the backside. While drifting, they induce charge into the nearest strips. Thus, spatial information about the particle crossing is generated. The strip charge can be read out by a chip directly connected to the strip implants. This method is called *DC coupled* readout. Alternatively, a thin layer of silicon dioxide SiO_2 can be used to electrically insulate the bulk and n^+ implants from additional aluminium readout strips placed above the strip implants. Thus, the induced signal in the strip implants couples capacitively (*AC coupling*) into the aluminium readout strips and can be read out by a chip. The CMS Phase-2 Outer Tracker uses n-in-p sensors with AC coupled readout for its silicon strip sensors. [CMS17c; Har17]

A 3D schematic of an n-in-p sensor used in the CMS experiment is shown in Figure 4.3b. To measure the bare sensor properties, dedicated probe and bond pads are accessible on the sensor surface. AC pads have direct contact to the aluminium strips, DC pads are connected with the strip implants using *vias* through the SiO_2. To isolate the individual strips from each other, highly p-doped areas called *p stops* are used. The bias ring is used to connect the electric potential on the sensor topside and connects to each DC pad using polysilicon resistors. The guard ring confines all sensor structures towards the sensor edges and can be used to shape the

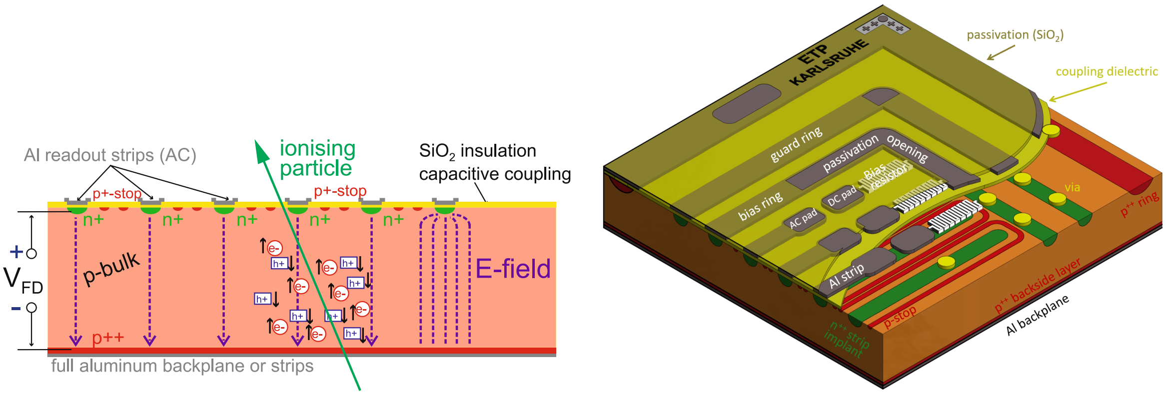

(a) **(b)**

Figure 4.3.: 2D (a) and 3D (b) schematic of an n-in-p silicon strip sensor. At the depletion voltage V_{FD} the space charge region has filled the complete bulk. Charge carriers generated by a crossing particle are separated by the electric field. An SiO$_2$ passivation layer covers the sensor surface except at dedicated spots needed for probing and wire-bonding. Modified from [Har17].

electric field. The complete sensor top surface is covered with a passivation layer of SiO$_2$ for protection. Only at dedicated areas the passivation is missing to allow contacts for probing and wire bonding.

4.2.3. Noise Sources in Silicon Sensors

Within silicon sensors, there are different contributions producing statistical fluctuations of the number of available electrons and holes during sensor operation. This effect is called *noise*. There are four main contributions adding up quadratically to the overall *equivalent noise charge* Q_n:

- The most prominent contribution originates from the load capacitance C_d

  $$Q_{C_d} = a + b \cdot C_d \; . \tag{4.4}$$

  For a silicon strip sensor the capacitance is mainly determined by the strip length. The parameters a and b are readout electronic specific constants.

- *Shot noise* is produced by the leakage current I_L and, thus, scales with temperature and the signal peaking time t_P of the readout electronics by

  $$Q_{I_L} = \frac{e}{2}\sqrt{\frac{I_L \cdot t_P}{q_e}} \; . \tag{4.5}$$

  The Euler number is denoted with e and the electron charge with q_e.

- The *parallel thermal noise* originating from the current through the bias resistance R_P is given by

  $$Q_{R_p} = \frac{e}{q_e}\sqrt{\frac{k_B T \cdot t_P}{2R_P}} \tag{4.6}$$

  and scales with temperature. The Boltzmann constant is denoted with k_B.

- The *serial thermal noise* characterized by the resistance of the aluminium strips R_S can be calculated via

$$Q_{R_S} = C_d \cdot \frac{e}{q_e} \sqrt{\frac{k_B T \cdot R_S}{6 t_P}} \; . \tag{4.7}$$

  This contribution is dependent on the sensor temperature as well.

In order to achieve a good signal to noise ratio with a silicon sensor, it is important to keep these noise contributions as small as possible by tuning the sensor parameters like strip length or inter-strip characteristics. [Har17]

4.3. Radiation Damage

The silicon detectors used in the CMS experiment are exposed to high particle fluxes during the LHC runtime. Traversing particles deposit energy in the silicon and can interact with the lattice atoms and, thus, change the properties of the detector material. This effect is called *radiation damage*. This section will only give a short overview about the microscopic and macroscopic effects of radiation damage. More details can be found in [Lut07] or [Har17]. It can be distinguished between bulk and surface defects which will be discussed separately in Sections 4.3.1 and 4.3.2.

4.3.1. Bulk Defects

Traversing particles can interact with the atoms in the detector bulk via strong and electromagnetic forces. This can result in permanent material changes like displacements of atoms inside the lattice, creation of vacancies or interactions via the strong force resulting in nucleus transformations. Figure 4.4 sketches a selection of common point defects appearing with irradiation in a silicon crystalline lattice. As the processes lead to additional energy levels in the band structure, the material properties change with irradiation. An increase of the detector's leakage current can be observed macroscopically due to new energy levels within the band gap. Additionally, the depletion voltage increases as new acceptor and donor levels change the effective doping concentration. As lattice defects can act as traps for electrons and holes, the charge collection efficiency decreases with irradiation.

The precise type and spatial distribution of defects strongly depends on the particle type and energy, as well as on the irradiation dose. As neutral particles only interact via the strong force with atoms, the emerging defects are forming clusters capable of covering long distances within the bulk. Charged particles can additionally interact via the electromagnetic force and form point like defects with a more uniform spread in the material. To compare radiation damage from different particles and energies, the *Non Ionising Energy Loss* (NIEL) hypothesis is used. On the assumption that the induced radiation damage depends only on the energy transferred during the collisions independently of particle type and energy, it is possible to quantify the damage. As standard the equivalent fluence of 1 MeV neutrons $[\Phi_{eq}] = 1\,\mathrm{n_{eq}}\,\mathrm{cm}^{-2}$ is used.

Annealing

It has been observed that the macroscopic changes to a silicon detector through irradiation, as e.g. increased leakage current, partially reverse with time after the end of irradiation. This effect is called *annealing* and can be used beneficially for the detector performance. Microscopically, lattice defects can either recombine or transform from short living defect types into more stable defects with different properties. Figure 4.5a illustrates the decrease of leakage current in

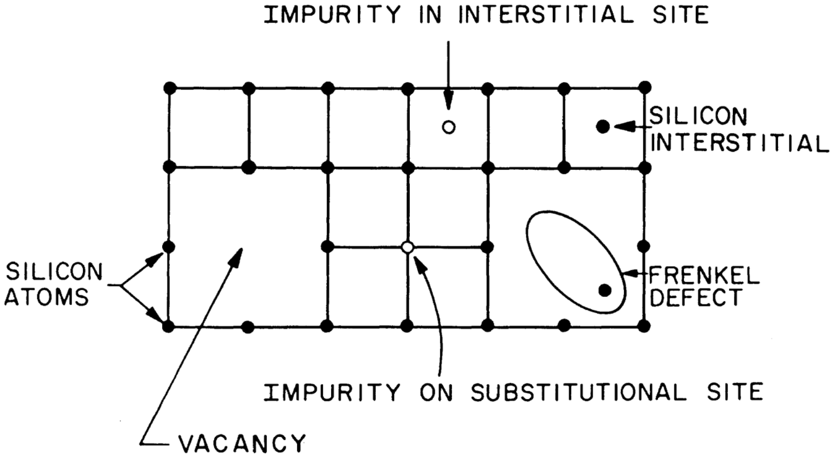

Figure 4.4.: Selection of radiation induced point defects. New energy levels are created by these changes to the lattice structure. This leads to a change of the detector properties. [Lut07]

irradiated detectors with time when kept at room temperature. As the mobility of lattice defects like interstitials or vacancies is strongly dependent on temperature, it is possible to influence the time scale of annealing effects by controlling the temperature. For temperatures below 0°C, annealing effects are negligible due to the vanishing atom mobility.

The annealing behavior of different sensor materials and designs has been subject to several research campaigns within the last years. A large number of irradiation campaigns have been performed within the LHC community to understand and parametrise the sensor performance during the LHC runtime. Additional data are gathered by the operation of the currently installed CMS tracker (e.g. the distribution of sensor leakage current with time). The *Hamburg model* describes the scaling of the effective doping concentration and of the leakage current with the annealing time [Mol99]. It has been shown that there is a proportionality between the volume-generated leakage current and the irradiation fluence. The proportionality factor α is called *damage rate*. By comparing the damage rate for different annealing temperatures and annealing times, it was found that each value of α can be matched with a corresponding equivalent annealing time at room temperature (21°C). Thus, the normalized equivalent annealing times at room temperature are used to quantify the sensor annealing. More details can be found in [Mol99].

While the leakage current decreases with increasing equivalent annealing time, the effective doping concentration N_{eff} shows a more complicated trend depicted in Figure 4.5b. Overall, N_{eff} is increased by irradiation. During the first minutes of annealing at 60°C, it shows a beneficial decrease within the *beneficial annealing* period. For longer annealing N_{eff} increases within the *reverse annealing.*

Taking into account all these effects is important to schedule dedicated annealing times for the CMS experiment during the LHC runtime in order to optimize the detector performance.

4.3.2. Surface Defects

Particles can also create radiation damage in the SiO_2 layer and in the interface between silicon and silicon dioxide. These effects are summarized under the name of *surface defects.* The main energy deposition is done via ionisation creating electron hole pairs. SiO_2 is an insulator and, therefore, the recombination rate is smaller than in silicon. This leads to a longer lifetime of the newly produced charge carriers. Already existing defects can capture the charge carriers.

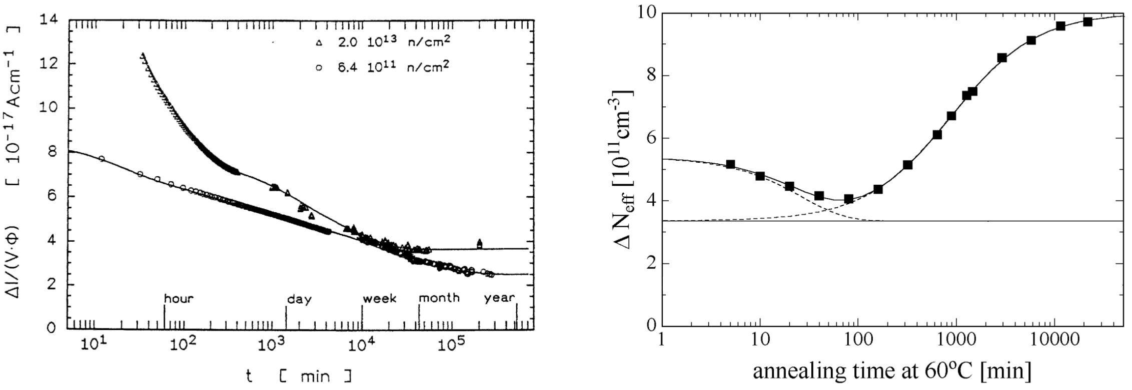

(a)

(b)

Figure 4.5.: (a) Dependence of the detector leakage current on the annealing time [Lut07]. Through the partial defect recombination and transitions from short living into more stable defects, the detector properties can be improved by annealing. (b) Change of the effective doping concentration with annealing [Mol99]. After a first decrease within the beneficial annealing, the concentration increases in the reverse annealing phase.

In presence of an electric field the charge carriers are separated within the oxide and can accumulate near the SiO_2-Si interface leading to macroscopic changes of the sensor properties, mainly for the inter-strip parameters like inter-strip capacitance and inter-strip resistance. Due to the higher mobility of electrons compared to holes, the overall oxid charge turns positive. This leads to the formation of an electron accumulation layer at the interface between silicon dioxide and silicon, significantly reducing the isolation between neighbouring strips. A more detailed treatment of surface damage can be found in [Lut07].

Part II.

Main

5

2S Module Assembly and Qualification Test System

For the Phase-2 Upgrade of the CMS Outer Tracker, 7680 2S modules and 5615 PS modules have to be built until 2025 to be integrated into the TB2S and TBPS ladders and the TEDD structures (see Section 3.2.1) afterwards. In 2029, the upgraded CMS detector will start operation in the High-Luminosity LHC phase. In order to realize this time line, the workload is shared between different institutes all over the world.

The *Institute of Experimental Particle Physics* (ETP) at *Karlsruhe Institute of Technology* (KIT) is one of the *2S module assembly centers* in the CMS community. To assemble modules of the highest quality with comparable results between all CMS module assembly centers, common assembly procedures, hardware and test systems are being developed. For 2S modules, the baseline assembly procedure is based on dedicated mechanical fixtures called jigs. The assembly line currently in preparation at ETP is presented in Section 5.1. At the end of the assembly process, each module has to be tested for its functionality before shipping it to the integration sites. Therefore, a test station has been developed at ETP within this thesis. It is called the *Outer Tracker* (OT) *Module Test Station* and its design is introduced in Section 5.2. Fully assembled modules are shipped to the *module integration centers* in the CMS community, where they are mounted on larger detector support structures called *ladders* and *dees* (see Section 3.2.1).

5.1. 2S Module Assembly at ETP

The current time schedule for the CMS Outer Tracker module assembly foresees an eight month long pre-production to slowly ramp up the module throughput starting in March 2023. Subsequently, a two years production period at full capacity will take over, ending in October 2025. As a 2S module assembly center, ETP plans to build between 1300 and 2000 2S modules during 400 working days. This results in an average production rate of three to five modules per day. To compensate for days with a lower module throughput, the production line at ETP will be designed with a maximum module throughput of six modules per day. The complete production line will be placed inside one large clean room guaranteeing small distances between the different assembly steps and, thus, minimizing the risk of contamination, transportation accidents and delays within the production process.

Figure 5.1 summarizes the 2S module assembly steps. Tests that need to be performed after each assembly step to monitor the module quality along the process are displayed additionally. The assembly process can be divided into two parts. First, the two silicon sensors are glued onto carbon fiber reinforced aluminium spacers forming the *bare module*. The corresponding assembly steps are shown in the first row of Figure 5.1 and are discussed in Section 5.1.1. The second part of the module assembly consists of attaching the hybrids to the bare module, connecting each sensor strip to the readout channels on the frontend hybrids and testing each channel for its functionality. The involved steps are summarized in Section 5.1.2. A detailed

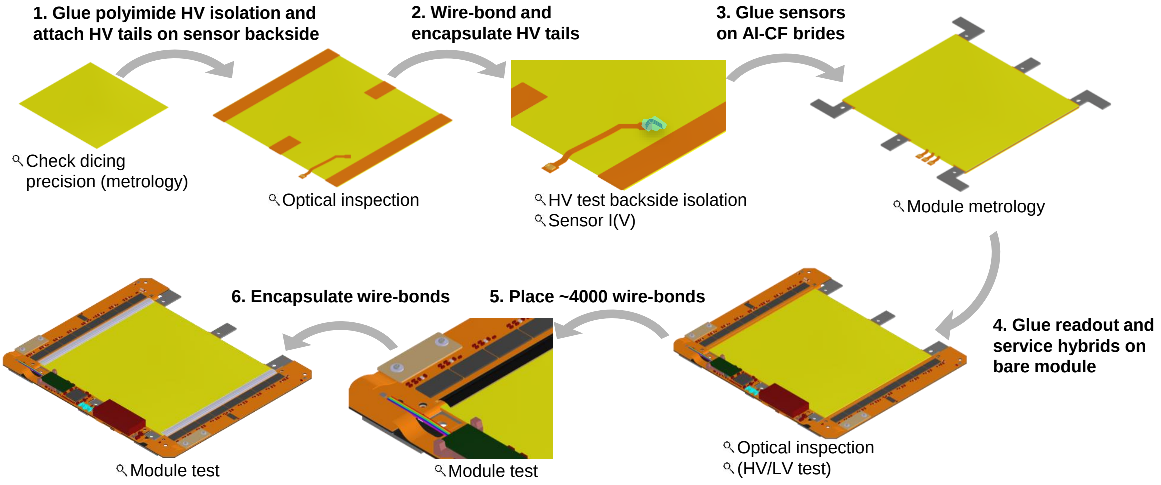

Figure 5.1.: Sketch of the 2S module assembly process. The upper row displays the necessary steps to build a bare module. After gluing polyimide strips onto the sensor backsides, the sensors are glued onto the same set of carbon fiber reinforced aluminium spacers. By attaching the hybrids to the module, connecting the hybrid readout channels with wire-bonds to the sensor strips and encapsulating the bond rows, the module assembly is completed. The tests performed during the individual assembly steps are marked with magnifying glasses. Updated from [Mai19].

description of the 2S module assembly process including a discussion of the necessary jigs can be found in [Mai19].

5.1.1. Bare Module Assembly

The bare module assembly starts with the reception of bare silicon sensors in the module assembly centers. The sensors are produced by the Japanese company *Hamamatsu Photonics K.K.* and sent to CERN for further distribution within the CMS community in small groups called *batches*. To continuously monitor the sensor quality during the production process, the batches are shipped to the CMS *sensor qualification control* (SQC) *centers* where sensor properties are measured for a sample of a few sensors to validate each sensor batch. Afterwards, the SQC centers send the sensors further to the module assembly centers.

As a main design feature of the new outer tracker modules, the p_T-discrimination logic relies heavily on a good strip-to-strip alignment of the two sensors in a module. For the 2S module assembly, the alignment of the sensors is guaranteed using precisely manufactured jigs with a common set of alignment pins against which the two sensors are pushed. Thus, the orientation of the outer sensor edges with respect to the strip implants is of high importance. As the rectangular sensors are cut out of the circular silicon wafers at the manufacturer (called *dicing*), the first test performed within the 2S module assembly process is the measurement of the dicing precision of the received sensors. Dedicated *metrology stations* have been developed within the CMS community for this task. At ETP, a semi-automatic station measures the angle between the dicing edge and the strip implants. A five megapixel camera mounted above a four-axis motor stage holding the sensors takes pictures along all four sensor sides. Using offline pattern recognition, it is possible to determine the dicing edge angle. The manufacturer is constrained to achieve a dicing precision of less than 200 µrad. The metrology station at ETP reaches a precision of ±25 µrad, which is sufficient to confirm the dicing quality before assembly. More details about the station can be found in [Mai19].

After the metrology measurement, 25 µm thick polyimide strips are glued to the sensor backsides at the positions where the carbon fiber reinforced aluminium (Al-CF) bridges will be placed in a later step. This is necessary to electrically isolate the sensor backside from the Al-CF bridges as the negative sensor bias potential of up to −1000 V is applied to the sensor backside while the bridges are connected to the ground of the mechanical support structures. A dispensing gantry applies a well defined amount of low viscosity epoxy resin at dedicated positions on the sensor backsides. By placing the sensor on a dedicated gluing jig, it is possible to precisely lower the polyimide strips via pick up tools onto the glue pattern. Additionally, the high voltage tails used to apply the bias potential to the sensor backside are glued at their positions in the same step. As there are slightly different HV tail geometries for top and bottom sensor, this gluing step defines the sensor position in the module. After glue curing, an optical inspection is made to guarantee a precise polyimide strip-to-sensor alignment and a uniform glue distribution.

To electrically connect the HV tail with the sensor backside, wire bonds are placed from an exposed pad on the HV tail to the sensor. Therefore, the sensors stay on the gluing jig which can be placed inside the wire bonding machine. To protect the wire bonds from mechanical damage, a small drop of silicone elastomer is placed on top using a manual dispenser. This procedure is called *encapsulation*.

When the encapsulation material has cured sufficiently to allow further handling, the sensors can be put into the *HV / I(V) Test Station* developed at ETP [Mai19]. Each sensor is placed onto a brass jig providing rails at the positions of the Al-CF bridges. Thus, only the polyimide strips have contact to the brass jig and it is possible to measure the isolation quality of the polyimide strips. A voltage of up to 1000 V is applied between the brass rails and the sensor backside (via the HV tail) and a custom electronic circuit monitors the current to detect electric sparks indicating insufficient isolation. Additionally, it is possible to measure the sensors leakage current in dependency of the bias voltage I(V) by connecting a bias needle to the bias ring on the sensor topside. This test allows to guarantee a basic sensor functionality before building the bare module as the SQC centers only test sensors on a sample basis and all sensors undergo shipping processes and handling steps before the start of module assembly. Only functional sensors with adequate HV isolation and I(V) characteristic proceed in the assembly process. More details about the HV / I(V) Test Station can be found in [Mai19].

To build the bare module, the two sensors equipped with polyimide strips have to be glued onto the Al-CF bridges. The first sensor is placed face-down onto a dedicated jig, pushed via springs against three alignment pins. To hold the sensor in place during the bare module assembly, vacuum is generated between the jig and the sensor. The bridges are coated with a boron nitrite filled epoxy resin and then lowered via positioning pins onto the first sensor. The second sensor is lowered onto the bridges and pushed in place using the same alignment pins and pushing springs as for the first sensor. Afterwards, the bare module stays in this configuration until the glue is cured.

As a final step during the bare module assembly, the strip-to-strip alignment of the two sensors is measured. The metrology station already described above allows to mount the bare module on the four-axes motor stage. Using a laser-based distance measurement, the alignment of the sensor edges of top and bottom sensor can be measured on all four bare module sides. By combining this measurement with the previously gathered results about the dicing quality of each individual sensor, the module's strip-to-strip alignment can be calculated. The setup at ETP achieves uncertainties on the strip-to-strip alignment of less than 40 µrad. The maximum allowed tilt between the strips is 400 µrad. [Mai19]

5.1.2. From the Bare Module to the Final Module

The two frontend hybrids (FEHs) and the service hybrid (SEH) are centrally designed and ordered by CERN. At the time of writing this thesis, the market survey for starting the final hybrid production is ongoing. From CERN, the hybrids are distributed to the module assembly centers. By connecting the SEH via its L-shaped connectors to the two frontend hybrids, a so-called *module skeleton* is built. Therefore, a dedicated aluminium plate has been designed at KIT to hold the hybrids in place. With the module skeleton, it is possible to perform a reception test of the hybrids before assembling them into the module to guarantee electrical functionality.

To glue the hybrids to the bare module, the same boron nitrite filled epoxy resin is used as for gluing the sensors to the Al-CF bridges. The bare module is placed in a dedicated assembly jig designed and produced at KIT by S. Maier. The glue is applied to the topside of the L-shaped corners of the Al-CF bridges. Without disconnecting the module skeleton, the hybrids can be lowered onto the gluing points and fixed at the nominal positions using alignment pins. When the glue has cured, the HV tails can be connected on the bottom side of the SEH and an optional HV / LV test can be performed checking the electrical integrity of the module skeleton. To check the connection of the HV tails to the SEH's HV circuit, a probe needle has to be placed on the top and bottom sensor bias ring to close the electric circuit. At ETP, this test is skipped to avoid the risk of damaging the bare module by placing the bias needle, as the HV bond connection was already tested in the HV / I(V) test.

For the next assembly step, the module is placed in a semi-automatic bonding machine of the type *Hesse Bond Jet 820*. In total 4064 readout bonds are placed between the frontend hybrid pads and the AC pads on the sensors. Additionally, bias bonds between the bias ring and dedicated ground pads on the FEHs are placed on each sensor corner. At the end of the bonding process, the wire bonds are manually optically inspected to check for obvious faults like e.g. missing wire bonds.

At this stage, the 2S module can be checked for its complete functionality for the first time. Therefore, the module is placed on an aluminium carrier providing two plexiglass plates above the two sensors to ease the module handling and minimize the risk of damage. Until the module integration into the detector support structures, the 2S modules stay on the same carrier plate. To perform the functional module tests, the module carrier is mounted in a dedicated station. Within the scope of this thesis a station to perform the functional tests with 2S and PS modules has been developed and is introduced in Section 5.2.

If the module has passed the functional testing, the wire-bonds are covered with an encapsulation material applied by a dispensing gantry over all four bond rows. This reduces the risk to damage the bonds during module handling and transport. Additionally, it has been observed that bonds can be damaged due to vibrations [Bol+03] or electrochemical corrosion. These risks are additionally reduced by the encapsulation. After the encapsulation, all modules are tested again for their complete functionality.

5.2. The Outer Tracker Module Test Station

The workload of assembling all outer tracker modules for the Phase-2 Upgrade of the CMS experiment is shared between the module assembly centers in the CMS community. This includes the development and fabrication of common assembly procedures and jigs as well as test systems to qualify the module assembly process. As presented for the 2S module assembly process in Section 5.1, each module – 2S and PS – will be tested for its complete functionality twice at the end of the assembly process (before and after encapsulation). Additionally, each integration center has to perform reception tests for each received module from the assembly sites. To achieve comparable test results between the different sites, it has been decided to develop a common test station and to define a common set of functional tests. Within this thesis, the *Outer Tracker* (OT) *Module Test Station* has been developed, produced and distributed to the CMS community. The station's design is summarized within this section and a first set of functional tests performed with prototype 2S modules is presented.

5.2.1. Conceptual Requirements

There are several requirements to be taken into account for designing a common test station for functional testing of 2S and PS modules during module production:

- **Providing hardware for testing the complete module readout chain:** The module functional tests at the end of the assembly procedure have to verify the functionality of the complete module readout chain and have to characterize the module quality. Therefore, the module test station needs to provide all hardware necessary to check for possible module defects as e.g. missing bonds or sensor strip defects.
- **Quick and safe module fixation:** The test station will be integrated in the module assembly work flow at the assembly sites. As each module needs to be tested twice inside the station, it is crucial to minimize the time needed to mount or remove modules in order not to slow down the production line. Therefore, a quick and easy to handle fixation mechanism needs to be developed to hold the modules in place. At the same time, the usage of loose parts like e.g. screws for module fixation has to be avoided in order to miminize the risk of damaging the modules during handling.
- **Compact design:** The module assembly is done inside clean room facilities. As clean room space is expensive compared to regular laboratory space and, thus, often limited at the assembly and integration sites, a compact station design is desirable to efficiently use the available space.
- **Environmental monitoring:** The functional module tests can be performed at room temperature as there are additional thermal module tests foreseen in dedicated setups at each assembly site. However, environmental parameters like air and module temperature as well as relative air humidity need to be monitored. Thus, it is possible to guarantee module operation within the necessary environmental conditions developed by the CMS community. It has been found that the electrical characteristics of 2S sensors deteriorates with increased relative humidity leading e.g. to an exponential increase of the leakage current called *breakdown*. Therefore, these sensors have to be operated below a relative humidity of 30% to achieve comparable test results. Additionally, information about environmental parameters simplifies the comparison of test results from different working days and institutes.
- **Compatibility with automated testing:** The station design needs to allow for automated module testing, minimizing the need for human interaction with the hardware during the complete test procedure.

Based on these requirements the design of the OT Module Test Station has been developed and is presented in the next section.

5.2.2. Test Station Design

2S and PS modules are placed on aluminium carriers after wire-bonding to simplify the handling and minimize the risk of damaging the modules. Thus, the OT Module Test Station is designed to house the modules on their respective carriers. As the geometries of the 2S and PS module differ substantially, each module type uses a dedicated carrier design. Both carrier designs are not finalized yet as the module designs themselves are still subject to several changes during the prototyping phase. 3D renderings of the current designs of both carriers are shown in Figure 5.2. Within this thesis, the four carrier sides are named *front*, *back*, *left*, and *right* as denoted in Figure 5.2. In 2021, the CMS community has agreed on assimilating the outer dimensions of both carrier types in order to simplify the design of test stations and transport equipment [CMS21b]. This includes the following decisions:

- The aluminium carrier plate has a thickness of 4 mm and outer dimensions of 197.5 mm × 176.6 mm for 2S modules and outer dimensions of 182.5 mm to 197.5 mm × 176.6 mm for PS modules. The exact length of the longer side of the PS module carrier is not yet fixed.

- Both carrier types will provide a clearance space of at least 10 mm along the two long edges of the carriers. This space can be used by external systems (e.g. fixation mechanisms) to contact the carriers.

- Both carrier types will use a common circuit board developed at Fermilab to provide a standardized *Molex* connector [Mol22] to external systems for applying the module voltages. The optical fiber emerging from the VTRx+ is connected to a sacrificial pigtail in order to mitigate the risk of breaking the fragile VTRx+ fiber or contaminating the optical connector at the VTRx+ during the module connections in several test systems. The fiber from the VTRx+ and the sacrificial pigtail are stored on the carrier and guided to an adapter providing an MPO connection to external systems. The positions of the MPO connector and the electric circuit board on the short edge of the module carriers are fixed and the same for 2S and PS module carriers.

- The position and dimensions of the bottom plexiglass plate are fixed for both carrier types. Additionally, the locations of four rubber feet on the bottom side of the carriers are fixed.

Taking into account these geometrical boundary conditions, a design for the fixture of the module carriers for the OT Module Test Station was developed. The fixture consists of a base plate onto which four corner plates are screwed. This configuration is shown in Figure 5.3a. To mount the modules, the left and back sides of the carrier are brought into contact with the four pins mounted in the corner plates. Then, the carrier is lowered onto all four corner plates. Thus, the front carrier edge gets in contact with two lateral spring pushers. These pushers hold the module carrier in place by pressing the carrier against the pins at the carrier back side. The four corner plates support the carrier at the bottom carrier edges as shown in Figure 5.3b. The fixture baseplate and the four corner plates are made of electrically conductive polyethylene with a thickness of 15 mm. This ensures that electrostatic charge cannot accumulate at the fixture's surface and secures the modules from electrostatic discharges.

A commercially available aluminium box developed by the German company *Gmöhling Transportgeräte GmbH* was identified as a suitable housing for the test station. As it is completely made of 1.5 mm thick aluminium, the box forms a Faraday cage and shields the modules from external electromagnetic influences. Lid and corpus are equipped with engaging profiles at their respective interfaces. Thus, the closed box also provides shielding against light. Due to limited availability of boxes by the producing company, it was necessary to order two different box types to provide enough boxes for the CMS community. The preferred type *G-Case A 1439/19* provides outer dimensions of 460 mm × 380 mm × 122 mm, and a total of 17 boxes was received. To reach the required number of 25 boxes, eight boxes of the type *G-Case A 1489/24* were ordered. These boxes differ from the preferred type by an increased height of

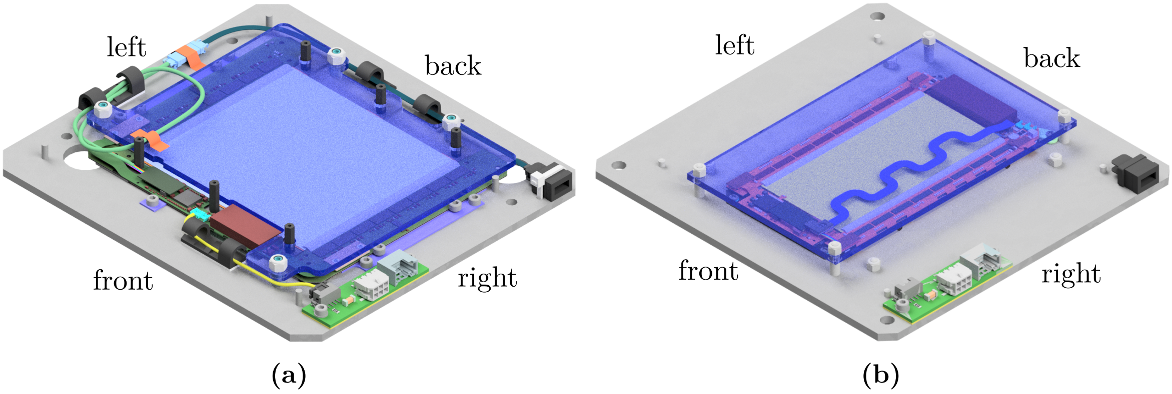

Figure 5.2.: 3D rendering of a 2S module (a) and a PS module (b) mounted on their respective aluminium carrier plates. To simplify the development of common test systems for 2S and PS modules, the outer dimensions and the electrical and optical connectors have been matched and fixed for both carrier types. While there have already been studies how to guide the electrical cables and optical fibers to the interface connectors for the 2S module carrier, only the location of the interface connectors is currently defined for the PS module carrier. Within this thesis, the four carrier sides are named *front*, *back*, *left*, and *right* as shown.

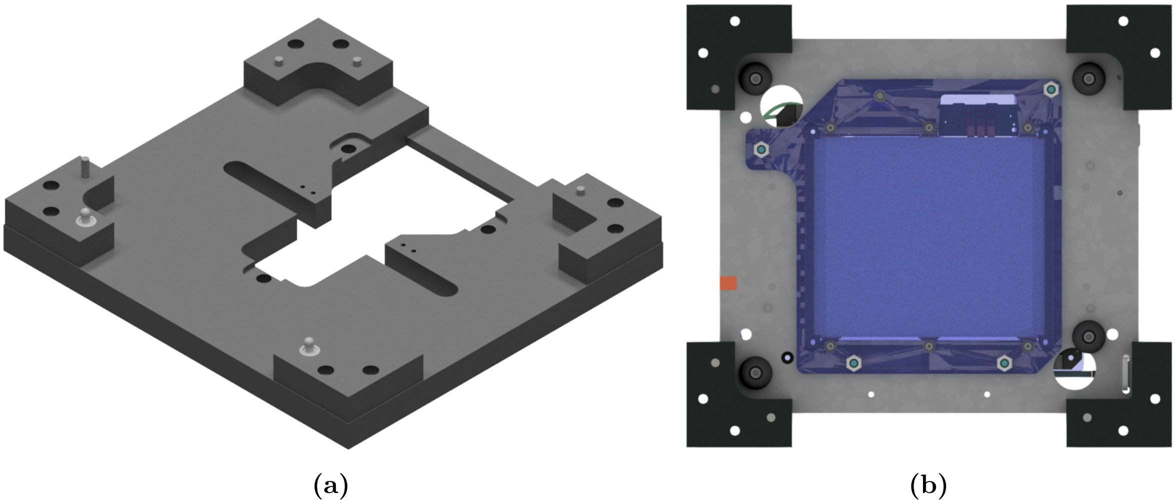

Figure 5.3.: (a) 3D rendering of the fixture design used to mount module carriers in the OT Module Test Station. It consists of a baseplate and four corner plates. (b) The four corner plates support the module carrier at the carrier edges. The base plate is not shown in this rendering.

the lid resulting in outer dimensions of 460 mm × 380 mm × 157 mm. Additionally, there are small differences in the boxes closing mechanisms, but this does not affect the boxes suitability for testing Outer Tracker modules.

Figure 5.4 displays the OT Module Test Station with all necessary components installed. The module fixture is screwed onto the bottom of the aluminium box. This connects the box electrically with the conductive polyethylene. Thus, the box needs to be put onto an electrostatic discharge safe table or mat at the institutes to ensure a successful removal of possible charge carriers.

The module test stations have to ensure that the modules are operated within the required environmental conditions. As the performance of the silicon sensors worsens with increased relative humidity, it has been specified to operate sensors and modules at relative humidities below 30%. Thus, each module test station is equipped with a 6 mm tube pass-through at the box backside to connect to a dry air supply. Using a manual valve at the side of the box, the air flux into the box can be controlled. The module tests will be carried out at room temperature and the estimated time to perform a complete set of functional tests during production is in the order of a few minutes. With respect to this short time scale and the goal to keep the required hardware for each test station as simple as possible, it has been decided to use passive module cooling via dry air rather than implementing an active cooling liquid circuit. Thus, parts of the dry air flux entering the module station is guided to two outlets installed in the box lid. These outlets are placed on top of the shielded DC-DC converters of the 2S and PS modules as these chips dissipate the most heat on the module. A second manual valve is used to control the dry air flux onto the modules. Air temperature and relative humidity are measured by an *SI7021-A20* sensor [Sil16]. A dedicated circuit board including an *Arduino Micro* microcrontroller board is used to read out the sensor.

In order to achieve a compact design, all external connections to the box are made on the box backside. Besides the already mentioned 6 mm tube pass-through for dry air, a cable gland is installed to insert the optical fiber. A dedicated 3D printed cylinder is used to enclose the fiber within the cable gland and achieve a light-tight feed-through. A USB-A connector allows to connect the Arduino Micro board to a readout computer. The module's high voltage is applied via an SHV connector. To guarantee operational safety of the station, the high voltage line is interrupted by a relay which only closes when the box is completely shut. Therefore, a magnetic reed relay and a corresponding magnet are installed in the box corpus and lid. The module's low voltage levels as well as the operation voltage of the reed relay of 5 V are applied via four banana connectors.

For a complete functional test of the module readout chain, it is necessary to generate charge in the sensors which is afterwards read out by the chips. This can e.g. be done using a radioactive source placed above the sensors. However, it is not clear that all clean room facilities and the personnel at the module assembly centers are certified by radiation protection to handle radioactive sources. Thus, a system based on infrared LEDs was developed at ETP to allow charge generation in both sensors of 2S modules. This system is called *Karlsruhe Infrared Array* and will be described in detail in Section 5.2.3. The test station design is fully compatible with the LED array design. The necessary adaptations to be done during the station assembly are described in Section 5.2.4. As using LEDs for charge generation in PS modules does not work for the PS-p sensor being covered by an aluminium carbon fiber base plate, the LED array will only be used for functional tests of 2S modules. Thus, two flavors of the OT Module Test Station exist: stations without the LED system (as shown in Figure 5.4) mainly used for PS module testing, and stations with the LED system mainly used for 2S module testing (shown in Figure 5.9).

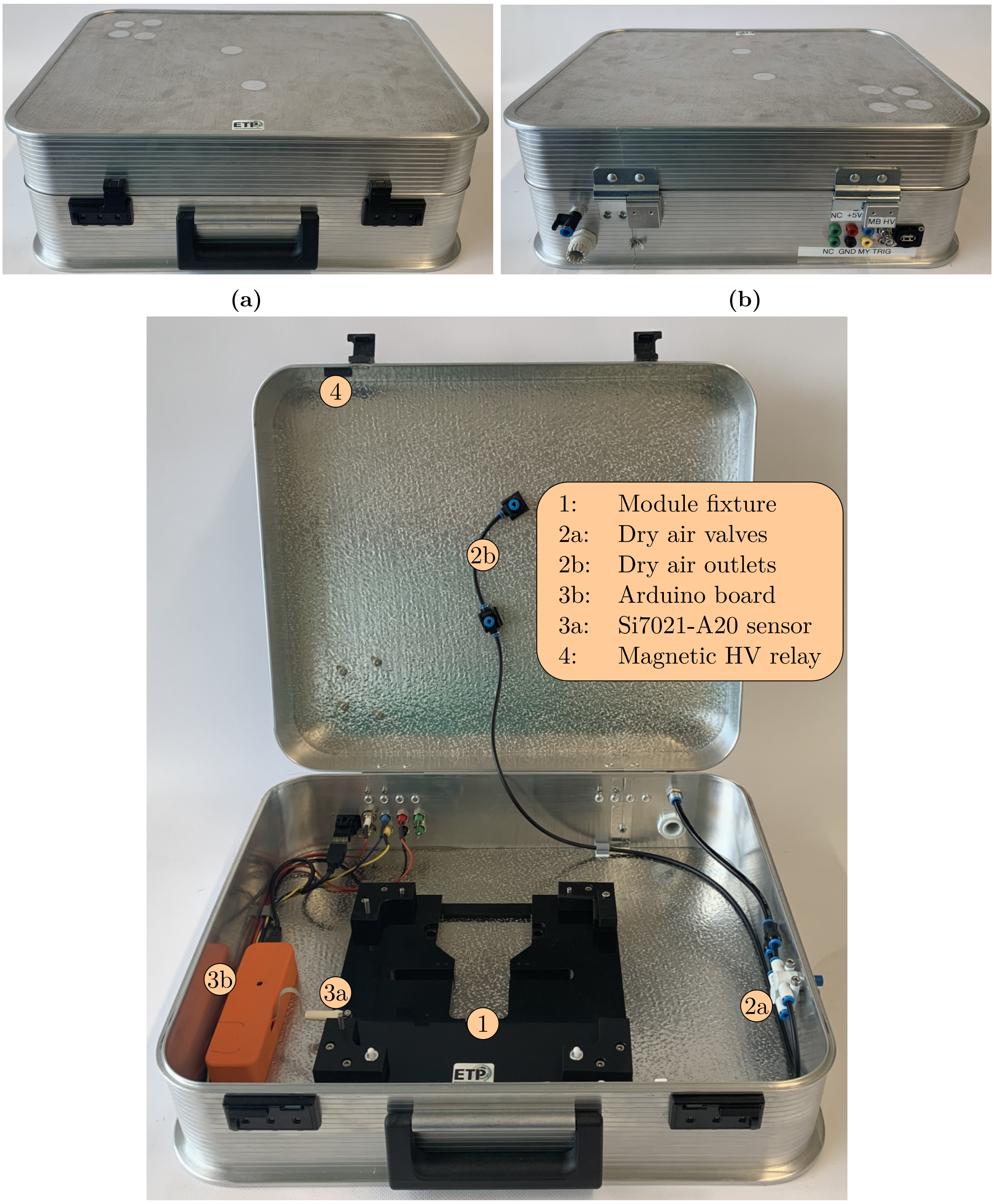

(a) **(b)**

(c)

Figure 5.4.: The OT Module Test Station equipped with all necessary components. A photo of the closed boxes is shown from the front (a) and the back (b). All external connections are realised at the backside of the box via patch panels. (c) A view of the inside of the box with mechanical module fixture, dry air guiding and *Arduino Micro* based environmental monitoring.

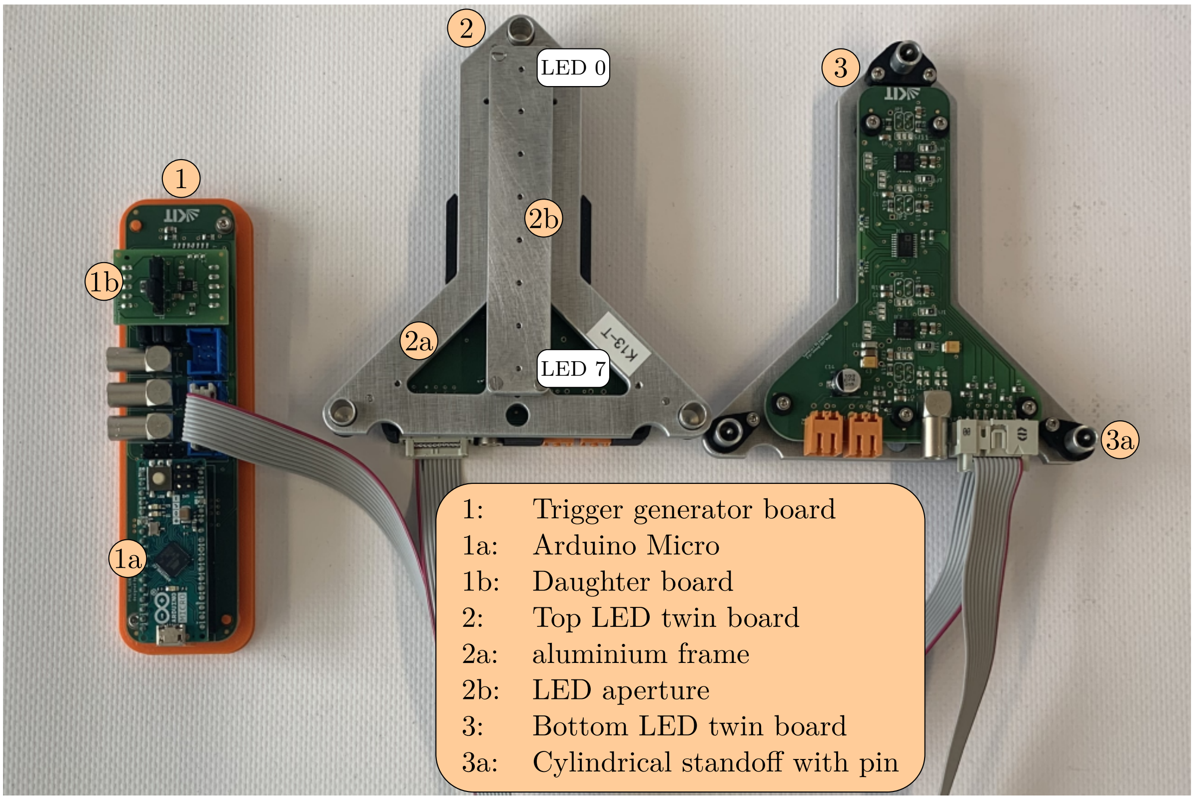

Figure 5.5.: A complete KIRA system consists of a trigger generator board and two LED twin boards to illuminate the top and bottom sensors of a 2S module. Each twin board houses eight LEDs covered by an aluminium aperture. The LEDs are numbered as indicated. The trigger pulse is transferred from the generator board to the twin boards via LEMO cables. A ribbon cable is used for I^{2}C communication between the Arduino and the chips on the twin boards. The twin boards are positioned using cylindrical standoffs above and below a 2S module mounted on its carrier.

5.2.3. The Karlsruhe Infrared Array

The *Karlsruhe Infrared Array* (KIRA) is a system to generate charge in silicon sensor modules using infrared light. For the usage in functional testing of 2S modules during module assembly, the KIRA system was designed to achieve full sensor illumination of top and bottom 2S sensors. The KIRA prototype development and commissioning was done within a master thesis supervised during this thesis and is described in detail in [Bra20]. The production and testing of the final KIRA system and its integration into the OT Module Test Station has been performed within the scope of this thesis. A complete KIRA system consists of a trigger generator board and two LED twin boards as shown in Figure 5.5.

The Trigger Generator Board

The main task of the trigger generator board is to create a well defined rectangular pulse which can be used to drive the LEDs and which serves as a trigger input for the module readout. As the module readout operates at the LHC bunch crossing frequency of 40 MHz, a pulse width of less than 25 ns is desired to create a defined light pulse within one readout chip clock cycle. A trigger frequency of a few kilohertz is adequate to keep the time for data taking short during

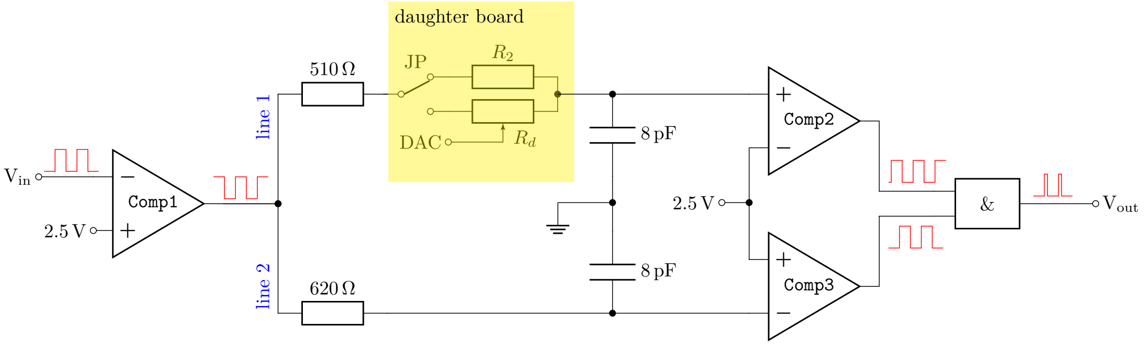

Figure 5.6.: Simplified schematic of the KIRA trigger generator circuitry. A rectangular pulse generated by a digital pin of an Arduino Micro is fed to the circuitry as V_{in}. By splitting the signal in two lines and delaying line one with respect to line two via different resistor capacitor elements, it is possible to generate a short rectangular pulse V_{out} using an AND gate. Modified from [Bra20].

functional testing. These characteristics can be achieved with a commercially available Arduino microcontroller board combined with a dedicated circuit board.

Due to its small form factor, an Arduino Micro board was chosen for the trigger generator board. The microcontroller generates a rectangular pulse with a duty cycle of 50% at one of its digital output pins reaching maximum frequencies of up to 100 kHz. This pulse is used as an input to a circuitry based on a design presented in [Wil04]. Figure 5.6 sketches the circuitry featuring two fast integrated circuits (ICs). After inverting the pulse using one input of a four channel comparator IC (`Comp1`), the signal is fed to two other channels of the comparator IC via resistor capacitor elements. By choosing different resistors in the two paths, it is possible to delay signal line one with respect to line two. Additionally, line two is inverted at the comparator IC `Comp3`. By using a fast AND gate IC, it is possible to generate a short rectangular pulse from the two comparator outputs for each rising edge of the input pulse. The output pulse length is defined by the time delay between the two signal lines and, thus, mainly by the resistance of R_2. Using a fixed resistance of $R_2 = 1.6\,\text{k}\Omega$ results in a pulse length of 20 ns.

To keep the KIRA system flexible for future applications, R_2 can be replaced by a digital rheostat R_d of the type *AD5272* [Ana13]. R_2 and the R_d are placed on a separate daughter board. Jumpers (JP) on the daughter board allow to choose between the two resistors. The resistance of the AD5272 chip can be selected in its internal DAC units via the I^{2}C protocol. The resulting trigger pulses for $R_2 = 1.6\,\text{k}\Omega$ and four DAC values for R_d are shown in Figure 5.7a. The lowest pulse length achievable with the digital rheostat is approximately 40 ns. As shown in Figure 5.7b, the digital rheostat can produce pulse lengths up to 5.6 µs. The trigger pulse V_{out} can be accessed at three LEMO connectors on the trigger generator board.

The Arduino board on the trigger generator board is additionally used to communicate with different chips within the KIRA system and the test station via the I^{2}C protocol. Therefore, the trigger generator board houses two additional connectors. One is used for a ribbon cable to connect to the LED twin boards. The second connector connects to the SI7021-A20 sensor for temperature and humidity reading which is installed in every test station. A picture and electrical schematics of the trigger generator board components can be found in [Bra20].

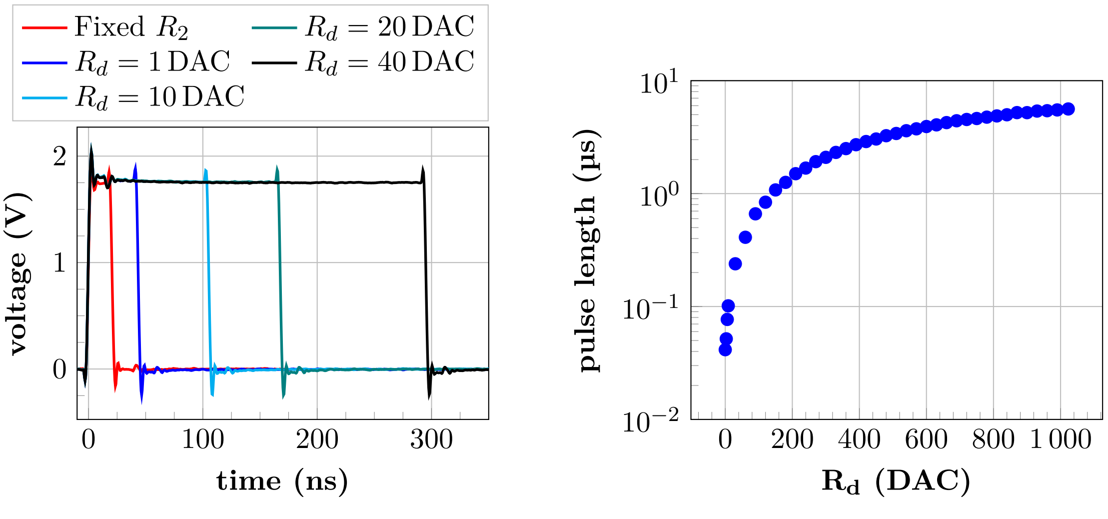

(a) (b)

Figure 5.7.: The KIRA trigger pulse length is defined by a fixed resistor $R_2 = 1.6\,\mathrm{k\Omega}$ or a digital rheostat R_d. (a) Using R_2, a pulse length of 20 ns is achieved. The lowest DAC setting of R_d corresponds to a pulse length of approximately 40 ns. (b) Scanning the full DAC range of R_d yields pulse lengths between 40 ns and 5.6 µs.

The LED Twin Boards

There are two LED twin boards in every KIRA system. Each board houses eight high power infrared LEDs of the type *SFH 4180S* made by *OSRAM Opto Semiconductors* [OSR21]. These LEDs emit light at a mean wavelength of 940 nm and achieve rise times of 9 ns and fall times of 16 ns. The LEDs are placed on a separate circuit board that is connected to the back side of a larger circuit board housing the LED driver circuits. To control the LED light output, the commercially available driver IC *iC-HG30* [iC-19] is used. It provides six independent voltage-controlled current sinks which can be operated at switching frequencies of up to 250 MHz. Each channel's current output can be individually controlled using a pulsed signal provided in *transistor-transistor-logic*. Different current levels per channel can be achieved by applying analog voltages to the IC control input pins.

Two iC-HG30 chips per twin board are used to control the eight LEDs. Each iC-HG30 channel receives the pulse from the trigger generator board which is passed to the twin boards via LEMO cables. An eight channel DAC *AD5675R* [Ana18] controls the current fed to each individual LED per trigger pulse and, thus, controls the LED intensity. The DAC is programmed via the $\mathrm{I^2C}$ protocol. Electrical schematics of the twin board components can be found in [Bra20]. The 16-bit DAC values correspond to voltage steps between 0 V and 2.5 V. It is possible to configure the DAC output to provide a voltage range up to 5 V but this setting is not used for measurements within this thesis.

To place the twin boards above or below a 2S module, the circuit boards are mounted on aluminium frames as shown Figure 5.5. Each frame provides three cylindrical standoffs whose positions coincide with three of the five mounting points of a 2S module on its carrier. Thus, the top twin board can be lowered onto the M2 spacer nuts holding the 2S module on the carrier plate. This aligns the eight LEDs on the bottom side of the KIRA system along the center line of the 2S sensor. For the bottom KIRA system, the system can be aligned with respect to the module using 1.5 mm pins glued into the cylindrical standoffs which fit into the M2 Allen screw heads on the bottom side of the carrier. To secure the sensitive LED surfaces from damage and to create equidistant light sources along the sensor, an aluminium aperture with eight 1.5 mm wide openings is placed above the LEDs. During operation, the apertures of bottom and top twin boards are in contact with the plexiglass plates on the module carriers. The LEDs are numbered from zero to seven as marked in Figure 5.5.

It has been shown in [Bra20] that placing the twin boards along the sensor center line allows to create enough charge to be seen by the strips on both sensor halves at the same time. Additionally, the ADC voltage range used to control the LED intensities is suitable to reach full illumination of all 2032 strips per 2S sensor. Thus, each LED is responsible to illuminate 127 strips per frontend hybrid during functional testing. Prior to using the KIRA system in functional testing, each system needs to be calibrated to fine tune the ADC settings for each LED. The calibration procedure and results are described in Section 5.2.5.

5.2.4. Implementation of KIRA in the Test Station

To allow automated module testing during production, the KIRA system needs to be integrated into the OT Module Test Station. Therefore, the module fixture baseplate has been adapted to the KIRA twin board design by adding a dedicated recess. This recess is already shown in Figure 5.3a. Using cylindrical standoffs, the bottom twin board is placed onto spiral springs protruding from dedicated drilled holes in the baseplate. As the baseplate recess only allows for lateral twin board displacements of approximately 1 mm, the board is held in place and pressed upwards by the springs. By adjusting the positions of the four corner plates mounted on the baseplate, a good alignment of the 2S module carrier (being in contact with the four alignment pins protruding from the corner plates) and the twin board can be achieved. Thus, the 1.5 mm pins in the twin board standoffs align automatically with the M2 Allen screw heads as described in the previous section. The bottom plexiglass plate gets into contact with the LED aperture and compresses the spiral springs slightly. Figure 5.8 summarizes this spring based alignment principle. As the positions of the M2 screws differ for a PS module carrier, the 1.5 mm pins of the bottom twin board cannot align. By compressing the spiral springs, the board gives way and the PS module carrier can be installed on the fixture.

After installing the 2S module in the test station, the top KIRA twin board is mounted manually onto the M2 spacer nuts. Therefore, the twin board has to be removed from its storage fixture mounted in the lid of the test station. Figure 5.9 shows the design of the OT Module Test Station including the KIRA system. A dedicated software test is integrated into the Ph2_ACF package to calibrate the KIRA systems and to perform functional KIRA tests.

5.2.5. Performance of the KIRA System

In total, 19 KIRA systems have been assembled at ETP. All KIRA components made of aluminium and all 3D printed parts have been manufactured in the mechanical workshop at ETP. The printed circuit boards have been manufactured at the company *Beta LAYOUT GmbH* [Bet22] which also equipped the boards with all electrical SMD components. All larger electrical components have been soldered onto the boards at ETP. Afterwards, all KIRA systems have been assembled and tested for their functionality. Therefore, the KIRA systems are installed into the OT Module Test Stations together with the same 2S prototype module. Each LED is turned on separately with varying intensities to measure and compare the signal seen by the 2S prototype. Thus, it is possible to compensate production-related differences like e.g. the alignment of the LEDs on the printed circuit boards and the aluminium aperture openings. The results of this KIRA calibration procedure are discussed within this section.

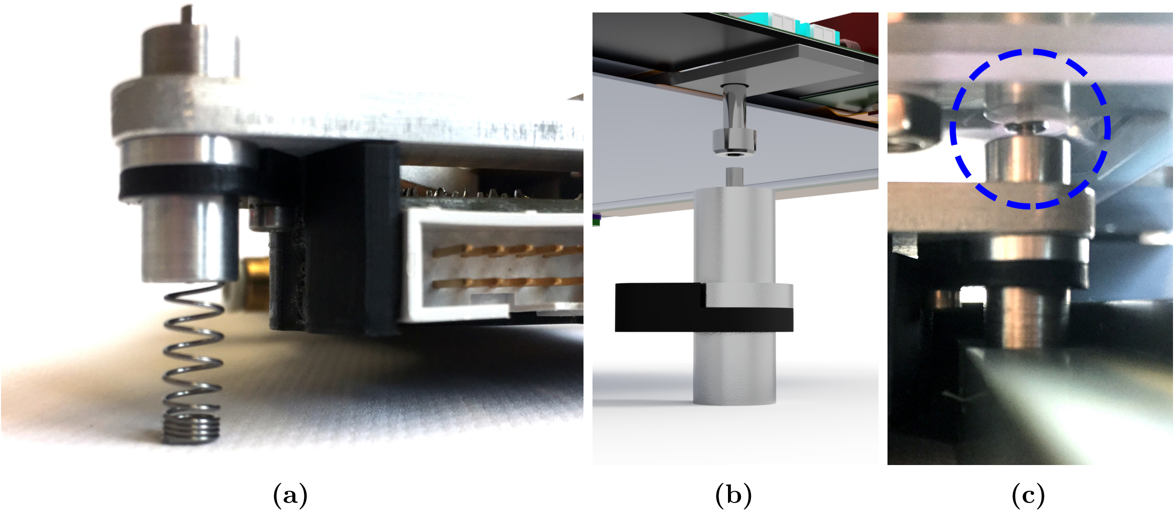
(a) (b) (c)

Figure 5.8.: Bottom KIRA twin board alignment principle. (a) The twin board is placed onto spiral springs protruding from the test station fixture. (b) By adjusting the position of the fixture corner plates, it is possible to reach a precise alignment between the 1.5 mm pins in the twin board circular standoffs and the M2 Allen screws in the 2S module carrier. (c) Successful alignment of the bottom twin board with the carrier. [Bra20]

Hit Latency Scan

To synchronize the KIRA system and the 2S module readout, the pulse generated by the trigger generator board is fed into the FC7 via a DIO5 FMC card [BW21]. Thus, the module readout is triggered at each KIRA pulse. To determine the correct hit latency setting, a latency scan has to be performed. Each latency scan is performed with one LED activated at a fixed intensity setting given by the corresponding DAC channel output. The readout chip threshold is set to be 50 V_{cth} away from the pedestal. By monitoring the number of detected hits per latency, it is possible to determine the correct delay between trigger reception and module readout buffer position.

Figure 5.10a displays the number of hits per frontend hybrid as a function of the latency setting for an LED intensity of 29 000 DAC. Larger latency values correspond to events detected earlier in time. The first hits are detected at a latency of 93 clock cycles in both hybrids. After a steep increase, the distributions reach a distinct maximum at a latency of 91 clock cycles followed by a decrease over ten clock cycles. Thus, the module detects hits over a time span of twelve clock cycles corresponding to 300 ns. This is unexpected in view of the configured pulse length of 20 ns but needs to be understood to identify the correct latency setting for module operation. To investigate if the latency scan profile is generated by the KIRA system itself, the LED light output following the 20 ns long trigger pulse is measured with a *TIA-950 Optical/Electrical Converter* [Inc22]. The converter is mounted above the aluminium aperture opening of one LED and its electrical signal is monitored together with the LED trigger pulse on an oscilloscope. The resulting measurements for three different LED intensities are shown in Figure 5.10b. At an intensity of 29 000 DAC the light intensity is too small to be detected by the optical to electrical converter. Thus, the intensity is measured at higher intensities between 31 000 DAC and 35 000 DAC. For all three shown intensities, the LED light output occurs 25 ns after the rising edge of the trigger signal and reaches its maximum 45 ns after the trigger. The pulse width does not increase with intensity and is characterized by a *full width at half maximum* (FWHM) of 25 ns. Additionally, a second, smaller, peak followed by an

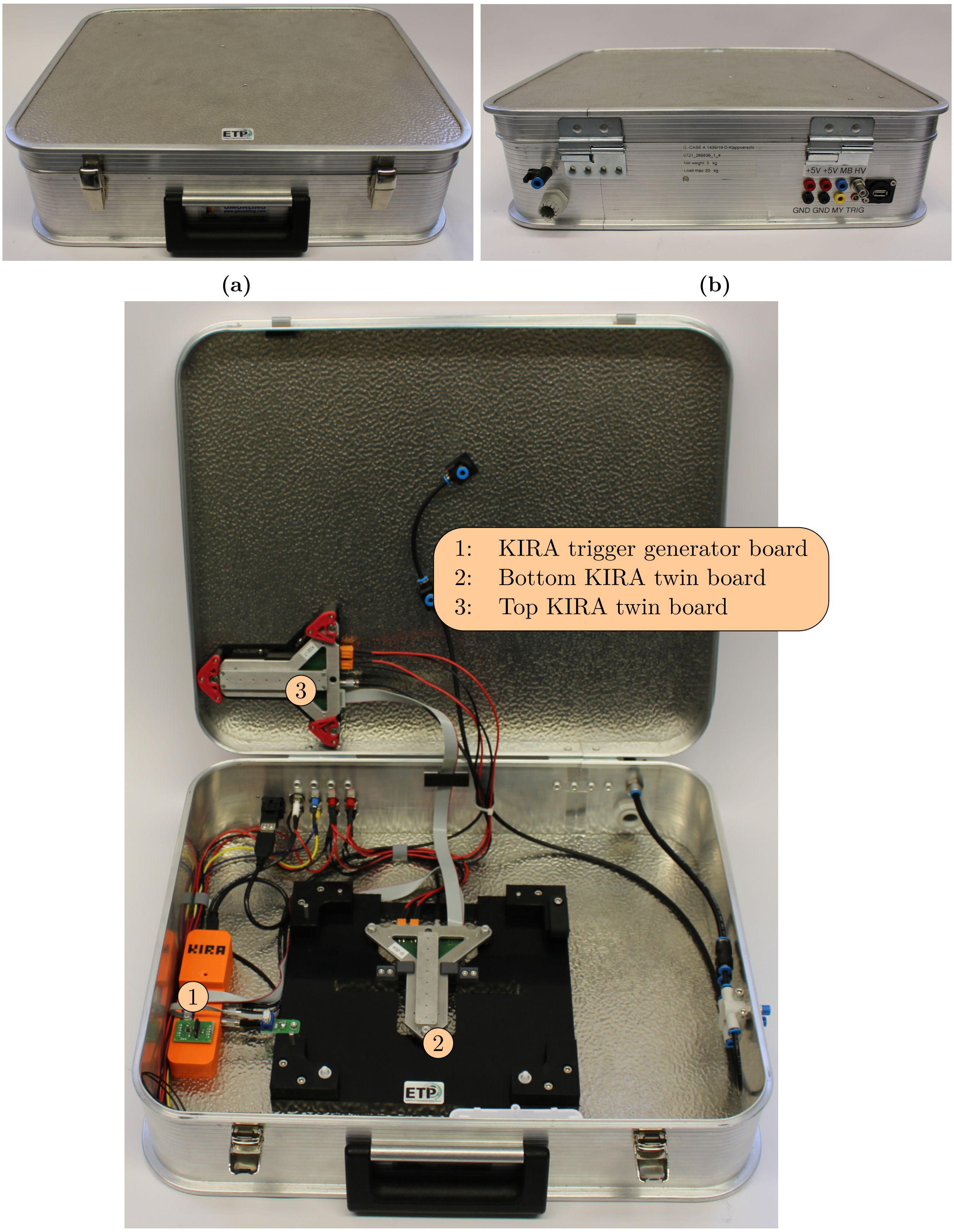

1: KIRA trigger generator board
2: Bottom KIRA twin board
3: Top KIRA twin board

(a) **(b)**

(c)

Figure 5.9.: The OT Module Test Station equipped with a KIRA system. Front (a) and back view (b) of the closed box. (c) In addition to the hardware presented in Figure 5.4, the KIRA trigger generator board is installed. While the bottom twin board is integrated into the mechanical carrier fixture, the top twin board is stored in a dedicated fixture mounted in the lid.

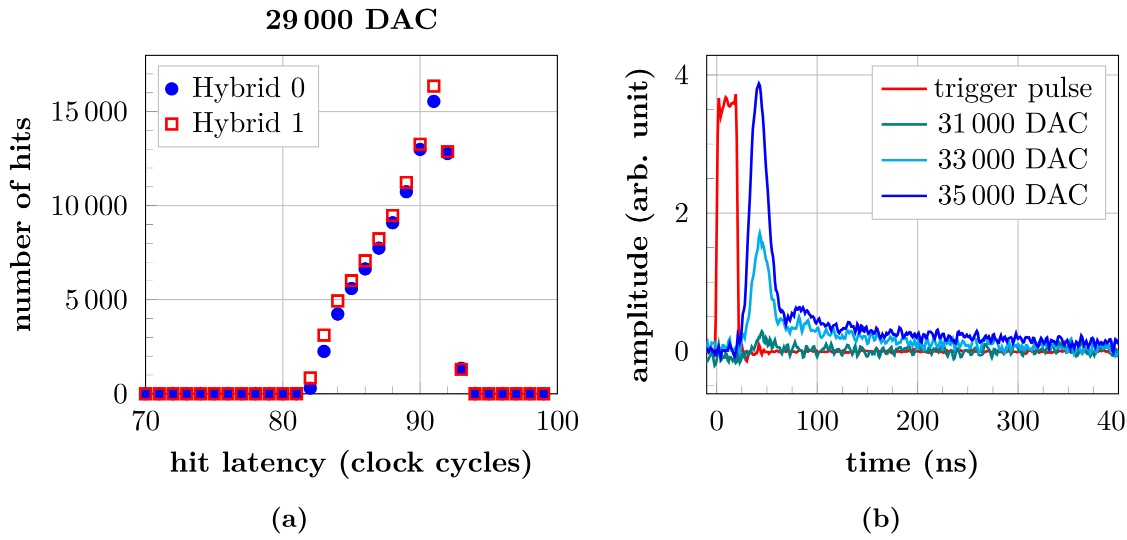

(a) (b)

Figure 5.10.: (a) KIRA latency scan at an intensity of 29 000 DAC. Only LED 2 of the top twin board is activated. A clear maximum in the number of detected hits per frontend hybrid is visible at a latency of 91 clock cycles. (b) The LED light output is measured for three different intensity settings as a function of time. The initial 20 ns long trigger pulse is shown in red. At all three intensities, the first light output occurs 25 ns after the rising edge of the trigger signal. The first intensity peak is followed by an afterglow with exponentially decreasing intensity over a time span of approximately 300 ns.

exponential decrease can be observed in the light output after the first maximum. Compared to the oscillations observed with early KIRA prototypes [Bra20], the effect is significantly reduced. However, the LEDs show a clear afterglow with exponentially decreasing intensity over a time span of up to 300 ns after the first intensity peak. This observation coincides with the observed hit profile at an intensity setting of 29 000 DAC shown in Figure 5.10a. For module operation at this LED intensity, the correct latency setting is 91 as the number of hits is at the maximum.

It has been observed in [Bra20] that the shape of the measured hit distributions during a latency scan changes significantly at higher LED intensities for early prototype versions of the KIRA system. To reproduce and investigate the origin of this effect, additional latency scans at intensities of 29 400 DAC, 30 200 DAC, and 31 000 DAC are conducted. Figure 5.11a displays the measured hit distributions seen by Hybrid 0 of the 2S prototype. For comparison, the corresponding hit distribution at an intensity of 29 000 DAC from Figure 5.10a is shown as well. At an intensity of 29 400 DAC, the primary maximum at a latency of 91 clock cycles coincides with the distribution at 29 000 DAC. However, the previously observed decrease for smaller hit latency settings is superimposed by a plateau emerging for latencies between 77 and 78 clock cycles. For intensity settings of 30 200 DAC and 31 000 DAC the number of hits for latencies below 91 clock cycles drastically increases resulting in new global maxima at a latency setting of 78 clock cycles. Additionally, the distribution is significantly increased over several clock cyles. This observation is in accordance with the prototype KIRA measurements presented in [Bra20]. However, an intuitive interpretation of the maximum bin as correct latency setting would introduce an unexpected dependency of the LED intensity to the timing of the measurement setup. The measurements displayed in Figure 5.10b show, that the KIRA system produces the maximum light output approximately 25 ns after the rising edge of the trigger signal independent of the LED intensity. Thus, further measurements are necessary to understand the origin of the presented latency scan distributions.

The spatial hit distribution on the 2S module is examined. Figure 5.11b displays the hit occupancy per hit latency setting and module channel for the LED intensity of 29 400 DAC. Channels connected to the top sensor are shown in the upper graph, while bottom sensor channels are summarized in the lower graph. Only channels of Hybrid 0 are plotted. The top sensor distribution shows a clearly visible beam spot profile detected by the strips located directly below LED 1. The first hits in the top sensor are detected at a latency setting of 93. At a latency setting of 91, the number of strips reaching a hit occupancy of one is maximal. This is the origin of the first peak observed in the distribution in Figure 5.11a. For lower latency settings and, thus, later time stamps, the hit profile narrows accordingly to the decrease observed for an LED intensity of 29 000 DAC shown in Figure 5.10a. Observing the top sensor channels outside the LED beam spot and all bottom sensor channels, channels with a low hit occupancy appear for latency settings between 82 and 90. These additional hits create the plateau observed at this LED intensity in Figure 5.11a. Additionally, an accumulation of hits can be seen in the bottom sensor strips located below the injection LED. As discussed in Section 4.1.2, the photon flux decreases exponentially inside silicon. Thus, the initial photon flux is reduced by 99.3% within the top 2S sensor, which has a physical thickness of 320 µm. Additionally, the sensor backplane is covered by an aluminium layer, further dampening the photon flux. Together with the observation that the accumulation of hits in the strips located below the illuminating top twin board LED occurs approximately 100 ns after the first hits are observed in the top sensor channels, these additional hits cannot be explained by primary photons sent out by the illuminating LED.

Using a higher LED intensity of 31 000 DAC results in the hit distribution shown in Figure 5.11c. The primary beam spot in the top channel strips located below LED 1 is clearly visible. As expected, increasing the light intensity leads to a wider beam spot illuminating more channels. The profile vanishes at a latency setting of 86, which is at earlier times compared to the lower intensity setting. Additionally, the hit occupancy of the channels outside the LED beam spot and for all channels in the bottom sensor increases drastically for events later than 75 ns after the first observed hits. Within up to 20 clock cycles, most of the hybrid channels show a hit occupancy of one. This effect leads to the significiant increase in number of hits per module and the appearance of additional plateaus for increasing intensities shown in Figure 5.11a. A possible cross talk between the individual LEDs in the two KIRA twin boards as origin of the observed hit distributions can be excluded. By disconnecting the bottom twin board and covering all aperture openings except the one of LED 2 for the top twin board, the same distributions are measured.

In view of these observations, the origin for the observed hit distributions has to be located inside the 2S module itself. To study the CBC and frontend hybrid behaviour as a response to the charge signal, threshold scans are performed for all hybrid channels at fixed latency settings. This allows to characterize the signal of each channel. By repeating these threshold scans for different latency settings, the dynamic behaviour of the charge readout can be resolved.

Pulse Shape Measurements

Figure 5.12 displays the hit occupancy of each top sensor channel on Hybrid 0 as a function of the chip threshold. For this measurement, KIRA LED 2 is illuminating the top sensor with an intensity of 29 000 DAC. The hit latency is set to 91. The charge generated by the infrared light in the strips located below the LED 2 is clearly visible. To quantify and compare the hit occupancy distributions, the threshold at which the occupancy reaches 50% is extracted. This threshold is marked in red in Figure 5.12 and is called *signal level* in the following. For higher

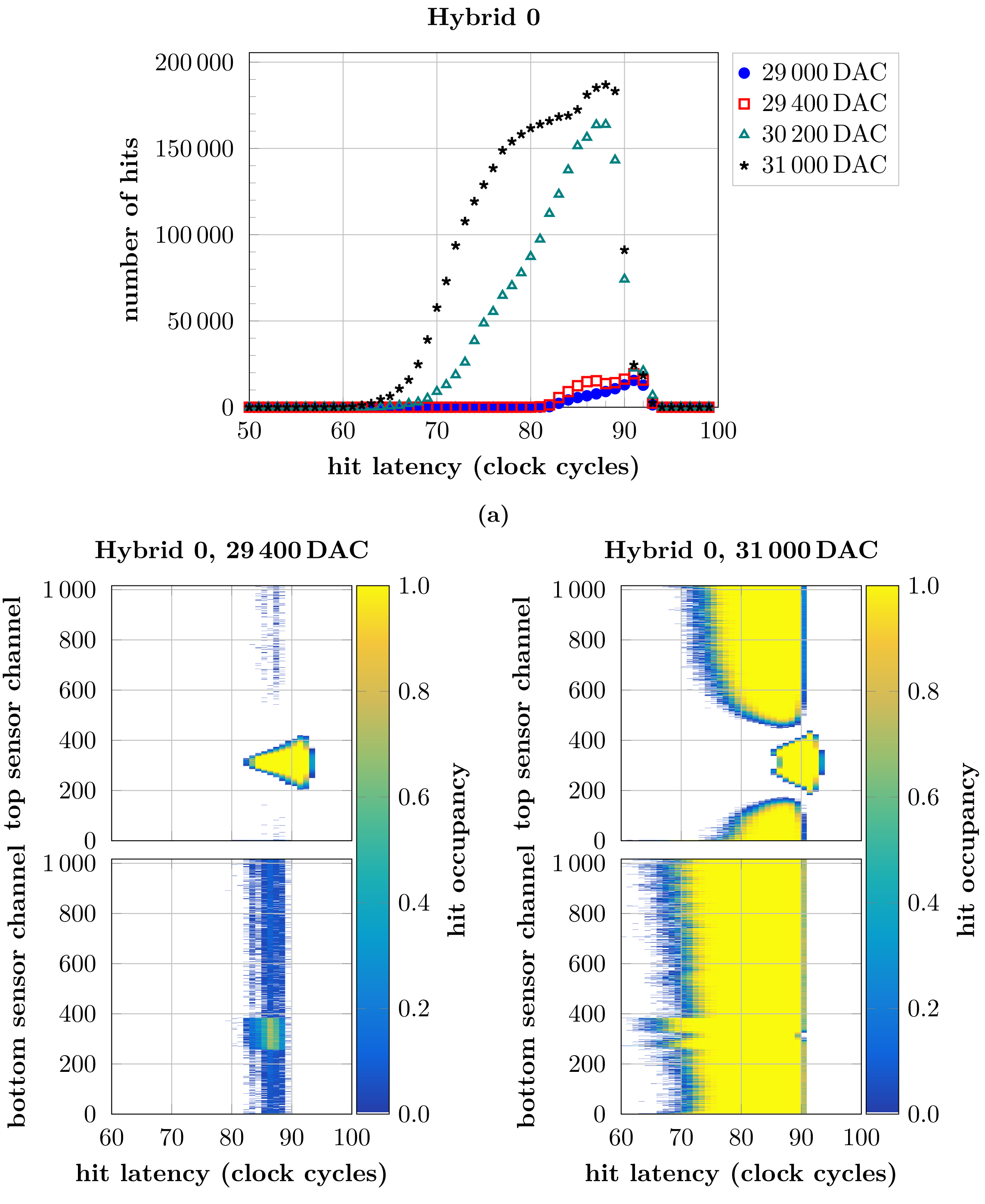

(a)

(b)

(c)

Figure 5.11.: KIRA hit latency scans for different LED intensities. (a) By plotting the number of hits per hybrid, different distributions can be observed at different intensities. For intensity settings above 29 000 DAC, the total number of hits significantly increases and the distributions' gobal maxima shift towards smaller latency settings. To investigate this effect, the spatial hit distributions on Hybrid 0 are shown as a dependency of the latency for intensity settings of 29 400 DAC (b) and 31 000 DAC (c). The upper graph shows top sensor channels and the lower graph bottom sensor channel. The color code indicates the hit occupancy of each channel.

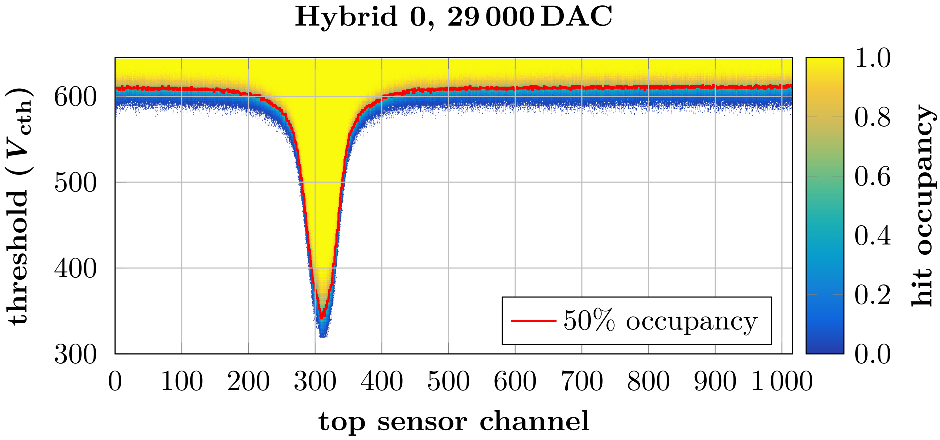

Figure 5.12.: Hit occupancy of all top sensor channels on Hybrid 0 as a function of the CBC threshold. The hit latency is set to 91 clock cycles. LED 2 on the top twin board is illuminating with an intensity of 29 000 DAC. For each channel, the threshold at which the hit occupancy reaches 50% is marked in red.

LED intensity settings, the generated charge in the sensor can saturate the analog frontend of the CBC channels located inside the center of the beam spot. Thus, the peak of the hit profile is cut. This effect occurs at a threshold setting of approximately 160 V_{cth} and is shown exemplary in Figure A.1 in the appendix for an LED intensity setting of 30 000 DAC.

By comparing threshold scans at different latency settings, a time profile of the charge readout is obtained. The signal level of the top sensor channels on Hybrid 0 is shown in Figure 5.13a for an LED intensity of 29 000 DAC and different latency settings. At a latency setting of 94 clock cycles, no hits from the LED are yet detected by the channels. Thus, the signal level coincides with the channels pedestals at 600 V_{cth}. As previously shown, a latency of 91 clock cycles corresponds to the nominal latency setting to detect the maximum number of hits generated by the infrared photons. While the illuminated channels show the expected pulse form, a shift of the signal level can be observed for all other channels outside the beam spot. Depending on the distance of the channels towards the LED beam spot, the signal level shifts to values up to 610 V_{cth}. At lower latency settings, this shift vanishes and all channels outside the beam spot return to the pedestal value. The signal seen by the illuminated channels decreases with time and the signal level reaches threshold values above the pedestal at 600 V_{cth} at latency settings lower than 85. At later times, the 50% occupancy level returns to the pedestal. This effect is the expected behaviour of the chip frontend during signal readout and has already been investigated in [Mai19]. However, the measurements presented within this chapter are performed with a significantly larger number of simultaneoulsy illuminated channels and larger pulse heights per channel as will be quantified later. Thus, the time constants for signal rise and fall times differ substantially in comparison with the observations presented in [Mai19]. At an LED intensity of 29 000 DAC, a signal rise time of less than 50 ns is observed for the central channel in the beam spot. The signal returns to a level above the pedestal within 225 ns.

The distributions measured at an LED intensity of 31 000 DAC are shown in Figure 5.13b. At this increased intensity, the effects discussed previously amplify. Within the illuminated area, the detected charge signal is large enough to saturate the CBC frontend as discussed previously. While the signal rise time stays within 50 ns, the signal level returns to values above the pedestal faster compared to the intensity setting of 29 000 DAC within the beam spot. Similar to the situation at the lower intensity setting, the signal level of channels outside the beam spot is shifted towards threshold values larger than 600 V_{cth} at a latency of 91 clock

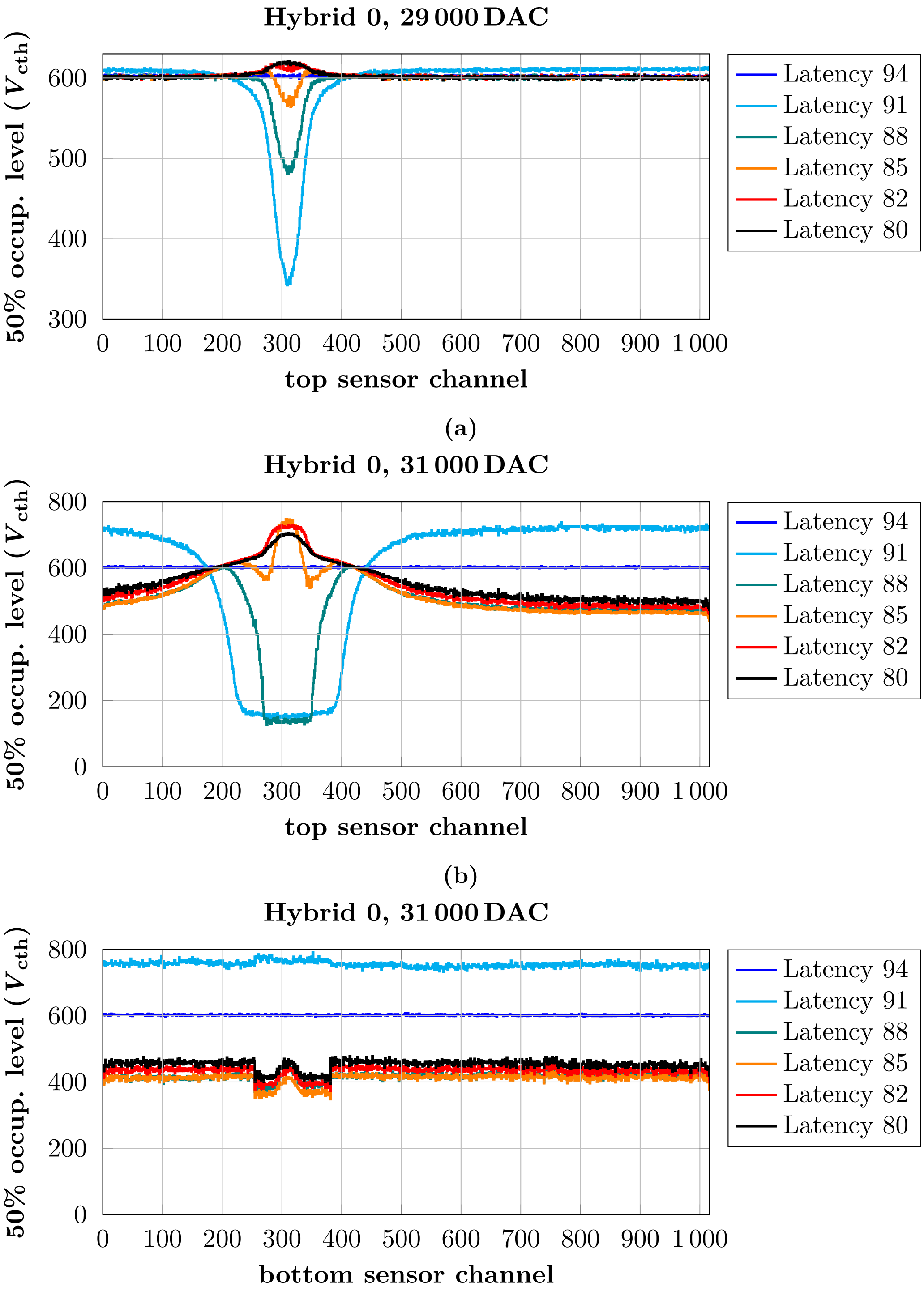

(a)

(b)

(c)

Figure 5.13.: Distribution of the 50% occupancy level per sensor channel on Hybrid 0 at different latencies and LED intensities. For all presented measurements, LED 2 of the top KIRA twin board was activated. (a) Data shown for the top sensor channels at an intensity setting of 29 000 DAC. For an LED intensity of 31 000 DAC, the 50% occupancy level is shown for top sensor channels (b) and bottom sensor channels (c) as a function of the latency setting. Note the different y axis scaling of (a) compared to (b) and (c).

cycles. At this latency, the signal level moves to approximately 700 V_{cth}. At a latency setting of 88, the signal level outside the beam spot reaches thresholds of about 500 V_{cth} before starting to approach the pedestal value. Figure 5.13c displays the distributions of the signal level with time for the bottom sensor channels on Hybrid 0. At the nominal latency setting of 91, most of the channels show signal levels at a threshold around the pedestal value of 600 V_{cth}. However, the observed signal levels show a significantly increased spread among neighbouring channels compared to the situation at a latency setting of 94 corresponding to times before the LED pulses appear in the sensor. Additionally, the bottom sensor channels located directly beneath the beam spot in the top sensor show a shift of the signal level towards higher V_{cth} values. For latency settings smaller than 91, the signal level of all channel shifts to threshold values of approximately 300 V_{cth} and starts to approach the pedestal values in a similar way as observed for the top sensor channels outside the beam spot. The 50% occupancy levels of all bottom sensor channels connected to CBC 2, which is connected to the strips in the center of the LED beam spot, are systematically shifted by approximately 60 V_{cth} towards smaller V_{cth} values.

Based on these observations, the hit distributions during the latency scans presented in Figure 5.11c can be explained. The readout chip threshold is fixed at 550 V_{cth} during these measurements. Due to the significant shift of the 50% occupancy level towards low V_{cth} units in response to the LED signal for latencies settings smaller than 91, the presence of non-vanishing hit occupancies in the top sensor channels outside the beam spot and in all bottom sensor channels arise. To understand the physical origins behind these effects, three different contributions need to be discussed.

1. **Common Sensor Bias Potential:** During the passage of a charged, minimum ionizing particle (MIP) through a 2S sensor, electron-hole pairs are generated along the particle's trajectory as described in Section 4.1.1. For a MIP, these charge carriers influence the sensor's electric field generated by the bias voltage of typically several hundreds of volts only insignificantly. In case of the KIRA system, the charge generation in the silicon sensors is done via photons with a wavelength of 950 nm. By increasing the LED intensity, the photon flux entering the sensor and, thereby, the number of charge carriers generated in the silicon increases exponentially. This behaviour is quantified on Page 61. Additionally, the KIRA system is designed to illuminate a significant area of the sensor with each LED, the charge signal introduced in the 2S sensors exceeds the signal generated by MIPs by a multiple. Following the studies presented on Page 61, a charge signal of $2.4 \cdot 10^7\,\mathrm{e}^-$ is generated in a 2S sensor when illuminated with one KIRA LED at an intensity of 31 000 DAC. For a MIP, a signal of approximately $2.2 \cdot 10^4\,\mathrm{e}^-$ is expected (see Appendix C.1.1). For a large charge signal, the sensor's electric field and its resistance can be influenced significantly by the additionally present charge carriers. A quickly changing sensor resistance imposes challenges to the high voltage power supply and can lead to changes of the applied sensor bias voltage depending on the power supply capabilities. This can be detected by the AC coupled 2S module readout electronics as a general effect seen by all channels connected to the affected sensor. For all measurements presented within this thesis, a *Keithley 2410 source meter* [Tek03] is used as high voltage power supply.

   Figure 5.14a displays the high voltage biasing circuitry implemented into the service hybrid design. The high voltage potential provided by the power supply V_{in} is applied to a low-pass filter before being split and applied to the top and bottom sensor backsides via the high voltage (HV) tails. Thus, the two sensor backsides are on the same potential at all times. This can explain the 50% occupancy level distributions observed in the bottom sensor when illuminating the top sensor. To separate the two backplanes, a 100 Ω resistor is soldered onto each HV tail circuit board before connecting it to the service hybrid.

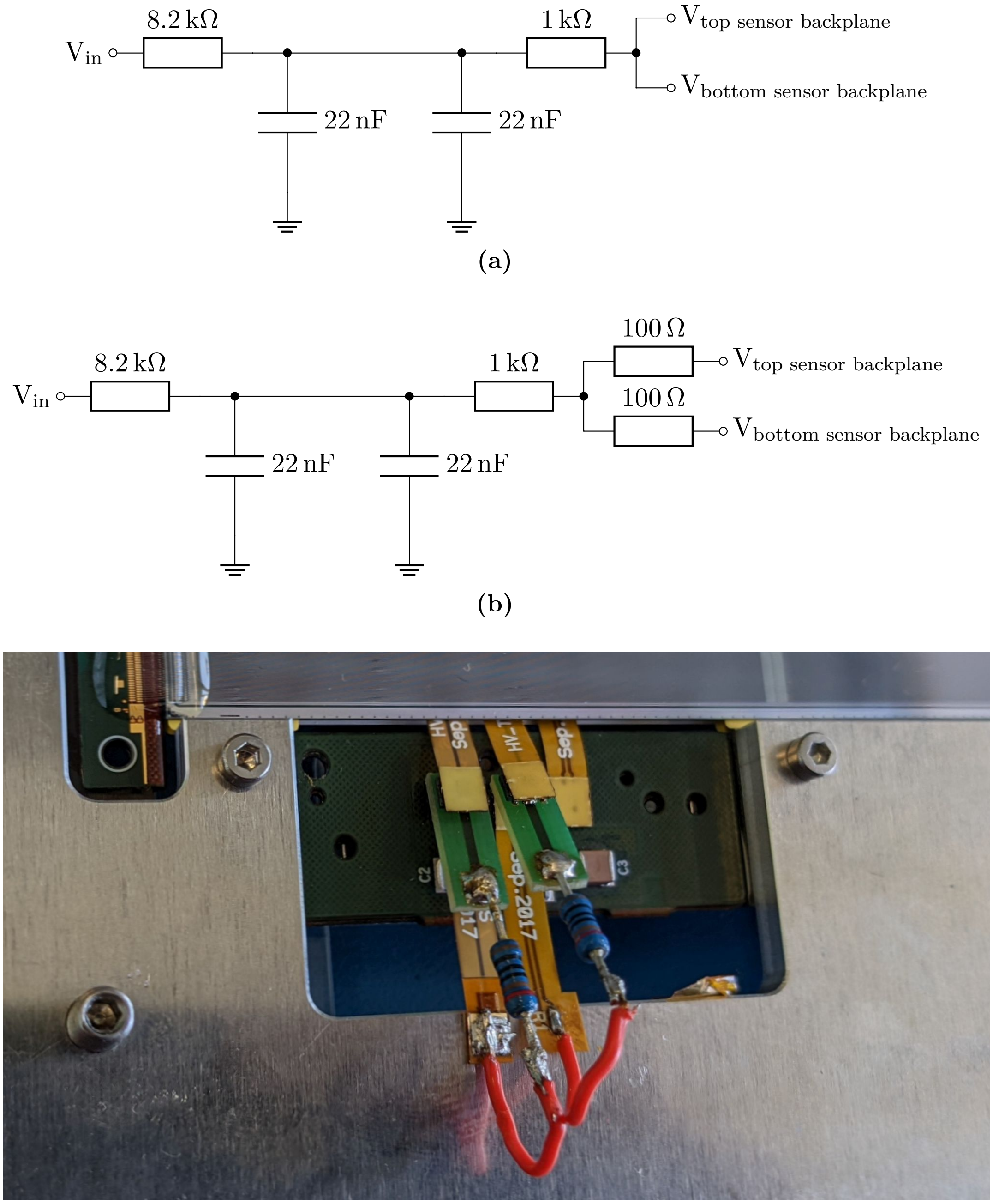

(a)

(b)

(c)

Figure 5.14.: Scheme of the 2S service hybrid high voltage biasing circuitry. (a) For all service hybrids assembled in 2S prototypes, the electric potential provided by a power supply V_{in} is applied to a low-pass filter. Afterwards the potential is applied to the top and bottom sensor backplanes via the high voltage tails. (b) To avoid the direct electrical connection between top and bottom sensor backplanes, two resistors are introduced into the high voltage tail circuitry. (c) Picture of the resistors added into the high voltage tail circuitry.

This configuration is indicated in Figure 5.14b and a photo is shown in Figure 5.14c. Repeating the KIRA latency scan with this configuration yields the distributions shown in Figure 5.15a. No hits are observed in the bottom sensor channels as the top sensor bias potential has no immediate influence onto the bottom sensor potential anymore. A change in the top sensor bias potential leads to a voltage drop at the 100 Ω resistor which results in a current through the resistor to recover the potential provided by the power supply. Thus, the additional resistance increases the recovery time of the top sensor bias potential following a LED pulse. This can be observed by comparing the distributions in Figure 5.15a and Figure 5.11c. To simplify direct comparison, data from the latter figure is displayed in Figure 5.15b. After installing the additional resistors, hits in the top sensor channels are detected for more than 40 clock cycles compared to only 20 clock cycles for the original biasing circuitry.

2. **Channel Crosstalk:** The observed shift of the 50% occupancy level in the strips located directly beneath the beam spot in the top sensor is explained by the frontend hybrid geometry. As introduced in Section 3.2.4, neighbouring CBC channels are alternatingly connected to top and bottom sensor strips. The frontend hybrids connect the CBC channels via traces to the wire-bond pads. Thus, traces for neighbouring channels are located next to each other. This geometry allows for signal coupling from one trace to its direct neighbours, which is called crosstalk. A measurement of the channel crosstalk on 2S frontend hybrids has already been performed in [Mai19]. Thus, signal seen by the top sensor channels influences the input of the analog frontend of the directly neighbouring analog CBC channel frontends.

3. **CBC Power Consumption:** The discontinuity of the 50% occupancy level observed for channels connected to CBC 2 in Figure 5.13c is explained by the power consumption of this specific chip. The eight KIRA LEDs per twin board are aligned with the central strips of each CBC for top and bottom sensor channels. Thus, the majority of signal is seen by one CBC when illuminating the sensor with one LED. The larger the detected signal, the higher the power consumption of the CBC frontends, in particular the amplifier stages. This can lead to changes in the internal reference voltage levels and, therefore, a shift of the 50% occupancy level, when the CBC is exposed to a large overall signal.

These three contributions explain the origins of the observed 50% occupancy level distributions following a KIRA LED light pulse. For using the KIRA system for functional testing of 2S modules, the described effects have no impact. As the trigger generator board can provide a maximum frequency of approximately 100 kHz, a trigger is sent every 10 µs or every 400 clock cycles at maximum. This leaves enough time for the bias voltage and the 2S readout electronics to recover from the last signal before the arrival of the next LED pulse. Each CBC channel is specified to recover from the signal of a *heavy ionizing particle* (HIP) of up to $2.5 \cdot 10^7\,\mathrm{e}^-$ within less than 2.5 µs [Pry19]. This charge specification for one channel is of the same order of magnitude as the signal generated in the 2S sensor for an LED intensity setting of 31 000 DAC. However, for the KIRA system, the charge is distributed over several channels. Thus, the observed time behaviour of the CBC channels in response to the LED generated charge signal is in agreement with the CBC specifications for operation in the CMS experiment. The correct latency setting for module operation can be identified easily by counting the number of hits detected per illuminated CBC and choosing the latency when this number is maximum. For all measurements presented in the following, the latency is set to 91.

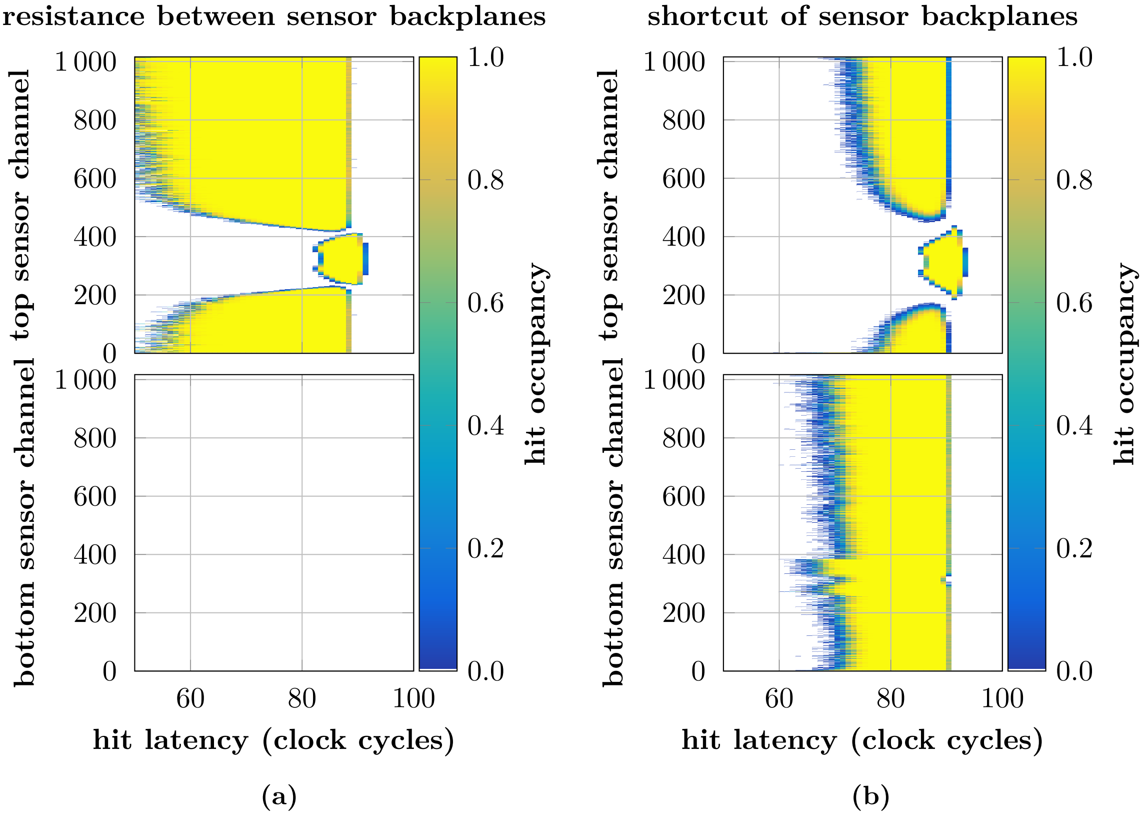

Figure 5.15.: The hit occupancy is shown as a function of the latency setting and the channel number of top and bottom sensor channels. (a) After separating the sensor backside bias potentials from each other using two resistors, the bottom sensor channels detect no hits after an LED light pulse from the top KIRA twin board. (b) For comparison, data taken with the original service hybrid high voltage biasing circuit are shown. Data shown for Hybrid 0. KIRA LED 2 of the top twin board was operated at an intensity of 31 000 DAC.

LED Charge Signal Analysis

To quantify the charge signal generated in a 2S sensor under illumination with one LED of the KIRA system, threshold scans at a fixed latency of 91 are performed. Plotting the hit occupancy as a function of the channel number and threshold setting results in plots as shown in Figure 5.12. By varying the LED intensity, the generated sensor signal can be changed and a conversion factor between intensity DAC units and electron equivalent can be determined. For each LED intensity, the 50% occupancy level for each channel is determined as indicated in Figure 5.12. Based on this information, the signal generated in the illuminated sensor area as well as the signal seen by the channel in the center of the beam spot can be extracted. As previously discussed, the 50% occupancy level of channels outside the beam spot varies for different LED intensities. To adapt for this effect, the threshold values $t_i^{50\%}$ at which the 50% occupancy level is reached per channel i are averaged for top sensor channels 762 to 1016 located outside the beam spot via

$$t_{\mathrm{ref}} = \frac{1}{254} \sum_{i=762}^{1016} t_i^{50\%} \ . \tag{5.1}$$

The charge signal s_i detected by channel i is given by

$$s_i = t_{\mathrm{ref}} - t_i^{50\%} \ . \tag{5.2}$$

Figure 5.16a displays the signal seen by the top sensor channel 317 located in the center of the LED 2 beam spot. An exponential increase of the detected charge is observed with linearly increasing LED settings until the CBC frontend saturates for intensity settings above 29 000 DAC. This increase is a result of the output current characteristics of the LED driver *iC-HG30* displayed in Figure 5.16c. The output current, named I(LDKx) in Figure 5.16c, is shown as a function of the analog input voltage V(CIx) provided to each driver channel via a DAC of the type *AD5675R*. For the measurements presented within this thesis, the maximum DAC output voltage is configured to be 2.5 V. For input voltages below 2.5 V, the output current scales exponentially with the voltage. For an intensity setting of 28 750 DAC, the channel in the center of the beam spot detects an equivalent charge of approximately 22 000 e^-. This charge is comparable to the signal generated by a minimum ionizing particle. As, however, not only one strip is illuminated at a time, the overall signal generated in the silicon sensor and seen by the readout electronics is significantly larger. The distribution shown in Figure 5.16b is obtained by summing up the charge signals s_i for all 127 top sensor channels of CBC 2 as a function of the LED intensity setting. For an intensity setting of 28 750 DAC, an equivalent charge of approximately $1.4 \cdot 10^6\,\mathrm{e}^-$ is generated in the sensor. Using an exponential fit, this value can be extrapolated to the intensity settings used for measurements in the previous sections. The overall sensor charge signal s_{tot} per intensity setting I_{LED} for one KIRA LED turned on can be approximated by

$$s_{\mathrm{tot}} \approx \exp(-76 + 0.003\,\mathrm{DAC}^{-1} \cdot I_{\mathrm{LED}})\,\mathrm{e}^- \ . \tag{5.3}$$

Based on this parametrisation, it gets apparent that the KIRA system can be used for module tests with varying demands on the generated charge signal. During *beam loss scenarios*, protons from the primary LHC beams can be released uncontrollably following some misfunction of the accelerator components [Sch+03]. At the LHC, several safety mechanisms are implemented to prevent any damage to crucial accelerator or detector components. If, however, a beam loss would happen near the CMS detector and parts of the primary beam enter the CMS tracker, the silicon sensors would detect a highly ionising event. Using the KIRA system, it is possible to study the of silicon sensors to highly ionising charge injections and predict from the results

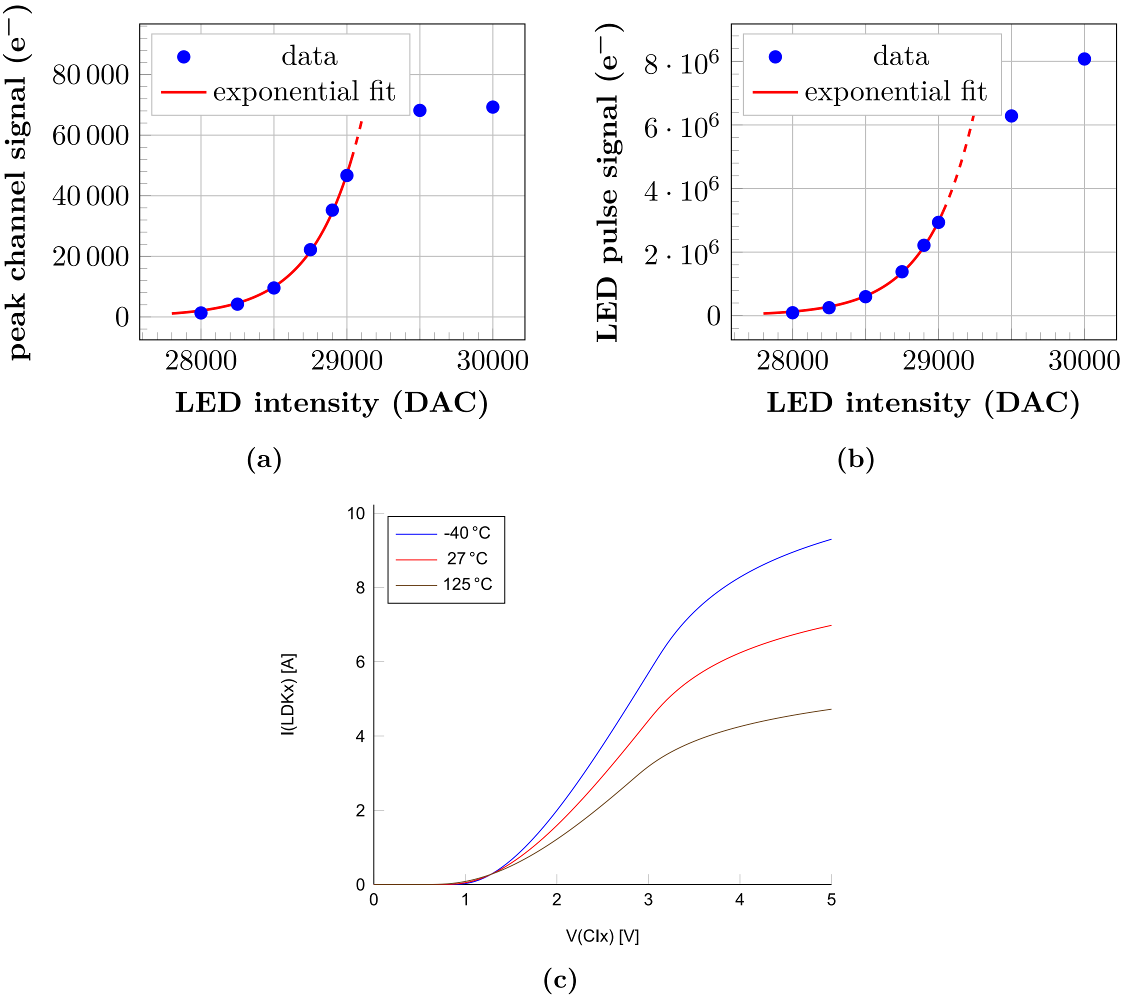

(a)

(b)

(c)

Figure 5.16.: (a) The signal detected by the channel located in the center of a KIRA LED beam spot is shown as a function of the LED intensity. For intensity settings above 29 000 DAC, the CBC frontend saturates. For lower intensities, an exponential increase of the signal is observed. (b) As each LED is illuminates a group of channels, the overall charge signal generated in the sensor is significantly larger than the signal seen by the central strip. (c) The exponential increase of signal with intensity is a consequence of the LED driver *iC-HG30*. Its output current increases exponentially with the applied control voltage provided by a DAC on the KIRA twin boards. For all measurements presented here, the DAC was configured to deliver at maximum an input voltage of 2.5 V. Taken from [iC-19].

the behaviour of 2S modules in response to a beam loss scenario. At the time of writing this thesis, a dedicated setup is under development at ETP to probe the voltage levels appearing at dedicated positions on a 2S sensor using oscilloscopes. Results are expected in autumn 2022.

2S Module Functional Testing with KIRA

When using the KIRA system during module functional testing, it is important to level the individual LED intensities within a KIRA system to compensate production-related differences. Therefore, the signal generated by each LED of each KIRA system is measured using the same 2S module prototype. To probe the functionality of all module channels, each of the eight LED needs to illuminate the top or bottom sensor channels of one complete CBC per hybrid. Thus, the intensity leveling is performed by increasing the intensity of each LED until all 127 strips of each CBC chip per hybrid register a hit occupancy of one. The resulting DAC settings indicate the nominal settings for KIRA tests during production. The measurements are performed at a latency setting of 91 and a relative threshold of 50 V_{cth}. The intensity is increased in steps of 100 DAC.

Figure 5.17a depicts the measured hit distribution for LED 1 on the bottom twin board. With increasing intensity settings, the illuminated sensor area is enlarged. The respective borders of CBC 1 are indicated as red dashed lines. At an intensity of 30 300 DAC the complete CBC bottom sensor channels are illuminated. Figure 5.17a displays the results gathered for the CBCs located on Hybrid 1. For both hybrids, the observed distributions are symmetrical. This proves that the twin board design achieves a homogeneous LED illumination for both sensor halves. By performing these measurements for every LED on the top and bottom twin boards, the nominal DAC settings for each LED are measured.

The nominal KIRA DAC settings depend on the geometry and material of the module carrier components. Details of the carrier design could still be changed in the future, e.g. the thickness or position of the top plexiglass plate. Thus, the KIRA intensity leveling needs to be repeated with the final production modules at each assembly site to define the individual necessary LED intensities for functional testing. The performed measurements have shown that the KIRA system is capable of providing enough intensity to be used for functional tests of 2S modules during the production period. An exemplary hit profile of a KIRA test with a 2S prototype is shown in Figure 5.17c. To spot defective channels more easily, the figure displays the hit occupancy subtracted from its expected value of one. The plot only shows data for the top sensor channels. Three defective channels on Hybrid 1 are clearly visible in the distribution. By combining this test result with additional functional tests like e.g. a channel noise measurement, the channel defect can be characterized. For the investigated 2S prototype, the three channels have unconnected wire-bonds, leading to a detected hit occupancy of zero during the KIRA functional test.

5.3. Summary

The Institute of Experimental Particle Physics is one of the 2S module assembly centers in the CMS community and plans to build at least 1300 modules until 2025. Therefore, a production line with dedicated assembly jigs and test systems is being developed. Within this thesis, a common test station for functional testing of 2S and PS modules at the end of the module assembly process has been developed, called *Outer Tracker Module Test Station*. The modules are installed in the station while mounted on their aluminium carrier plates. A simple fixation mechanism featuring spring pushers and alignment pins hold the carrier plates in place. By using electrically conductive polyethylene, the modules are secured from electrostatic discharges during handling. A commercially available aluminium box provides a light tight housing for

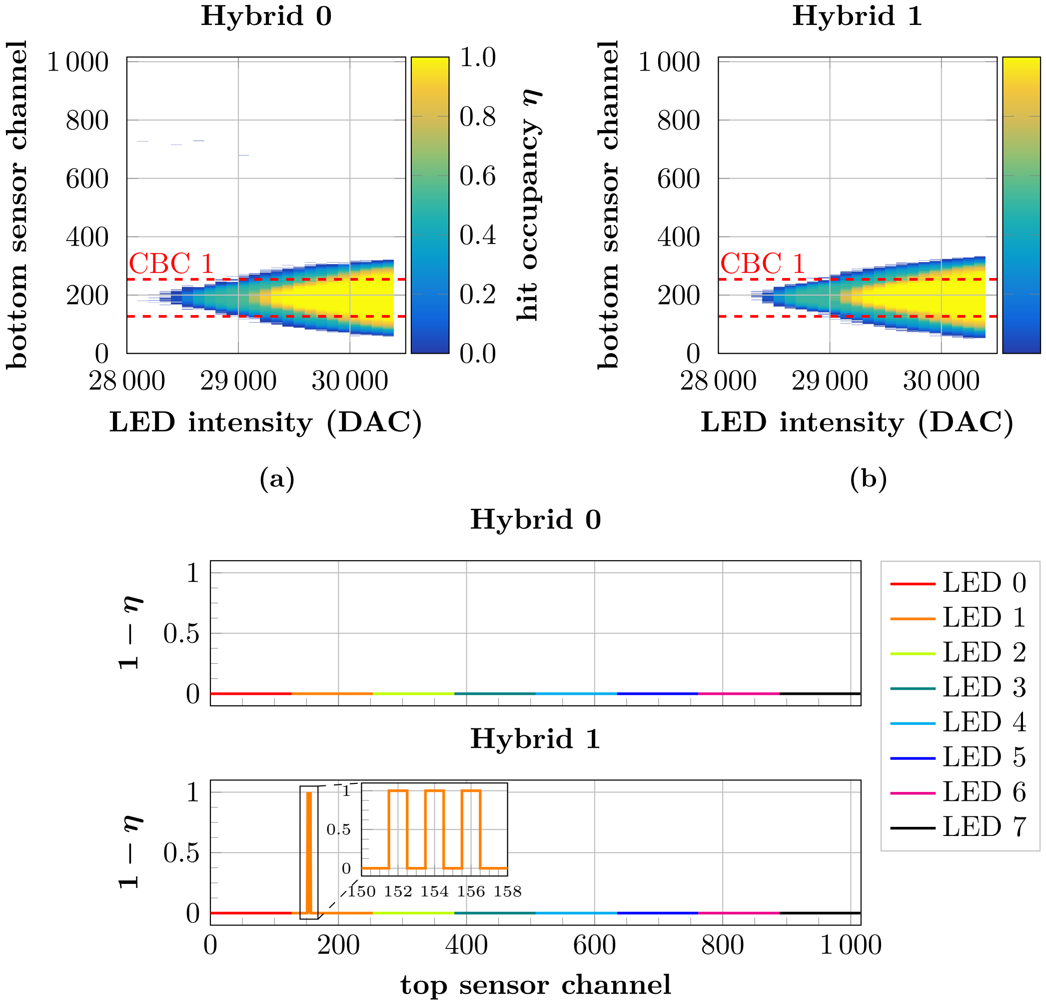

(a)

(b)

(c)

Figure 5.17.: The hit occupancy is measured as a function of the KIRA LED intensity setting and shown for all bottom sensor channels on Hybrid 0 (a) and Hybrid 1 (b). For each LED, the nominal intensity setting is given by the intensity at which all channels of the mainly illuminated CBC show a hit occupancy of one. In this example, the nominal intensity setting is 30 300 DAC. KIRA LED 1 is activated and a relative threshold of 50 V_{cth} is chosen. The latency is set to 91. (c) Result of a KIRA functional test performed with a 2S prototype at nominal LED intensities. By subtracting the measured hit occupancy values η from one, defective channels showing fewer hits than expected can be spotted easily as peaks. The investigated 2S prototype has three channels with unconnected wire-bonds, resulting in a hit occupancy of zero during the KIRA test.

module testing and shields its interior from electromagnetic radiation. A magnetic reed relay ensures the interruption of the high voltage potential when accidentally opening the box. The station provides the possibility to flush it with dry air, and air temperature and relative humidity are monitored via an Arduino-based sensor readout.

To allow testing of all 2S module channels for the functionality of the complete readout chain, the Karlsruhe Infrared Array (KIRA) has been produced within this thesis. One KIRA system consists of two twin boards with a row of eight LEDs each that are placed above and below the silicon sensors of a 2S module. The LEDs are aligned with the center of the 2S sensors illuminating the two sensor halves symmetrically. An Arduino-based trigger generator board produces a 20 ns long trigger pulse used to activate the LED drivers. It is possible to extend the trigger pulse length up to 5.6 µs. Additionally, each individual LED can be controlled in its intensity. Testing of the KIRA system together with the latest 2S module prototypes proves the capability of the KIRA system for functional module testing. A homogeneous illumination of all sensor channels can be achieved by leveling the LED intensities. Additionally, the charge generated in the silicon sensors from a LED pulse is quantified. Studies at large intensity settings show that the silicon sensors' bias potential can be influenced by a large amount of externally generated charge. To further understand the behaviour of the voltage levels on the silicon sensor while illumination, also in view of a possible beam loss scenario in the CMS tracker, custom designed hardware is in preparation to allow monitoring of voltages at dedicated sensor areas using oscilloscopes.

6

Functional Tests of 2S Module Prototypes

Prior to the start of module production for the Phase-2 Upgrade of the CMS Outer Tracker, several prototype modules are built. These modules allow to develop and qualify adequate techniques and tools to assemble modules of the highest precision and quality throughout the production phase. Additionally, the prototype modules fulfill a crucial role in qualifying the combined performance and interplay of all module components at an early development stage. Thus, all prototype modules are subject to a variety of functional tests to spot and fix potential weaknesses with regard to the usage in the CMS experiment.

This chapter summarizes the functional tests performed with the first full size 2S module prototypes providing the full optical readout chain. Section 6.1 introduces the prototypes used within this thesis. The results of module performance studies performed in the laboratory are summarized in Section 6.2. The module detection efficiency can be measured at beam test setups. Section 6.3 discusses the results of beam test campaigns performed with 2S module prototypes built with unirradiated and irradiated silicon sensors.

6.1. 2S Modules Investigated

As already introduced in Section 3.2.5, two types of prototype modules, called 8CBC3 modules and 2S prototypes, are investigated within this thesis. Between 2019 and 2022, in total 13 module prototypes have been assembled at the Institute of Experimental Particle Physics (ETP). Each module is named by its prototype version and an incrementing number. Due to the limited availability of service hybrids in the CMS community, some prototype modules can only be read out via an electrical interface board. For comparability reasons, the functional test results of these modules are not presented in this thesis. An overview of all module prototypes built at ETP providing the optical readout chain until May 2022, is given in Table 6.1.

Six 8CBC3 modules have been assembled with an optical readout chain at ETP. Within those, two modules have been assembled for the usage at two module integration sites in Strasbourg and Lyon. Thus, these modules have only been subject to a few functional tests at the end of the assembly process prior to the shipment. Besides testing the module functionality directly after the assembly, the module performance during the HL-LHC runtime has to be studied. Therefore, it is crucial to irradiate and test module prototypes at an early stage. As not all electrical components on the prototype frontend and service hybrids are radiation tolerant, only the 2S sensors can be irradiated for 8CBC3 modules. Two sensors have been irradiated with 25 MeV protons to a fluence of $4.6 \cdot 10^{14}\,\mathrm{n_{eq}\,cm^{-2}}$ at the *Karlsruhe Compact Cyclotron*. This fluence corresponds to 94% of the expected fluence for 2S modules in the ultimate scenario of the HL-LHC. Additionally, the two sensors were annealed to two different equivalent annealing times prior to the module assembly. This allows to quantify the influence of annealing on the module performance. The top sensor has acquired an equivalent annealing time of ten days at room temperature, while the annealing of the bottom sensor is chosen to be 200 days at room temperature. These annealing times have been chosen to simulate different LHC operation scenarios. During its operation, the silicon sensors in the tracker are cooled to around $-20°\mathrm{C}$.

Table 6.1.: Overview of the 2S module prototypes used for functional testing within this thesis. Only module prototypes with an optical readout chain are noted. The first six modules are 8CBC3 modules, the remaining modules are 2S prototypes.

module name	sensor distance	year	comment
KIT_8CBC3_1	1.8 mm	2019	
KIT_8CBC3_2	1.8 mm	2020	assembled for IPHC Strasbourg
KIT_8CBC3_3	1.8 mm	2020	sensors irradiated to $4.6 \cdot 10^{14}\,\mathrm{n_{eq}\,cm^{-2}}$
KIT_8CBC3_5	1.8 mm	2020	
KIT_8CBC3_6	1.8 mm	2020	assembled for IP2I Lyon
KIT_8CBC3_7	1.8 mm	2021	
KIT_2S_1	1.8 mm	2021	
KIT_2S_2	1.8 mm	2021	
KIT_2S_3	1.8 mm	2021	
KIT_2S_5	4 mm	2021	special geometry for noise investigations
KIT_2S_6	1.8 mm	2021	

Thus, no annealing is accumulated during the LHC operation. However, an average yearly annealing of 14 days at room temperature is foreseen to be added during the year end technical stops. This annealing time allows to reduce the leakage current and to influence the charge collection efficiency beneficially. For the currently planned 12 years of operation (excluding the possible ultimate scenario) of the High-Luminosity LHC, this results in an expected annealing of 168 days at room temperature. In case of unforeseen repair phases, the detector might accumulate more annealing than originally planned. Therefore, the bottom sensor has been annealed to 200 days to probe the module performance at the end of detector runtime. To cross-check earlier laboratory measurements, a short annealing time has been chosen for the top sensor. Using the irradiated and annealed silicon sensors, a 2S module is assembled. This module is called *KIT_8CBC3_3* and will be named the *irradiated module* in the following sections. Together with the remaining three 8CBC3 module prototypes, the irradiated module was used in laboratory-based studies and beam test campaigns.

With the availability of the latest generation of 2S module prototype components in 2021, six 2S prototypes have been built at ETP. The module called KIT_2S_4 module was assembled with irradiated sensors and frontend hybrids and is not investigated within this thesis. Until the time of writing of this thesis, all 2S prototypes are used extensively for noise measurements, thermal studies, beam tests and data acquisition system developments.

The functional test results performed with 8CBC3 modules and 2S prototypes will be summarized in the following sections. The main focus is set onto tests performed with 8CBC3 modules due to their early availability with respect to the timeline of this thesis.

6.2. Laboratory Based Module Performance Studies

6.2.1. Measurement Setups

The 2S module protoytpe tests presented in this section are performed within different setups. This section gives a short overview about the features of the individual setups.

Outer Tracker Module Test Station

The Outer Tracker Module Test Station is described in detail in Section 5.2. The 2S module prototypes mounted on their carriers are inserted onto an ESD safe polyethylene plate. The station allows module testing at room temperature and provides the possibility to perform tests with the KIRA system.

Cooled 2S Module Readout Station

To perform temperature-stabilized measurements within the expected temperature ranges that 2S modules will have to withstand during operation in the CMS tracker, a dedicated station has been developed at ETP within a master thesis. It is called *The Cooled 2S Module Readout Station* (COMORES) within this thesis. A detailed description of the station's functionality and performance can be found in [Kop18]. A picture of the setup is shown in Figure 6.1a. The 2S modules are placed with their carriers on two copper jigs which are mounted on top of four Peltier elements. By controlling the supply voltage of the Peltier elements, the temperature of the copper jigs can be controlled. To avoid overheating, the backside of the Peltier elements is in contact with an additional copper block that is flown through by a cooling liquid. The cooling liquid is provided by a chiller and can reach temperatures down to −10°C. The minimal achievable temperature of the copper jigs is −46°C. A scintillator is placed below the module to perform signal studies using radioactive sources. The mechanics are placed within an aluminium box acting as a Faraday cage, thermal shielding and protection against external light.

COMORES achieves a temperature stabilization on the 2S module prototypes by cooling the aluminium carrier plate below the modules via the copper jigs. This approach results in a significant temperature gradient between the controlled jig temperature and the temperature levels on the modules. Therefore, detailed thermal studies had to be performed to measure the temperature levels on the 2S module prototypes, e.g. the silicon sensor temperatures for different copper jig temperature settings.

Climatic Chamber Setup

To reduce the thermal gradient between the different module components measured within COMORES, a climatic chamber is used. The chamber is of the type *Kambic KK-190 CHLT* [Kam22] and can reach air temperatures between −40°C and 180°C. It is also possible to control the relative humidity of the air inside. A picture of the chamber is shown in Figure 6.1b. As the chamber volume is cooled via the air inside the volume, a more homogeneous temperature distribution between the module components can be achieved compared to the situation in the Cooled 2S Module Readout Station.

6.2.2. Noise Studies with 8CBC3 Modules

With the availability of the first 8CBC3 prototype hybrids, the module assembly centers have started building and testing prototype modules. A crucial parameter to define the functionality of all individual readout channels is their noise. As introduced in Section 3.2.6, it is measured by scanning the channel occupancy as a function of the applied CBC threshold in the absence of external signal. Assuming a purely Gaussian distributed noise, the resulting distribution can be described by an error function as the binary readout results in an integrated noise spectrum. By performing an error function fit, the pedestal and noise of each channel can be determined. This section summarizes the noise studies performed with 8CBC3 modules.

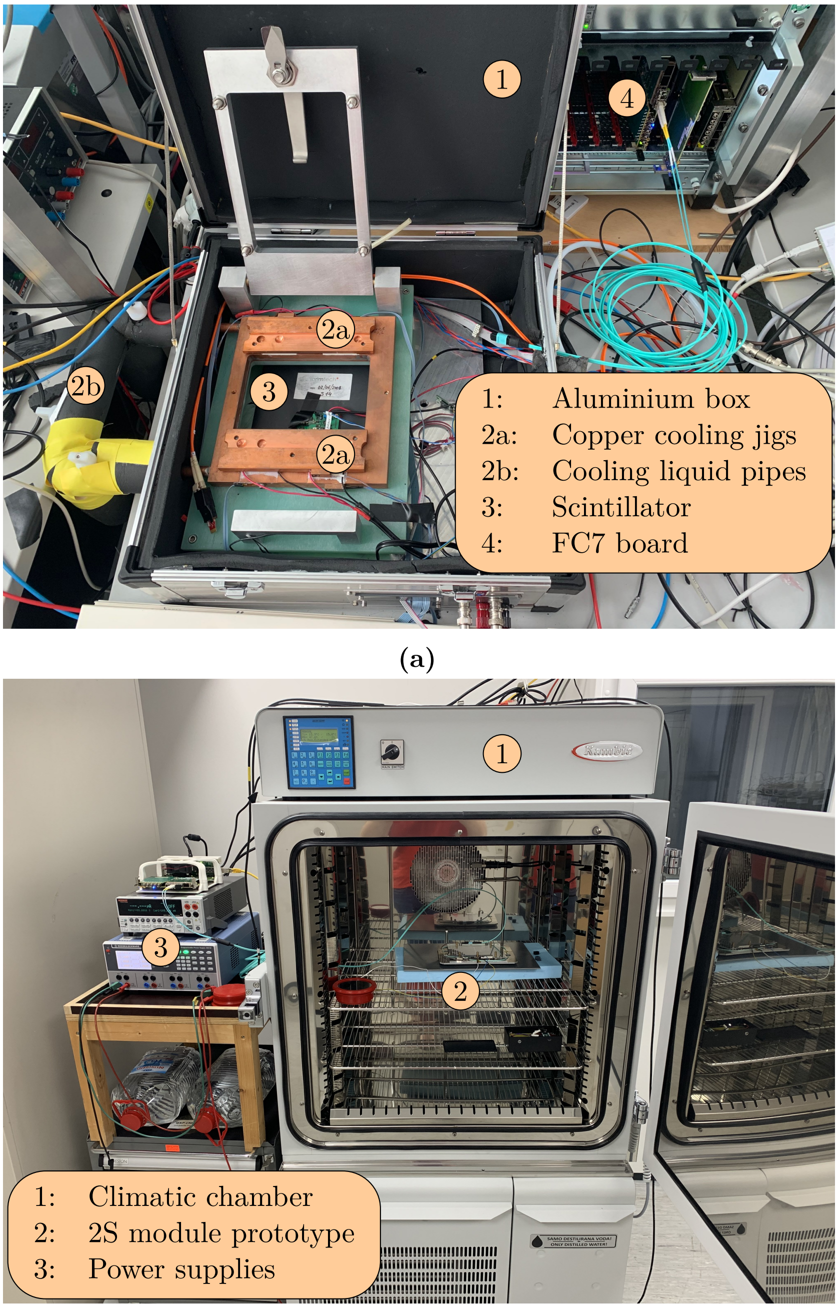

(a)

(b)

Figure 6.1.: Experimental setups used to perform laboratory based studies with 2S module prototypes. (a) The Cooled 2S Module Readout Station allows to control the temperature of the aluminium carrier via Peltier elements mounted below two copper jigs. The minimum reachable jig temperature is −46°C. An aluminium housing provides shielding against external light and electromagnetic influences and acts as thermal shielding. (b) To enable a direct cooling of all module components, a climatic chamber is used. Air temperatures down to −40°C can be reached.

Optimized Grounding Configuration

As a first test after receiving the frontend hybrids and the service hybrid for the module assembly, a *module skeleton* can be assembled. Therefore, the service hybrid is connected to the two frontend hybrids. As the CIC chips are not bump-bonded to the 8CBC3 frontend hybrids, separate circuit boards called *mezzanine cards* with the CICs are plugged onto the frontend hybrids. This test is done to guarantee fully functional electrical components for the module assembly. As no sensors are attached, the load capacitance of each channel is small, which results in a low noise (compare Equation (4.4)). Figure 6.2a summarizes the resulting noise values for each module channel in a histogram. Data from the module skeleton are shown in green. An average noise value of 2.4 V_{cth} is observed, corresponding to an equivalent noise charge (ENC) of approximately $375\,\text{e}^-$, based on the conversion introduced in Section 3.2.7.

After finishing the module assembly, the noise measurements are repeated. For 8CBC3 modules, it is possible to read out the frontend hybrids individually via an electrical interface board connected to the hybrids instead of using the CIC mezzanine cards and the service hybrid. The resulting noise values are shown in blue in Figure 6.2a. An average noise value of 6 V_{cth} or approximately $940\,\text{e}^-$ is observed. This corresponds well with the specified noise of the CBC's pre-amplifier and post-amplifier stages of $\leq 1000\,\text{e}^-$ [Pry19]. After connecting the CIC mezzanine cards to both frontend hybrids, the module is read out via the optical link. The extracted channel noise is shown as orange dashed line. The noise shows a wide spread with values between 10 V_{cth} and 20 V_{cth} and a mean of 13 V_{cth}. This is more than twice the expected chip noise and in disagreement with the electrical module readout presented previously. The origin for this noise increase is identified in different electrical ground levels of the 8CBC3 module and its aluminium carrier. During the electrical readout, the aluminium carrier is directly connected to the ground of the electrical interface board via screws. This ground level is additionally directly connected to the ground lines of the frontend hybrids via the electrical connectors between interface board and hybrids. The ground of the electronic circuit board is provided by the low voltage power supply used to create the voltage levels for all chips. During the optical module readout, one common ground level is provided to the module via the low voltage connector on the service hybrid. For the noise measurement shown as dashed orange line, the module was fixed on the aluminium carrier via screws at the five fixation points in the Al-CF bridges. As this fixation does not provide a low ohmic contact, the carrier can act as an antenna and introduce noise into the module. To avoid this effect, an additional grounding of the carrier plate is necessary. Best noise results have been found by using the shortest possible connection between carrier and module connecting dedicated grounding pads on the frontend hybrids via screws to the carrier. This configuration is depicted in Figure 6.2b. The resulting noise distribution is shown as a dotted red line in Figure 6.2a. It coincides well with the distribution measured using the electrical readout and yields the expected average noise value below $1000\,\text{e}^-$. All 8CBC3 module measurements presented in the following are performed with an electrical connection between carrier and frontend hybrids if not stated otherwise. In most of the cases, this connection is realised via screws. However, using short cables with a length of about 2 cm has yielded comparable results.

The histograms shown in Figure 6.3a compare the noise distributions for bottom and top sensor channels using the previously described grounding configuration. Top sensor channels are marked in red and bottom sensor channels are marked in blue. Data are shown for module KIT_8CBC3_1. With an average noise value of 6.2 V_{cth}, the bottom sensor channels show a higher noise than the top sensor channels. This distribution is expected, as the CBC chips are bump-bonded on the top surface of the frontend hybrids. To connect channels of the CBCs with the bottom sensor, the hybrid provides a fold-over, routing the signal lines from the chips on the top side to bond pads located at the bottom side of the hybrid. Thus, the load capacitance

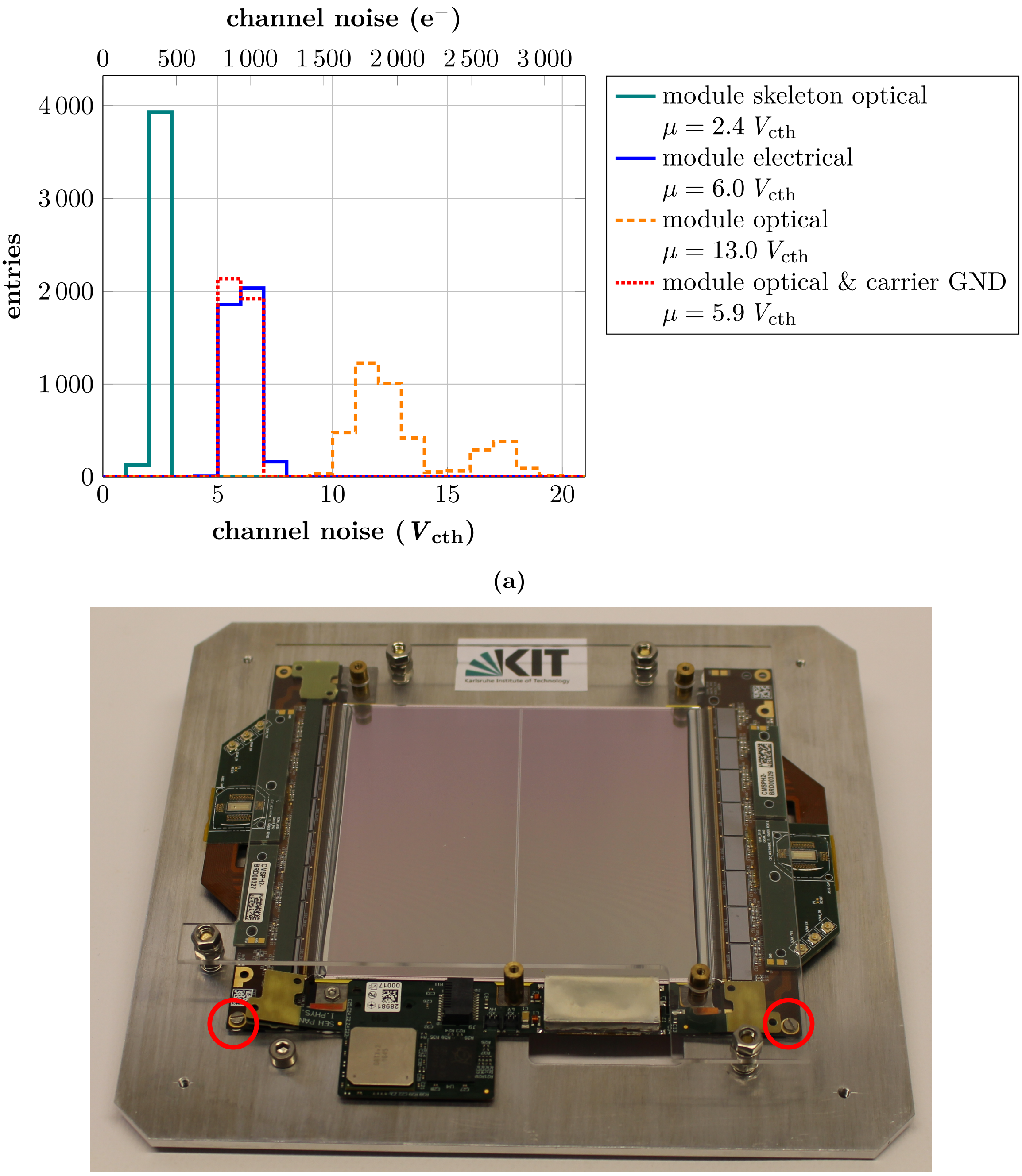

(a)

(b)

Figure 6.2.: (a) Comparison of the channel noise before and after module assembly of module KIT_8CBC3_1 at a bias voltage of 300 V. The top x axis shows the channel noise in electron equivalent. While the channel noise is small for a module skeleton, the measured noise increases to approximately 1000 e$^-$ after module assembly. However, this value is only achievable after grounding both frontend hybrids via screws to the aluminium carrier plate below the module. The electrical module readout was performed per frontend hybrid via an external interface board. (b) The connection between frontend hybrids and module carrier is realised via screws as indicated in the red circles. Using short cables yields comparable noise results.

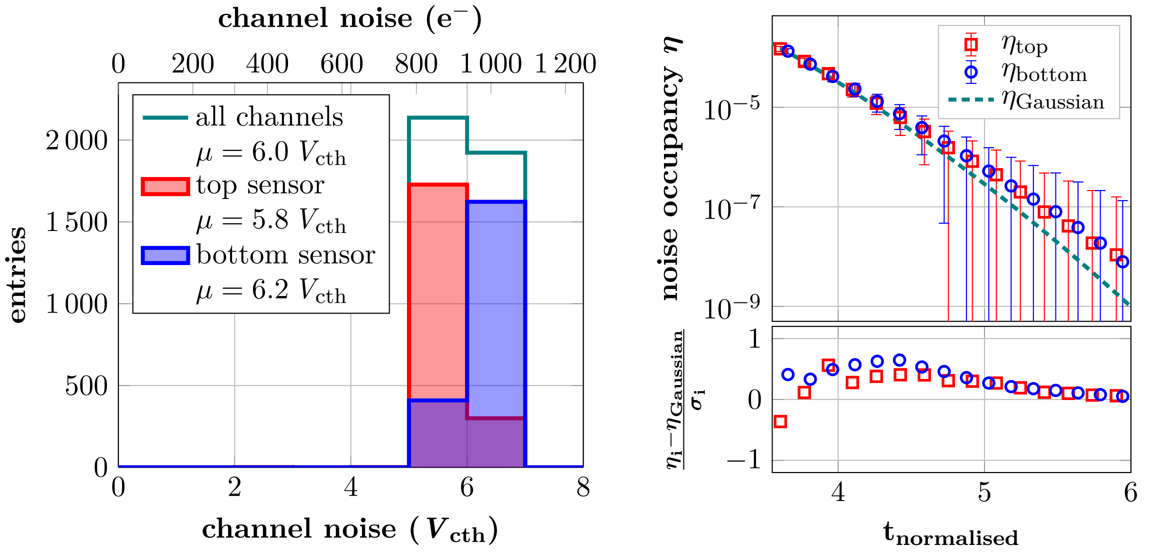

(a) (b)

Figure 6.3.: (a) Channel noise distribution for top and bottom sensor channels. Due to a foldover in the frontend hybrid design, the capacitive load connected to bottom sensor channels is larger than for top sensor channels. This leads to an increased noise level for the bottom sensor channels. Data are shown for module KIT_8CBC3_1 at a bias voltage of 300 V. (b) The noise occupancy is measured as a function of the relative threshold setting in units of the average channel noise per silicon sensor with module KIT_8CBC3_5. The statistical uncertainties σ_i for each threshold setting are calculated as the standard deviation of the mean of a binomial distribution (see Equation (6.6)). The resulting data points coincide well with the expectation from a purely Gaussian noise distribution η_{Gaussian}, shown as dashed green line. The module bias voltage is 300 V and 500 000 events are read out for each threshold setting.

of bottom sensor CBC channels is higher than the one for top sensor CBC channels. This leads to an increased noise level following Equation (4.4). This effect is also visible in the channel noise measured for a module skeleton as shown in Figure B.1 in the appendix.

To verify the assumption of Gaussian distributed module noise, the noise occupancy is measured as a function of the CBC threshold with 500 000 events per threshold setting with module KIT_8CBC3_5. These data sets allow to compare the module noise level with the Gaussian expectation. By normalising the relative CBC threshold t_i to the average noise level μ_i observed for top and bottom channels via

$$t_{\text{normalised}} = \frac{t_i}{\mu_i}\ , \tag{6.1}$$

the noise occupancy distributions η_i for both sensors can be directly compared in one plot. The resulting graph for $3.5 \leq t_{\text{normalised}} \leq 6$ is shown in Figure 6.3b. The data points coincide well with the assumption of a Gaussian distributed noise shown as green dashed line.

Noise Consistency Measurements

With an increasing number of module prototypes, the consistency of the channel noise can be checked among the prototypes. Figure 6.4a shows the channel noise histograms for five unirradiated 8CBC3 modules with optical readout. Small differences in the average channel noise can be observed between the modules. By averaging the mean values of the individual noise distributions and converting the values from V_{cth} units into electron equivalents, a mean module noise of $(967 \pm 57)\,\mathrm{e}^-$ results. The uncertainty is calculated as the standard deviation of the mean value. Thus, all module prototypes yield consistent noise levels compatible with the expectation of less than $1000\,\mathrm{e}^-$. Two main contributions can be identified to explain the observed spreading of the noise levels between the prototypes.

1. The channel noise is determined by an error function fit to the hit occupancy distributions. Thus, the statistical uncertainty of each channel noise value is determined by the number of events N_{events} taken at each threshold setting during the hit occupancy measurement. Data presented in Figure 6.4a are gathered with $N_{\mathrm{events}} = 100$. To evaluate the resulting uncertainty on the module noise, the noise measurement is repeated 19 times with the same module and $N_{\mathrm{events}} = 100$. Figure 6.4b shows a histograms of the extracted mean channel noise distribution in blue for module KIT_8CBC3_5. The standard deviation of the mean value is calculated to be $9\,\mathrm{e}^-$. By increasing the number of events to $N_{\mathrm{events}} = 1000$, the results can be significantly influenced. The resulting distribution is shown in red in Figure 6.4b. As the standard deviation of the mean decreases to $2\,\mathrm{e}^-$, the increased number of events lead to a more robust module noise measurement. During the module functional testing during production, N_{events} should be chosen large enough to reduce the statistical uncertainties of the measured module noise below the systematic uncertainties. However, an increase of the number of events leads to an increase of the duration of the measurement routine. The choice of $N_{\mathrm{events}} = 1000$ is a tradeoff between minimizing the statistical uncertainties and minimizing the measurement time.

2. The statistical uncertainties discussed previously can only partially explain the spread in module noise of the measured 8CBC3 modules. The module noise is dependent on the module temperature. All noise measurements presented previously have been performed in the Cooled 2S Module Readout Station. However, the cooling circuit has been deactivated, and the measurements have been performed at the ambient laboratory temperature. As the presented measurements have been performed on several days within the year, small temperature differences in the order of ±2°C are possible. This introduces a systematic uncertainty onto each measurement result. To estimate this uncertainty, the module noise was measured at different temperatures by turning on the cooling circuit. Results are presented in [Bra20] for module KIT_8CBC3_1. Figure 6.4c summarizes the module noise as a function of the silicon sensor temperature measured with the thermistor placed on the top sensor high voltage tail. The module noise increases with temperature, which is expected following the temperature dependent noise contributions discussed in Section 4.2.3. For temperatures between 5°C and 20°C, a linear increase of noise with temperature is observable. A linear regression yields a slope of approximately $2.3\,\mathrm{e}^-\,\mathrm{K}^{-1}$. Therefore, the discussed temperature differences of ±2°C between the measurements can be converted into a systematic contribution of $\pm 4.6\,\mathrm{e}^-$.

The discussed statistical uncertainties and the influence of temperature fluctuations on the module noise cannot explain the spread in module noise. Additional effects like e.g. production related differences between the electrical module components or small resistance differences in the connection between frontend hybrids and carrier can influence the channel noise between different module prototypes. However, these effects are difficult to quantify and will not be further investigated within this thesis.

The gathered results show a consistent noise level throughout all 8CBC3 modules. For comparison, the observed maximum difference of $140\,\mathrm{e}^-$ between the measured noise levels

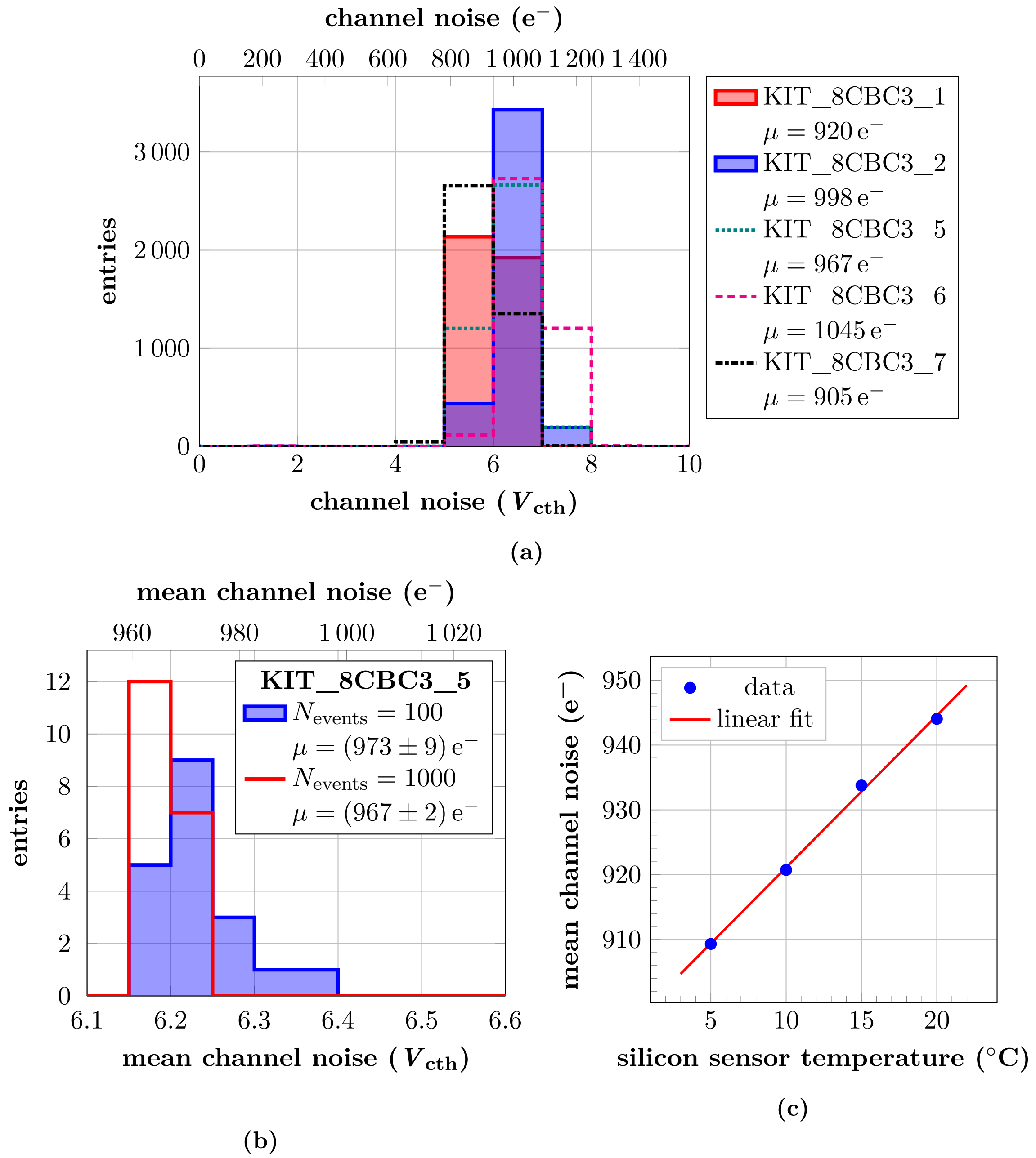

(a)

(b)

(c)

Figure 6.4.: (a) The channel noise distributions are measured for all optical 8CBC3 modules built at ETP. The top x axis shows the channel noise in electron equivalent. Small variations in the mean channel noise can be observed between the measurements. (b) To quantify different contributions to the noise variation between the measurements presented in (a), the noise measurement has been repeated 19 times for module KIT_8CBC3_5. For each measurement, the mean module channel noise is calculated and filled in a histogram. With increasing number of events per threshold setting N_{events} during the noise measurement, the noise variation reduces. Data shown in (a) have been taken with $N_{\text{events}} = 100$ and $N_{\text{events}} = 1000$. (c) An additional contribution leading to a variation of noise is identified within temperature fluctuations. The module noise is proportional to temperature. To quantify the effect at room temperature, a linear regression has been performed. Data taken from [Bra20].

and the uncertainty of $\pm 57\,\mathrm{e}^-$ are smaller than the smallest threshold setting unit of 1 V_{cth} corresponding to $156\,\mathrm{e}^-$.

Module Performance with Irradiated Sensors

Module KIT_8CBC3_3 has been assembled with sensors irradiated with protons to a fluence of $4.6 \cdot 10^{14}\,\mathrm{n_{eq}\,cm^{-2}}$. To operate the silicon sensors at stable leakage current levels, it has to be cooled to temperatures below 0°C. Therefore, the channel noise is measured with the Cooled 2S Module Readout Station at a silicon sensor temperature of about −20°C. The resulting distribution is shown in Figure 6.5a for a bias voltage of 600 V. An average channel noise level of $830\,\mathrm{e}^-$ is observed for the optimal grounding configuration. This is consistent with the temperature dependency measurement for unirradiated 8CBC3 modules presented in Figure 6.4c when extrapolating the linear fit to −20°C. An average channel noise level of $(840 \pm 9)\,\mathrm{e}^-$ is expected. However, the sensor leakage current increases significantly with irradiation. Figure 6.5b compares the module leakage current for the unirradiated module KIT_8CBC3_1 measured at approximately 20°C sensor temperature and module KIT_8CBC3_3 operated at a sensor temperature of approximately −20°C. The module leakage current I_L increases by approximately three orders of magnitudes. This leads to an increase of the shot noise contribution to the overall module noise according to Equation (4.5). Measurements of the module noise dependency on the strip leakage current I_L^{strip} are presented in [Dro21]. For strip leakage currents up to 2.8 µA, the increase of CBC noise due to increasing I_L^{strip} can be approximated by a linear dependency with slope

$$m = (0.419 \pm 0.002)\ V_{\mathrm{cth}}\,\mu\mathrm{A}^{-1}\ . \tag{6.2}$$

Similar to [Dro21], the strip leakage current of module KIT_8CBC3_3 can be approximated by dividing the module leakage current by the number of readout channels. This leads to a mean strip leakage current of 0.26 µA at a bias voltage of 600 V. For module KIT_8CBC3_1, a strip leakage current of 0.29 nA results. According to Equation (6.2), a noise difference of 0.1 V_{cth} or $17\,\mathrm{e}^-$ is expected between the unirradiated and irradiated module. Thus, the expected increase in noise is of the same size as the uncertainties of the noise measurement and the linear extrapolation. However, this study will be repeated as soon as new irradiated modules are available to increase the data set. Additional studies of the module performance of module KIT_8CBC3_3 are described in Section 6.3.

6.2.3. Noise Studies with 2S Prototypes

The latest 2S prototype components arrived in 2021 at the module assembly sites. As introduced in Section 3.2.5, the latest service hybrid design includes the bPOL chips as DC-DC converters, the lpGBT chip and the VTRx+ module for the first time. To implement these chips in the service hybrid design, major changes to the routing scheme had been made. As presented previously in Section 6.2.2, the noise performance of 8CBC3 modules can be significantly improved by grounding the individual frontend hybrids to the module carrier plate. After installing the modules in larger structures, this configuration is not realisable anymore due to space limitations. Therefore, an additional grounding possibility has been added to the service hybrid. By extending the service hybrid with a grounding pad onto the Al-CF bridge at one of the module fixation points, the module ground level can be connected by a screw to external structures as e.g. the aluminium carrier plate. This geometry allows to connect the module ground to all external structures at a central point.

Similar to the noise measurements performed with the first 8CBC3 module prototypes, the module noise of the new components is compared before and after assembly. The resulting

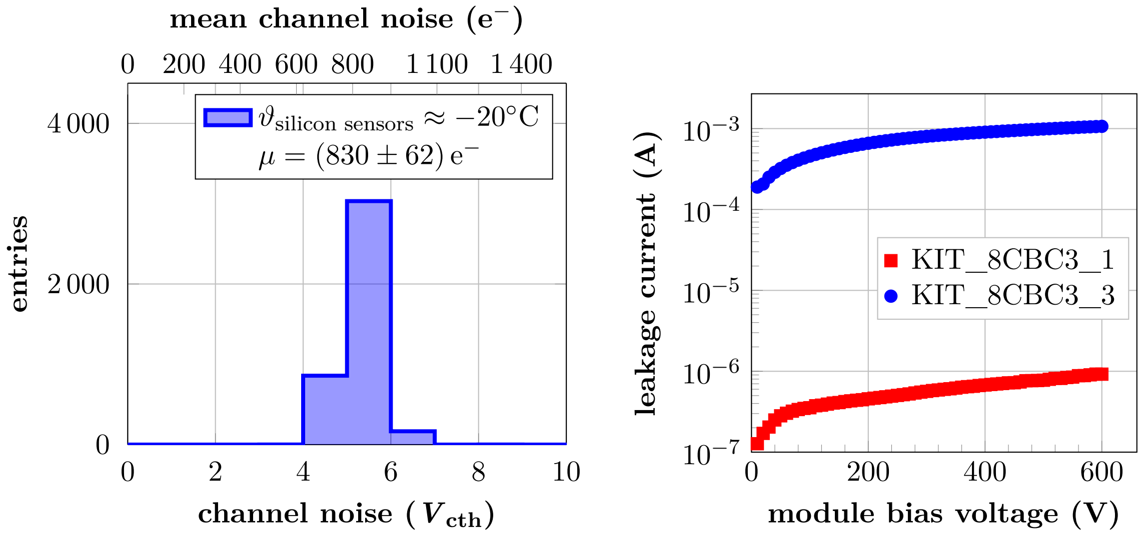

(b)

(a)

Figure 6.5.: (a) Channel noise of module KIT_8CBC3_3 assembled with silicon sensors irradiated with protons to a fluence of $4.6 \cdot 10^{14}\,\text{n}_{\text{eq}}\,\text{cm}^{-2}$. The measurements are performed at a sensor bias voltage of 600 V and at a sensor temperature of −20°C. (b) Comparison of the module leakage current for different bias voltage settings for module KIT_8CBC3_1 (unirradiated) and module KIT_8CBC3_3 (irradiated sensors). The leakage current increases by three order of magnitudes through the irradiation.

distributions are summarized in Figure 6.6a. The module skeleton noise shown in green stays unchanged at approximately 375 e$^-$. The channel noise distribution of a 2S prototype placed on the aluminium carrier without adding any ground connections between carrier and module is shown in orange. As for the 8CBC3 module, this configuration yields high noise levels around 12 V_{cth}. By connecting the ground contact at the SEH to the carrier plate, the distribution shown in red is measured. The connection is realised by a screw protuding the carrier plate and a brass nut connecting the screw to the ground pad on the SEH. A photo of this configuration can be seen in Figure 6.6b. The channel noise decreases significantly and the distribution width reduces. However, the resulting average module noise of 1200 e$^-$ is larger than the expected noise level measured with 8CBC3 modules. For comparison, the average module noise of all investigated 8CBC3 module prototypes is marked as black dashed line in Figure 6.6a. Therefore, the frontend hybrids have been grounded additionally via screws to the aluminium carrier plate. This reduces the module noise further to approximately 1100 e$^-$ but still does not yield a comparable noise level to the 8CBC3 modules. Similar noise levels are observed with all other 1.8 mm 2S prototpyes measured at ETP. A comparison of the individual channel noise distributions is shown in Figure B.3. The average module noise of all 2S prototypes is $(1112 \pm 53)\,\mathrm{e}^-$.

A globally increased noise level implies the need to operate 2S modules at a higher threshold to suppress noise hits sufficiently. However, choosing a higher threshold reduces the detection efficiency of the module. Together with irradiation effects in the detectors, this can have a significant influence on the tracking performance in the CMS detector during the HL-LHC runtime. Therefore, the origin of the increased noise for 2S prototypes has to be found and suppressed as much as possible.

Noise Contributions

Similar to the investigations performed with the 8CBC3 modules (see Section 6.2.2), the noise occupancy of 2S prototypes is measured as a function of the CBC threshold. The resulting data are compared with the expectation of a purely Gaussian noise distribution. The data sets for top and bottom sensor are shown in Figure 6.7a. Only the SEH ground contact is connected during these measurements. The noise occupancies measured for the top sensor are compatible with the Gaussian expectation. The bottom sensor data set shows a significant excess compared with the Gaussian expectation within the whole data range. This indicates that an additional noise component is present in the 2S prototypes, mainly affecting the bottom sensor. Similar results are observed after adding the frontend hybrid ground connections.

The spatial hit distribution can be displayed as a function of the event number as shown in Figure 6.7b. The hit distribution is shown for the bottom sensor channels of the right frontend hybrid. The observable horizontal structure within individual events indicate that a majority of module channels detect a hit at the same time. This effect is called *common mode noise* and introduces an excess of hits with respect to a purely Gaussian noise distribution. For comparison, the event display of an 8CBC3 module at a comparable threshold is shown in Figure B.2.

To investigate the origin of these module noise contributions, a set of measurements is performed to test possible explanations. A summary of the tests performed at ETP is given in the following.

Non-invasive Noise Investigations

By plotting the mean channel noise per CBC as a function of the CBC id, a spatial noise distribution across the two frontend hybrids can be visualized. The corresponding plot is shown

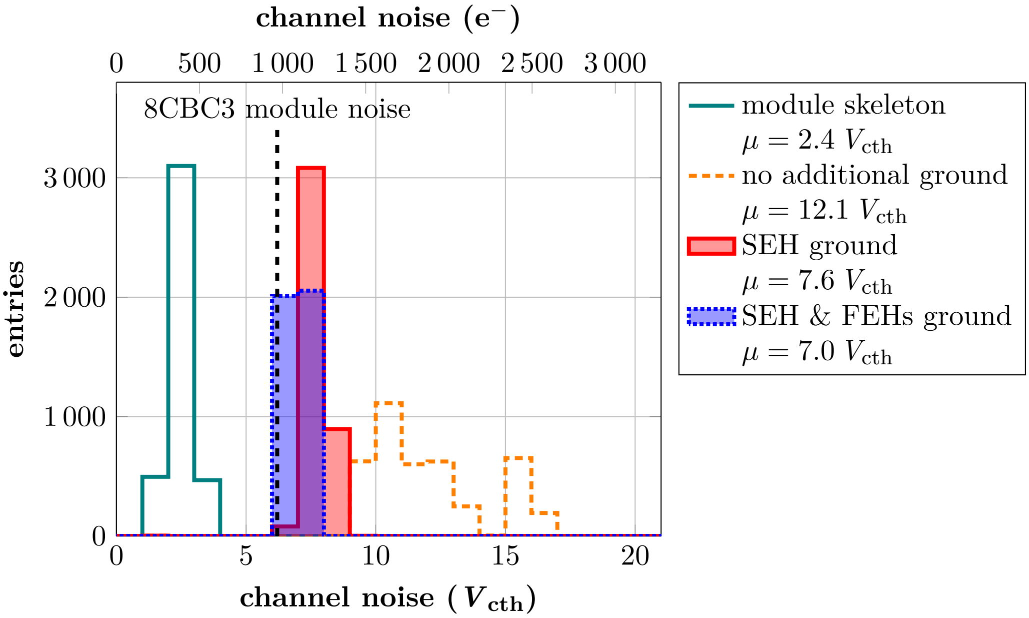

(a)

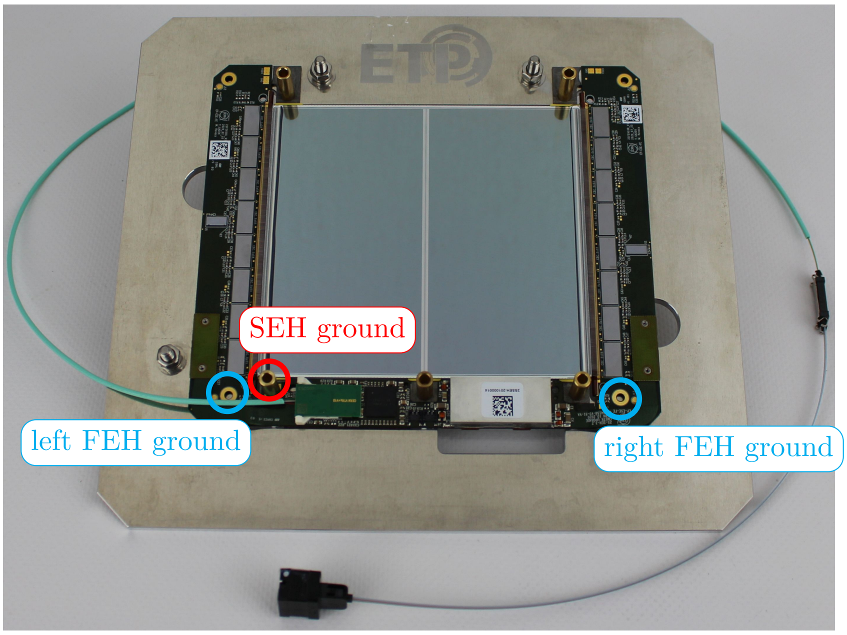

(b)

Figure 6.6.: (a) The channel noise of module KIT_2S_1 is compared for different grounding configurations. Prior to module assembly, the noise of the module skeleton is measured and shown in green. Placing the fully assembled module on its carrier plate without additional grounding connections leads to a high channel noise as shown in orange. By connecting the grounding pad on the service hybrid shown in (b) in red via a conductive nut, the average channel noise can be reduced to 7.6 V_{cth}. As this value is larger than the average noise level observed for 8CBC3 modules marked as a dashed line, additional grounding connections of the frontend hybrids to the carrier plate are added as shown in cyan in (b). The resulting noise is still approximately 1 V_{cth} higher than the noise level of the 8CBC3 modules.

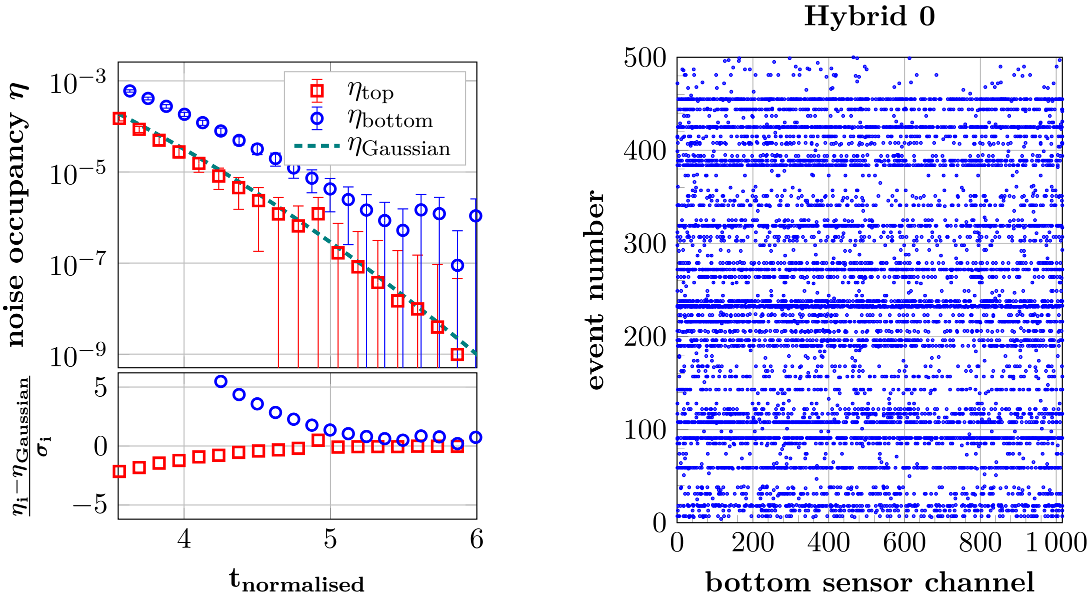

(a) **(b)**

Figure 6.7.: (a) The noise occupancy is measured as a function of the normalised threshold for module KIT_2S_1. While the top sensor data shown in red are consistent with the expectation of a Gaussian distributed channel noise shown as dashed green line, the bottom sensor occupancies show a significant excess. (b) By plotting the hits registered in the bottom sensor channels of the right frontend hybrid per event, the spatial distribution of hits can be studied. A clear horizontal structure is visible for some events indicating the presence of a common mode noise contribution. The relative threshold is set to be 2.5 times the average channel noise. The bias voltage is set to 300 V for all measurements.

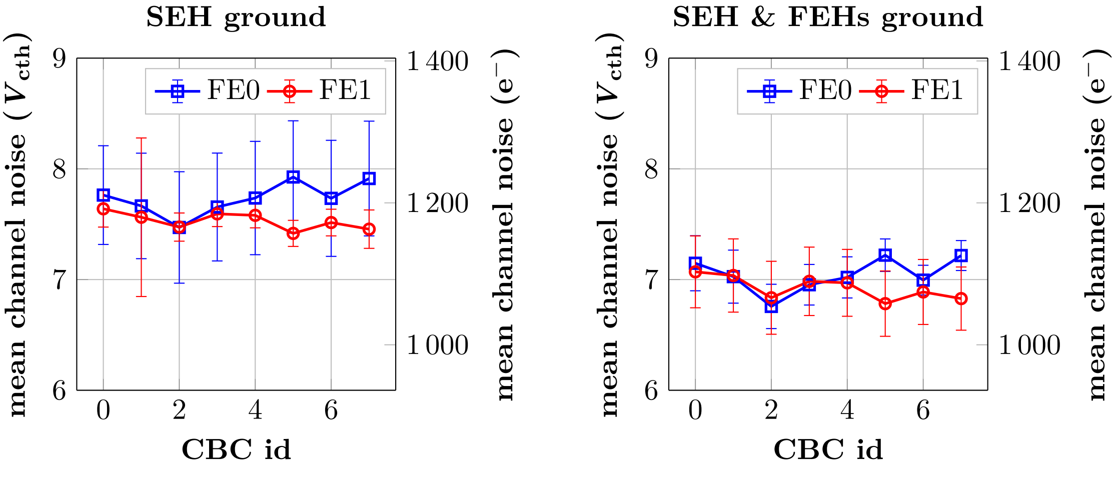

(a)

(b)

Figure 6.8.: The mean channel noise per CBC is shown as a function of the CBC id. The module configuration with only the SEH ground connected to the carrier plate is shown in (a). By additionally connecting the frontend hybrid grounds to the carrier plate, the distributions shown in (b) result. No trend can be observed between the two frontend hybrids and the CBCs. Therefore, the increased noise observed in the 2S prototypes is a common effect affecting all module channels in a similar way.

in Figure 6.8a for module KIT_2S_1 with only the SEH ground connected to the carrier plate. The channel noise measured on the right frontend hybrid is shown in blue and the noise of the left frontend hybrid marked in red. No trend can be observed between the different chips and frontend hybrids. Figure 6.8b displays the results gathered from the same module by connecting additionally the two frontend hybrid ground connections to the carrier plate. Also within this configuration, no trend can be observed between the chips and frontend hybrids. Therefore, the noise increase is a common effect for all readout channels.

During testing of the 2S prototypes, it has been found that the silicon sensor leakage current increases drastically when applying the low voltage (LV) potential of 10 V. This effect is visualized in Figure 6.9a measuring the module leakage current as a function of the applied bias voltage. The combined leakage current of both sensors is shown in green before applying the module LV. A leakage current of approximately 1 µA is measured at a bias voltage of 300 V. After turning on the LV, the leakage current level increases by a constant offset of approximately 3 µA. The origin of this effect is identified within the VTRx+ module. Working as optoelectronic transceiver, it generates infrared light at a wavelength of 850 nm when biased [Ola+20]. As shown in Figure 6.9b, a transparent plastic cover is installed above the optical VTRx+ components. Additionally, the optical fibers leaving the VTRx+ module are uncovered for about 2 cm. This leads to light leakage during module operation that explains the observed offset between the leakage current characteristics. As the data transmission is performed by intensity modulation, this light can act as a noise source for the AC coupled CBC readout. However, no increase in the channel noise can be observed towards the position of the VTRx+ module located next to the strips of CBC zero on the left frontend hybrid. Therefore, only diffuse light from the lasers could explain the noise increase.

To test this hypothesis, the VTRx+ module is disconnected from the service hybrid and its plastic cover and the optical fiber is covered with black tape. Figure 6.9c shows a photo of the taped chip after reconnecting it to the service hybrid. By remeasuring the leakage current characteristic, the shielding performance of the tape can be evaluated. Data are shown in blue in Figure 6.9a. The data points coincide well with the points measured with deactivated LV. Therefore, the light emission is highly suppressed. The module noise levels before and after covering the VTRx+ module are compared in Figure 6.9d. The two distributions coincide well within the statistical uncertainties. Thus, the modulated light emitted by the VTRx+ on the same module does not increase the noise of 2S prototypes.

Another possibility to explain the noise increase is a change of gain of the CBCs between 8CBC3 modules and 2S prototypes. As the 2S prototype noise level is approximately 16% higher than the one of 8CBC3 modules, the chip gain would need to be increased by the same amount. However, both frontend hybrid prototype versions are equipped with the same CBCs of version 3.1 and no changes have been implemented in the hybrid design in the analog signal path from the sensor to the chips. To experimentally rule out this hypothesis, a ^{90}Sr source is placed above an 8CBC3 module and a 2S prototype and the integrated charge spectrum is measured by performing threshold scans. These measurements are performed in the Cooled 2S Module Readout Station and the signal of a scintillator placed below the modules is used for triggering the 2S readout. The resulting data are displayed in Figure B.4. The signal distribution of the 2S prototype is compatible with the distribution measured for the 8CBC3 modules taking into account an increased noise at low threshold settings. For comparison, the expected signal spectrum with a 16% increased gain is shown in addition. Thus, this measurement could clearly identify such increase in gain but does not observe such an effect.

Additional tests have been performed within the CMS community to reduce the module noise by adding additional grounding connections at dedicated contacts on the frontend hybrids. These studies showed no significant decrease of noise compared to the best value of 7 V_{cth} achieved at ETP by grounding each frontend hybrid via one screw to the aluminium carrier plate. Together with the fact that a large majority of the changes between 8CBC3 modules and 2S prototypes have been implemented in the service hybrid design, these results hint towards a problem located on the service hybrid. Special attention is drawn towards the DC-DC converter stages as they are active electrical components operating at frequencies in the low megahertz regime. Therefore, it has been decided to assemble a new 2S prototype including additional components to allow dedicated investigations of the 2S module powering circuitry.

Invasive Noise Investigations

A dedicated 2S prototype has been assembled at ETP to investigate the origin of the increased noise level of 2S prototypes. This prototype houses additional hardware components compared to the 2S module baseline design and is called KIT_2S_5. A picture of the fully assembled module can be seen in Figure 6.10a. It is a 4 mm module variant with a second stump bridge. A second set of high voltage (HV) tails is glued to the sensors on the hybrid free module side. The two sets of HV tails can be seen Figure 6.10b showing the fully assembled bare module. The additional HV tails allow to bias the silicon sensors via a custom designed electronic circuit board called *2S power plate*. This board copies the sensor bias voltage and low voltage ground circuitry of the service hybrid. The 2S power plate is glued onto the Al-CF bridges at the hybrid free module side. The ground pads on the frontend hybrids are connected via wire-bonds to the low ground level of the power plate. As the lpGBT chip on the service hybrid has a problem with the I^2C line used to communicate with the left frontend hybrid, two external cables are used to connect to a spare I^2C controller. These additional cables have already been added to other 2S prototypes within the CMS community and do not influence the module noise level. The various tests performed to probe different hypotheses for the origin of the increased module noise developed within the CMS community are summarized in the following.

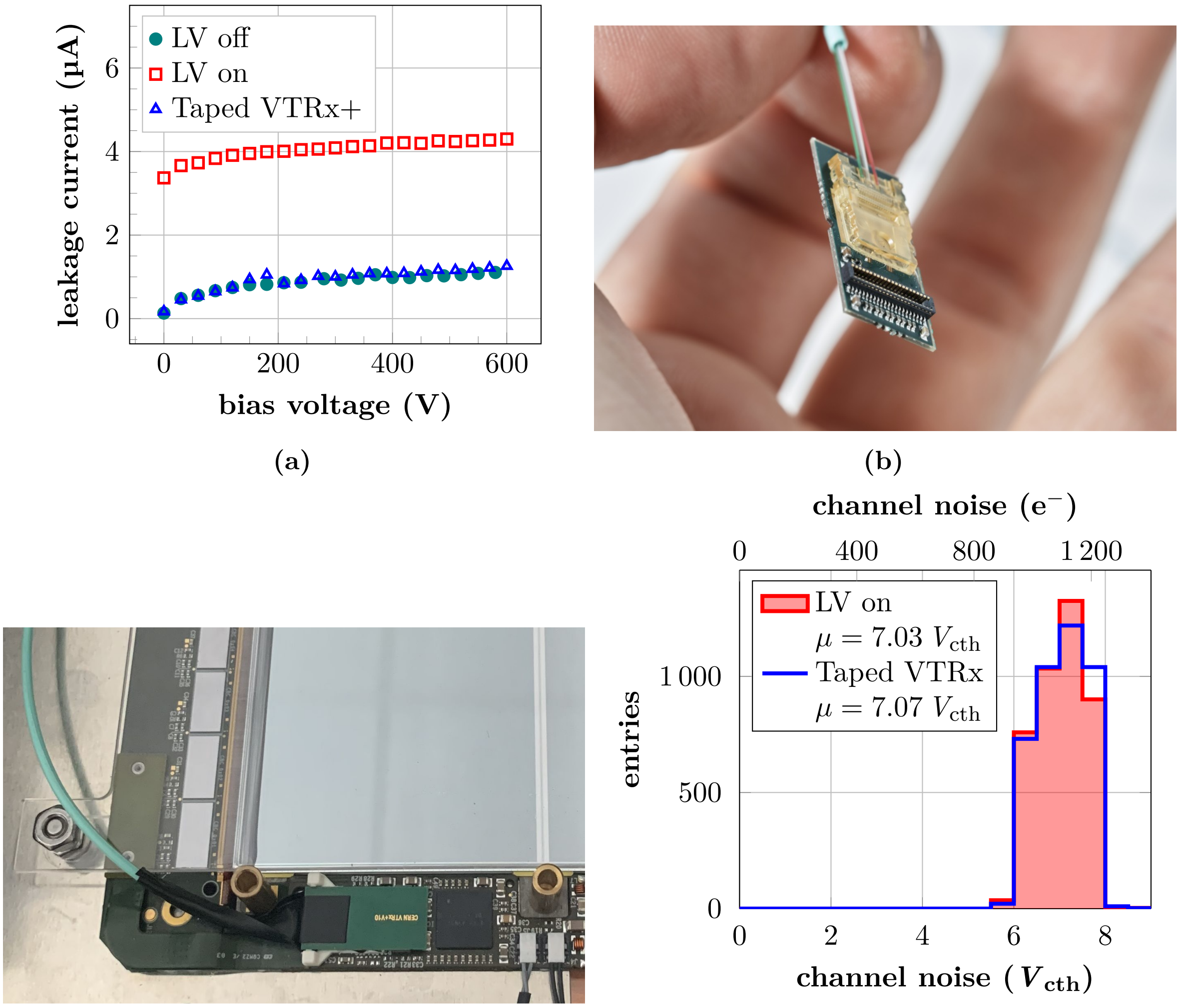

(a) **(b)**

(c) **(d)**

Figure 6.9.: Investigations of the influence of VTRx+ light on the 2S prototype noise. (a) The module leakage current is measured as a function of the bias voltage before and after turning the low voltage on. The corresponding curves are shown in green and red, respectively. Due to a transparent cover over the optical components of the VTRx+ module shown in (b), the emitted light increases the leakage current by about 3 µA. By covering the VTRx+ module with black tape as shown in (c), the light leakage can be reduced effectively, as the leakage current shown in blue drops back to the level with unpowered VTRx+ module. (d) Taping the VTRx+ module has no influence on the channel noise.

Figure 6.11 compares the mean channel noise gathered for each module configuration. The bias voltage for all tests is set to 350 V and the low voltage to 10.3 V if not specified otherwise.

I: DC Ground Loop via Silicon Sensors' Bias Rings During the module wire-bonding, the ground pads of the frontend hybrids are connected to the silicon sensor bias rings. Typically, both frontend hybrid grounds are connected to the bias rings of both sensors. This configuration introduces a DC ground loop within the module as the frontend hybrid ground levels are additionally connected with each other via the service hybrid. For slightly different ground potentials within the hybrids this could lead to small currents introducing noise. To exclude this effect, the ground pads of the right frontend hybrid are only connected to the top sensor bias ring. Similarly, the ground pads of the left frontend hybrid are connected to the bottom sensor bias ring. After connecting the ground flap of the service hybrid and biasing the sensors via the HV tails below the service hybrid, a module noise of $(8.3 \pm 0.6)\ V_{\text{cth}}$ is measured. This value is larger than the average channel noise observed for the 1.8 mm module variants investigated in the previous section and shown as orange dashed line in Figure 6.11. This effect is consistent with measurements performed with 4 mm module variants at other institutes in the CMS community and needs to be further investigated. However, the DC ground loop introduced by connecting both frontend hybrid grounds to both sensor bias rings does not generate increased module noise.

II: Additional Grounding Connections on Frontend Hybrids To validate the measurements performed at other institutes, additional grounding connections are added to the frontend hybrids. Each frontend hybrid provides two dedicated ground pads that can be used to connect via screws to the aluminium carrier plate. These pads are marked G1 to G4 as indicated in Figure 6.10a in cyan. Additionally, the power plate ground level can be connected via an external cable to the ground level of the low voltage power supply. However, all combinations of possible connections did not yield any significant improvement in module noise. These measurements coincide with the observations made at other institutes. Only the noise measurement with the lowest average noise level is shown as an example in Figure 6.11. As all these additional connections are intended to stabilize the ground line of the 2S prototypes, the observations indicate that the increased noise is not caused by differently fluctuating ground potentials on the hybrids.

III: Investigation of Silicon Sensor Biasing Circuitry An additional origin for noise can be a ripple on the modules bias voltage potential which is applied to the silicon sensors. Due to the fluctuating bias voltage, the potential at the strip implants is fluctuating and a signal is induced in the readout channels leading to noise. Therefore, the behaviour of the high voltage circuitry is investigated. A schematics of the service hybrid high voltage circuitry is shown in Figure 6.12a. The potential provided by the power supply is applied to a low-pass filter before reaching the sensor backside. All previously presented measurements have been performed with the second set of high voltage tails disconnected from the power plate. By adding this connection, the silicon sensor backplane is coupled a second time to the module ground potential via the low-pass filter capacitance on the power plate. The module noise in this configuration is reduced to $(6.9 \pm 0.5)\ V_{\text{cth}}$ and is shown as configuration IIIa in Figure 6.11. Additionally providing the bias voltage potential from the power supply to the power plate does not yield further noise improvements. These observations lead to the interim conclusion that noise couples into the electrical lines of the HV tails situated below the service hybrid. By adding the additional capacitive connection to ground far away from the service hybrid, the jitter on the silicon sensor bias voltage is reduced.

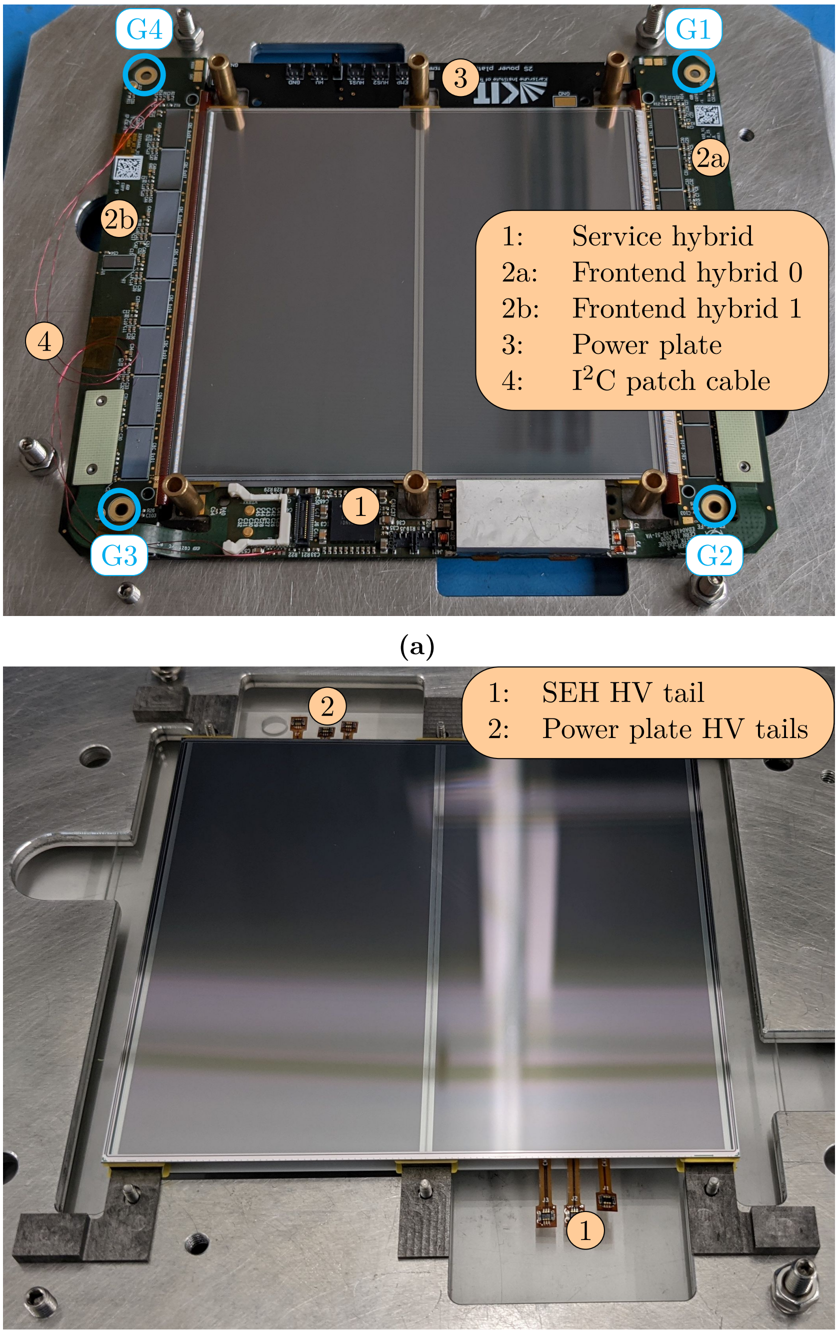

(a)

(b)

Figure 6.10.: To investigate the origin of the increased module noise, module KIT_2S_5 is assembled. (a) Opposite to the service hybrid, a power plate is glued onto the Al-CF fibers to allow biasing of the silicon sensors via a second set of HV tails shown in (b). Two additional cables have to be soldered between service hybrid and the left frontend hybrid due to a problem with one of the I^{2}C controllers. During module testing, different grounding configurations are tested. The frontend hybrids' grounds can be connected at four dedicated pads labeled G1 to G4.

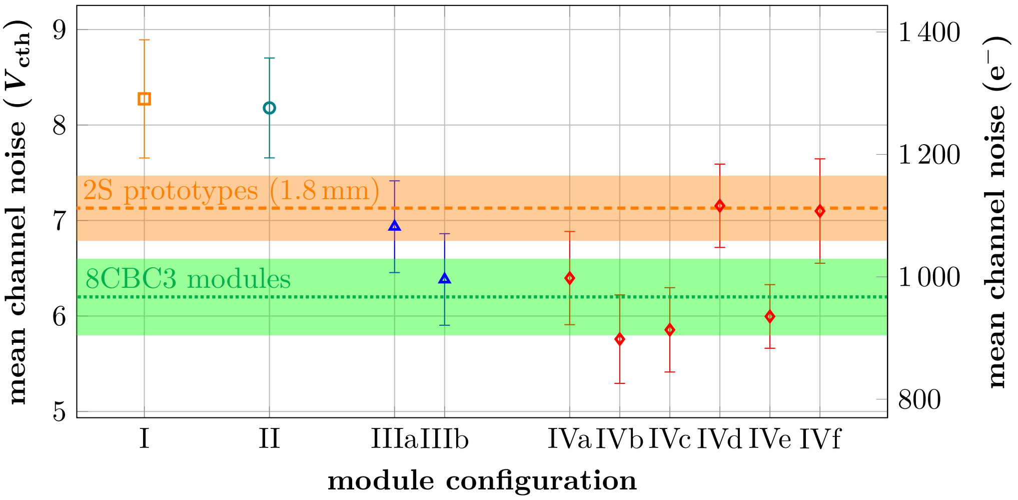

Figure 6.11.: Module KIT_2S_5 is tested with different configurations to investigate the influence on the mean channel noise (symbols in the plot). A description of the individual configurations is given in the text. The average module noise range of all 8CBC3 modules and all 2S prototypes tested at ETP are shown as green and orange areas, respectively.

Following this hypothesis, noise measurements are performed after disconnecting the HV tails below the service hybrid. The bias voltage is applied solely via the power plate and its HV tails. A further reduction of 0.5 V_{cth} is achieved as can be seen in Figure 6.11 labeled as configuration IIIb. A noise of $(6.4 \pm 0.5)\ V_{\mathrm{cth}}$ lies within the observed spread of the 8CBC3 module prototypes shown as green area in Figure 6.11. However, it is still higher than the average noise level observed for all tested 8CBC3 modules leaving the possibility to find further improvements. Additionally, the origin of the increased noise has not yet been identified, as the HV tails are passive components.

IV: Influence of DC-DC converter on Module Noise As the HV tails are located directly beneath the bPOL chips and coils, the influence of the DC-DC converter stages on the module noise is investigated. During the operation of the converter stages, electromagnetic radiation is produced that can introduce noise into the module if not shielded adequately. The service hybrid design includes an aluminium cover soldered above the DC-DC converter components. It has been shown that this shield reduces the peak of the electromagnetic emissions by a factor of 30 [CMS17c]. Additionally, this design has proved to shield the module sufficiently for all earlier service hybrid prototypes. To investigate if the newest service hybrid prototypes provide reduced shielding of the electromagnetic radiation through the circuit board, the DC-DC block is wrapped in copper foil as can be seen in Figure 6.12b. The HV tails stay unconnected and are kept outside the copper foil. The resulting module noise is shown as configuration IVa in Figure 6.11 and does not change compared to the previously presented module configuration. Therefore, the fluctuations on the bias voltage potential are not caused by electromagnetic radiation leaving the DC-DC converter. This result is in accordance with the measurement of the mean CBC noise as a function of the CBC id shown in Figure 6.8a and Figure 6.8b where no noise increase is observed for chips near the bPOL chips.

The DC-DC converter additionally produces noise propagating via the input and output power lines. It can be distinguished between *differential mode* and *common mode* noise. However, all service hybrid prototypes are tested at dedicated centers in the CMS community

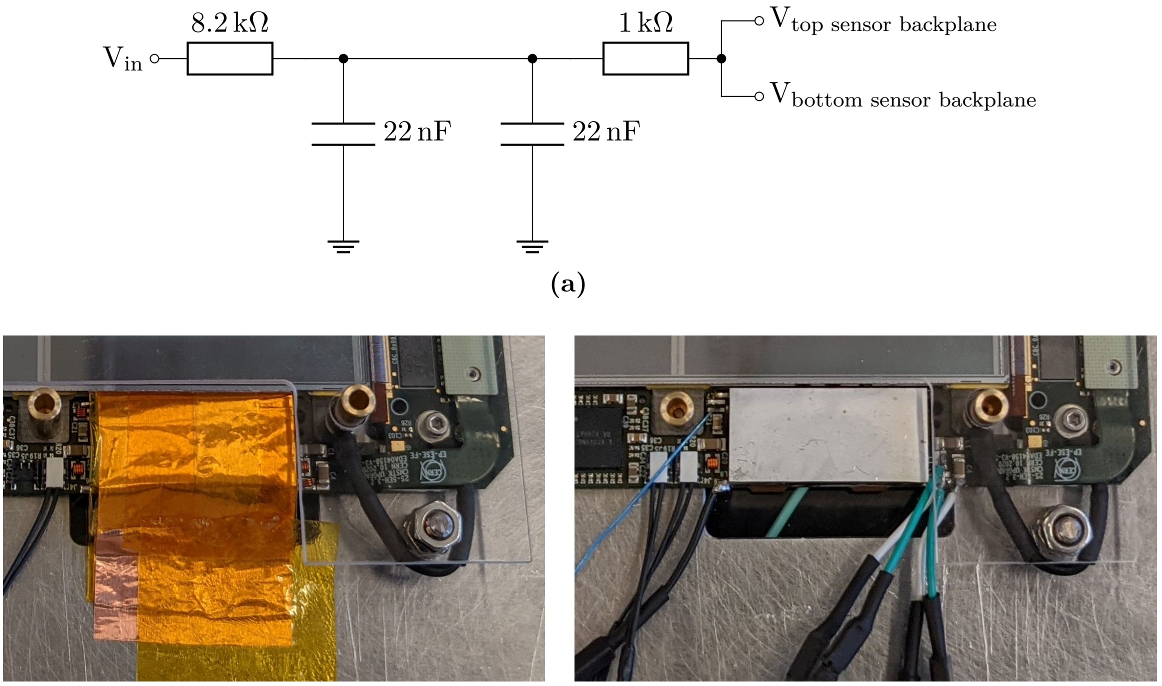

(a)

(b)

(c)

Figure 6.12.: (a) Schematics of the high voltage circuitry to bias the silicon sensors in a 2S module. The bias voltage V_{in} provided by a power supply is conducted via a low-pass filter to the HV tails and the sensor backplanes $V_{\text{top sensor backplane}}$ and $V_{\text{bottom sensor backplane}}$. (b) To shield possible electromagnetic radiation emerging from the DC-DC converter stages, a copper tape is wrapped around the service hybrid. (c) By soldering additional cables, it is possible to provide the chip voltage levels externally to the service hybrid behind the DC-DC stage. This allows to operate the DC-DC converter free of electrical load or to operate the module with turned off bPOL chips.

and both noise contributions are measured. These tests do not show significantly increased noise contributions for the latest prototypes [CMS17c]. To investigate the influence of the DC-DC converter stage onto the module noise, a low voltage bypass is installed by soldering additional cables to the module. Besides soldering the cables necessary to provide the two voltage levels of 2.5 V and 1.25 V after the DC-DC stage, additional sensing wires are used to automatically control the voltage levels on the module. A photograph of the DC-DC converter circuitry including the bypass cables is shown in Figure 6.12c. With this configuration, it is possible to turn off the DC-DC converter stage and to power the module directly. This leads to an additional reduction of the noise level to (5.8 ± 0.5) V_{cth} marked as IVb in Figure 6.11. This noise level conincides with the lowest noise levels observed for 8CBC3 modules. Removing all previously introduced grounding connections on the frontend hybrids (G1 to G4), reconnecting the HV tails on the service hybrid and removing all electrical connections of the power plate to module KIT_2S_5 (HV tails, ground wire-bonds and high voltage cable) yields the same noise level. The corresponding measurement is marked as IVc in Figure 6.11.

By applying 10 V to the service hybrid, the DC-DC converter stages can be switched on. However, their load is minimal as the bypass cables are still attached to provide the electronic power for module operation. In this configuration marked as IVd in Figure 6.11, the module noise increases to (7.2 ± 0.4) V_{cth}. By comparing this latest configuration with configuration I, the only difference is given by the electrical load of the bPOL chips. Therefore, a fraction of the module noise is dependent on the load of the DC-DC converter. To investigate this effect further, the module noise is measured as a dependency of the input power of the bPOL chips. After powercycling the chips, a voltage of approximately 10 V has to be applied for the converter stages to turn on. Afterwards, the voltage can be reduced down to a voltage of 7 V. Measurements are performed with module KIT_2S_5 operated in configuration IVd and module KIT_2S_1. For the latter module, only the service hybrid ground is connected to the carrier plate. Data are presented in Figure 6.13. For both modules, the module noise decreases with decreasing power consumption. A maximum decrease of 0.4 V_{cth} can be achieved by reducing the input voltage from 10 V to 7.5 V. However, a reduction in input voltage implies an increase in current consumption of the DC-DC converter stages. Higher currents require thicker power cables in the CMS detector which introduces more passive material to the detector volume. An additional feature can be observed in both plots. At specific input voltage levels, the output power shows a distinct peak. This *ripple* is a distinct feature of the bPOL12V_v4 chip. Operating the modules within this region leads to a significantly increased noise. As the appearance of the ripple is also load dependent, it takes place at different input voltages for module KIT_2S_5 (no load on the DC-DC stage) and module KIT_2S_1 (full load). For both modules, the ripple appears at significantly lower voltages as the target operation voltage of 10 V. Thus, this ripple cannot be responsible for the increased noise observed within the 2S prototypes.

Additional noise measurements have been performed with only the top sensor HV tail connected to the service hybrid while leaving the bottom sensor tail unconnected. Thus, no bias voltage is applied to the bottom sensor. Additionally, the DC-DC converter is operated normally, providing all necessary voltage levels to the module, and only the SEH ground is connected to the module carrier. A drastic increase in the noise level of all bottom sensor channels is observed, resulting in a mean bottom sensor channel noise of (43.4 ± 10.9) V_{cth}. This is expected as the sensor capacitance is at its maximum for a bias voltage of 0 V leading to an increase of the noise contribution caused by the load capacitance C_d (see Equation (4.4)). Observing the average channel noise of the top sensor channels, an average noise value of (6.0 ± 0.3) V_{cth} is measured, which is marked as configuration IVe in Figure 6.11. This value is in good agreement with the noise level observed for 8CBC3 modules. Repeating this measurement with only the bottom sensor HV tails connected yields comparable results for the noise level of

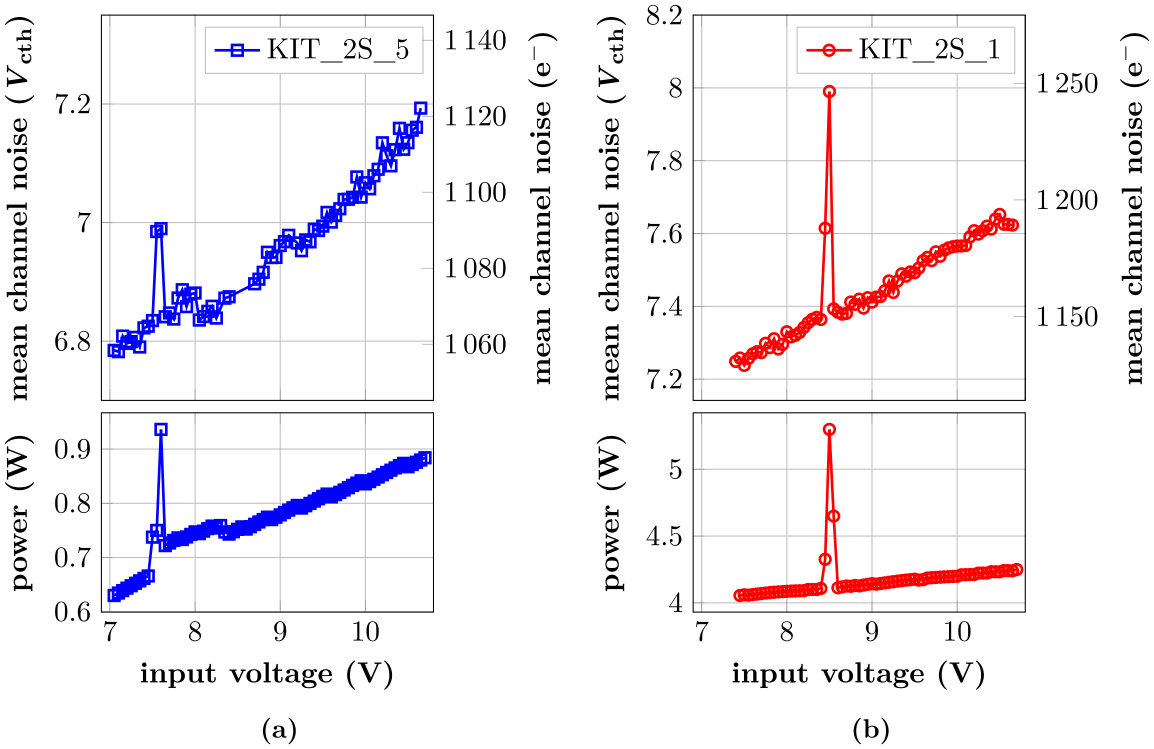

Figure 6.13.: Influence of the low voltage level onto the DC-DC power and the module noise. Data are shown for module KIT_2S_5 in (a) and module KIT_2S_1 in (b). With decreasing power consumption of the DC-DC converter, the module noise decreases. For both measurements, a peak in the power consumption is observed leading to a noise increase. This effect is a known feature of the bPOL chip version in use.

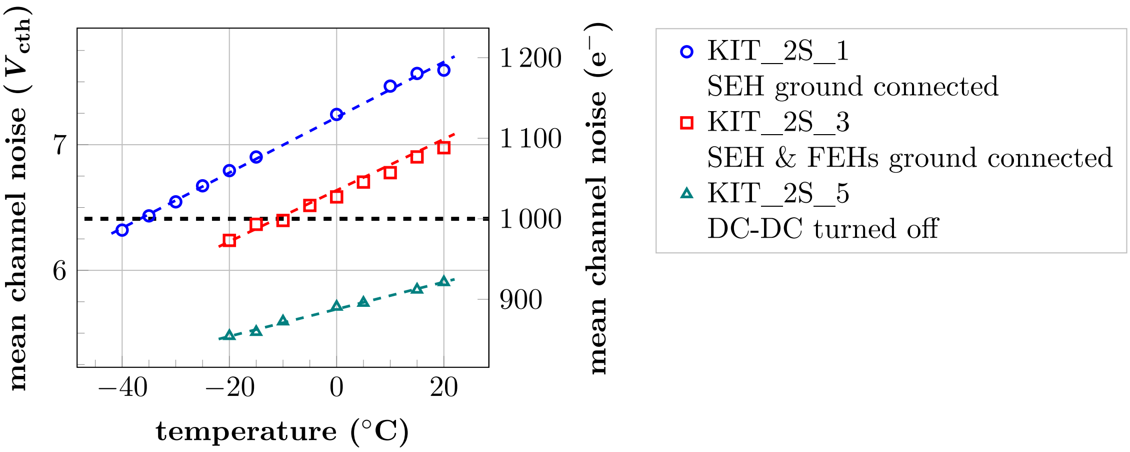

Figure 6.14.: Three 2S prototypes are tested within a climatic chamber for their noise dependency on the temperature. Each module is set up in a different grounding configuration. All datasets show a linear decrease of the noise with a decrease of temperature. Only by adding a direct grounding connection between the frontend hybrids and the carrier plate, or by turning off the DC-DC converter, a module noise of less than $1000\,e^-$ is reached at a sensor temperature of −20°C. Each module is operated at a bias voltage of 300 V.

the bottom sensor channel. Based on these observations, a new hypothesis for the origin of the increased module noise level is developed [Pit22]. As indicated in Figure 6.12a, the two sensor backplanes are connected directly with each other via the HV tails. This electrical configuration can be seen as resonant circuit with the two sensor backplanes forming a capacitor and the HV tails acting as inductor. With the DC-DC converter stages acting as external source, oscillating currents through the HV tails between the two sensor backplanes can be generated in the LC circuit. By disconnecting one of the HV tails, the LC circuit is interrupted and no oscillating currents can flow, leading to low channel noise. Following this hypothesis, a $100\,\Omega$ resistor is soldered onto each HV tail circuit board as indicated in Figure 5.14b and shown in Figure 5.14c. An average channel noise of $(7.1 \pm 0.5)\ V_{\mathrm{cth}}$ is measured and marked as configuration IVf in Figure 6.11. Changing the resistance to $1\,\mathrm{k}\Omega$, $10\,\mathrm{k}\Omega$ and $100\,\mathrm{k}\Omega$ yields comparable results. The noise level is comparable to the one measured with bypassed but powered DC-DC converter and larger than the noise level observed for 8CBC3 modules. However, a significant reduction of noise can be achieved compared to the original module operation shown in configuration I by adding a resistor to the HV tail circuit design. Including the resistors as *surface-mount devices* does not change the outer dimension of 2S modules and, thus, does not need any adaptations of the detector structures as ladders and dees.

Thermal Dependency

All noise measurements presented previously are perfomed at room temperature. Within the CMS detector, 2S modules will be operated at sensor temperatures of approximately −20°C. As discussed in Section 6.2.2 for 8CBC3 modules, the module noise decreases with temperature. To quantify the influence of cooling onto the module noise of 2S prototypes, modules KIT_2S_5, KIT_2S_1 and KIT_2S_3 are tested within a climatic chamber. Before each noise measurement, the air temperature is set and after the climatic chamber has reached the desired temperature an additional waiting time of 30 minutes is added to let all module components accomodate to the environment.

Figure 6.14 illustrates the temperature dependency of the mean channel noise for the three modules. Each module is set up in a different grounding configuration during the measurement. The service hybrid ground is connected to the carrier plate for all modules. Module KIT_2S_3 additionally houses direct screw connections between the frontend hybrids and the carrier plate. For measurements with module KIT_2S_5, the DC-DC converter is turned off and the module is powered via the low voltage bypass. All three noise distributions show the expected decrease with decreasing temperature. Only connecting the SEH ground is not enough to reach the desired module noise of $1000\,\mathrm{e}^-$ or less marked as dashed line in Figure 6.14 at sensor temperatures of $-20°$C. By adding the frontend hybrid grounding connections, this limit is reached. However, further decreasing the noise level below this limit corresponds to an increase of the safety margin to guarantee efficient module operation during the complete HL-LHC runtime. Therefore, it is crucial to find a solution to reduce the module noise leading to a shift of the data points towards the measurement results gathered with module KIT_2S_5.

Conclusions of 2S Prototype Noise Studies

Based on the studies presented in this section, some conclusions can be drawn concerning the origin of the increased noise level observed for 2S prototypes. The measurements performed with module KIT_2S_5 show that the bPOL chips on the service hybrid raise the module noise. The observations of a globally increased noise level across all module channels and the measurement results gathered from wrapping the DC-DC stage in copper foil rule out a radiative coupling of noise in the readout electronics. However, strong evidence is found that the DC-DC stage introduces noise into the sensor bias voltage potential applied to the sensors via the HV tails located beneath the DC-DC block on the service hybrid. A correlation between the direct electric connection of the two sensor backplanes in the high voltage circuitry and the increased module noise is observed. By introducing resistors into the HV tails, the module noise level can be improved.

In view of these results, several changes to the service hybrid circuitry design are discussed currently by the electronics working group at CERN. Besides adding resistors to the HV tails, a duplication of the low-pass filter is under discussion to bias each silicon sensor via a separate filter circuit. Additionally, connections to the ground planes in the service hybrid's multi-layer printed circuit board are relocated in the next service hybrid design to potentially mitigate problems with AC voltage couplings into the planes below the DC-DC converter. Additional changes are introduced to the frontend hybrid design to allow for additional ground connections compatible with the space requirements in the ladder and dee mechanics of the CMS detector. The arrival of this next generation of hybrids at the module assembly sites is expected for beginning of 2023.

6.2.4. Thermal Resilience Tests

Data taking runs during the HL-LHC era will be interrupted by scheduled shutdown times. An overview of the operation schedule is given in Section 3.1. During these shutdowns, it is possible to keep the tracker volume at low temperatures. However, phases of warming up the detector are used to introduce beneficial annealing effects to the silicon sensor modules. Additionally, in case of unforseen problems it can become necessary to warm the detector to room temperature for maintenance. During these phases, the complete tracker has to withstand thermal stress. To validate the robustness of the 2S module design against thermal stress at an early stage, 2S prototypes are subject to thermal cycles. Cycles are performed within the climatic chamber at ETP with module KIT_2S_1 and with the Cooled 2S Module Readout Station using module KIT_2S_3. For module KIT_2S_1, the maximum module temperature

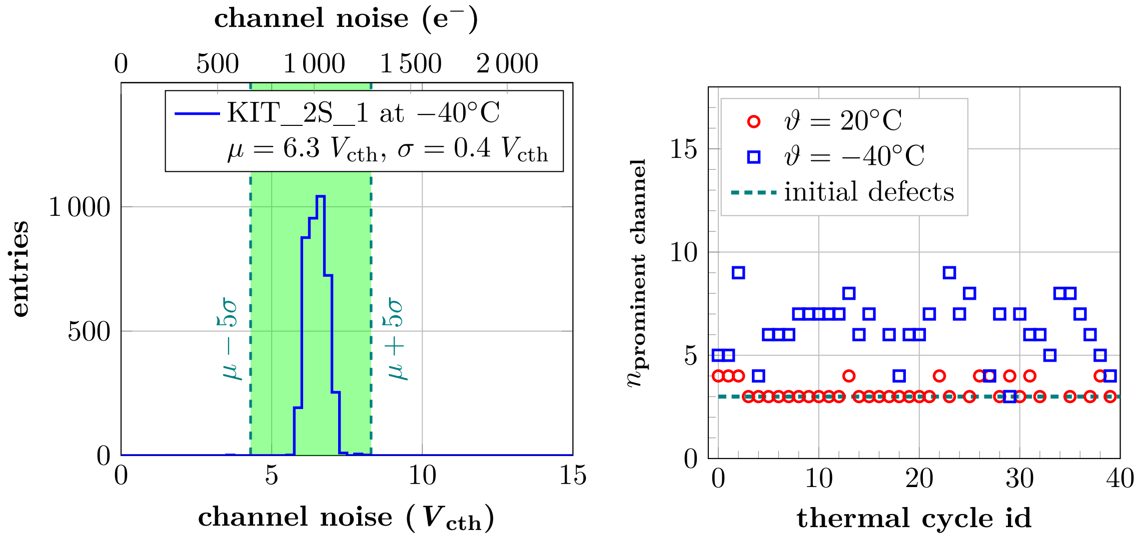

(a)

(b)

Figure 6.15.: Monitoring of channel noise during thermal cycling of module KIT_2S_1. (a) A noise measurement is performed at each temperature extremum. To monitor defective channels, the number of channels $n_{\mathrm{prominent\ channel}}$ with noise outside the range $\mu \pm 5\sigma$ are counted. (b) Plotting $n_{\mathrm{prominent\ channel}}$ over the thermal cycle id allows to monitor the module functionality during cycling. Data taken at the temperature minimum of −40°C are shown in blue, data measured at 20°C are shown in red. Prior to thermal cycles, three defective channels have been identified. This is indicated as green dashed line.

is chosen to be 20°C while the minimum temperature is set to −40°C. During thermal cycling of module KIT_2S_3, the minimum temperature is −20°C. At each thermal extremum, the temperature is kept constant for at least 30 minutes before setting the next temperature. To cool down from 20°C until reaching a stable temperature of −40°C, the climatic chamber needs approximately 70 minutes. Warming up is done within 30 minutes. In the Cooled 2S Module Readout Station, cooling down from 20°C to −20°C measured on the silicon sensors takes approximately 20 minutes. Warming up to 20°C is performed within five minutes. During the thermal cycles, the modules are neither biased nor powered except when read out.

To monitor the module functionality, an offset calibration is performed with module KIT_2S_1 at each temperature extremum and the channel noise is measured. This allows to compare the channel noise distributions during the cycling steps to spot defects appearing on the module. For each noise measurement, the number of channels $n_{\mathrm{prominent\ channel}}$ with a noise outside the range $\mu \pm 5\sigma$ is determined with μ being the average channel noise of a measurement and σ being the standard deviation of the mean value. This criterion is visualized in Figure 6.15a for a noise measurement performed at −40°C. Channels with noise values outside the green area are further investigated. Figure 6.15b displays the number of channels with a noise level outside the 5σ range as a function of the thermal cycle number. Prior to the measurements in the climatic chamber, three unconnected module channels have been identified. This number is indicated as green dashed line. Data taken during thermal cycling are shown in red for noise measurements performed at 20°C and in blue for measurements at −40°C. The data set taken at 20°C only shows small deviations from the expected number of broken channels. A maximum deviation of +2 channels is observed. At −40°C, $n_{\mathrm{prominent\ channel}}$

deviates significantly from the expectation. The spread of data points increases compared to the distribution measured at high temperatures. However, no overall increase of $n_{\text{prominent channel}}$ can be observed with increasing cycle number within the data sets. This indicates that no damage is done to the module during thermal cycling.

To understand the differences between the data sets at high and low temperatures, data from channels with noise outside the 5σ range are further investigated. Figure 6.16a shows an example of the hit occupancy as a function of applied threshold and channel number for neighbouring channels to a channel detected with a prominent noise level. In this case, a low noise level is extracted from the threshold scan for channel 376. The noise occupancy distribution of this channel and its direct adjacent channels are shown in Figure 6.16b. Channel 376 shows a shifted pedestal value compared to its neighbouring channels. Therefore, the occupancy distribution is cut off during the measurement before reaching occupancies larger than 40% as the software algorithm in use stops the threshold scan when reaching a global module hit occupancy of 95%. Additionally, the analysis algorithm to determine the channel noise from the threshold scan is not optimized for partially cut off distributions. Therefore, the channel noise is significantly underestimated for this channel. This leads to labeling the channel as defective during the thermal cycle analysis described above. The origin of the appearances of channels with shifted pedestals during the noise measurement is situated within the CBC3.1 chip. Due to a bug in some CBCs, some chip register programmed via the $\mathrm{I^2C}$ interface can change their value involuntarily while setting other registers or changing $\mathrm{I^2C}$ register maps. Mainly channel offset registers are affected by this bug, which leads to the observed occupancy distributions with shifted pedestals. Additionally, this effect happens more frequently for chips operated at cold temperatures [PU22]. Affected chips can be rejected during testing before bump-bonding them onto the final version of frontend hybrids to avoid this problem in the CMS tracker. By comparing the channel pedestals for identified low noise channels during the thermal cycle analysis, this event category can be identified and $n_{\text{prominent channel}}$ can be corrected. The corrected distribution are shown in Figure 6.16c. Both data sets are compatible with the number of initial defects and prove that no damage was done to module KIT_2S_1 during 40 thermal cycles.

Module KIT_2S_3 is cycled 20 times. During this thermal cycling no intermediate noise measurements are performed. Thus, the noise distributions are compared at a sensor temperature of 20°C before and after performing the thermal cycles. No change in the channel noise distributions is observed. The corresponding plots are shown in Figure B.5.

6.2.5. Summary of Module Performance Studies

To evaluate the 2S module design and the interplay of all module components well before the final components are available, prototype modules are assembled and thoroughly tested as soon as the components become available. The results of laboratory-based performance studies with 8CBC3 modules and 2S prototypes are summarized within this section. A crucial parameter to define the module functionality is the average channel noise. For 8CBC3 modules, an average noise level of approximately $970\,\mathrm{e}^-$ is detected within all module prototypes. This value is compatible with the specification of the CBC channel noise of less than $1000\,\mathrm{e}^-$. Additionally, the measured noise distributions are compatible with the expectation of Gaussian distributed noise. However, it is necessary to connect the ground level of the frontend hybrids directly via a screw or short cable to the potential of the module carrier in order to reach noise levels within the CBC specifications.

Based on these observations, a new grounding connection was introduced into the service hybrid version used in 2S prototypes. The module ground can be connected to the carrier plate or other external structures via a screw at a central point on the service hybrid. Measuring

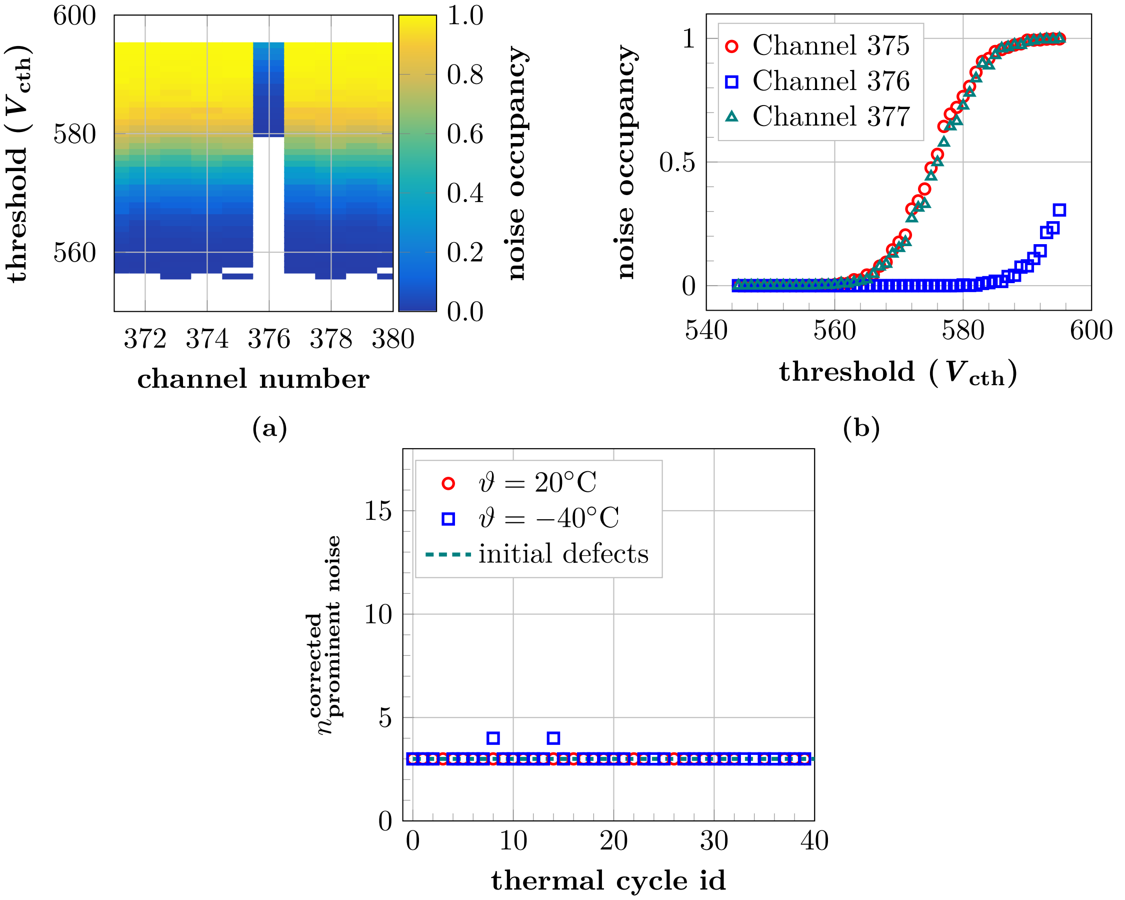

(a) (b)

(c)

Figure 6.16.: Due to a bug in the CBC3.1 chips, an unvoluntary modification of channel offsets can happen while writing other $\mathrm{I^2C}$ registers. This leads to individual channels with shifted pedestals during the noise measurement. (a) One example of a shifted hit occupancy distribution is shown as a function of threshold for channel 376. (b) Investigating the channel noise occupancy distributions indicates that the hit occupancy distribution of channel 376 is cut off due to the software algorithm in use. Therefore, the channel noise of channels with shifted pedestals is underestimated leading to the distributions shown in Figure 6.15b. (c) After correcting all channels with shifted offsets manually, the resulting distribution of $n_{\text{prominent channel}}$ is consistent with the expectation of three defective channels observed prior to thermal cycling.

the module noise in this configuration yields a significantly increased noise of approximately 1190 e^-. Connecting the frontend hybrid grounds via screws to the carrier as performed for the 8CBC3 modules does not improve the noise level to values within the CBC specification. Analysing the noise distributions reveals a significant deviation of the bottom sensor noise from the expectation of purely Gaussian distributed noise. An additional component of common mode noise is present in the 2S prototypes. To investigate the origin of this increased noise level, several hypotheses are investigated. Strong evidence is found that the increased noise is generated by the bPOL chips on the service hybrid. The generated noise couples into the high voltage circuitry and leads to a changing sensor bias potential observable as noise at the readout chips. Part of this noise can be suppressed by adding resistors to the HV tails, removing the direct electrical contact between top and bottom 2S sensor.

To check the resilience of the 2S module design against thermal stress, thermal cycles are performed with several 8CBC3 modules and 2S prototypes. By monitoring the channel noise during cycling, it is possible to spot the appearance of defective channels due to thermal stress. However, no damage is detected during thermal cycling, proving the 2S module design to be robust.

6.3. Beam Tests

Laboratory based setups allow to quickly and easily test basic module properties as, e.g., the channel noise, the detection of channel defects or the modules' resilience against thermal stress. To probe the full module readout chain starting with charge generation in the silicon sensors, cosmic muons or radioactive sources can be used. However, typical laboratory setups reach their limitations to measure module detection efficiencies for the hit and stub data streams. Beam test facilities provide setups to illuminate particle detectors with particle beams and measure the particle trajectories by dedicated hardware. These setups can be used to quantify module detection efficiencies and resolutions. Several beam test campaigns have been performed with 2S module prototypes within the last years. This chapter summarizes the tests performed at the beam test facility at *Deutsches Elektronen-Synchrotron* (DESY) in Hamburg, Germany. Measurements have been performed with unirradiated 8CBC3 modules and the irradiated 8CBC3 module. Analyses performed on a subset of data gathered during these beam tests using different analysis definitions are published in [Kop+21].

6.3.1. Setup at the DESY Test Beam Facility

A test beam facility is operated at the electron synchrotron *DESY II* at DESY [Die+19]. The facility offers three beam lines for external users to perform measurements in a particle beam. The user can choose between an electron or positron beam with variable energies between 1 GeV to 6 GeV. The beam is produced by guiding the primary DESY II electron beam onto carbon fiber targets. The resulting bremsstrahlung photons are converted to electron/positron pairs via a metal plate. The resulting beam is collimated using a magnetic field and enters the individual beam lines.

Hardware at the Beam Line

The setup used for the beam test measurements is shown in Figure 6.17. An EUDET-type beam telescope provided by the test beam facility is installed in the beam line. The telescope consists of six MIMOSA 26 monolithic active pixel sensor planes [Bau+09]. The MIMOSA 26 devices provide an active area of approximately 2 cm × 1 cm and each pixel has a size of 18.4 µm × 18.4 µm. Based on the hits detected by all six planes, the particle beam trajectory can be reconstructed and interpolated to the position of additional detector layers inside the telescope. These additional detector layers are called *devices under test* (DUTs). Depending on the beam energy and telescope geometry, it is possible to reach spatial resolutions of less than 10 µm for the predicted track intersection point for DUTs mounted in the telescope center. Details about the telescope tracking performance can be found in [Jan+16]. The setup's coordinate system is oriented with the z axis along the beam propagation direction as indicated in Figure 6.17. The origin of the coordinate system is placed in the center of the first telescope plane hit by the beam.

All measurements described in the following were performed with an 8CBC3 module installed as DUT in the center of the telescope. Thus, the DUT divides the telescope layers into three *upstream* and three *downstream* planes. The 8CBC3 module was mounted inside a light-tight box and screwed onto a custom designed copper block that can be cooled by circulating cooling liquid. Thus, it is possible to operate the module at different temperatures by connecting an external chiller unit. The 8CBC3 module is oriented with the bottom sensor facing the upstream telescope planes. The module box is installed on a three axis motor stage allowing for translations in the x-y-plane and rotations around the y axis. The MIMOSA 26 are read out via a rolling-shutter, meaning that all pixels are not read out simultaneoulsy but each column is read out separately. This leads to a a readout integration time of 115.2 µs. As additionally, the data acquisition system returns two data frames per readout, the MIMOSA 26 data provide a timing granularity of more than 200 µs. To gather telescope track information with 25 ns granularity matching the 2S module readout, an additional timing reference detector is installed between the downstream telescope planes. Depending on the test beam campain, either an ATLAS *FE-I4* pixel single chip assembly [Bar10] or a CMS *Phase-1 BPIX* module [Ada+21b] was used. Two crossed scintillators are mounted in front of the first upstream telescope planes to generate a trigger signal. An EUDET-type *trigger logic unit* (TLU) receives the scintillator triggers and synchronizes the readout of all detectors in the setup. All measurements have been performed with an electron beam and beam energies between 4 GeV and 6 GeV. At these energies, electrons provide a similar energy deposition in 2S sensors as minimum ionizing particles as shown in Figure C.1 as shown in Figure C.1 in the appendix.

Data Acquisition

For data acquisition, the EUDAQ framework [Liu+19] is used. The framework provides a central *RunControl* module to control all additional software modules and to coordinate data taking using a state machine. Each detector type is configured and read out by a dedicated EUDAQ *producer*. During the *initialisation* and *configuration* state, all producers prepare the connected hardware for data taking. Necessary parameters are parsed via central configuration files. After successfully configuring all software modules, data taking runs can be started. Each producer gathers data of its detector and sends them via the *Transmission Control Protocol* to the *DataCollector* module. The DataCollector module combines the detector data streams event by event and stores the result into files for off line analysis.

6.3.2. Offline Track Reconstruction

The offline track reconstruction is performed using the *EUTelescope* framework [Bis+20]. This framework provides dedicated software modules for separate tasks in the track reconstruction chain. Each module can be configured using dedicated configuration files. Data within the EUTelescope framework are stored via the *Linear Collider I/O* (LCIO) *Event Data Model* [Apl+12]. For monitoring, additional plots are created and saved in the data analysis framework *ROOT* [BR96] by each module. A typical sequence of software modules used during

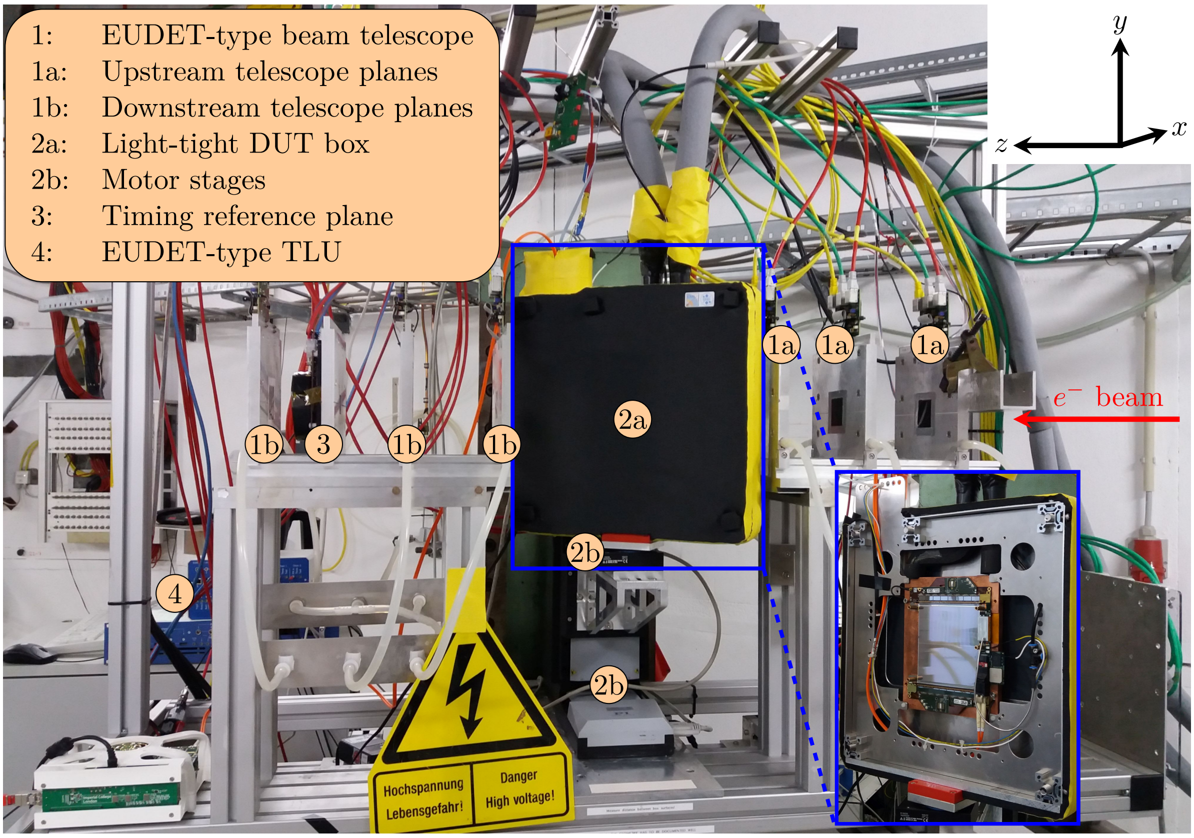

Figure 6.17.: The setup used for beam tests of 8CBC3 modules at the DESY test beam facility. The 8CBC3 modules are mounted inside a light-tight box installed in the center of the telescope. A view of the module on its copper cooling jig is shown in the blue rectangle. The grey cooling pipes connect the copper jig to a chiller unit. Two crossed scintillators are mounted in front of the first telescope plane to generate a trigger signal.

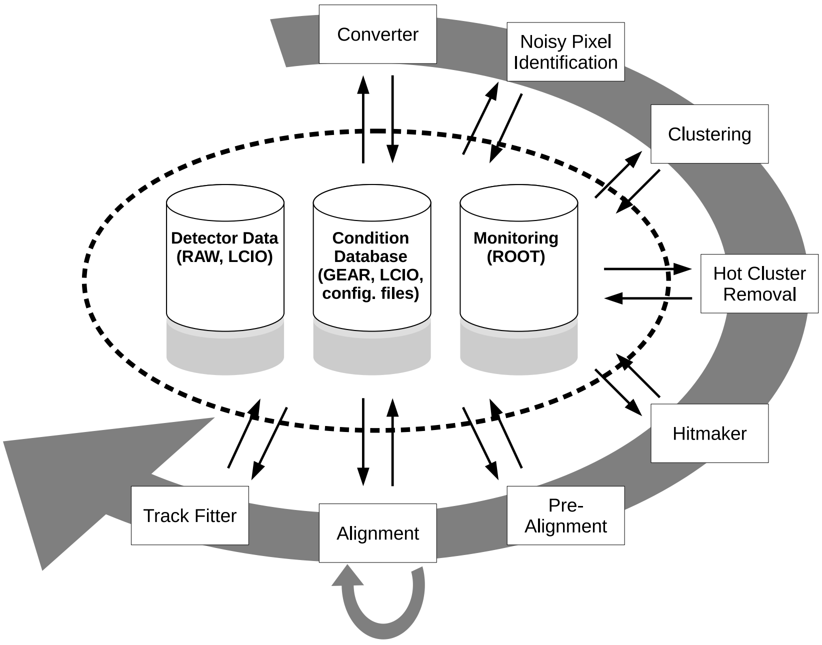

Figure 6.18.: The typical sequence of software modules used during track reconstruction of beam test data within the EUTelescope framework. [Bis+20]

track reconstruction is shown in Figure 6.18. For the analysis performed within this thesis, the individual analysis steps to reconstruct tracks are explained in the following. A detailed description of the software module functionalities can be found in [Bis+20].

Data Conversion and Noisy Channel Identification

As the data files produced by the EUDAQ DataCollector are stored in a custom file format, data are converted into the LCIO format in a first step. Afterwards, the resulting LCIO files can be read by the *NoisyPixelFinder* module. The hit occupancy of each readout channel is calculated for all telescope planes and the DUT on a subset of events per data run. Thus, channels with hit occupancies above a definable threshold are identified as noisy and saved in a separate database for later processing steps. For the MIMOSA 26 sensors, pixels with hit occupancies above one permille are marked as noisy. Due to the larger strip dimensions of 2S sensors, this limit is set to two percent for the DUT.

Clustering and Spatial Hit Location

As a next step, the data set of each detector layer is scanned event per event to find hits in adjacent readout channels. Adjacent hits are grouped to *clusters*. Clusters containing previously identified noisy channels are removed from the data set.

The *HitMaker* module is used to convert the cluster positions from the local detector channel numbering schemes into the telescope coordinate system. The cluster center is calculated by weighting the channel coordinates x_i with the detected amount of charge q_i following

$$x_{\text{center}} = \frac{1}{Q} \sum_i x_i q_i \ , \tag{6.3}$$

where Q denotes the sum of all charges q_i detected in the cluster. A separate geometry configuration file provides input about the spatial arrangement of the detector layers in the setup. Based on this information, local coordinates are transformed into the telescope coordinate system. The distances along the z axis between the detector planes was measured with a tapeline during the beam test. This method results in z position measurements with an accuracy of a few millimeters.

Alignment and Track Fitting

The alignment of the individual detector planes is performed in several steps. Assuming no beam divergence, the cluster positions detected by the first telescope plane in the beam is propagated to all other detector planes. For each plane the difference between the detected cluster position and the propagated position is calculated in x and y direction. These distances are called *residuals*. By comparing the mean residuals for a set of events, it is possible to extract a first, rough correction for x and y shifts of the individual detector planes.

Starting from this pre-aligned geometry, an iterative alignment procedure is started searching for track candidates in the telescope data while minimizing the track residuals on all telescope planes and the reference plane. For the minimization, the *Millepede II* package [Blo22] is used. Track finding and fitting is done using the *General Broken Line* approach [Kle12]. Thus, it is possible to take multiple scattering effects into account that the electrons at the DESY test beam facility undergo due to their energy of a few gigaelectronvolt. During the alignment, the DUT positions stay fixed and are treated as passive scattering planes.

After a successful alignment of the telescope planes, tracks are reconstructed within the complete data set based on the information of all six telescope planes. Track information and the interpolated intersection points of the track with the DUT sensors and with the reference plane sensor are stored in a ROOT file for further analysis.

6.3.3. DUT Alignment

As the DUT sensor planes are kept at a fixed position during the automated telescope and reference plane alignment, their positioning in the beam needs to be adjusted separately. Therefore, the residuals in x and y are calculated allowing to determine the DUT misalignment. After a successful update of the setups geometry file, the track fitting step is repeated to update the interpolated intersection points with the DUT sensors. The two silicon sensors of the 2S module prototypes are treated as independent planes and aligned individually. The alignment steps are explained in the following using data of the top 2S sensor.

Starting from a rough alignment in the x-y plane based on the x and y residuals, the alignment of the DUT sensor along the z axis is performed. The DUT z position is varied around the expected position measured with the tapeline. At the correct z position, the x and y residual distributions show the smallest width. The initial x residual distribution is shown in Figure 6.19a in red. Figure 6.19b displays the *root mean square* (RMS) of the x residual distribution for different z shifts. A clear minimum is visible at a shift of approximately $-1\,\mathrm{mm}$. Using a quadratic function, the minimum position is extracted and taken as z position correction for the sensors.

To correct for DUT rotations around the z axis, the mean value of the x residual $\langle x_{\mathrm{res}} \rangle$ is plotted against the y coordinate of the interpolated track intersection point y_{track}. The resulting distribution is shown in Figure 6.19c in red. For a perfectly aligned DUT, the average over all track residuals does not depend on the track position, and, thus, is constant at $0\,\mu\mathrm{m}$ along the y coordinate. Using a linear fit, the rotational misalignment is extracted and corrected. When achieving a flat residual distribution, the offset from $0\,\mu\mathrm{m}$ corresponds to the misalignment of the DUT's x position. Similarly, it is possible to correct for DUT rotations around the x axis

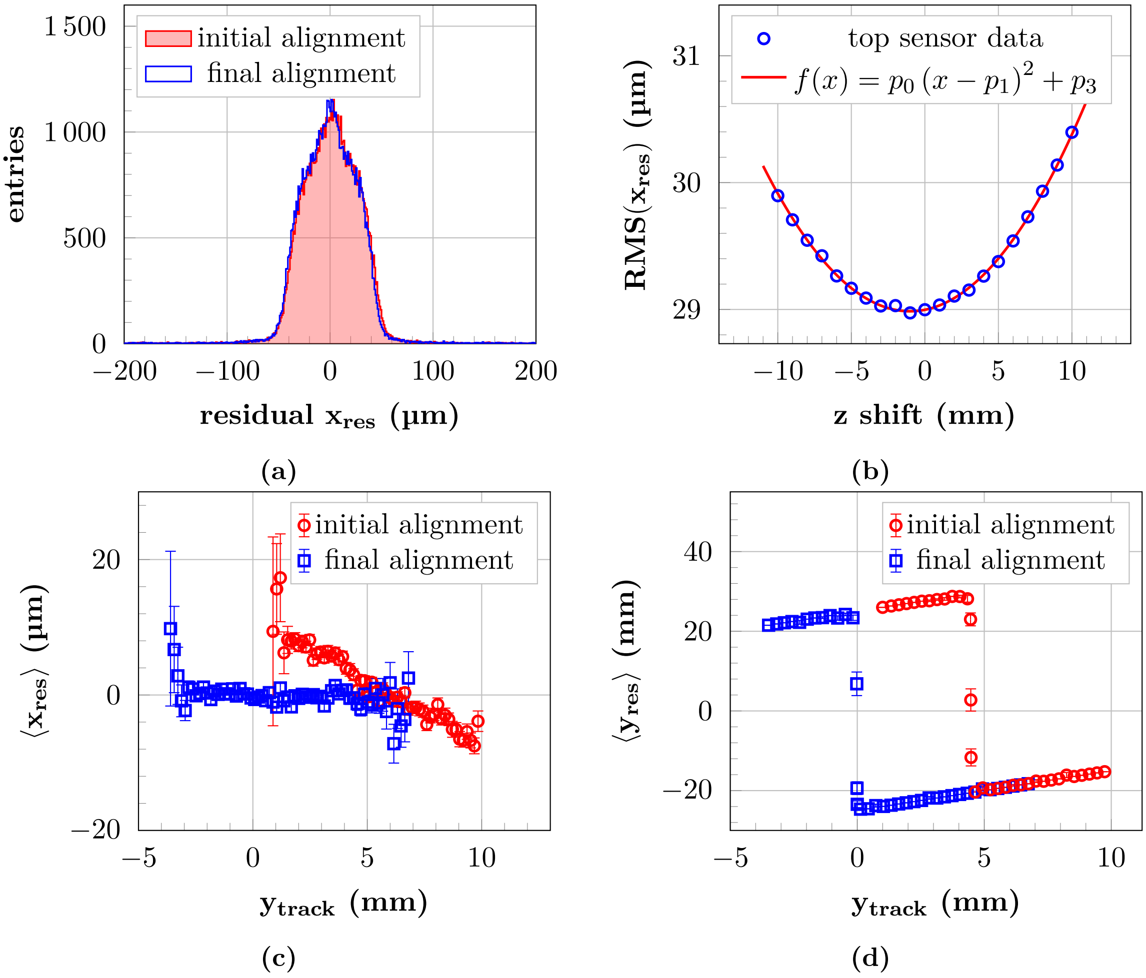

Figure 6.19.: Validation plots used to align the DUT sensors during the beam test analysis. (a) Monitoring the x residual distribution allows to detect shifts of the DUT position along the x axis. Corrections are applied if the mean of the distribution is not close to 0 µm. (b) By scanning the root mean square of the x residual distribution as a function of the z position of the DUT, it is possible to place the detector at the correct z position. (c) To correct for rotations around the z axis, the mean value of the x residual is plotted against the y coordinate of the interpolated track intersection point. Data from the automatic rough EUTelescope alignment are shown in red. Data after the manual alignment are shown in blue. (d) Shifts of the DUT along the y axis can be spotted by monitoring the average y residual as a function of the y coordinate of the track intersection point. However, this alignment step is only possible, when the beam illuminates the center of the 2S sensors.

using the average x residuals as a function of x_{track}. The resulting x residual distribution after these alignment steps is shown in Figure 6.19a in blue.

The sensitivity of the DUT towards rotations around the y axis is low due to the strip length of five centimeters. Thus, no corrections for these rotations are performed during the DUT alignment. However, it is possible to correct for shifts of the DUT along the y axis if the beam illuminates the central area of the module. The resulting mean residual y_{res} distribution as a function of y_{track} is shown in Figure 6.19d. As introduced before, the EUTelescope Hitmaker module calculates the cluster center positions by weighting the channel coordinates with the detected amount of charge per channel. As the CBC provides a binary channel readout, no information is gathered about the individual channel charges. Thus, the reconstructed cluster position lies always in the geometrical center of the cluster channels. This implies that the y coordinate of clusters in a 2S sensor is set to the center of the corresponding strips. Therefore, the y residual shows a transition from positive values to negative values for tracks hitting the center of the 2S sensors. This is used to correct for shifts along the y axis.

6.3.4. Analysis Definitions

To analyse the performance of the 2S module prototypes based on the aligned data sets, the following definitions are used.

Noise Occupancy

The noise occupancy η_{noise} is defined as the probability to detect one hit per readout event and channel without any external charge generation in the silicon sensors. Therefore, noise occupancy measurements have been performed with the electron beam turned off.

Module Cluster and Stub Efficiency

The main goal of the beam test analysis is to link reconstructed tracks to clusters seen by the 2S module prototypes mounted as DUT. As already mentioned earlier, the time resolution of the MIMOSA 26 devices provides a readout integration time of 230.4 µs. Thus, a variety of tracks is reconstructed per telescope readout frame. To identify the subset of tracks with correct timing to be detected within the 25 ns long readout integration time of the 2S module prototypes, the cluster information of the timing reference detector is used. By calculating the residuals of interpolated track intersection points on the reference plane and the detected clusters, this subset can be determined. Only tracks with reference plane residuals inside a predefined window are considered for further analysis. The window size is chosen as the pixel dimensions of the reference plane sensor. This results in selection criteria for residuals (called *residual cut* in the following) of

$$\left|x_{\mathrm{res}}^{\mathrm{ref}}\right| \leq 250\,\mu\mathrm{m} \qquad \text{and} \qquad \left|y_{\mathrm{res}}^{\mathrm{ref}}\right| \leq 50\,\mu\mathrm{m}$$

for the FE-I4 single-chip detector and

$$\left|x_{\mathrm{res}}^{\mathrm{ref}}\right| \leq 150\,\mu\mathrm{m} \qquad \text{and} \qquad \left|y_{\mathrm{res}}^{\mathrm{ref}}\right| \leq 100\,\mu\mathrm{m}$$

for the BPIX module.

For each track linked to a reference plane cluster, the interpolated track intersection with the two DUT sensors is compared to the detected module clusters. Thus, it is possible to define detection efficiencies for clusters and stubs. Similar to the selection criteria for hits in the reference plane, clusters with x residuals inside a predefined window of size $d_{\mathrm{cut}}^{\mathrm{DUT}}$ are

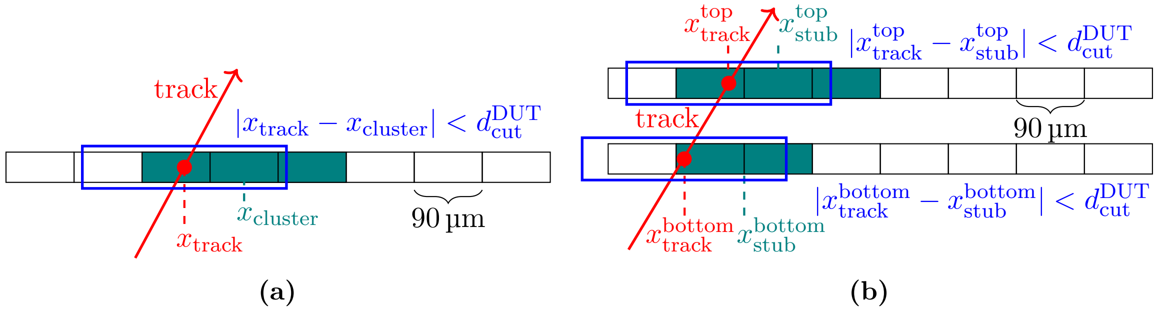

Figure 6.20.: Illustrations of the definition of cluster and stub efficiency used for the beam test analysis. (a) A cluster is called efficient, if its x residual $|x_{\text{track}} - x_{\text{cluster}}|$ is smaller than a pre-defined cut $d_{\text{cut}}^{\text{DUT}}$. (b) To define a stub to be efficient, the x residuals of its position in the seed sensor (bottom sensor) and the x residual of its calculated bend position in the correlation sensor (top sensor) have to be smaller than $d_{\text{cut}}^{\text{DUT}}$.

considered to be efficient. This criterion is sketched in Figure 6.20a. Due to the large strip length of five centimeters, no cut is applied to the y residuals. By counting the number of tracks fulfilling the residual cuts on the reference plane $n_{\text{ref tracks}}$ and the number of clusters fulfilling the residual cut on the DUT sensors $n_{\text{efficient clusters}}$, the cluster efficiency is defined as

$$\epsilon_{\text{cluster}} = \frac{n_{\text{efficient clusters}}}{n_{\text{ref tracks}}} \,. \tag{6.4}$$

The cluster efficiency criterion is extended to be applicable to the module stub information. As introduced earlier, a stub is characterized by the stub position and the stub bend. The stub position indicates the location of the cluster center in the seed sensor. The bend code specifies the offset between the cluster center in the correlation sensor and the stub position. Thus, the cluster center in the correlation sensor can be calculated combining the stub position and the bend. For the beam test measurements presented within this thesis, the bottom 2S sensor acts as seed sensor as it is hit by the electron beam first. A stub is defined as efficient, if the stub position in the seed sensor $x_{\text{stub}}^{\text{bottom}}$ and the calculated bend position in the top sensor $x_{\text{stub}}^{\text{top}}$ have both an x residual smaller than $d_{\text{cut}}^{\text{DUT}}$. This is indicated in Figure 6.20b. The stub efficiency is defined as

$$\epsilon_{\text{stub}} = \frac{n_{\text{efficient stubs}}}{n_{\text{ref tracks}}} \,. \tag{6.5}$$

The statistical uncertainty for cluster and stub efficiency is given by the standard deviation of the mean of a binomial distribution given by

$$\sigma_{\epsilon_i} = \sqrt{\frac{\epsilon_i\,(1-\epsilon_i)}{n_{\text{ref tracks}}}} \tag{6.6}$$

with $i \in \{\text{cluster}, \text{stub}\}$.

To determine the optimal setting for $d_{\text{cut}}^{\text{DUT}}$, the influence of different values of $d_{\text{cut}}^{\text{DUT}}$ on the cluster and stub efficiency and the width of the x residual distributions is investigated. The results are displayed in Figure 6.21. The cluster efficiencies of top and bottom sensor are shown in Figure 6.21a together with the stub efficiency. For small values of $d_{\text{cut}}^{\text{DUT}}$, the efficiencies are small as only parts of the reconstructed tracks lie within the residual cut around the cluster centers. While increasing the residual cut, the efficiencies raise and reach a plateau at cuts of

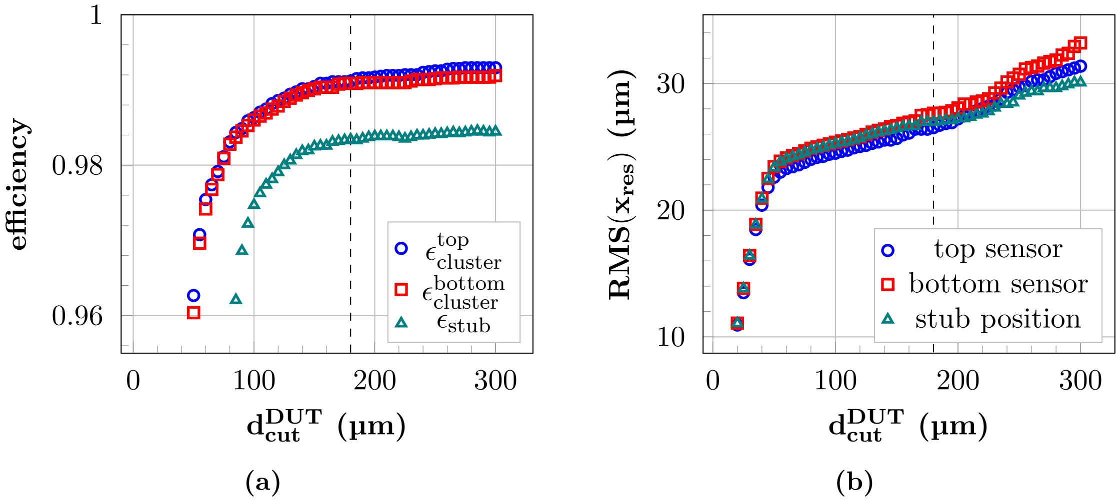

Figure 6.21.: Dependency of the residual cut $d_{\text{cut}}^{\text{DUT}}$ on efficiencies and resolutions in the beam test analysis. (a) The cluster efficiencies of top and bottom sensor reach a plateau for residual cuts around 180 µm. The stub efficiency follows the product of the cluster efficiencies. For large $d_{\text{cut}}^{\text{DUT}}$, differences between top and bottom sensor cluster efficiencies can be observed which are caused by the different annealing states. (b) With larger residual cuts, the width of the residual distributions increases. For the beam test analysis, a value of $d_{\text{cut}}^{\text{DUT}} = 180\,\mu\text{m}$ is chosen and marked in both figures as dashed line. Data have been taken with the irradiated module at a bias voltage of 600 V and a threshold of $6000\,\text{e}^-$.

around 180 µm. For residual cuts larger than 220 µm, the efficiencies increase slightly as events with a large, asymmetric cluster width around the track intersection point are additionally accepted by the efficiency criterion. Such clusters are mainly generated by δ electrons. The stub efficiency distribution follows the product of the cluster efficiencies as for the detection of a stub, clusters in both sensors are necessary and the clusters are independently generated in the two sensors. Figure 6.21b displays the RMS of the residual distributions for top and bottom sensor clusters and the RMS of the stub position residual. With increasing residual cut, the resolution increases as events with large residuals are accepted and enlarge the tails of the residual distributions. Thus, the optimal choice of a value for $d_{\text{cut}}^{\text{DUT}}$ is a tradeoff between achieving large efficiencies and a small resolution. Within this thesis, a residual cut of 180 µm is used. This corresponds to twice the 2S strip pitch and is marked as dashed lines in Figure 6.21.

TDC

During 2S module operation at the LHC, the accelerator clock will be shared with all detectors to synchronize the signal readout with the particle arrivals. This allows to choose a constant phase between accelerator clock and 2S data acquisition clock in order to sample the charge pulse always at the maximum. However, the clocks of the 2S module data acquisition framework and the DESY II accelerator are asynchronous during the beam tests. This introduces a random phase between the arrival times of individual particles and the sampling of the charge signal in the CBC frontend. Thus, the signal is not consistently sampled in its maximum, resulting in varying detection efficiencies at different phases. To compensate for this effect, the 2S readout firmware samples the trigger arrival time with 320 MHz and encodes the phase difference with respect to its internal 40 MHz clock domain via a time-to-digital converter as *TDC phase*.

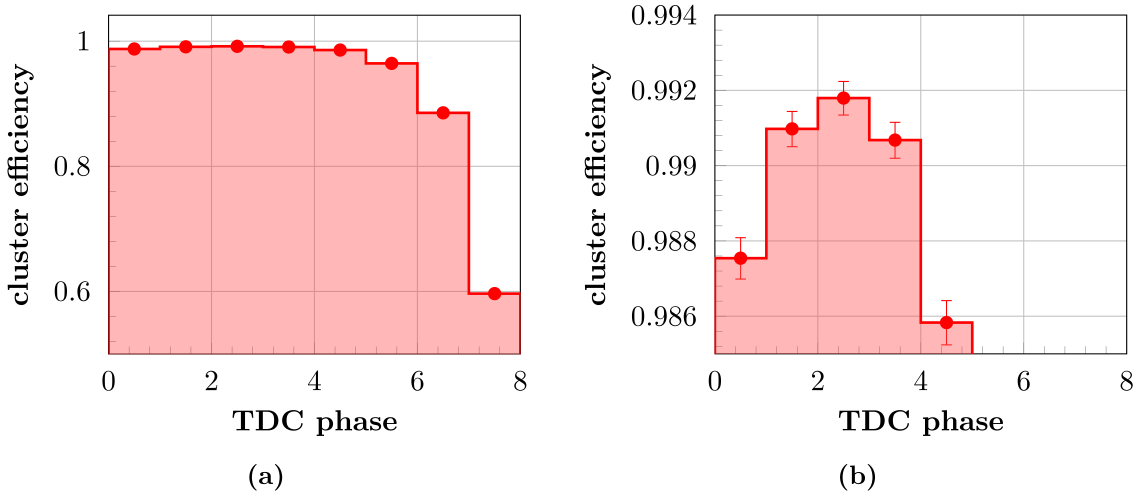

Figure 6.22.: (a) During the DESY beam test, the accelerator clock and the clock of the 2S module data acquisition framework are asynchronous. Thus, the cluster efficiency is dependent on the TDC phase. (b) By zooming in on the five most efficient bins, the statistical uncertainty becomes visible. During the analysis, only the most efficient TDC bin is used. Data have been taken with the irradiated module at a bias voltage of 600 V and a threshold of 6000 e^-.

When evaluating the cluster efficiency as a function of the TDC phase, a distribution as shown in Figure 6.22a is obtained.

In order to extract meaningful results regarding the operation of 2S modules at the LHC, a cut on the TDC phase is introduced during the analysis. Figure 6.22b displays a zoomed version of the cluster efficiency as a function of the TDC phase with the five most efficient bins. The error bars indicate the statistical uncertainty of each bin. While the statistical uncertainty for each bin is in the order of 0.1%, a systematic uncertainty of 0.2% or more will be introduced when taking into account more than the most efficient bin during the analysis. Thus, only the most efficient TDC phase is taken into account for all further analyses.

Channel Masking

A few channels of the 2S module prototypes used during the beam tests are defective due to unconnected wire-bonds or scratches on the sensor surfaces. These defects have already been observed at the end of module assembly and their origin has been identified to be incidents during bare sensor testing and module assembly. Thus, the affected channels are masked during the beam test analysis in order to prevent their influence on the result of the module efficiency and resolution studies. Tracks with DUT intersection points inside a masked channel are ignored during the analyis. As described above, the NoisyPixelFinder module identifies readout channels with large hit occupancies. During the EUTelescope analysis chain, hits from these channels are removed from the data set together with clusters that are adjacent to noisy channels. As only clusters are removed from the DUT data, but no track information is removed from the telescope data set, this can introduce artificial inefficiencies. To avoid this, strips adjacent to noisy channels are masked during the 2S analysis.

6.3.5. Signal and Noise Studies

To compare the particle detection efficiency of 2S modules at the beginning and end of lifetime of the HL-LHC measurement program, threshold and bias voltage scans have been performed during the beam tests with unirradiated modules and the irradiated module. For these measurements, the 2S modules are oriented perpendicularly to the electron beam direction. This minimizes the travelling distance of the electrons within the silicon sensors. Thus, the generated charge signal is minimal.

Bias Voltage Dependency

During the beam tests, data have been taken at different module bias voltages between 25 V and 800 V. Based on the knowledge of the channel noise extracted prior to the voltage scans, a common threshold is chosen for all CBCs in these runs to suppress noise hits. For the unirradiated module, a threshold of 5500 e^- is set, which is equivalent to six times the average module noise. For the irradiated module, the threshold applied is 6000 e^-, corresponding to seven times the average module noise.

Figure 6.23a displays the cluster efficiencies of top and bottom sensor for an unirradiated and the irradiated module. Data from the unirradiated module are shown in blue. The cluster efficiencies of both sensors coincide within the statistical uncertainties over the whole voltage range. This is expected, as both sensors are of the same layout and biased with the same voltage. With increasing voltage, the cluster efficiency increases as the depletion zone in the silicon sensors grows and the detected charge signal increases. At a voltage of 180 V, the cluster efficiency reaches a constant plateau at 99.9%. To explain these effects, the sensor capacitance as a function of the bias voltage is shown in blue in Figure 6.23b for the bottom sensor. The measurement has been performed prior to the module assembly with the bare sensor placed in a dedicated probe station. The sensor capacitance decreases until reaching a constant level at the depletion voltage. The depletion voltage can be determined to be approximately 280 V. With increasing width of the depletion zone, the charge signal seen by the sensor strips increases. This can be illustrated by extracting the average cluster width from the beam test data. The resulting distribution is shown in Figure 6.23c in blue. For bias voltages up to the depletion voltage, the increase in signal charge results in wider clusters. At higher voltages the cluster size stays constant. The transition from the cluster size increase to the constant plateau coincides with the observation from the capacitance characteristics. However, the cluster efficiency saturates already at a voltage lower than the depletion voltage. This results from the definition of the cluster efficiency, which is independent of the overall cluster charge. A cluster is called efficient as soon as one strip detects enough charge to be above the CBC threshold. Before irradiation, this charge is significantly smaller than the maximum charge expected for a fully depleted sensor.

With irradiation, the sensor characteristics change and the collected charge at the readout strips decreases while the depletion voltage increases. Thus, significantly larger bias voltages are needed with irradiated sensors to achieve comparable cluster efficiencies as measured before irradiation. Only for bias voltages of 600 V and above, the cluster efficiency reaches levels above 99% (see red curves in Figure 6.23a). Besides showing a flattening of the increase in efficiency for high bias voltages, no constant plateau is reached. This is in accordance with the capacitance measurements shown in red in Figure 6.23b and the average cluster size versus bias voltage setting shown in Figure 6.23c. Both distributions indicate that the irradiated sensor is not yet fully depleted. Thus, charge signal increases for all measured bias voltages, explaining the observed increase of the cluster efficiencies.

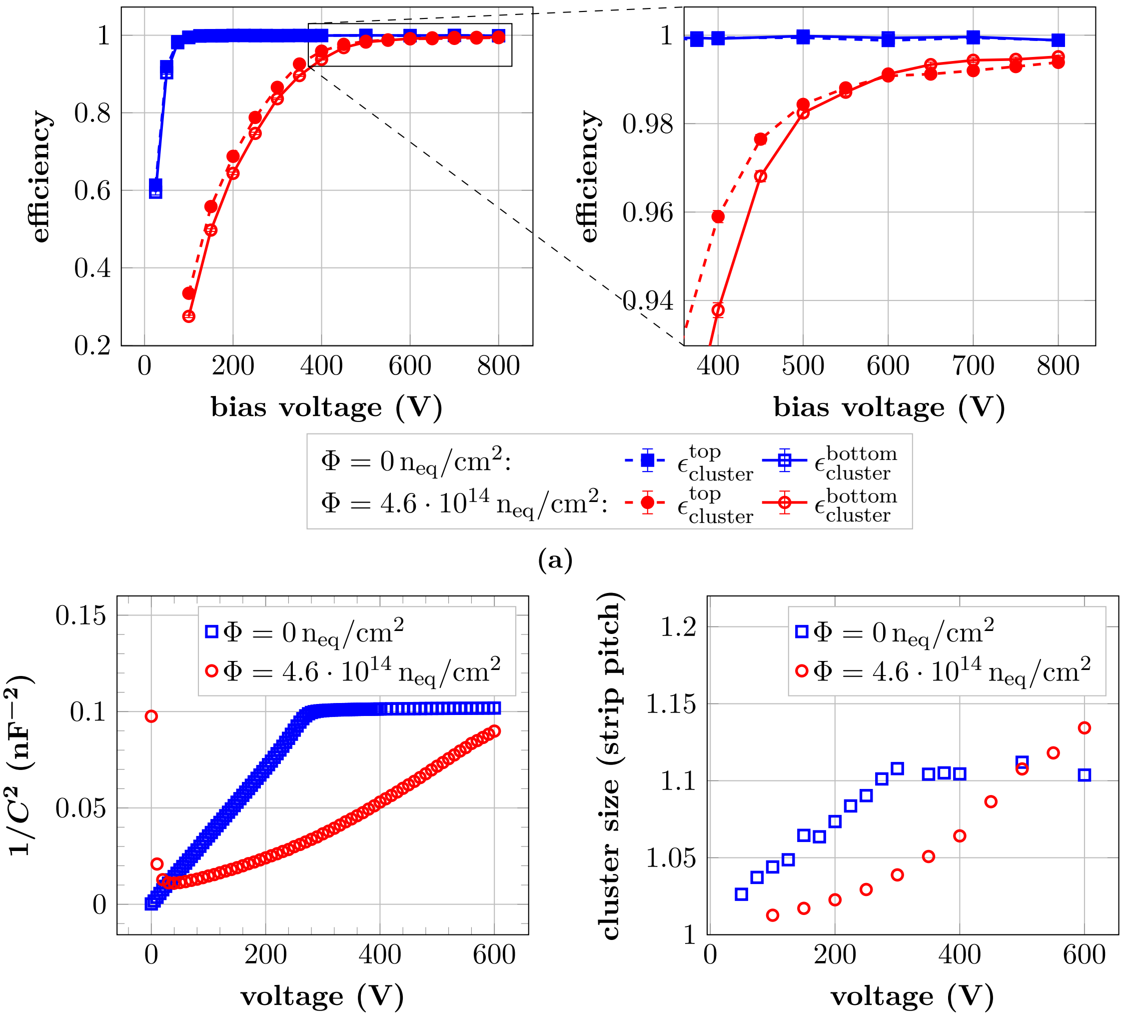

(a)

(b)

(c)

Figure 6.23.: (a) The cluster efficiency is measured as a function of the module bias voltage for an unirradiated 8CBC3 module (blue) and the irradiated 8CBC3 module (red). While the efficiencies of top and bottom sensor coincide for the unirradiated module, they differ for the irradiated module due to the different sensor annealing states. A zoomed version of the rectangle marked in the left plot is shown on the right. (b) The bare sensor capacitance as a function of the bias voltage was measured prior to the module assembly at a probe station. Before irradiation (blue dataset), the sensor depletion voltage can be extracted to be 280 V. After irradiation, the sensor capacitance does not reach any constant plateau anymore within the measurement range. (c) The average cluster width is extracted for each bias voltage from the test beam data. For bias voltages up to the depletion voltage, the cluster size increases. Beam test data have been taken at a threshold of 5500 e$^-$ for unirradiated modules and 6000 e$^-$ for the irradiated module.

For the irradiated module, a difference in the cluster efficiencies of top and bottom sensor is observed. For voltages below 600 V, the top sensor reaches a higher efficiency than the bottom sensor. For voltages between 600 V and 800 V this effect is inverted. The origin for this behaviour can be found in the different annealing states of the two sensors. While the top sensor has an equivalent annealing time of ten days at room temperature, the bottom sensor is annealed to an equivalent time of 200 days at room temperature. As introduced in Section 4.3.1, annealing influences the sensor performance including the charge collection efficiency. This effect has been subject to several studies within the high energy particle physics community. A summary of signal measurements performed after irradiation including annealing is given in [Fis20]. Data are gathered with sensor test structures called *babysensors* from PS-s wafers. One of the studies is a signal measurement using an analog *Beetle* chip [Aga+04] integrated into an *ALiBaVa* setup [Mar+07]. A ^{90}Sr source is placed above an irradiated babysensor and the generated charge is measured for different voltages and for different annealing times. To compare the analog signal measurements of the beetle chip with the binary readout information gathered from the CBC, the *seed signal* is studied. For each cluster, the strip detecting the largest signal is called *seed strip*. The seed signal sums up all charges detected by the seed strips during the ^{90}Sr measurement. Figure 6.24 shows the seed signal dependency of the annealing time for three different sensor bias voltages. The sensor is irradiated with 23 MeV protons to a fluence of $4 \cdot 10^{14}\,\mathrm{n_{eq}\,cm^{-2}}$. The measurements are performed at a sensor temperature of approximately -20°C. The equivalent annealing times of the two 2S sensors in the irradiated 8CBC3 modules are marked as blue dashed lines. At a bias voltage of 400 V, the seed signal shows an increase for equivalent annealing times below 30 days and a decrease for annealing times larger than 100 days. This leads to a larger seed signal at ten days equivalent annealing time than at 200 days. For a bias voltage of 600 V the previously observed decrease for large annealing times disappears. The measured seed signal at 200 days of annealing is slightly larger than the one at ten days. By further increasing the bias voltage to 800 V, an increase of the seed signal within the whole annealing time range can be observed. This results in a significantly larger seed signal at 200 days of annealing compared to the value at ten days. From this results, it can be concluded that the charge collection efficiency is dependent on the bias voltage and the annealing time. The cluster efficiencies measured in the beam test are consistent with the presented ALiBaVa measurement as the top sensor shows a higher efficiency than the bottom sensor for bias voltages below 600 V. For larger voltages, the bottom sensor is more efficient due to the larger sensor signal.

Threshold Dependency

The module detection efficiency and the noise occupancy are dependent on the readout threshold applied for the measurement. At low threshold settings, the detection efficiency is maximal and decreases with increasing threshold, as a growing portion of the sensor signal is not read out anymore. The same effect applies to the module noise occupancy. However, for optimal detector operation, the noise occupancy needs to be minimized while the detection efficiency is maximized. Thus, the choice of the threshold setting for 2S module operation is a tradeoff between achieving a reasonably low noise occupancy and reaching the best detection efficiency possible. To determine the optimal threshold setting before and after irradiation, data have been taken for different threshold settings during the beam tests.

Figure 6.25 compares the module noise occupancy in green for an unirradiated and the irradiated 8CBC3 module as a function of the relative threshold. The upper x axis shows the threshold in electron equivalent. Data are shown for the nominal bias voltage settings of 300 V before irradiation and 600 V after irradiation. As expected, the noise occupancy shows a sharp decrease over several order of magnitues with increasing threshold for both

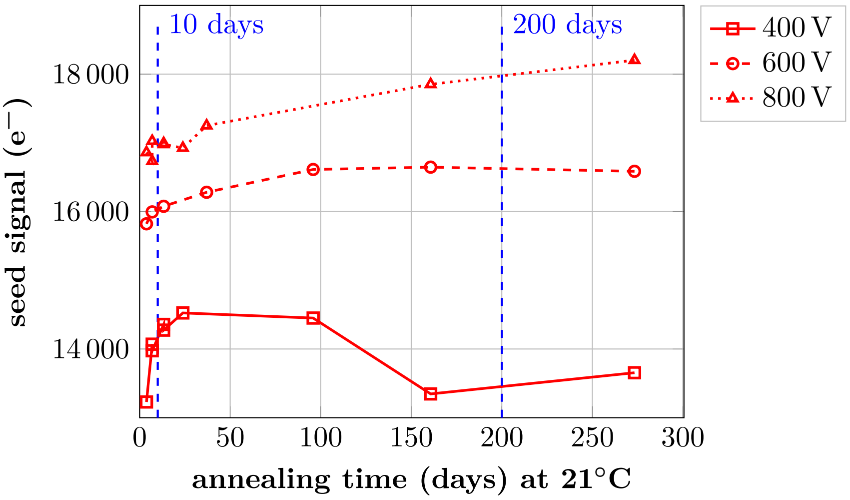

Figure 6.24.: Analog measurement of the seed signal at different bias voltages and annealing times with a PS-s baby sensor. Data taken from [Fis20]. The sensor is irradiated with 23 MeV protons to a fluence of $4 \cdot 10^{14}\,\mathrm{n_{eq}\,cm^{-2}}$. A ^{90}Sr source was used to create charge in the silicon sensor. The charge readout was performed using an ALiBaVa system [Mar+07]. The annealing states of the top and bottom sensor in the irradiated 8CBC3 module are marked as blue dashed lines. Measurements are performed at a sensor temperature of approximately −20°C.

modules. The noise occupancy measured with the unirradiated module is slightly higher than the one of the irradiated module. This is consistent with the noise values measured during the electrical calibration procedure described in Section 3.2.6 performed prior to data taking at the beam test setup. Module noise values of 6.3 V_{cth} and 5.4 V_{cth} were measured during the procedure assuming Gaussian distributed noise for the unirradiated and the irradiate module, respectively. As a reminder, the irradiated module was cooled down to approximately −17°C sensor temperature while the unirradiated module was measured at room temperature. This temperature difference is the main origin for the difference in noise. For both modules, a noise occupancy below 10^{-5} is achieved for thresholds above 4400 e^-. This value is three orders of magnitudes smaller than the expected channel occupancy due to particle hits of one percent for outer tracker modules during the HL-LHC operation [CMS17c]. Therefore, noise hits are highly suppressed to allow efficient data taking for thresholds above 4400 e^-.

The cluster efficiencies of top and bottom sensor are shown in Figure 6.25 on the right y axis. For the unirradiated module, the cluster efficiencies are shown in blue. They coincide for both sensors within the statistical uncertainties over the complete measurement range. For thresholds up to 9000 e^-, the efficiencies are at a constant plateau above 99.8%. At larger thresholds, the efficiencies decrease. Data from the irradiated module at a bias voltage of 600 V are shown in red. Compared to the unirradiated case, no plateau with constant efficiency is visible and the cluster efficiency starts decreasing at significantly lower threshold settings. This is expected as the signal amplitude reduces with irradiation. A maximum efficiency of 99.6% is reached for both sensors at a threshold of 4500 e^-. For increasing thresholds, the cluster efficiency decreases. The bottom sensor is more efficient for thresholds above 5000 e^- which corresponds to the expectation from the different sensor annealing states discussed in the previous section. To enlarge the sensor signal, the bias voltage can be increased to 800 V. The corresponding efficiencies are shown in orange in Figure 6.25. As the sensor signal increases, higher efficiencies are observable compared to the data at a bias voltage of 600 V.

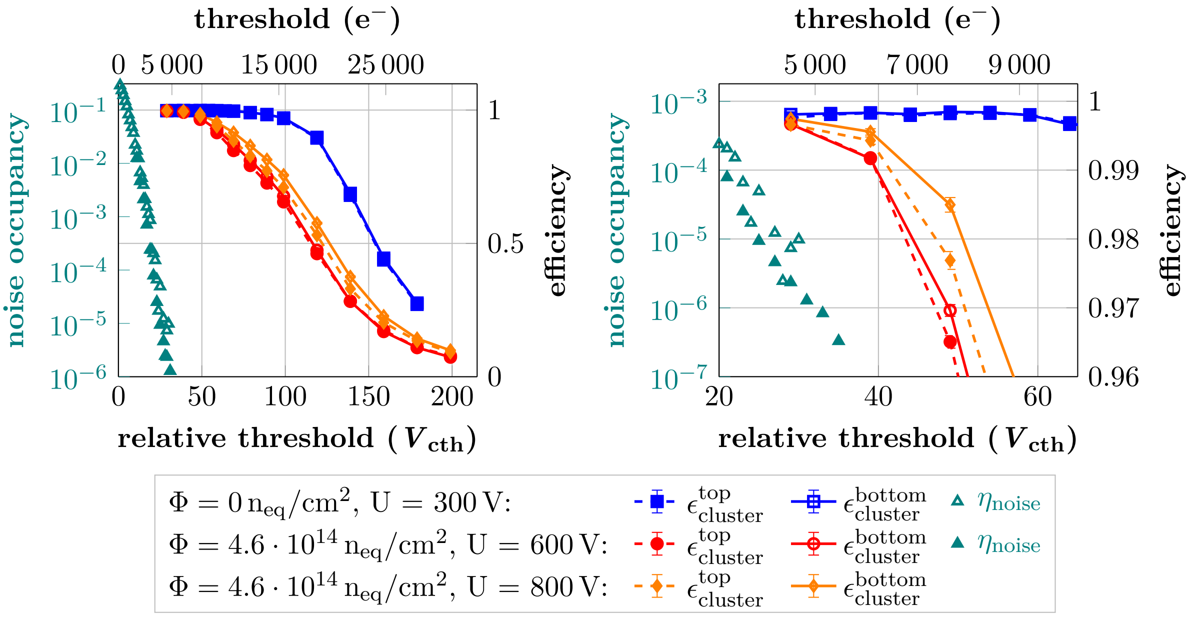

Figure 6.25.: The noise occupancy and cluster efficiency before and after irradiation as a function of the CBC threshold. The upper x axis shows the threshold values converted from V_{cth} units into electron equivalent. Noise occupancies are shown on the left y axis, efficiencies are shown on the right y axis. The noise occupancy measurement for the unirradiated module is performed in a smaller threshold range compared to the measurement performed with the irradiated module. Efficiencies measured with an unirradiated 8CBC3 module are shown in blue at a bias voltage of 300 V. Efficiencies measured with the irradiated 8CBC3 module are shown in red and orange for bias voltages of 600 V and 800 V, respectively. The right plot shows a zoomed version of the left plot.

In view of the presented results, it can be concluded that a threshold of 4500 e^- allows excellent module performance for unirradiated modules. The noise occupancy is below 10^{-5} while achieving a cluster efficiency of 99.8%. After proton irradiation to a fluence of $4.6 \cdot 10^{14}\,n_{eq}\,cm^{-2}$, the efficiency drops to 99.6% at this threshold. Due to the cooling, a slightly lower noise occupancy was observed allowing to further reduce the threshold to 4000 e^- while still not exceeding a noise occupancy of 10^{-5}. This leaves the possibility of a small additional increase in cluster efficiency. If larger thresholds should be necessary during the module operation in CMS, an increase of the bias voltage to 800 V is beneficial for the detection efficiency. However, a higher bias voltage leads to higher leakage currents and, thus, higher power consumption of the module.

In-Strip Efficiency

To further investigate the origin of the decreasing cluster efficiency after irradiation, the efficiency is studied as a function of the interpolated track position. With spatial track resolutions of less than 10 µm, it is possible to probe the efficiency distribution in between strips of the 2S sensors. To increase the dataset, the x coordinate of each track intersection point inside the illuminated area is taken modulo the strip pitch of 90 µm to project all x coordinates into the coordinates of one strip. Figure 6.26a compares the results before and after irradiation. Only data from the bottom sensors are shown. To decrease the statistical uncertainties, the two most efficient TDC bins have been taken into account for the analysis of the irradiated module. The coordinate system is chosen in such a way that the center of the strip implant is located at $x = 45\,\mu m$.

The unirradiated module shows a constant efficiency at the expected level of 99.8% for all track impact points within the strip. After irradiation, the shape of the efficiency distribution changes. For track coordinates $25\,\mu m \leq x \leq 65\,\mu m$, the cluster efficiency reaches a plateau at an average value of 99.7%. For smaller and larger x values, the efficiency decreases towards the borders of the strip. This effect is generated by charge sharing of the sensor signal between neighbouring strips. For tracks interacting in the sensor directly below the center of a strip, the majority of charge is collected by the superjacent strip. For track intersection points below the border of two readout strips, the charge is shared in equal parts between both strips. The CBC provides binary readout, only detecting individual strip signals above a threshold. Together with the effect that the charge signal decreases with irradiation, the observed efficiency distributions in Figure 6.26a are qualitatively explained.

A similar investigation can be performed for the 2S sensor center where the two rows of strips face each other. Figure 6.26b shows the cluster efficiency as a function of the y coordinate of the track intersection point for $-500\,\mu m \leq y \leq 500\,\mu m$. The center line of the sensor is located at $y = 0\,\mu m$. Comparable to the previously presented results, the cluster efficiency is constant within the shown area for the unirradiated module. Due to charge sharing, the cluster efficiency shows a distinct drop at the strip row separation within a region of ±40 µm around $y = 0\,\mu m$. This is compatible with the spatial separation of the strip implants at the sensor center of 68 µm.

All global efficiencies presented in this section during the bias voltage dependency and threshold dependency investigations, have been calculated as average efficiency from datasets where the center of the sensor was illuminated. The beam spot has an area of approximately $14\,mm \times 9\,mm$. Compared to the strip length of 5 cm, the relative portion of the inefficient area in the 2S sensor center is overestimated by the limited beam spot compared to the complete sensor surface. Scaling the measured efficiency distributions correspondingly to the complete sensor surface, the cluster efficiency increases by 0.1%. Thus, this systematic uncertainty is comparable to the statistical uncertainty.

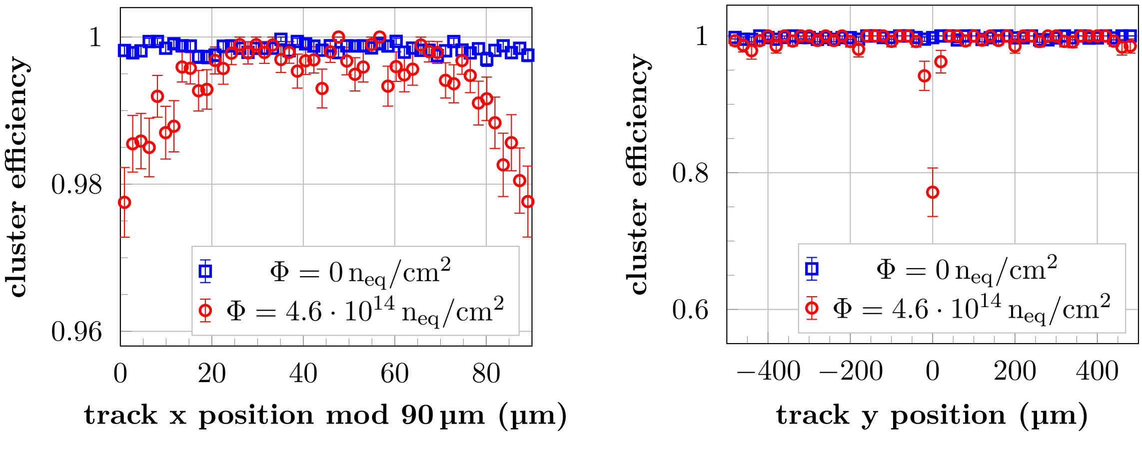

(a) (b)

Figure 6.26.: In-strip efficiencies in x and y direction. (a) The x position of the track intersection point on the bottom sensor is projected into the coordinates of one strip. The strip implant is centered at 45 µm, each strip is 90 µm wide. Due to charge sharing between the strips, the strip signal decreases for track intersection points in the boundary region of a strip. This results in a decrease of the cluster efficiency for these areas after irradiation. (b) A similar observation is made for the 2S sensor center area, where the two rows of strips face each other. Data are exemplarily shown for the bottom sensor. Data before irradiation are shown in blue and wer taken at a bias voltage of 300 V. Data from the irradiated module are marked in red and a bias voltage of 600 V was applied. A threshold of 6000 e^- was used for both datasets.

6.3.6. Stub Detection Efficiency

For the 2S module performance within the CMS Outer Tracker, the stub detection efficiency is a crucial parameter to achieve good Level-1 trigger performance. Therefore, the stub detection performance of 2S module prototypes is investigated in beam tests. Similar to the cluster efficiency studies presented in the previous section, the module stub efficiency is evaluated with the module oriented perpendicularly to the electron beam. For all measurements, the programmable maximum cluster width in the stub finding algorithm is set to four strips. All stub window offsets are programmed to be zero and the stub window size is set to 4.5 and five strips for the irradiated and unirradiated modules, respectively.

Bias Voltage Dependency

The stub efficiency is dependent on the bias voltage applied to the sensors as displayed in Figure 6.27a. The data points for the unirradiated 8CBC3 module are shown as blue squares. Similar to the cluster efficiency, the stub efficiency increases with increasing bias voltage, as the sensor signal increases for voltages below the depletion voltage. For voltages above 180 V, the stub efficiency stays at a constant level of 99.4% up to a voltage of 400 V. Knowing the cluster efficiencies of top and bottom sensor, the measured stub efficiency values can be compared with the expectation of two independent sensors given by the product of the two cluster efficiencies. In this product, the cut on the cluster size of four strips at maximum has to be taken into account. Therefore, the cluster efficiencies $\epsilon^{i}_{\text{cluster} < 5}$ with $i \in \{\text{top}, \text{bottom}\}$ are evaluated for both sensors and their product is shown as dashed green line in Figure 6.27a.

The product of cluster efficiencies is significantly larger than the measured stub efficiencies. This results from the fact that the two strip rows in a 2S sensor are read out by a different set of CBC chips located on the two frontend hybrids. During the cluster efficiency analysis, no residual cut on the y coordinate is applied. Thus, a track in the center region of the sensor is identified efficiently if at least one of the sensor halves detects a cluster in a strip nearby fulfilling the x residual cut. This keeps the cluster efficiency at a high value within the central sensor region, as shown in Figure 6.26b. For the generation of a stub, it is however important that both sensor layers detect a cluster within the same sensor half as no cluster information is shared between the frontend hybrids. For exactly perpendicular particle incidence onto the 2S module prototypes, this condition is fulfilled for the majority for tracks. However, already a slight misalignment of the DUT box, resulting in a rotation of the module around the y axis, has a measurable impact. Additionally, multiple scattering effects may also create inclined particle trajectories inside the telescope. These tracks are another source that creates cluster combinations in the center of the sensor leading to the observed decrease in stub efficiency. Figure 6.27b displays the stub efficiency as a function of the y coordinate of the track intersection point. The sensor center is situated at $y = 0\,\mu\text{m}$. A clear drop of the stub efficiency in the sensor center can be observed within an area of ±40 µm. This effect leads to the observed discrepancy between the product of the sensor cluster efficiencies and the measured stub efficiencies. For confirmation, the sensor area with $-40\,\mu\text{m} < y < 40\,\mu\text{m}$ is masked and the stub efficiency is re-evaluated. The resulting data points are shown as green squares in Figure 6.27a. These points coincide well with the product of the sensor cluster efficiencies respecting the statistical uncertainties.

The same effect can be observed after irradiation. Data are shown in orange and red in Figure 6.27. Besides already showing inefficiencies in the center of the region in the cluster efficiency distribution shown in Figure 6.26b, the product of the cluster efficiencies results in efficiency values larger than the measured stub efficiencies. With the central area of the sensor masked, the resulting stub efficiency data points fit to the expectation from the cluster

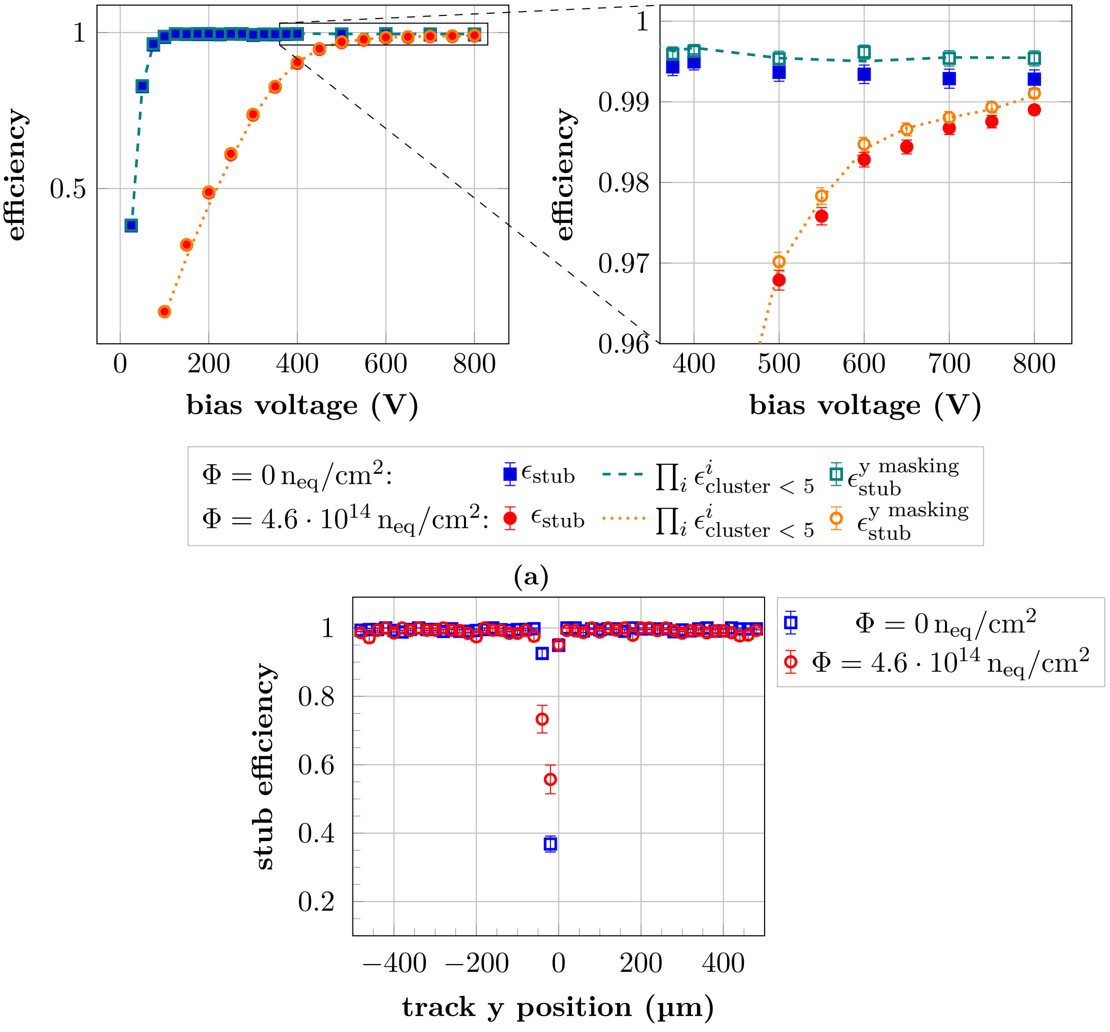

(a)

(b)

Figure 6.27.: (a) Dependency of the stub efficiency from the sensor bias voltage for the unirradiated and irradiated 8CBC3 module. The measured stub efficiencies are shown as blue and red markers. For comparison, the product of the cluster efficiencies of bottom and top sensor are shown as dashed and dotted lines. Due to a drop of the stub efficiency in the center of the 2S sensors where the two rows of strip face each other, the stub efficiency is measured lower than the expectation of cluster efficiencies product. The green and orange markers show the efficiencies after masking the central area of the sensor with $-40\,\mu\mathrm{m} \leq y \leq 40\,\mu\mathrm{m}$. These points coinicide well with the product of cluster efficiencies. The right plot shows a zoomed version of the area marked with a rectangle in the left plot. (b) The stub efficiency is shown as a function of the y position of the track intersection point. A distinct dip is observable before and after irradiation in the central area as the two rows of strips are read out by CBCs on different frontend hybrids and no cluster information is shared between the hybrids. For the unirradiated module, data are taken at a threshold of $5500\,\mathrm{e}^-$ and at a bias voltage of 300 V. For the irradiated module, a threshold of $6000\,\mathrm{e}^-$ is set and the module is operated at a bias voltage of 600 V.

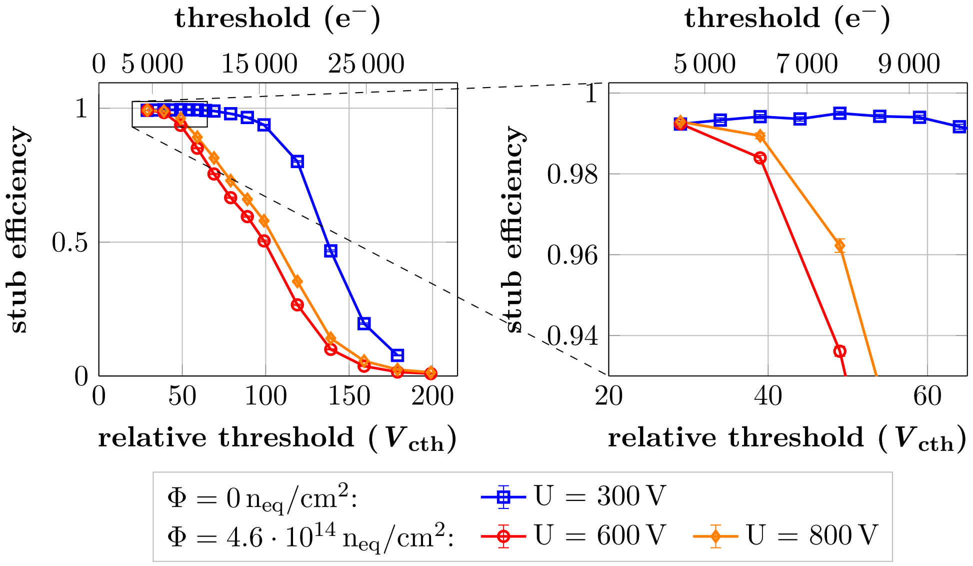

Figure 6.28.: The stub efficiency is dependent on the CBC threshold. Data before irradiation are shown in blue. The upper x axis gives the threshold setting in electron equivalent. Before irradiation, the stub efficiency stays at a constant level of 99.4% up to thresholds of 9000 e⁻ for a bias voltage of 300 V. At higher thresholds, the efficiency decreases. After irradiation, the stub efficiency reaches a maximum of 99.2% at a threshold of 4500 e⁻ and decreases for all larger thresholds significantly at a bias voltage of 600 V. By increasing the voltage to 800 V, the loss in efficiency for thresholds larger than 4500 e⁻ can be partially compensated. The marked rectangular area is enlarged in the right plot.

efficiencies within the statistical uncertainties. A quantitative comparison of the stub efficiency in the central region before and after irradiation as shown in Figure 6.27b is not possible, as the presented measurements have been performed during two independent beam test campaigns with individual setups. Thus, a comparable rotation of the module around the y axis can neither be guaranteed nor corrected during alignment due to the coarse spatial resolution of the strip sensors in the y direction.

Threshold Dependency

The threshold dependency of the stub efficiency is shown in Figure 6.28. Similar to the cluster efficiency, the stub efficiencies are maximal for the measurements with the lowest threshold of 4500 e⁻. Before irradiation, a stub efficiency of 99.4% is achieved which stays constant up to thresholds of 9000 e⁻. For larger thresholds, the stub efficiency decreases. After irradiation, the stub efficiency has its maximum at 99.2% when appyling a bias voltage of 600 V. Compared to the case before irradiation, the stub efficiency drops already at a threshold of 6000 e⁻ to approximately 98% and decreases further with increasing threshold. By increasing the bias voltage to 800 V, this decrease can be mitigated. The maximum stub efficiency, found at the lowest measured threshold, is only slightly influenced by the bias voltage increase. This indicates, that this threshold is small enough to detect most of the charge signal seen by the strip implants. Further lowering the threshold will not increase the stub efficiency significantly.

6.3.7. Performance of Transverse Momentum Discrimination

To study the transverse momentum discrimination performance, the 2S module is rotated with respect to the beam to emulate bent particle trajectories. During the beam test campaigns performed within this thesis, these rotation scans have only been performed with the irradiated 8CBC3 module.

Stub Efficiency Turn-on Characteristic

Figure 6.29 shows the stub efficiency of the irradiated module as a function of the angle setting on the rotation stage. The CBC threshold was set to $6000\,\mathrm{e}^-$. The error bars are indicating the statistical uncertainties on the stub efficiency given by Equation (6.6). For an angle setting of 0°, the expected stub efficiency of 98.7% results. When rotating the module to positive or negative angles, the stub efficiency stays at a high level until reaching angles around approximately ±14°. At these angles a sharp drop of the stub efficiency to zero is observed. Through the increasing module tilt, the electron beam generates clusters in bottom and top sensor with increasing spatial offsets between the respective cluster centers. When this offset exceeds the programmed stub correlation window size of ±4.5 strips, no valid stubs are identified anymore and, therefore, the stub efficiency decreases. For large tilting angles above 20°, the stub efficiency is zero. The observed behaviour is called *stub turn-on characteristic* and can be modeled by an error function of the form

$$f(\vartheta, p_0, p_1, p_2, p_3) = 1 - \frac{1}{2}\left(p_0 + p_1 \cdot \operatorname{erf}\left(\frac{\vartheta - p_2}{p_3}\right)\right) \tag{6.7}$$

with four parameters p_i and $\vartheta \geq 0°$. Within this parametrisation, p_2 is always positive. While p_0 allows to shift the function along the stub efficiency values and is expected to have a value near one, p_1 allows to scale the error function allowing to adapt to the efficiency plateau for angles around 0°. The parameter p_2 characterizes the position of the inflection point in the turn-on curve and p_3 indicates the turn-on curve width.

To determine the four parameters p_0 to p_3, a fit of Equation (6.7) to the data is performed. In a first step, only positive angles are used, as this dataset offers a finer sampling of the turn-on characteristic than the dataset with negative angles. The second step consists of repeating the fit for the negative angles. As all stub window offset registers are set to zero, the turn-on characteristic has to be symmetrical around the angle corresponding to perpendicular particle incidence. Based on this knowledge, the parameters p_0, p_1 and p_3 are fixed to the values determined during the first fit and only p_2 is re-evaluated for the dataset with negative angles. The resulting fit functions are shown as dashed and dotted lines in Figure 6.29. The two fit results for p_2 including statistical uncertainties are

$$p_2^{\geq 0} = (13.973 \pm 0.004)° \qquad \text{and} \qquad p_2^{\leq 0} = (15.009 \pm 0.004)° \ .$$

However, the fit is characterized by a χ^2 normalised by the number of degrees of freedom of 96, indicating that the measurement is dominated by systematic uncertainties. As the dominant systematic uncertainty, the angular precision of the rotation stage needs to be taken into account. It is estimated to be ±0.05°. To propagate this uncertainty onto the fit parameters p_i, the following steps are performed:

1. For each data point shown in Figure 6.29, a uniformly distributed random number ϑ_r is generated with $-0.05° \leq \vartheta_\mathrm{r} \leq 0.05°$ and added to the nominal angle setting.

2. The error function fit described previously is repeated on the newly created dataset and the resulting parameters p_i' are stored.

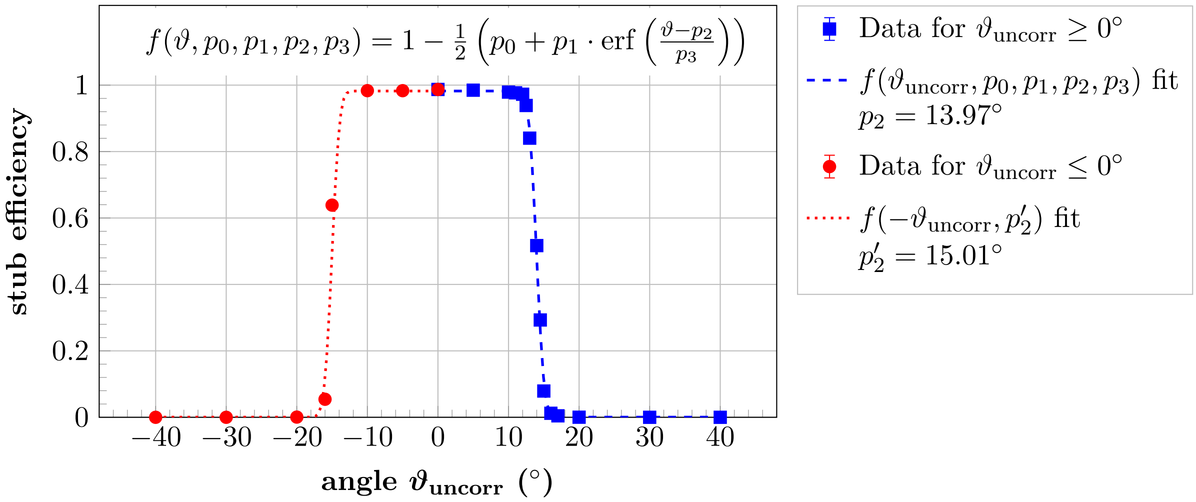

Figure 6.29.: The stub efficiency is shown as a function of the rotation stage angle. The error bars indicate the statistical uncertainties on the stub efficiency. The alignment of the rotation stage at a setting of 0° into a perpendicular position to the beam axis was performed "by eye" leaving the possibility of a small misalignment. To correct for this, an error function fit is performed to the data for positive and negative angular settings independently. Using the knowledge, that the distribution is symmetrical around the angle corresponding to perpendicular particle incidence, a misalignment of 0.52° can be extracted.

3. Steps one and two are repeated 1000 times. Afterwards, the systematic uncertainties on the parameters p_i are given by the maximum and minimum observed deviation of p_i' from the original parameters p_i.

This leads to the fit results

$$\begin{aligned} p_0 &= 1.017 \pm 0.001 \text{ (sys.)} \pm 0.004 \text{ (sta.)} \ , \\ p_1 &= 0.982 \pm 0.001 \text{ (sys.)} \pm 0.004 \text{ (sta.)} \ , \\ p_2^{\geq 0} &= [13.973 \pm 0.04 \text{ (sys.)} \pm 0.004 \text{ (sta.)}]^\circ \ , \\ p_2^{\leq 0} &= [15.009 \pm 0.04 \text{ (sys.)} \pm 0.004 \text{ (sta.)}]^\circ \text{ and} \\ p_3 &= [1.191 \pm 0.04 \text{ (sys.)} \pm 0.006 \text{ (sta.)}]^\circ \ . \end{aligned}$$

Thus, the uncertainties of parameters p_2 and p_3 are dominated by the systematic uncertainties. The small discrepancy between the two values for p_2 can be caused by two main factors.

- A misalignment of the DUT for rotations around the y axis during data taking leads to a systematic shift of the turn-on curve. As the stub information is produced directly on the module, the turn-on characteristic cannot be influenced by the alignment procedure performed during the off line analysis. During the beam test, the alignment of the rotation stage at a setting of 0° is made "by eye". This can easily explain small misalignments of the rotation stage.

- If the two silicon sensors are not perfectly aligned during module assembly, this misalignment can influence the stub turn-on characteristic. A shift of the two sensors along the axis perpendicular to the strip implants leads to an overall shift of the turn-on curve.

For the irradiated module, the metrology measurements performed with the bare module during asssembly resulted in a neglegible rotation between the sensor strips and a relative shift of the two sensors of less than 4 µm. For this sensor misalignment, a shift of the turn-on characteristic of 0.15° is expected as determined via a Monte Carlo simulation. Further details about the simulation results are given on Page 122. Together with the angle offset of the rotation stage at an angular setting of 0°, the observed shift of the turn-on curve can be explained. To discuss the transverse momentum discrimination performance of the 8CBC3 module, the rotation stage angle settings $\vartheta_{\text{uncorr}}$ are transformed via

$$\vartheta = \vartheta_{\text{uncorr}} + \vartheta_{\text{correction}}$$

with

$$\vartheta_{\text{correction}} = \frac{1}{2}\left(p_2^{\leq 0} - p_2^{\geq 0}\right) = 0.52^\circ \ .$$

This leads to a symmetrical stub turn-on characteristics around 0° with a parameter $p_2 = 14.49^\circ$. The effects of misaligned sensors on the module performance are studied separately on Page 122.

The rotation angle can be converted into a transverse momentum equivalent for different 2S module locations in the barrel part of the CMS detector. Taking into account the CMS magnetic field strength of $B = 3.8\,\text{T}$, the transverse momentum equivalent is given by

$$p_T[\text{GeV}] \approx \frac{0.57 \cdot R[\text{m}]}{\sin(\vartheta)} \ . \tag{6.8}$$

Figure 6.30 displays the stub turn-on characteristic as a function of the transverse momentum evaluated for the 2S module closest to the interaction point in the Phase-2 Outer Tracker at $R = 68.7\,\text{cm}$. The upper x axis indicates the corresponding DUT rotation axis. The selected correlation window size of ±4.5 strips corresponds to a transverse momentum threshold of $p_T \geq 1.5\,\text{GeV}$. The turn-on characteristics has a width of 123 MeV, resulting in a relative momentum resolution of

$$\sigma_{p_T} = \frac{p_3}{p_2} \approx 8\% \ .$$

2S Module Sensor Distance Analysis

The measured position of the inflection point in the stub turn-on curve can be compared with its expectation extracted from the 2S module geometry. The investigated 8CBC3 modules have been assembled with Al-CF bridges and hybrids developed for the 1.8 mm module variant. With a stub window size of ±4.5 strips, the stub efficiency should be one for a cluster center offset of 4.5 strips between top and bottom sensor clusters and it should be zero for an offset of 5 strips. Thus, the position of the turn-on inflection point can be estimated via

$$\vartheta_{\text{inflection point}} = \frac{1}{2}\left(\arctan\left(\frac{4.5 \cdot 90\,\mu\text{m}}{1.8\,\text{mm}}\right) + \arctan\left(\frac{5 \cdot 90\,\mu\text{m}}{1.8\,\text{mm}}\right)\right) \approx 13.4^\circ \ . \tag{6.9}$$

However, this estimation only considers the cluster offsets and neglects sensor effects during charge generation like varying track incidence angles due to multiple scattering, charge sharing and readout noise. These effects have to be taken into account to reproduce the cluster distribution in the 2S sensors realistically. Therefore, a Monte Carlo simulation is performed to study the stub turn-on characteristic.

A sketch of the implemented model is shown in Figure 6.31a. The two silicon sensors have a physical thickness of 320 µm with a 30 µm deep implant on the sensor backside, reducing

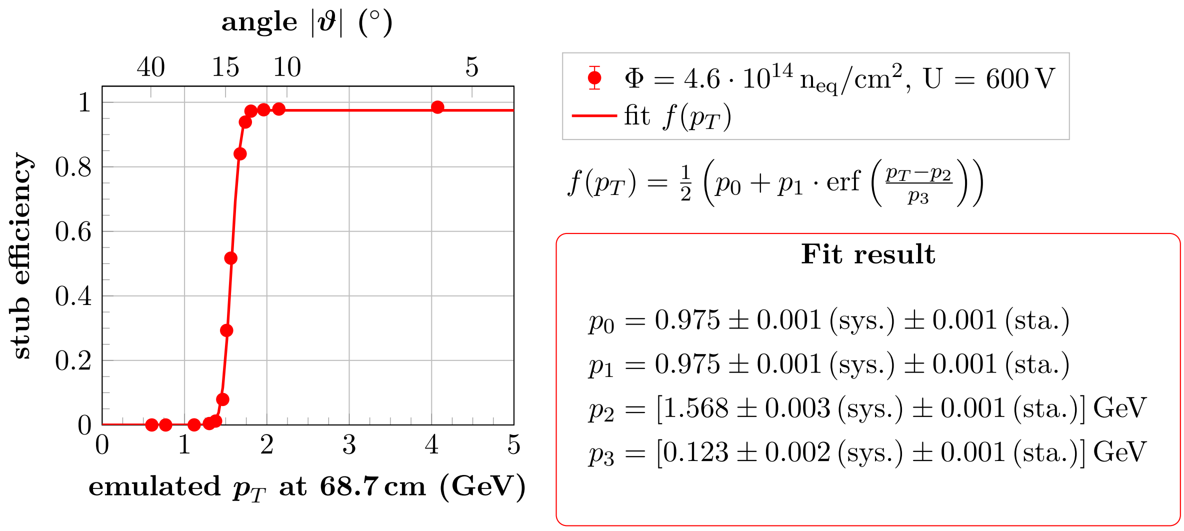

Figure 6.30.: The rotation angles of the DUT can be converted into an equivalent transverse momentum value for a 2S module at a radial distance $R = 68.7\,\mathrm{cm}$ from the interaction point. The upper x axis shows the corresponding angle setting. As expected, the stub efficiency is zero for low transverse momenta and shows a steep increase at $p_T \approx 1.5\,\mathrm{GeV}$. The error function fit yields a width of $p_3 = 123\,\mathrm{MeV}$. The error bars indicate the statistical uncertainties which lead to a $\chi^2/\#\mathrm{NDF}$ of 106. The systematic errors are determined as described previously for Figure 6.29.

the active thickness to 290 µm. The implant is marked as grey area in the sketch. The two sensors are oriented back-to-back in the module with a spatial distance d measured between the centers of the sensors active areas. Track trajectories are defined as straight lines identified by an incidence position x_{seed} on the top surface of the seed sensor and the track incidence direction given by a normally distributed random variable with expectation value ϑ and standard deviation σ_ϑ. By introducing a randomly varying tracking angle, the effect of multiple scattering in the beam test can be simulated. The incidence position x_{seed} is varied uniformly along the top side of the seed sensor. To determine the charge signal generated in the silicon sensors, one Landau distributed random number is created giving the average number of generated electron-hole pairs per micrometer. Following [Har17], numbers above 500 are discarded resulting in a distribution characterized by a most probable value of 76 and a mean of 108. The track trajectory is divided into 1 µm long parts called *tracklets*. A charge signal with the value of the Landau distributed random number is assigned to each tracklet. The tracklet charges are assigned to the nearest readout strips using the charge sharing model characterized by the weights

$$w_{\mathrm{left}} = \frac{(1-\tilde{x})^p}{(1-\tilde{x})^p + \tilde{x}^p} \qquad \text{and} \qquad w_{\mathrm{right}} = \frac{\tilde{x}^p}{(1-\tilde{x})^p + \tilde{x}^p}\ . \tag{6.10}$$

The coordinate $\tilde{x}$ indicates the relative position in between two strip implants with $\tilde{x} = 0$ being the center of the left strip and $\tilde{x} = 1$ being the center of the right strip. The charge sharing parameter p is set to five [Mai19]. Figure 6.31b displays the two weights as a function of $\tilde{x}$. To emulate the noise of the readout system, a random number is generated following a normal distribution with a mean of $0\,\mathrm{e}^-$ and a width of $1000\,\mathrm{e}^-$. This random number is added to the strip charges. Afterwards, the binary readout is emulated by changing the hit information of strips with a charge signal above a threshold of $6000\,\mathrm{e}^-$ from zero to one. Directly neighbouring channels with a hit information of one are then combined to clusters. Based on the cluster information of both sensor layers, the stub algorithm is evaluated and the stub efficiency is defined as

$$\epsilon_{\text{stub}}^{\text{sim}} = \frac{n_{\text{reconstructed stubs}}}{n_{\text{simulated tracks}}} \tag{6.11}$$

with $n_{\text{reconstructed stubs}}$ being the number of valid stubs detected per simulation run and $n_{\text{simulated tracks}}$ giving the total number of simulated tracks per run.

To reproduce the data measured in the beam test, the simulation can be tuned using the two free parameters σ_ϑ and d. The effect of these parameters onto the simulated turn-on characteristic is shown in Figure 6.31c and Figure 6.31d. As expected from geometrical considerations, a change of the sensor distance d leads to a shift of the inflection point position while the width of the turn-on characteristic stays constant. Larger sensor distances lead to an inflection point at lower angles. By varying the standard deviation of the track incidence angle σ_d, the width of the turn-on curve can be changed while leaving the position of the inflection point unchanged. By scanning both parameters independently and comparing the results with the parameters $p_2^{\text{beam test}}$ and $p_3^{\text{beam test}}$ extracted from the beam test data, optimal simulation settings for the sensor distance and track angle standard deviations can be extracted. The scan results are shown in Figure 6.32a and Figure 6.32b. A second order polynome regression is performed to determine the optimal settings for d and σ_ϑ to describe the data with the model. The resulting values are

$$d^{\text{sim}} = (1.652 \pm 0.005)\,\text{mm} \qquad \text{and} \qquad \sigma_\vartheta^{\text{sim}} = (0.70 \pm 0.04)^\circ \ .$$

The propagated uncertainties indicate the dominant systematic errors indicated as light blue areas in Figures 6.32a and 6.32b.

The sensor distance resulting from the simulation model is significantly smaller than the expected sensor distance of $d = 1.8\,\text{mm}$. There are two factors leading to this discrepancy. The first effect is related to the design of the carbon fiber reinforced aluminium bridges. During the module assembly of the irradiated module, the latest available bridge prototypes have been used. However, the thickness of the bridges responsible to achieve the sensor spacing has been defined at a time when the decision about the final design of the 2S sensor thickness has not yet been taken. Historically, sensors with a physical thickness of 320 µm and an active thickness of 200 µm measured from the top sensor surface showed the most promising results for outer tracker modules. Thus, the bridges have been designed to achieve a distance of 1.8 mm between the centers of the active sensor areas. A spacing $d_{\text{spacing}} = 1.36\,\text{mm}$ is needed as shown in the left half of Figure 6.33. This spacing is achieved by the Al-CF bridges, the polyimide strips and the glue layers. As introduced in Section 3.2.3, a sensor design with an active thickness of 290 µm was chosen after a qualification campaign to be used in the CMS Outer Tracker modules. With the bridge thickness unchanged, the latest 2S module prototypes achieve a distance of only 1.71 mm between the active sensor centers. This is illustrated in the right half of Figure 6.33.

After considering this reduced sensor distance, a difference of 60 µm between the simulated and expected sensor distance remains. This discrepancy can either be generated by a reduced sensor distance of the module itself compared to the expectation or an systematic uncertainty introduced at the beam line e.g. through a inaccurate rotation stage. To investigate this, the irradiated module was placed inside a digital microscope of the type *Keyence VHX-6000* [Key22]. The microscope allows to rotate its camera by 90°. This is used to observe the sensor edges on the module side at which no hybrids are placed. A photo of the setup is shown in Figure 6.34a together with the microscope image in which the sensor distances are measured digitally. An uncertainty of 10 µm onto each distance measurement is estimated. The module

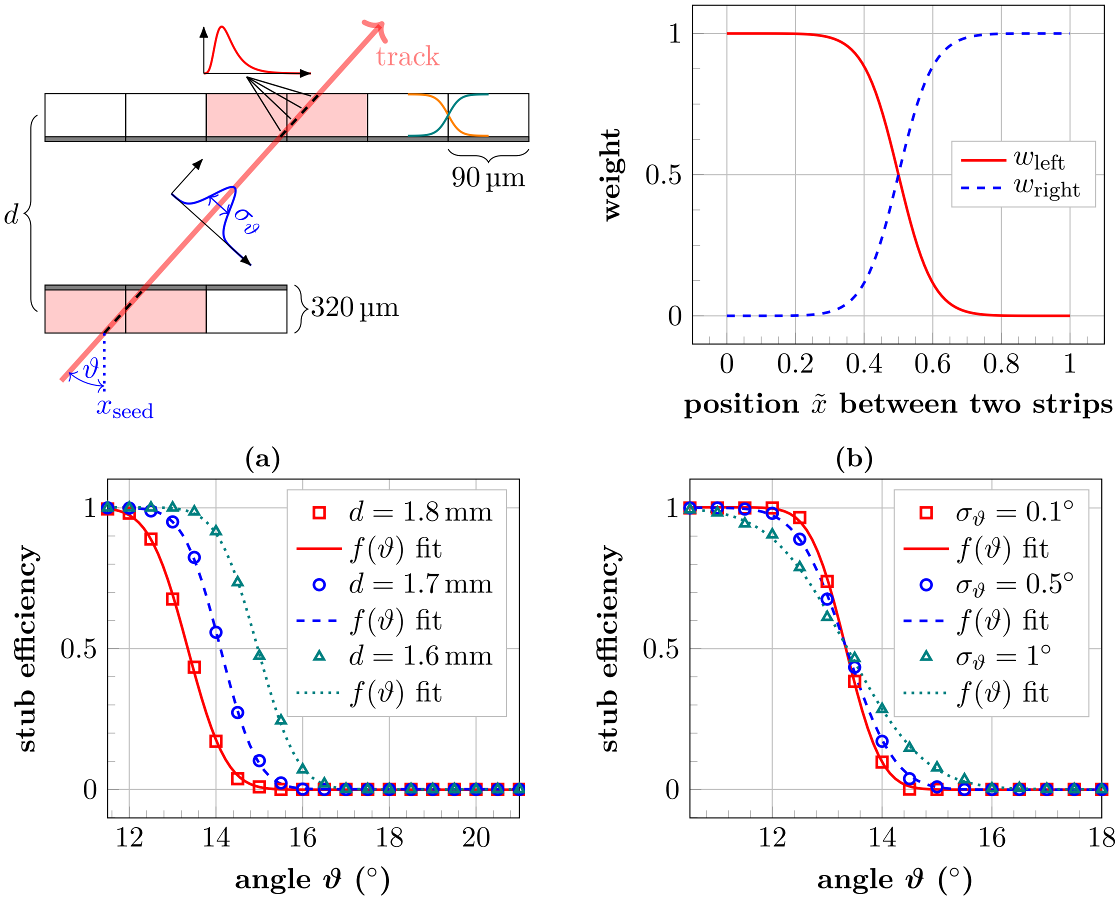

(a) (b)

(c) (d)

Figure 6.31.: (a) Sketch of the implemented processes in a Monte Carlo simulation to reproduce the stub efficiency turn-on characteristic. To emulate charge generation in the silicon sensors, a Landau distributed random number is created and assigned to 1 µm long tracklets along the track line. The simulation provides two free parameters d and σ_ϑ to tune the model to the experimental data. (b) The tracklet charge is split between two neighbouring strips using the weights w_{left} and w_{right} depending on the tracklet position $\tilde{x}$ in between two strips. At $\tilde{x} = 0$, the center of the left strip is located. At $\tilde{x} = 1$, the right strip is centered. (c) By changing the sensor distance parameter d, the position of the inflection point can be adjusted. (d) The parameter σ_ϑ influences the width of the turn-on characteristic. The fit function $f(\vartheta)$ is given by Equation (6.7).

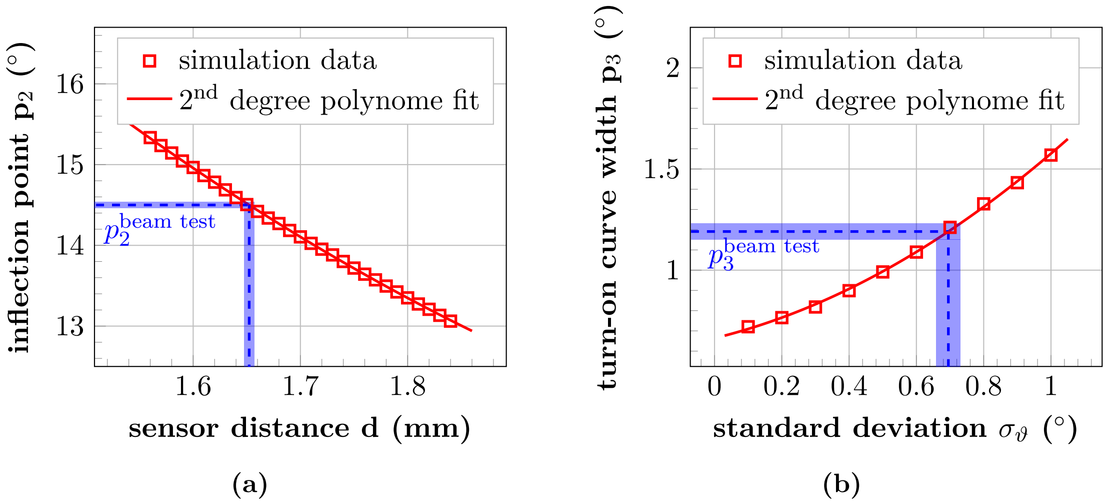

Figure 6.32.: To determine the simulation input parameters to reproduce the beam test measurements best, a scan of the sensor distance d and the track angle standard deviation σ_ϑ is performed. (a) By scanning d, the optimal setting can be extracted to describe the experimentally observed position of the inflection point $p_2^{\text{beam test}}$. (b) A scan of σ_ϑ yields the optimal setting to model the width of the turn-on curve $p_3^{\text{beam test}}$. The systematic uncertainties are indicated as light blue areas.

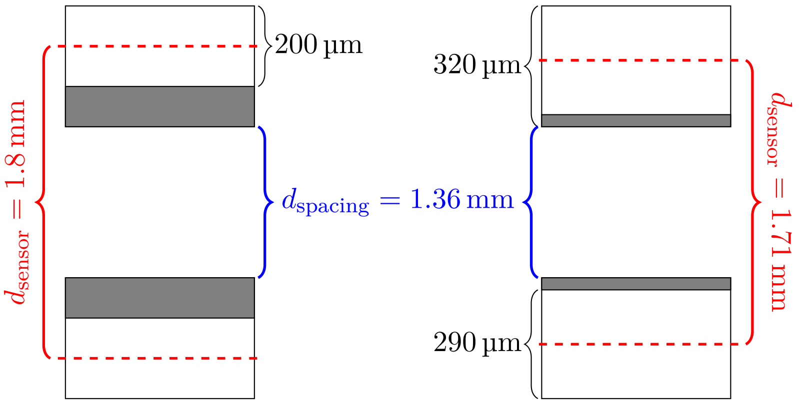

Figure 6.33.: For 2S modules, the sensor distance is measured from the centers of the active silicon sensor areas. Historically, the 2S module design was optimized for silicon sensors with a physical thickness of 320 µm and an active thickness of 200 µm measured from the sensor topside. This configuration is shown in the left half of the sketch. To reach a sensor distance of 1.8 mm, a spacing $d_{\text{spacing}} = 1.36$ mm needs to be achieved with Al-CF bridges, polyimide strips and glue layers. After a five year qualification campaign, silicon sensors with an active thickness of 290 µm have been identified to be best suitable for outer tracker modules. As for the investigated module prototypes, the module spacing was not adapted to the new sensors, a sensor distance of 1.71 mm results. This configuration is shown in the right half of the sketch. The sketch is not to scale!

is placed on a translation stage and the sensor distances are measured at dedicated points y along the module side. The resulting distances are shown in Figure 6.34b. The measurements performed directly adjacent to the Al-CF bridges at $y = \pm 40\,\mathrm{mm}$ are compatible with the expected sensor distance of 1.71 mm. However, a clear decrease of the sensor distance can be observed towards the center of the module at $y = 0\,\mathrm{mm}$. The minimal distance is measured to be $1.652\,\mathrm{mm} \pm 0.01\,\mathrm{mm}$. This value corresponds well with the result extracted from the MC simulation presented above. During the beam test, only parts of the 2S sensor could be illuminated by the beam due to the limited acceptance of the beam telescope. The red area in Figure 6.34b indicates the beam spot located in the center of the module. The beam spot coincides with the area of smallest sensor distance. Thus, this decrease in sensor distance towards the center of the module is the second effect explaining the discrepancy observed between original expectation and simulation. Combining these information, it can be concluded that the data from the stub turn-on characteristic are well understood and reproduced by the Monte Carlo simulation.

The sensor distance measurements have been repeated with four additional 8CBC3 module prototypes. The measurement results are shown in Figure C.2. All modules show a decrease of the sensor distance of approximately 40 µm to 60 µm towards the center of the module compared with the distances measured near the Al-CF bridges. As this change in sensor distance happens along the y axis parallel to the strips, it cannot be compensated by the stub algorithm offsets for different areas of the module. Therefore, the influence of the observed sensor bow on the module stub efficiency turn-on curve is evaluated using the Monte Carlo simulation. The data points shown in Figure 6.34b are interpolated using cubic splines. These interpolation is used in the simulation to vary the sensor distances per simulated track. The resulting turn-on characteristic is shown in Figure 6.35 in red. For comparison, a simulated turn-on characteristic with a constant sensor distance of 1.71 mm is shown in blue. As already shown previously, a change in sensor distance does not influence the width of the turn-on curve. The position of the inflection point and, thus, the threshold for the p_T trigger is reduced by 23 MeV for the varying sensor distance. Increasing the stub window size by half a strip at a constant sensor distance of 1.71 mm yields a p_T threshold of $p_2 = 1.47\,\mathrm{GeV}$. Thus, it is not possible to compensate the effect of the sensor bow by adapting the stub window size accordingly. However, the influence of the sensor bow reduces the p_T trigger threshold by 1.5%. This change will not influence the transverse momentum discrimination performance of the CMS tracker significantly. Additionally, the change in sensor distance bow will be significantly reduced for 2S modules with a second stump bridge (see Section 3.2.4). The additional stump bridge introduces an additional sensor support point at $y = 0$ in Figure 6.34b.

Influence of Sensor Misalignment

During the assembly of the irradiated module, the strip-to-strip alignment was measured using a metrology station. A shift of 4 µm between top and bottom sensor strips in the direction orthogonal to the strip implants is observed . To study the effect of such shifts on the stub efficiency distribution, the Monte Carlo simulation presented previously is refined allowing for shifting the two sensors with respect to each other. The simulation parameter σ_ϑ is set to 0° for the results presented in the following. The correlation window size is set to ±4.5 strips. Figure 6.36a compares the stub turn-on characteristics for different shifts s between top and bottom sensor. With increasing sensor misalignment, the curve's inflection point shift towards higher p_T. Additionally, the distribution width increases as expected from geometrical considerations of charge sharing effects between strips. A shift of 4 µm as measured for the irradiated module leads to a shift of the turn-on curve inflection point by approximately 20 MeV or 0.15°. For 2S module assembly, a shift of $s \leq 100\,\mu\mathrm{m}$ is specified. The resulting turn-on

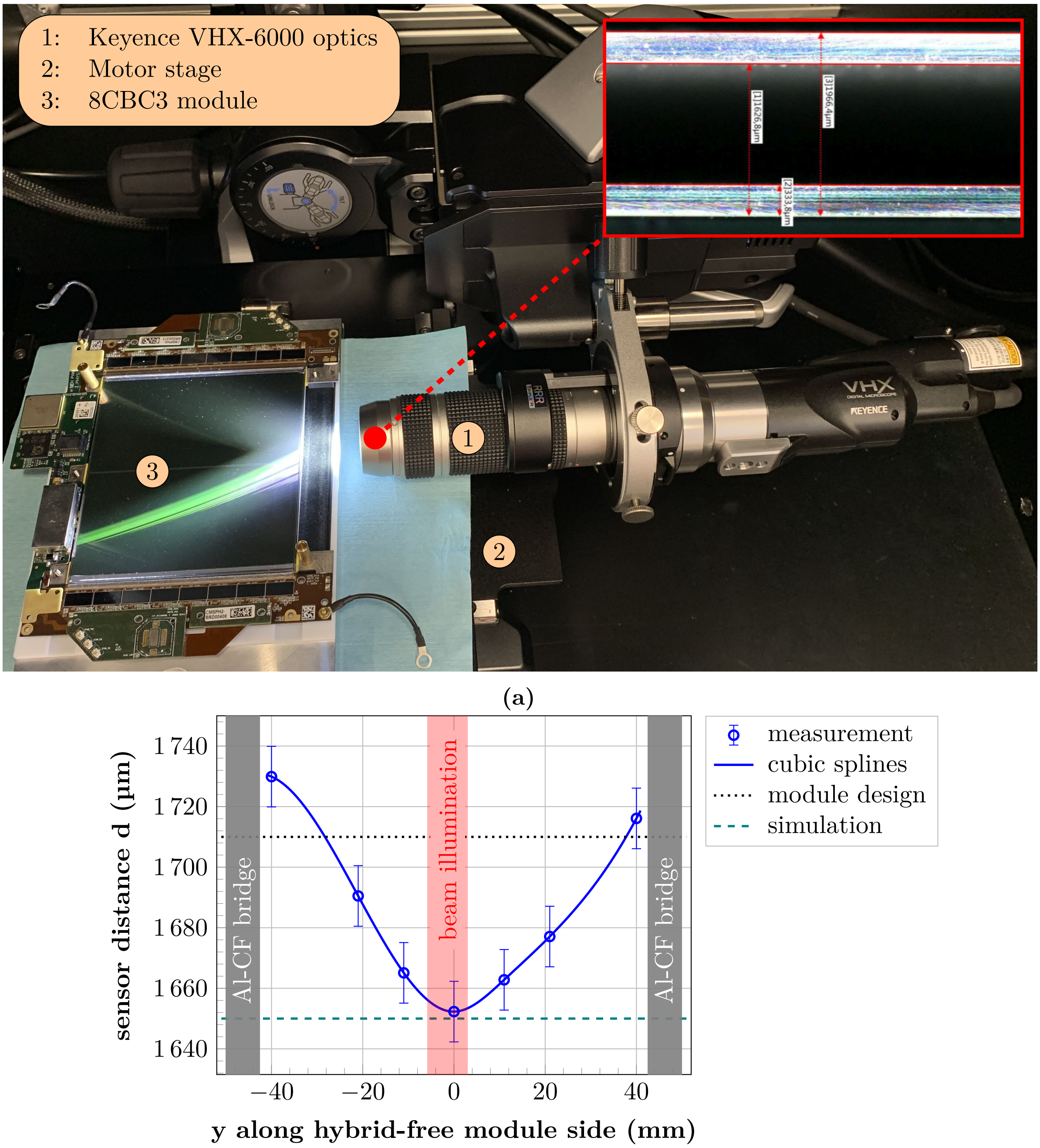

(a)

(b)

Figure 6.34.: The sensor distance d between the two 2S sensors is measured for the irradiated module. (a) The module is placed in a *Keyence VHX-6000* optical microscope. The microscope optics can be rotated by 90° as shown in the photo. This allows to measure the sensor spacing along the hybrid-free module side via the microscope software. A picture of the picture seen by the microscope and the measurements performed is shown in the red rectangle. (b) The sensor distance is dependent of the position y along the hybrid-free module side. A change in distance of up to 60 µm can be measured. The uncertainty on the distance measurement is estimated to be ±10 µm.

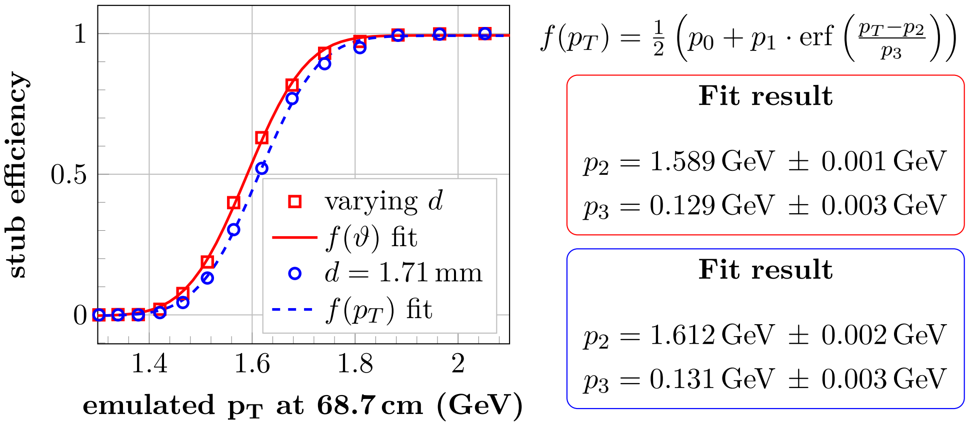

Figure 6.35.: The varying sensor distances d observed in the 8CBC3 module prototypes influences the p_T discrimination performance. To quantify this effect, a Monte Carlo simulation of the stub turn-on curve is performed with varying d and compared with the nominal constant sensor distance $d = 1.71$ mm.

characteristic for maximal shift is shown in Figure 6.36a in black. A significant increase of the p_T threshold by 474 MeV occurs and would introduce an inhomogeneous p_T discrimination performance of neighbouring modules for different sensor shifts. However, this effect can be reduced using the knowledge of the strip-to-strip alignment measured during module assembly. By adjusting the stub logic offset with its resolution of ±0.5 strips, it is possible to minimize the spreading of the p_T threshold to ±87 MeV between different 2S modules. independent of this correction, the goal during module assembly is to minimize the sensor shift as much as possible as any shift introduces an asymmetric turn-on characteristic for positive and negative trajectory curvatures.

Sensor shifts along the direction of the strip implants are specified to be smaller then 200 µm. These shifts have no influence on the shape of the stub turn-on characteristic. However, larger shifts lead to an increased inefficient area for stub detection in the sensor center (compare Figure 6.27b).

As a third strip-to-strip alignment specification, the rotation φ between the sensor strips is required to be smaller then 400 µrad during 2S module assembly. A rotation of the sensor strips with respect to each other introduces a broadening of the stub turn-on characteristic as shown in Figure 6.36b. Comparing the curve widths for no rotation and maximum allowed rotation, the curve widens by 34 MeV.

These findings can be used as input for a simulation of the tracking performance of the CMS detector under HL-LHC conditions. However, such a simulation is beyond the scope of this thesis.

Stub Noise

As shown previously, the module stub efficiency drops to zero outside the correlation window. Following the stub efficiency definition introduced in Section 6.3.4, this means that no stub information is found with stub position and stub bend code matching a reconstructed track. However, a stub efficiency of zero in this definition does not imply that the module stub data stream is empty. It has been found that in a fraction of the analysed events, stubs are detected whose positions fulfill the efficiency criterion in the seed sensor. This effect is called *stub noise* within this thesis.

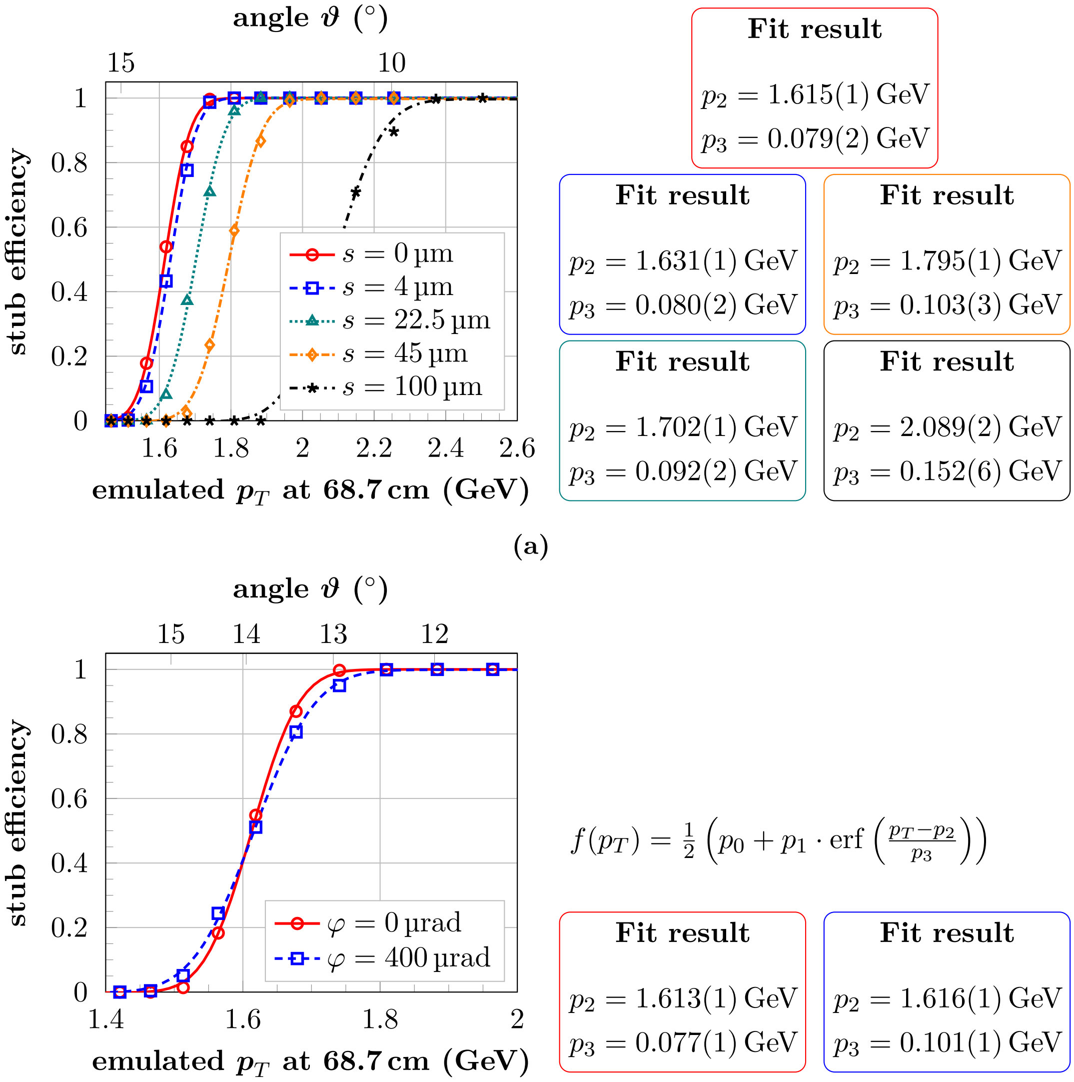

(a)

(b)

Figure 6.36.: Influence of 2S sensor misalignments during assembly onto stub efficiency turn-on characteristic. Simulations are performed with a stub window size of ±4.5 strips, a sensor distance of $d = 1.71\,\mathrm{mm}$ and $\sigma_\vartheta = 0°$. (a) Introducing a shift s orthogonal to the direction of the strip implants between the two sensors in a 2S module leads to a shift of the stub efficiency turn-on curve. (b) For rotations of the 2S sensors with respect to each other, the turn-on characteristic broadens.

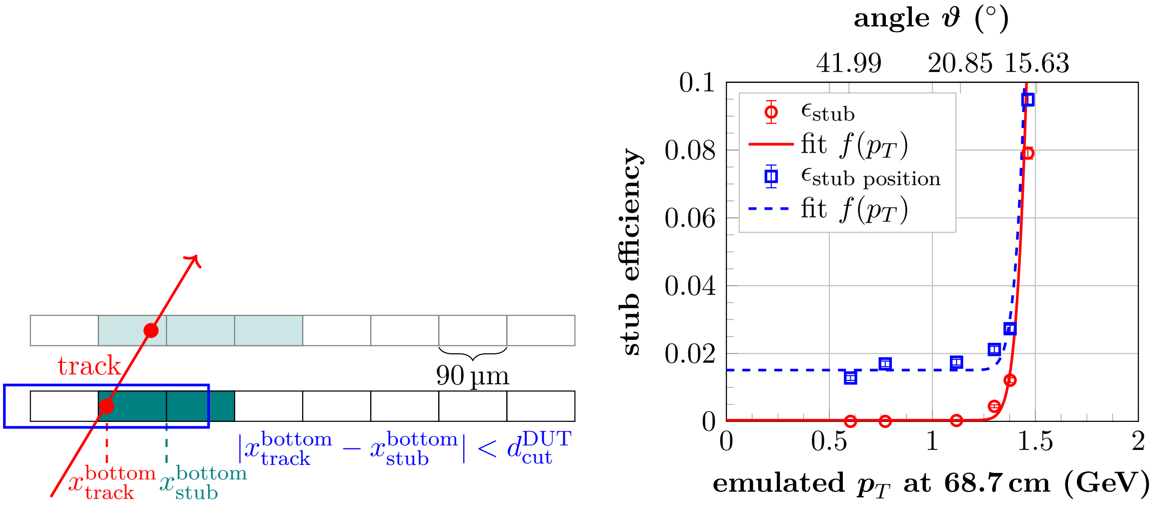

(a) (b)

Figure 6.37.: (a) To study the effect of stub noise, the stub position efficiency is defined by loosening the stub efficiency criterion. A stub is defined as efficient, if its stub position has an x residual smaller than $d_{\mathrm{cut}}^{\mathrm{DUT}} = 180\,\mu\mathrm{m}$. (b) The stub position efficiency shows efficiencies of approximately 1.7% for rotations corresponding to tracks passing outside the stub correlation window.

To study the origin of stub noise, the stub efficiency definition is loosened to be only applied to the stub position. A stub position is defined as efficient, if it has an x residual smaller than $d_{\mathrm{cut}}^{\mathrm{DUT}}$. This criterion is illustrated in Figure 6.37a. Analog to the other efficiency definitions, $d_{\mathrm{cut}}^{\mathrm{DUT}}$ is chosen to be 180 µm. This results in the stub position efficiency

$$\epsilon_{\mathrm{stub\ position}} = \frac{n_{\mathrm{efficient\ stub\ positions}}}{n_{\mathrm{ref\ tracks}}} . \tag{6.12}$$

A comparison of the stub efficiency and the stub position efficiency as a function of the emulated p_T is shown in Figure 6.37b. Outside the stub correlation window, a stub position efficiency of approximately 1.7% is observed while the stub efficiency is zero. The events passing the stub position efficiency criterion are investigated by comparing track, cluster and stub information on an event basis to identify the origin of stub noise.

A data set with the DUT rotated to an angle of 30° is chosen for the stub noise analysis. Graphical event displays are used to identify different contributions to the stub noise and to develop sets of conditions to automatically distinguish between the different contributions. The following two event categories have been identified:

1. **Multiple track events:** It is possible that several particle tracks cross the DUT within a time window of less than 25 ns. These tracks can either be two independent electrons from the primary beam crossing the telescope or the second trajectory is a secondary particle created during an interaction of the primary electron with one of the upstream telescope planes. As only tracks with hits in at least five of the telescope layers are reconstructed during the analysis, it strongly depends on the trajectory if tracking information for both tracks are available in the events. However, the DUT shows a distinct cluster distribution for this event category as can be seen in Figure 6.38a. Two neighbouring clusters are detected within both sensor layers with a similar distance between their cluster centers as they are produced by similarly inclined tracks. The stub correlation window of one of the seed sensor clusters is shown as dashed blue rectangle. If the two tracks occur

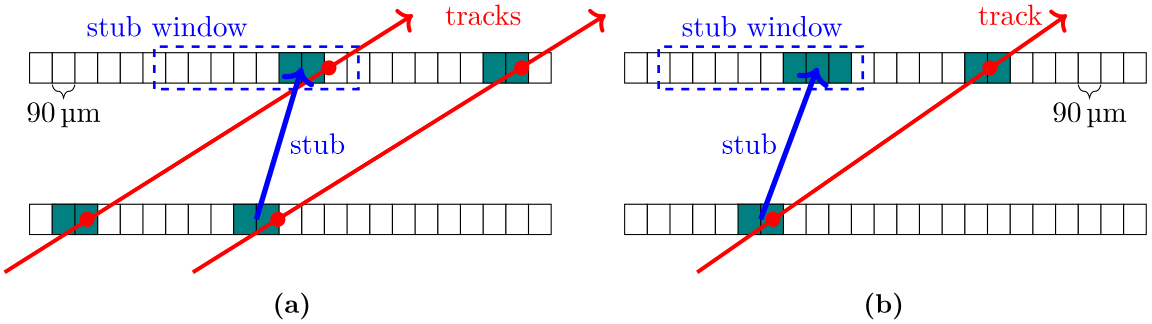

Figure 6.38.: To categorise stub noise events, three event categories are defined based on the observed event displays. (a) Events with two or more parallel tracks crossing the DUT at close distance can create accidental cluster combinations in seed and correlation sensor that allow the detection of a valid stub. (b) When a secondary particle is created by the primary beam electrons when crossing the seed sensor layer, it is possible to create an accidental correlation with a sensor cluster within the correlation window.

Table 6.2.: Comparison of the absolute and relative fractions of event categories creating stub noise.

event category	number of events	relative fraction
multiple tracks	265	64.2%
secondary particles	148	35.8%
total number of stub noise events	413	100%

close to each other, a seed sensor cluster generated by one of the tracks can generate a valid stub together with the cluster created by the second track in the correlation sensor. To identify events belonging to this category, one of the following criteria needs to be fulfilled:

- Events with at least two clusters per sensor with respective cluster center differences of less than three strips are detected.
- Two tracks are reconstructed in close distance with at least one corresponding cluster in the seed sensor and two corresponding clusters in the correlation sensor.

2. **Secondary particle events:** A valid stub can additionally be produced by a secondary particle generated by the primary beam electrons when crossing the seed sensor layer. An exemplary event display is shown in Figure 6.38b. This category is identified during the analysis by searching for events with only one cluster in the seed sensor within an area of ±20 strips around the stub position and with two or more clusters within the correlation window in the correlation sensor.

Table 6.2 compares the absolute and relative fraction of events in the two presented categories. The majority of stub noise events originate from multiple track events. Approximately one third of the events are categorised as secondary particle events.

This non-vanishing stub detection rate outside the correlation window leads to a higher stub rate to be sent out via the available bandwidth to the Level-1 trigger system during CMS operation. As long as the available bandwidth does not get saturated, the two event categories will not influence the transverse momentum discrimination performance within the Level-1 trigger system significantly. The observed signature of multiple track events is only possible to be achieved in the tracker with particles at low transverse momenta. Two different scenarios are possible. In the first scenario, the particle trajectories generate a stub noise event in only one module layer. When reaching the next module layer, the spatial cluster distribution of the trajectories does not fulfill the stub algorithm requirements anymore (e.g. due to slightly different transverse momenta leading to different curvatures). However in the Level-1 trigger algorithm, all tracker module data are combined to perform a curved trajectory regression. Stubs only seen by one module without connection to other trajectory candidates are rejected within the algorithm. In the second scenario, the low transverse momentum particle creates stub noise events within several module layers. However, the generated stubs do not fit to a reasonable trajectory as their respective stub positions are shifted with respect to each other and their bend information does not point towards a physical trajectory. To generate the signature of an event in the secondary particle category, the primary trajectory has to be caused by a particle with low transverse momentum. This implies that also the generated secondary particle has low transverse momentum and will not create additional stubs in the other module layers. Therefore, also this category will not influence the Level-1 trigger decision performance significantly.

If the additional stub data exceed the available bandwidth, it is possible to lose stub information from high transverse momentum particles. Depending on the module position and stub noise data rate, this can have a significant impact on the Level-1 trigger performance. To quantify this influence based on the measurements presented previously is difficult as the observed relative fractions per event category are specific to the beam test setup and beam energy. Thus, a detailed simulation of the tracker and the expected particle rates during the HL-LHC phase is necessary to understand the impact of stub noise onto the operation of the CMS detector. At the time of writing this thesis, such simulation studies have been started.

Summary of Beam Test Studies

To measure the detection efficiencies of hit and stub data streams with 2S modules, beam test setups can be used. Dedicated facilities provide hardware to illuminate particle detectors with a particle beam while measuring the particle trajectories with separate detectors. The results of beam test campaigns with 8CBC3 modules at DESY were presented within this section. Studies have been performed with unirradiated modules and a module assembled with sensors irradiated with protons to a fluence of $4.6 \cdot 10^{14}\,\mathrm{n_{eq}\,cm^{-2}}$.

Before irradiation, cluster efficiencies of 99.9% and stub efficiencies of 99.4% are reached at up to thresholds of $9000\,\mathrm{e^-}$ and at a bias voltage of 300 V. Noise occupancies below 10^{-5} are measured for thresholds above $4500\,\mathrm{e^-}$. Thus, a threshold setting close to $4500\,\mathrm{e^-}$ guarantees efficient detector operation at the start of the HL-LHC phase. The irradiated sensors yield a smaller signal due to radiation damage. Thus, the efficiencies decrease at smaller threshold values compared to the unirradiated sensors. At a threshold of $4500\,\mathrm{e^-}$, the cluster efficiency drops to 99.6% for bias voltages of 600 V and 800 V. The stub efficiency reaches 99.2% and the noise occupancy stays below 10^{-5} at the same module operation conditions. Thus, efficient module operation is guaranteed at the beginning and end of runtime of the HL-LHC phase.

To evaluate the transverse momentum discrimination performance, the 8CBC3 modules are rotated with respect to the particle beam to emulate bent particle trajectories. At low rotation angles, the stub efficiency is constant at its maximum level until the tilt is large enough to generate cluster combinations in top and bottom sensor that do not fulfill the stub logic anymore. A sharp drop of the stub efficiency to zero is observed. For a stub window size of ±4.5 strips, this drop occurs at rotation angles of ±14.5°, which can be translated to a transverse momentum threshold of 1.5 GeV for the 2S module located closest to the interaction point. By comparing the observed position of the drop in the stub turn-on curve with a Monte Carlo simulation based on the expected module geometry, a decrease in the sensor distance between top and bottom sensor relative to the expectation from the 2S module design is observed. In the center of the module, the distance between the centers of the two active sensor areas is reduced by approximately 50 µm compared to the design value for perfectly flat sensors.

Additional investigations are performed to understand the appearance of stubs near reconstructed particle tracks for large rotation angles. This effect is called stub noise and is generated by events with two parallel trajectories crossing the modules at close distance or by secondary particle trajectories. Stub noise can deteriorate the Level-1 trigger performance of the CMS experiment if the additional stub data exceed the available transmission bandwidth. To quantify this, more detailed studies of the CMS tracker and the LHC physics are necessary.

Part III.

Summary and Outlook

7

Summary and Outlook

The *Large Hadron Collider* (LHC) in Geneva, Switzerland, is a particle accelerator operated with protons or heavy ions to study the properties of known particles and search for new physics. In two storage rings, particle beams are accelerated in opposite directions and can be brought to collision at dedicated interaction points along the accelerator ring. For proton-proton collisions, a center-of-mass energy of 14 TeV can be reached at luminosities of more than $2 \cdot 10^{34}\,\mathrm{cm}^{-2}\,\mathrm{s}^{-1}$. In 2029, it is planned to start the operation of the *High-Luminosity LHC* (HL-LHC) at a nominal luminosity of $5 \cdot 10^{14}\,\mathrm{cm}^{-2}\,\mathrm{s}^{-1}$. By exploiting the safety margins of the accelerator and experiment components, luminosities up to $7.5 \cdot 10^{14}\,\mathrm{cm}^{-2}\,\mathrm{s}^{-1}$ can be reached. An increase in luminosity implies higher particle rates for all components to cope with. To ensure efficient data taking during the HL-LHC phase, the accelerator and its experiments needs to be upgraded before 2029.

The *Compact Muon Solenoid* (CMS) experiment is one of the four large experiments at the LHC. The upgrade work in preparation for the HL-LHC is summarized under the name *Phase-2 Upgrade.* Besides others, a completely new silicon tracker will be installed in the CMS experiment before 2029. The new tracker design achieves improved radiation tolerance, increases the density of readout channels in the tracker volume and achieves a better two-track separation. By installing specialised detector modules in the outer part of the tracker, information about the transverse momentum of charged particles is generated that is used in the CMS *Level-1 trigger* system. These modules are called p_T*-modules* and are assembled with two parallel silicon sensors. When a particle crosses a p_T-module, charge is generated in both sensor layers and is read out by a common set of chips. Such cluster combinations in bottom and top sensor are called *stubs.* The CMS magnetic field bends the trajectories of charged particles. High p_T particles follow trajectories with a smaller curvature than low p_T particles. This translates into different spatial displacements of the detected clusters in the two sensor layers depending on the particles' p_T. The readout chips calculate this spatial displacement per cluster combination. Only for displacements below a configurable value, information about the cluster position and spatial displacement is sent to the Level-1 trigger. This corresponds to a selection of particles with transverse momenta above a configurable threshold. Depending on the position of the p_T-modules in the CMS Outer Tracker, two different type of modules are used called *PS modules* and *2S modules.* PS modules are assembled of a macro-pixel sensor sensor and a strip sensor and are positioned closer to the beam line than the 2S modules assembled with two silicon strip sensors. For 2S modules, the readout chip connected to the silicon sensor strips is called *CMS Binary Chip* (CBC). The CBC has implemented the stub logic and provides a binary readout, detecting only signals with pulse heights above a configurable threshold.

The *Institute of Experimental Particle Physics* (ETP) at *Karlsruhe Institute of Technology* is one of the 2S module assembly centers within the CMS community. It is planned to build between 1300 and 2000 of the necessary 7680 2S modules at ETP until 2025. A dedicated module assembly line has to be set up for this module production and dedicated hardware needs to be developed to assemble modules of the highest quality. Within the scope of this thesis, a test station has been constructed to perform functional tests of fully assembled modules at the end of the assembly process. It is called *Outer Tracker* (OT) *Module Test Station* and was produced for all module assembly centers in the CMS community. The station consists of a 1.5 mm thick, commercially available aluminium box which provides a light-tight volume to operate the modules. Additonally, the box shields the modules from external electromagnetic influences. With outer dimensions of 460 mm × 380 mm × 157 mm at maximum, the box offers a compact design to efficiently use the available clean room space at the assembly sites. A mechanical fixture made of electrically conductive polyethylene allows to mount the modules with their respective carriers in the test station. Using lateral spring pushers, the carrier plates are pushed against pins. Thus, the the carrier is fixed at its position without using loose parts like e.g. screws that would increase the risk of damaging the module during handling. The box provides electrical connections for all necessary module voltage levels at its backside. To secure the operator and prevent damaging the modules, the high voltage potential is interrupted by a reed relay inside the box in case the lid is not completely closed. A dry air supply can be connected to the box via a 6 mm tube pass-through to flush the box with dry air. Two manual valves allow to control the dry air flow inside the box at two outlet positions. Thus, the environmental requirements for module operation of reaching a relative humidity below 30% can be realised. The ambient air temperature and the relative humidity level are monitored by a sensor read out by an Arduino board.

For a complete test of the module readout chain, it is necessary to generate charge in the silicon sensors to be read out by the chips. For this purpose, the *Karlsruhe Infrared Array* (KIRA) was produced within this thesis. It provides two LED arrays of eight infrared LEDs each to be placed above and below the sensors of a 2S modules. Each LED can be controlled in its intensity and, thus, a configurable amount of charge can be generated in the modules for functional testing. The LED pulse length can be set to values between 25 ns and more than 5 µs making the KIRA system flexibel for applications beyond the scope of 2S module functional testing during production. The beam spot was measured as a function of the LED intensity, showing that all KIRA LEDs together can illuminate every silicon sensor strip. For functional module testing, a combination of CBC threshold and LED intensity is chosen such that all channels of one CBC detect hit occupancies of one. Defective channels can be identified by monitoring deviations from the expected hit occupancy. Additionally, the time dependency of the pulse shape detected by the CBC channels for different LED intensities was investigated. At large intensity settings, enough charge carriers are created in the silicon sensors to significantly influence the electric field created by the bias voltage. Changes in the bias voltage are detected by the CBCs via dynamic shifts of the channels' signal levels relative to the applied threshold. This leads to the detection of additional hits for channels outside the beam spot until the bias potential has recovered.

The OT Module Test Stations have been shipped together with the KIRA systems to the module assembly and integration centers in January 2022. With its flexibility in choosing different LED intensities and light pulse lengths, the KIRA system will be used for various tests with module prototypes until the start of module production in 2023. It is planned to continue studying the influence of LED pulses at high intensities and varying pulse lengths on the voltage potentials on a 2S sensor. Therefore, a dedicated setup is currently under development at ETP allowing to probe different positions on a silicon sensor with oscilloscopes. The measurement results can help to predict the behaviour of a 2S module in the CMS tracker in case of a highly ionising event following a *beam loss scenario* [Sch+03].

With the arrival of the first 2S module prototype components providing the full optical readout chain in 2019, *8CBC3 modules* have been built to study the combined performance of all module components. A crucial parameter to define the functionality of all readout channels is their noise level. Within this thesis, it was found that the average channel noise depends on the module grounding configuration with respect to the aluminium carrier plate below the module. Only by adding a direct connection between the two frontend hybrids and the carrier plate, a module noise of less than 1000 e^- can be reached, which is compatible with the CBC design specifications. In this configuration, the noise distributions are compatible with the assumption of Gaussian distributed noise and consistent noise levels are observed throughout all assembled 8CBC3 modules at ETP. One of the 8CBC3 modules was assembled with sensors irradiated with protons to a fluence of $4.6 \cdot 10^{14}\,\mathrm{n_{eq}\,cm^{-2}}$. Due to the increased leakage current, it is operated at sensor temperatures of approximately −20°C. No increase in noise is observed compared to unirradiated modules at comparable sensor temperatures.

Based on the noise results of 8CBC3 modules, an additional grounding possibility was introduced into the next version of the service hybrid. Additionally, this service hybrid version houses new DC-DC converter chips and opto-electrical converters. The latest module prototypes using this service hybrid version are called *2S prototypes*. In the scope of this thesis, the noise performance of 2S prototypes was studied as well. Measuring the average channel noise leads to noise levels which are incompatible with the CBC specification mentioned earlier. Several attempts have been performed to reduce the noise by adding various additional grounding connections between module and carrier plate. A minimum module noise of approximately 1100 e^- was achieved. It was found that the noise distributions measured for the channels connected to the bottom sensor show a significant deviation from Gaussian distributed noise. To investigate the origin of this increased noise level, a dedicated module was assembled at ETP to allow invasive changes of the module electronics. Strong evidence was found that the module noise is increased significantly when the DC-DC converter is powered. Additionally, it was shown that a majority of the increased noise couples into the module via the high voltage circuitry biasing the silicon sensors. Adding resistors between the two sensor backplanes in the next service hybrid version will help to mitigate part of the increased module noise.

The noise measurement results presented within this thesis were communicated to the electronics working group at CERN and several changes are added to the next version of frontend and service hybrids. The arrival of the new components at the module assembly sites is expected for beginning of 2023. After assembling the first modules using these components, the presented noise studies need to be repeated to investigate the effect of the design changes onto the module performance.

During HL-LHC operation, the CMS tracker will be cooled to reach sensor temperatures around −20°C. Therefore, the 2S modules need to be able to withstand thermal stress. To investigate the module design, several module prototypes have been subject to thermal cycles within this thesis. Monitoring the channel noise during thermal cycling showed that no damage was introduced to the modules. For module production, it is planned to perform thermal cycles with every module. Therefore, dedicated setups called *burn-in stations* are currently under development to enable automated and unattended thermal cycling of 2S modules. At ETP, it is planned to commission the station within 2022.

Besides characterizing the module noise, it is important to measure the detection efficiencies of the modules' cluster and stub data streams. Therefore, several module prototypes were measured in beam test setups. Within this thesis, unirradiated 8CBC3 modules and the 8CBC3 module assembled with irradiated sensors were investigated. The results allow to compare the module performance at the beginning and end of runtime of the HL-LHC. For both scenarios, cluster efficiencies of more than 99% and stub efficiencies of more than 98% can be reached at CBC thresholds smaller than 5000 e^- and bias voltages of 300 V before irradiation and 600 V after irradiation. At the same time, noise occupancies of at least three orders of magnitudes smaller than the expected channel occupancy due to particle hits for 2S modules in the CMS tracker are observed. This allows to perform efficient data taking throughout the complete HL-LHC phase. The performance of the transverse momentum discrimination logic was investigated by rotating the module assembled with irradiated sensors with respect to the particle beam. The resulting stub turn-on characteristic shows a maximum stub efficiency for small rotation angles. Depending on the size of the chosen stub correlation window, the stub efficiency drops to zero at larger angles. To compare the measurement with the expectation, a Monte Carlo simulation of the particle beam crossing the 2S module is developed. Good agreement is found between simulation and measurement. By geometrical considerations, the rotation angle can be converted into a transverse momentum equivalent assuming a defined module position in the CMS tracker. For this thesis, the 2S module closest to the interaction point was chosen. A relative transverse momentum resolution of eight percent results. Extending the Monte Carlo simulation allows to study the influence of sensor misalignments introduced to the module during assembly onto the p_T discrimination performance. Additionally, the detection of stubs at large module rotation angles called *stub noise* was investigated. It was shown that stub noise is generated by multiple tracks crossing the module at close distance and by secondary particles emerging from the interaction of the primary beam with one of the silicon sensors. As the appearance of these processes strongly depends on the experimental setup, a more detailed CMS detector simulation needs to be envisaged to quantify the influence of stub noise onto the Level-1 trigger performance.

Beam test studies are an important tool to characterize module detection efficiencies and resolutions. With the arrival of the next version of 2S module components, the presented beam test studies will be repeated. Additionally, the performance of 2S modules assembled with irradiated hybrids and sensors is currently investigated and more studies are planned for 2023. These tests lead the way to the start of the Outer Tracker module production between 2023 and 2025. In 2029, it is planned to start data taking in the HL-LHC era.

Part IV.

Appendix

A

Outer Tracker Module Test Station

A.1. The Karlsruhe Infrared Array

A.1.1. Pulse Shape Measurements

When illuminating a 2S module with the LEDs of the KIRA system, the signal generated in the sensors can be large enough to saturate the CBC frontend. This case is shown in Figure A.1. Data is taken with LED 2 of the top KIRA twin board activated and operated at an intensity of 30 000 DAC. The central channels of the beam spot show a saturation at a threshold setting of approximately 160 V_{cth}.

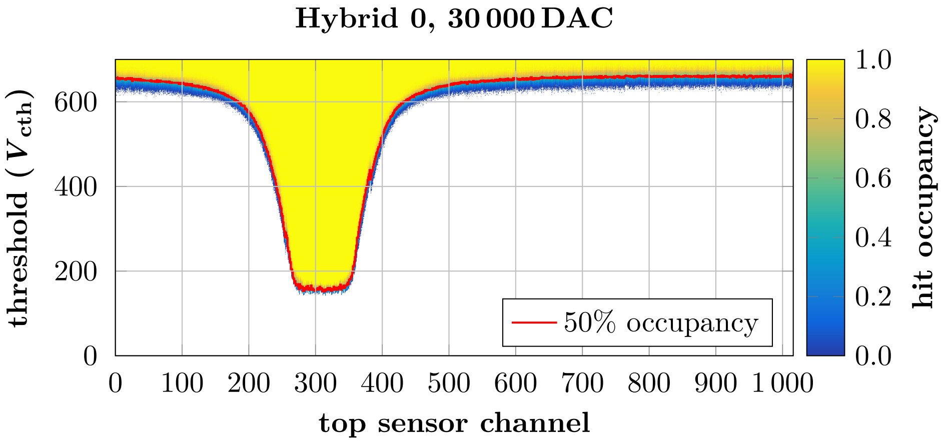

Figure A.1.: Hit occupancy of all top sensor channels on Hybrid 0 as a function of the CBC threshold. The hit latency is set to 91 clock cycles. LED 2 on the top twin board is illuminating with an intensity of 30 000 DAC. The CBC analog frontend saturates for high signals at threshold values of approximately 160 V_{cth}. The thresholds at which each channel reaches an occupancy of 50% are marked in red.

B

Laboratory Based Module Performance Studies

B.1. Noise Studies with 8CBC3 Modules

B.1.1. Skeleton Noise for Top and Bottom Sensor Channels

Figure B.1 displays the channel noise distribution for top and bottom sensor channels of the skeleton of module KIT_8CBC3_2. Due to the foldover in the frontend hybrid design, the capacitive load connected to the bottom sensor channels is larger than for the top sensor channels. Following Equation (4.4), this leads to increased noise levels. The average channel noise of the bottom sensor channels is approximately 0.3 V_{cth} larger compared to the top sensor channels.

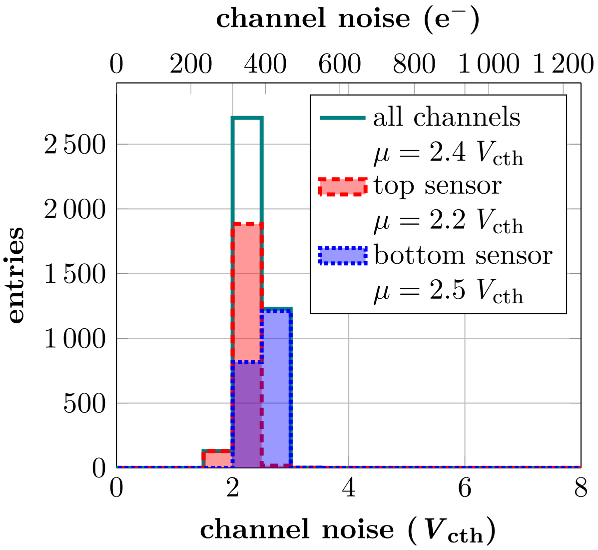

Figure B.1.: Channel noise distribution for top and bottom sensor channels of the KIT_8CBC3_2 module skeleton. Due to the hybrid foldover the bottom sensor channels show increased noise levels of approximately 0.3 V_{cth} compared to the top sensor channels.

B.1.2. Event Display of Noise Events

To understand the noise contributions of an 8CBC3 module prototype, an event display can be generated from the data gathered during a noise occupancy scan. The spatial hit distribution as a function of the event number is shown in Figure B.2. The distribution of hits within the events is mostly uniform except for a few events showing a horizontal accumulation of hits. During these events, several channels detect a hit. This events are generated by *common mode noise*. Compared to the results presented for 2S prototypes in Section 6.2.3, the common mode noise contributions are minimal.

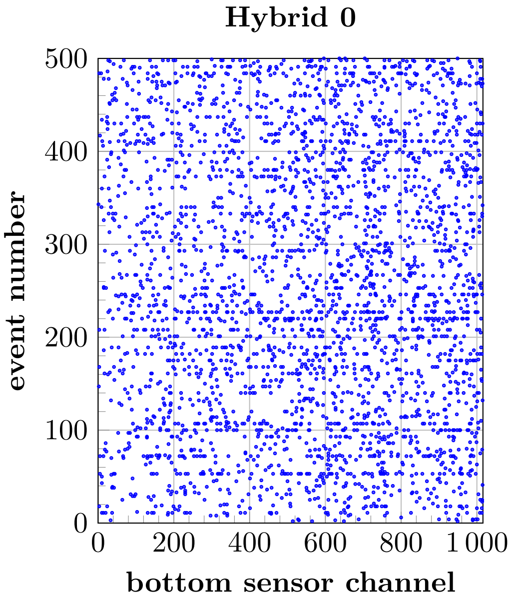

Figure B.2.: Spatial distribution of noise hits for an 8CBC3 module as a function of the event number. Only a minimal contribution from common mode noise events to the overall noise can be observed. Data are taken at a bias voltage of 300 V and a relative threshold of 2.5 times the average channel noise.

B.2. Noise Studies with 2S Prototypes

B.2.1. Channel Noise of all 1.8 mm 2S Prototypes at ETP

To compare the average channel noise of all 2S prototypes built at ETP, noise histograms are filled for each module. The resulting distributions are shown in Figure B.3. The average noise is calculated to $(1112 \pm 53)\,\mathrm{e}^-$. While the statistical uncertainty is comparable to the spread observed among 8CBC3 modules, the average noise level of 2S prototypes is increased by approximately $150\,\mathrm{e}^-$.

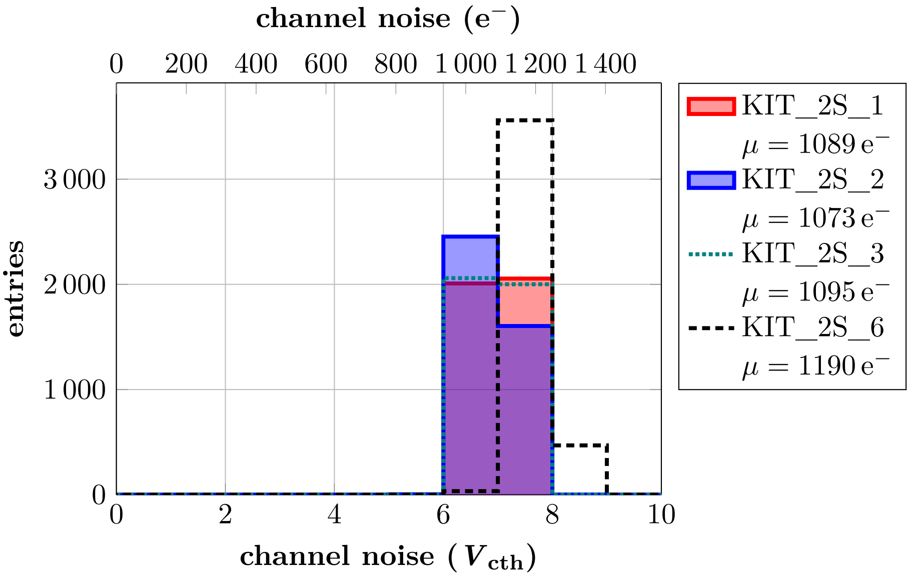

Figure B.3.: Channel noise distributions of all 1.8 mm 2S prototypes built at ETP. The top x axis shows the channel noise in electron equivalent. Data are taken at a bias voltage of 300 V and with $N_{\mathrm{events}} = 100$.

B.2.2. Investigation of CBC Gain Increase Hypothesis

The average channel noise measured for 2S prototypes is approximately 16% larger than the one of 8CBC3 modules. One hypothesis to explain this noise increase is an increased CBC gain in the signal readout chain. To check this hypothesis, a ^{90}Sr source is placed above an 8CBC3 module and a 2S prototype and threshold scans are performed. A scintillator placed below the modules is used to generate a trigger signal for the module readout. As the radioactive source is emitting electrons at random times, particle crossings through the module happen asynchronous to the module's operation clock. Therefore, the detection efficiencies varies with the time difference of signal sampling and particle arrival time. More detailed information can be found in Section 6.3.4. To compensate for this effect, only the most efficient TDC phase is taken into account during the analysis. Additionally, the *cluster occupancy* η_{cl} is shown, which is defined as

$$\eta_{cl} = \frac{\text{number of clusters per triggered event}}{\text{number of triggered events}} \ . \tag{B.1}$$

The resulting data sets for an 8CBC3 module and a 2S prototype are shown in Figure B.4 in blue and red, respectively. For comparison, the expected data set of an 8CBC3 module with a gain increased by 16% is shown in green. The measured distribution for the 2S prototype is compatible with the one from 8CBC3 modules. Therefore, the hypothesis of an increased CBC gain as an explanation for the increased noise level of 2S protoytpe can be ruled out.

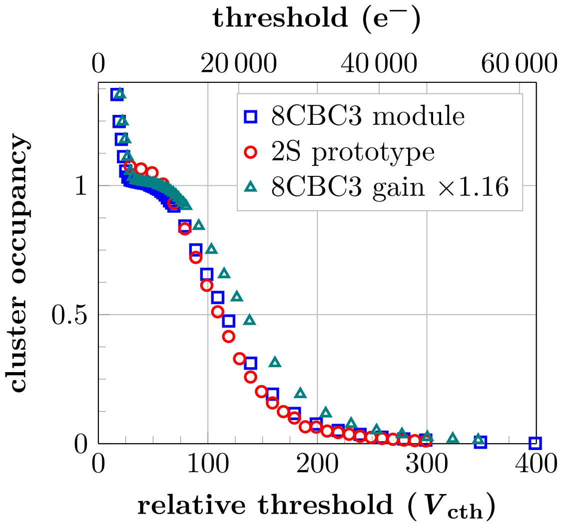

Figure B.4.: Signal spectrum of a ^{90}Sr source for an 8CBC3 module and a 2S prototype in blue and red, respectively. The 8CBC3 module data set is scaled by the factor 1.16 and displayed in green.

B.3. Thermal Resilience Tests

The 2S prototypes are tested for their resilience against thermal stress to spot potential design weaknesses before integrating modules into the CMS tracker. The KIT_2S_3 module is tested in the Cooled 2S Module Readout Station with thermal cycles performed between 20°C and −20°C silicon sensor temperature. In total, 20 thermal cycles are performed. The channel noise is measured before starting the thermal cycles and remeasured after finishing all 20 cycles. The resulting noise distributions are shown in Figure B.5. No significant change of the channel noise characteristics can be observed. Therefore, no damage is done to the module during thermal cycling.

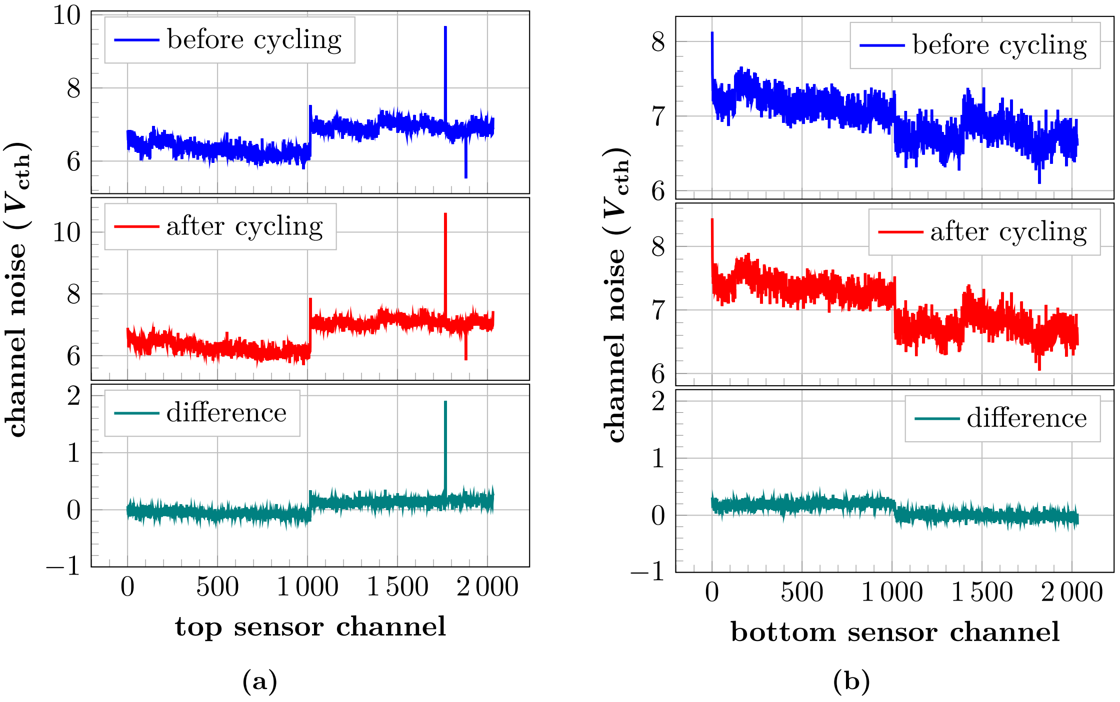

(a) **(b)**

Figure B.5.: Channel noise characteristic of module KIT_2S_3 before and after 20 thermal cycles. No significant change of the channel noise characteristics can be observed for the top sensor channels shown in (a) and the bottom sensor channels displayed in (b). The measurements are performed at a bias voltage of 300 V.

C
Beam Tests

C.1. Performance of Transverse Momentum Discrimination

C.1.1. Energy Deposition of Beam Test Electrons in Silicon

During the beam tests presented within this thesis, an electron beam with energies between 4 GeV and 6 GeV are used. The energy deposition of electrons at these energies is simulated using the software framework *Allpix*^{2} [Spa+18]. For the simulation, one 2S sensor is approximated as 290 µm thick, fully depleted silicon volume with strip implants on its top side. The volume is placed in vacuum and a particle beam with perpendicular incidence onto the sensor surface is simulated. The raw sensor signal is digitized at the strip implants. No threshold is applied to the strip signal during simulation of the readout electronics. Additionally, no electronic noise is added to the signal. The simulated cluster charge distribution for a particle beam with electrons at an energy of 6 GeV and a beam with muons at an energy of 100 GeV is shown in Figure C.1. Both distributions coincide well and yield a maximum at approximately 22 000 e^-. The configuration files used to perform the simulation are given in Listing C.1, Listing C.2 and Listing C.3.

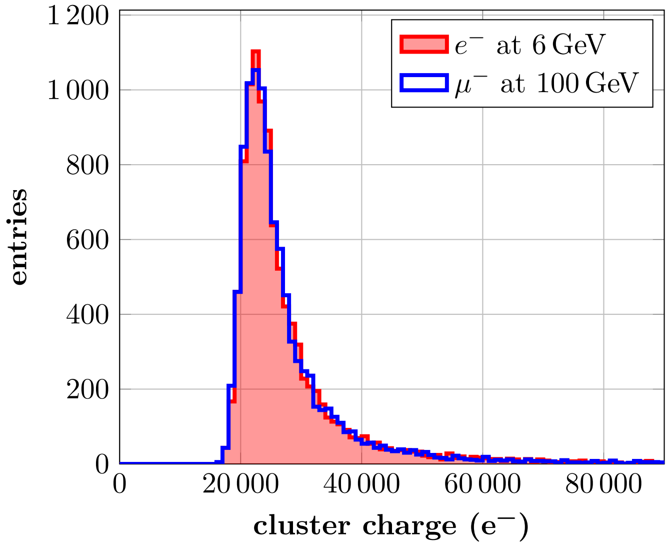

Figure C.1.: Simulated cluster signal produced in a 290 µm thick 2S sensor. Simulations are performed within the *Allpix*^{2} framework.

Listing C.1: Main configuration file for the *Allpix*^{2} simulations.

```
[Allpix]
log_level = "INFO"
log_format = "DEFAULT"
detectors_file = "2Smodule_detector.conf"
number_of_events = 5000

[GeometryBuilderGeant4]
world_material = "vacuum"

[DepositionGeant4]
physics_list = FTFP_BERT_LIV
particle_type = "e-"
source_energy = 6GeV
source_position = 0um 0um -500um
source_type = "beam"
beam_size = 2mm
beam_direction = 0 0 1
number_of_particles = 1
max_step_length = 1um
output_plots = true

[ElectricFieldReader]
model = "linear"
bias_voltage = -300V
depletion_voltage = -280V
output_plots = true

[GenericPropagation]
temperature = 293K
charge_per_step = 10
output_plots = true

[PulseTransfer]
max_depth_distance = 5um

[DefaultDigitizer]
electronicnoise = 0e
threshold = 0e
threshold_smearing = 0e

[DetectorHistogrammer]
name = "detector1"
max_cluster_charge = 500ke

[ROOTObjectWriter]
```

Listing C.2: Geometry file for the *Allpix*^{2} simulations.

```
[detector1]
type = "2Ssensor"
position = 0 0 0
orientation = 0 0 0
```

Listing C.3: 2S sensor definition within the *Allpix*^{2} simulations.

```
type = "monolithic"
number_of_pixels = 1016 2
pixel_size = 90um 50mm
sensor_thickness = 290um
```

C.1.2. 2S Module Sensor Distance Analysis

The distance between the two 2S sensors in the 8CBC3 modules built at ETP is measured with an optical microscope as described in Section 6.3.7. For all modules, a significant decrease of the sensor distance (called *bow*) can be measured in the center of the module. The uncertainty of each measurement point is estimated to be ±10 µm. Thus, the observed trend to smaller sensor distances with increasing module identification number is not significant.

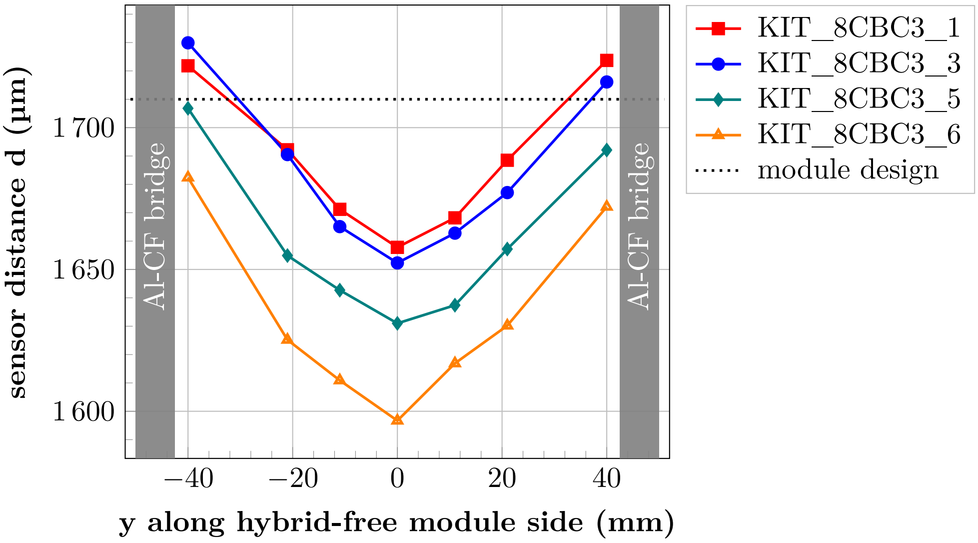

Figure C.2.: The sensor distance is measured along the hybrid-free module side with an optical microscope. All 8CBC3 modules show a significant decrease of the sensor distance towards the center of the module. Each data point carries an uncertainty of ±10 µm.

List of Figures

List of Tables

Bibliography

[Ada+20] W. Adam et al. *Experimental study of different silicon sensor options for the upgrade of the CMS Outer Tracker.* In: Journal of Instrumentation 15.04 (Apr. 2020), P04017. DOI: `10.1088/1748-0221/15/04/p04017` (cited on p. 15).

[Ada+21a] W. Adam et al. *Selection of the silicon sensor thickness for the Phase-2 upgrade of the CMS Outer Tracker.* In: Journal of Instrumentation 16.11 (Nov. 2021), P11028. DOI: `10.1088/1748-0221/16/11/p11028` (cited on p. 15).

[Ada+21b] W. Adam et al. *The CMS Phase-1 pixel detector upgrade.* In: Journal of Instrumentation 16.02 (Feb. 2021), P02027–P02027. DOI: `10.1088/1748-0221/16/02/p02027` (cited on p. 96).

[Aga+04] M. Agari et al. *Beetle — a radiation hard readout chip for the LHCb experiment.* In: Nuclear Instruments and Methods in Physics Research Section A: Accelerators, Spectrometers, Detectors and Associated Equipment 518.1 (2004), pp. 468–469. ISSN: 0168-9002. DOI: `https://doi.org/10.1016/j.nima.2003.11.058` (cited on p. 107).

[Ana13] Analog Devices. *AD5272 - 1024-Position, 1% Resistor Tolerance Error, I^2C Interface and 50-TP Memory Digital Rheostat.* 2013. URL: `https://www.analog.com/media/en/technical-documentation/data-sheets/AD5272_5274.pdf` (cited on p. 47).

[Ana18] Analog Devices. *Octal, 16-Bit nanoDAC+ with 2 ppm/° C Reference, I^2C Interface.* 2018. URL: `https://www.analog.com/media/en/technical-documentation/data-sheets/ad5671r_5675r.pdf` (cited on p. 48).

[Apl+12] S. Aplin et al. *LCIO: A persistency framework and event data model for HEP.* In: *2012 IEEE Nuclear Science Symposium and Medical Imaging Conference Record (NSS/MIC).* 2012, pp. 2075–2079. DOI: `10.1109/NSSMIC.2012.6551478` (cited on p. 96).

[Apo+17] G. Apollinari et al. *High-Luminosity Large Hadron Collider (HL-LHC): Technical Design Report V. 0.1.* Geneva, 2017. DOI: `10.23731/CYRM-2017-004` (cited on pp. 3, 11).

[Arn+06] L. Arnaudon et al. *Linac4 Technical Design Report.* Tech. rep. CERN-AB-2006-084. CARE-Note-2006-022-HIPPI. revised version submitted on 2006-12-14 09:00:40. Geneva: CERN, Dec. 2006. URL: `https://cds.cern.ch/record/1004186` (cited on p. 5).

[Bai+07] G. Baiatian et al. *Design, Performance, and Calibration of CMS Hadron-Barrel Calorimeter Wedges.* Tech. rep. CMS-NOTE-2006-138. 1. Geneva: CERN, May 2007. DOI: `10.1140/epjc/s10052-008-0573-y` (cited on p. 9).

[Bar10] M. Barbero. *FE-I4 chip design.* In: PoS VERTEX 2009 (2010), p. 027. DOI: `10.22323/1.095.0027` (cited on p. 96).

[Bau+09] J. Baudot et al. *First test results Of MIMOSA-26, a fast CMOS sensor with integrated zero suppression and digitized output.* In: *2009 IEEE Nuclear Science Symposium Conference Record (NSS/MIC).* 2009, pp. 1169–1173. DOI: `10.1109/NSSMIC.2009.5402399` (cited on p. 95).

[Ben+04] M. Benedikt et al. *LHC Design Report.* CERN Yellow Reports: Monographs. Geneva: CERN, 2004. DOI: `10.5170/CERN-2004-003-V-3` (cited on p. 5).

[Ber+19] G. Bergamin et al. *CIC2 Technical Specification*. Sept. 30, 2019. URL: `https://espace.cern.ch/Tracker-Upgrade/Electronics/CIC/Shared%20Documents/Specifications/CIC2_specs_v1p0.pdf` (cited on pp. 19, 21).

[Bet22] Beta LAYOUT GmbH. *PCB-Pool*. 2022. URL: `https://de.beta-layout.com` (cited on p. 49).

[Bis+20] T. Bisanz et al. *EUTelescope: A modular reconstruction framework for beam telescope data*. In: Journal of Instrumentation 15.09 (Sept. 2020), P09020–P09020. ISSN: 1748-0221. DOI: `10.1088/1748-0221/15/09/p09020` (cited on pp. 96, 98).

[Blo22] V. Blobel. *Millepede II - Draft Manual*. Jan. 2022. URL: `https://www.desy.de/~kleinwrt/MP2/doc/html/draftman_page.html` (cited on p. 99).

[Bol+03] G. Bolla et al. *Wire-bonds failures induced by resonant vibrations in the CDF silicon detector*. In: *2003 IEEE Nuclear Science Symposium. Conference Record (IEEE Cat. No.03CH37515)*. Vol. 3. 2003, 1641–1645 Vol.3. DOI: `10.1109/NSSMIC.2003.1352193` (cited on p. 40).

[BR96] R. Brun and F. Rademakers. *ROOT - An Object Oriented Data Analysis Framework*. In: *AIHENP'96 Workshop, Lausane*. Vol. 389. 1996, pp. 81–86 (cited on p. 96).

[Bra20] J. Braach. *Functional Tests of 2S Detector Modules for the CMS Phase 2 Outer Tracker Upgrade including the Development of an IR LED Array*. MA thesis. Karlsruhe Institute of Technology (KIT), 2020 (cited on pp. 46–50, 52, 74, 75).

[BW21] E. van der Bij and T. Wlostowski. *fmc-dio-5chttla FMC 5-channel Digital I/O module*. 2021. URL: `https://ohwr.org/project/fmc-dio-5chttla/wikis/home` (cited on p. 50).

[CER16] CERN. *FEASTMP Radiation and magnetic field tolerant 10W DC/DC converter module*. 2016. URL: `https://espace.cern.ch/project-DCDC-new/Shared%20Documents/FEAST2Mod_Datasheet_gb2016.pdf` (cited on p. 21).

[CER21] CERN. *bPOL2V5_V3.3 Radiation tolerant Synchronous Step-Down Buck DC/DC converter*. 2021. URL: `https://espace.cern.ch/project-DCDC-new/Shared%20Documents/bPOL2V5_V3.3%20datasheet%20rev1.pdf` (cited on p. 22).

[CER22a] CERN. *bPOL12V_V6 Radiation tolerant 10W Synchronous Step-Down Buck DC/DC converter*. 2022. URL: `https://espace.cern.ch/project-DCDC-new/Shared%20Documents/bPOL12V_V6%20datasheet%20V1.1.pdf` (cited on p. 22).

[CER22b] CERN. *The HL-LHC project*. Feb. 2022. URL: `https://hilumilhc.web.cern.ch/content/hl-lhc-project` (cited on p. 12).

[CG13] J. Chistiansen and M. Garcia-Sciveres. *RD Collaboration Proposal: Development of pixel readout integrated circuits for extreme rate and radiation*. Tech. rep. Geneva: CERN, June 2013. URL: `http://cds.cern.ch/record/1553467` (cited on p. 12).

[Chi13] A. Chilingarov. *Generation current temperature scaling*. Tech. rep. Lancaster University, UK, Jan. 30, 2013. URL: `https://cds.cern.ch/record/1511886` (cited on p. 29).

[CMS00] CMS. *CMS TriDAS project: Technical Design Report, Volume 1: The Trigger Systems*. Technical Design Report CMS. 2000. URL: `https://cds.cern.ch/record/706847` (cited on p. 10).

[CMS08] CMS Collaboration. *The CMS experiment at the CERN LHC*. In: Journal of Instrumentation 3.08 (Aug. 14, 2008), S08004–S08004. DOI: `10.1088/1748-0221/3/08/S08004` (cited on pp. 8, 9).

[CMS12] CMS Collaboration. *CMS Technical Design Report for the Pixel Detector Upgrade.* Tech. rep. CERN-LHCC-2012-016. CMS-TDR-11. CERN, Sept. 2012. URL: `https://cds.cern.ch/record/1481838` (cited on pp. 8, 9).

[CMS17a] CMS Collaboration. *Particle-flow reconstruction and global event description with the CMS detector.* In: Journal of Instrumentation 12.10 (Oct. 2017), P10003–P10003. DOI: `10.1088/1748-0221/12/10/P10003` (cited on p. 9).

[CMS17b] CMS Collaboration. *Public CMS Luminosity Information.* Dec. 4, 2017. URL: `https://twiki.cern.ch/twiki/bin/view/CMSPublic/LumiPublicResults` (cited on p. 7).

[CMS17c] CMS Collaboration. *The Phase-2 Upgrade of the CMS Tracker.* Tech. rep. CERN-LHCC-2017-009. CMS-TDR-014. Geneva: CERN, June 2017. URL: `https://cds.cern.ch/record/2272264` (cited on pp. 4, 12–19, 29, 86, 88, 108).

[CMS21a] CMS Collaboration. *Selection of the silicon sensor thickness for the Phase-2 upgrade of the CMS Outer Tracker.* In: (Sept. 2021). URL: `https://cms.cern.ch/iCMS/user/noteinfo?cmsnoteid=CMS%20NOTE-2021/008` (cited on p. 14).

[CMS21b] CMS Outer Tracker Module Working Group. *Freezing of PS and 2S Module Carriers.* Mar. 2021. URL: `https://indico.cern.ch/event/991718/#4-freezing-of-ps-and-2s-module` (cited on p. 42).

[CMS22] CMS. *CMS Tracker Phase-2 Acquisition & Control Framework.* 2022. URL: `https://gitlab.cern.ch/cms%5C_tk%5C_ph2/Ph2%5C_ACF/` (cited on p. 22).

[CMS97a] CMS. *The CMS hadron calorimeter project: Technical Design Report.* Technical Design Report CMS. Geneva: CERN, 1997. URL: `https://cds.cern.ch/record/357153` (cited on p. 9).

[CMS97b] CMS Collaboration. *The CMS electromagnetic calorimeter project: Technical Design Report.* Technical Design Report CMS. Geneva: CERN, 1997. URL: `http://cds.cern.ch/record/349375` (cited on p. 9).

[Die+19] R. Diener et al. *The DESY II test beam facility.* In: Nuclear Instruments and Methods in Physics Research Section A: Accelerators, Spectrometers, Detectors and Associated Equipment 922 (2019), pp. 265–286. ISSN: 0168-9002. DOI: `https://doi.org/10.1016/j.nima.2018.11.133` (cited on p. 95).

[Dro21] A. Droll. *Performance Studies on 2S Module Prototypes for the Phase-2 Upgrade of the CMS Outer Tracker.* PhD thesis. Karlsruhe Institute of Technology (KIT), 2021 (cited on pp. 26, 76).

[EB08] L. Evans and P. Bryant. *LHC Machine.* In: Journal of Instrumentation 3.08 (2008), S08001–S08001. DOI: `10.1088/1748-0221/3/08/s08001` (cited on pp. 5, 7).

[Fel+18] L. Feld et al. *Service Hybrids for the Silicon Strip Modules of the CMS Phase-2 Outer Tracker Upgrade.* Tech. rep. Geneva: CERN, Oct. 2018. DOI: `10.22323/1.343.0127` (cited on p. 21).

[Fis20] R. Fischer. *Bestrahlungstests an Siliziumstreifensensoren für das Phase-2-Upgrade des CMS-Spurdetektors.* BA thesis. Karlsruhe Institute of Technology (KIT), 2020 (cited on pp. 107, 108).

[Fle+21] I. Fleck et al., eds. *Handbook of Particle Detection and Imaging.* 2nd ed. 2021. Springer eBook Collection. Cham: Springer International Publishing, 2021. ISBN: 9783319937854. URL: `https://doi.org/10.1007/978-3-319-93785-4` (cited on p. 28).

[Gad+18] T. Gadek et al. *Front-end hybrids for the strip-strip modules of the CMS Outer Tracker Upgrade*. Tech. rep. Geneva: CERN, Oct. 2018. DOI: `10.22323/1.343.0019` (cited on p. 17).

[Gre08] M. A. Green. *Self-consistent optical parameters of intrinsic silicon at 300K including temperature coefficients*. In: Solar Energy Materials and Solar Cells 92.11 (2008), pp. 1305–1310. ISSN: 0927-0248. DOI: `https://doi.org/10.1016/j.solmat.2008.06.009` (cited on p. 28).

[Har17] F. Hartmann. *Evolution of Silicon Sensor Technology in Particle Physics*. 2nd ed. Springer, Nov. 3, 2017. ISBN: 978-3-319-64434-9. DOI: `10.1007/978-3-319-64436-3` (cited on pp. 29–31, 118).

[HM06] W. Herr and B. Muratori. *Concept of luminosity*. In: (2006). DOI: `10.5170/CERN-2006-002.361` (cited on p. 7).

[iC-19] iC-Haus. *iC-HG30 6A Laser Switch*. 2019. URL: `https://www.ichaus.de/upload/pdf/HG30_datasheet_B1en.pdf` (cited on pp. 48, 62).

[Inc22] T. T. Inc. *TIA-950 O/E Converter*. 2022. URL: `https://hep.ph.liv.ac.uk/twiki/pub/CleanroomTestStands/SetupTCT/TIA950Manualforscreen.pdf` (cited on p. 50).

[Jan+16] H. Jansen et al. *Performance of the EUDET-type beam telescopes*. In: EPJ Techniques and Instrumentation 3.1 (Oct. 2016). ISSN: 2195-7045. DOI: `10.1140/epjti/s40485-016-0033-2` (cited on p. 96).

[Kam22] Kambic d.o.o. *Climatic Chamber KK-190 CHLT*. 2022. URL: `https://www.keyence.de/products/microscope/digital-microscope/vhx-6000/index%5C_pr.jsp` (cited on p. 69).

[Key22] Keyence Deutschland GmbH. *Digitalmikroskop Modellreihe VHX-6000*. 2022. URL: `https://www.keyence.de/products/microscope/digital-microscope/vhx-6000/index%5C_pr.jsp` (cited on p. 119).

[Kha+17] V. Khachatryan et al. *The CMS trigger system*. In: Journal of Instrumentation 12.01 (Jan. 2017), P01020–P01020. DOI: `10.1088/1748-0221/12/01/p01020` (cited on p. 10).

[Kle12] C. Kleinwort. *General broken lines as advanced track fitting method*. In: Nuclear Instruments and Methods in Physics Research Section A: Accelerators, Spectrometers, Detectors and Associated Equipment 673 (May 2012), pp. 107–110. DOI: `10.1016/j.nima.2012.01.024` (cited on p. 99).

[Kop+21] R. Koppenhöfer et al. *Beam test results of silicon sensor module prototypes for the Phase-2 Upgrade of the CMS Outer Tracker*. In: Journal of Instrumentation 16.12 (Dec. 2021), p. C12033. DOI: `10.1088/1748-0221/16/12/c12033` (cited on p. 95).

[Kop18] R. Koppenhöfer. *Conception and validation of test stations to electrically qualify silicon strip modules for the CMS Phase II Upgrade*. MA thesis. Karlsruhe Institute of Technology (KIT), 2018 (cited on p. 69).

[Lay97] J. G. Layter. *The CMS muon project: Technical Design Report*. Technical Design Report CMS. Geneva: CERN, 1997. URL: `https://cds.cern.ch/record/343814` (cited on p. 9).

[Lec18] A. Lechner. *Particle interactions with matter*. In: CERN Yellow Rep. School Proc. 5 (2018), 47. 22 p. DOI: `10.23730/CYRSP-2018-005.47` (cited on p. 27).

[Liu+19] Y. Liu et al. *EUDAQ2—A flexible data acquisition software framework for common test beams.* In: Journal of Instrumentation 14.10 (Oct. 2019), P10033–P10033. DOI: `10.1088/1748-0221/14/10/p10033` (cited on p. 96).

[lpG21] lpGBT Team. *lpGBT Manual.* 2021. URL: `https://lpgbt.web.cern.ch/lpgbt/v0/` (cited on p. 22).

[Lut07] G. Lutz. *Semiconductor Radiation Detectors.* ISBN: 978-3-540-71678-5 (Print) 978-3-540-71679-2 (Online). Springer, 2007. DOI: `10.1007/978-3-540-71679-2` (cited on pp. 31–33).

[Mai19] S. Maier. *Assembly and qualification procedures of 2S modules and high rate tests of the CMS Binary Chip for the Phase 2 Upgrade of the CMS Outer Tracker.* PhD thesis. Karlsruhe Institute of Technology (KIT), 2019 (cited on pp. 24, 38, 39, 55, 59, 118).

[Mar+07] R. Marco-Hernández et al. *Alibava : A portable readout system for silicon microstrip sensors.* In: (2007), 5 p. DOI: `10.5170/CERN-2007-001.412` (cited on pp. 107, 108).

[MCW21] P. Moreira, J. Christiansen, and K. Wyllie. *GBTX Manual V0.19.* 2021. URL: `https://espace.cern.ch/GBT-Project/GBTX/Manuals/gbtxManual.pdf` (cited on p. 21).

[Mob19] E. Mobs. *The CERN accelerator complex - 2019. Complexe des accélérateurs du CERN - 2019.* General Photo. July 2019. URL: `https://cds.cern.ch/record/2684277` (cited on p. 6).

[Mol22] Molex Electronic Solutions. *Micro-Fit 3.0 Receptacle Housing, Dual Row, 6 Circuits, UL 94V-0, Low-Halogen, Black.* 2022. URL: `https://www.molex.com/molex/products/part-detail/crimp_housings/0430250600` (cited on p. 42).

[Mol99] M. Moll. *Radiation Damage in Silicon Particle Detectors.* PhD thesis. University of Hamburg, 1999. URL: `https://mmoll.web.cern.ch/mmoll/thesis/` (cited on pp. 32, 33).

[Nod+18] B. Nodari et al. *A 65 nm Data Concentration ASIC for the CMS Outer Tracker Detector Upgrade at HL-LHC.* Tech. rep. Geneva: CERN, Oct. 2018. DOI: `1747420` (cited on p. 19).

[Ola+20] L. Olantera et al. *Versatile Link+ Transceiver Production Readiness.* In: PoS TWEPP2019 (2020), p. 055. DOI: `10.22323/1.370.0055` (cited on pp. 22, 81).

[OSR21] OSRAM Opto Semiconductors. *SFH 4180S OSLON P1616 High Power Infrared Emitter (960 nm).* Oct. 2021. URL: `https://dammedia.osram.info/media/resource/hires/osram-dam-9174003/SFH%204180S_EN.pdf` (cited on p. 48).

[Pit22] M. Pittermann. *Increased 2S prototype noise due to LC circuit of silicon sensor biasing circuitry.* Personal communication. May 2022 (cited on p. 90).

[Pra17] C. Pralavorio. *Record luminosity: well done LHC.* In: (Nov. 2017). URL: `http://cds.cern.ch/record/2295027` (cited on pp. 3, 7).

[Pry19] M. Prydderch. *CBC3.1 User Manual.* July 18, 2019. URL: `http://www.hep.ph.ic.ac.uk/ASIC/cbc3.1/CBC3p1_User_Manual_V1p4.pdf` (cited on pp. 19–21, 59, 71).

[PU22] M. Prydderch and K. Uchida. *I^2C bug of CBC3.1.* Personal communication. 2022 (cited on p. 93).

[PV15] M. Pesaresi and P. Vichoudis. *FC7 User Manual*. Nov. 12, 2015. URL: `https://espace.cern.ch/project-FC7/Documents/fc7_user_manual.pdf` (cited on p. 22).

[Ros03] L. Rossi. *The LHC superconducting magnets*. In: Conf. Proc. C 030512 (2003), p. 141 (cited on p. 7).

[Sak19] T. Sakuma. *Cutaway diagrams of CMS detector*. In: (May 2019). URL: `https://cds.cern.ch/record/2665537` (cited on p. 8).

[Sch+03] R. Schmidt et al. *Beam Loss Scenarios and Strategies for Machine Protection at the LHC*. In: 693 (Dec. 2003). DOI: `10.1063/1.1638351` (cited on pp. 61, 134).

[Sil16] Silicon Laboratories. *Si7021-A20 I^2C Humidity and Temperature Sensor*. 2016. URL: `https://www.silabs.com/documents/public/data-sheets/Si7021-A20.pdf` (cited on p. 44).

[Spa+18] S. Spannagel et al. *Allpix2: A modular simulation framework for silicon detectors*. In: Nuclear Instruments and Methods in Physics Research Section A: Accelerators, Spectrometers, Detectors and Associated Equipment 901 (2018), pp. 164–172. ISSN: 0168-9002. DOI: `https://doi.org/10.1016/j.nima.2018.06.020` (cited on p. 147).

[Tek03] Tektronix, INC. *2410 and 2410-C SourceMeter Specifications*. 2003. URL: `https://download.tek.com/document/2410RevD_DocSpec.pdf` (cited on p. 57).

[Uch+18] K. Uchida et al. *The CBC3 readout ASIC for CMS 2S-modules*. Tech. rep. Geneva: CERN, Jan. 2018. URL: `https://cds.cern.ch/record/2312215` (cited on p. 17).

[Vas+17] F. Vasey et al. *The Versatile Link Application Note*. Jan. 6, 2017. URL: `https://espace.cern.ch/project-versatile-link/public/Versatile%20Link%20Public%20Documents/Application%20Note/Versatile%20Link%20Application%20Note%20v2.7.pdf` (cited on p. 21).

[Wil04] J. Williams. *Signal Sources, Conditioners and Power Circuitry*. 2004. URL: `https://www.analog.com/media/en/technical-documentation/application-notes/an98f.pdf` (cited on p. 47).

[Zyl+20] P. A. Zyla et al. *Review of Particle Physics, 2020-2021. RPP*. In: PTEP 2020 (2020), 083C01. 2093 p. DOI: `10.1093/ptep/ptaa104` (cited on pp. 25–27).

Acknowledgments — Danksagung

Finally, I want to express my greatest thanks to all the people that helped and supported me during my scientific work in the last years that led to this thesis. Abschließend möchte ich mich bei allen bedanken, die mich in den letzten Jahren auf meinem wissenschaftlichen Weg begleitet und unterstützt haben und dadurch das Erstellen dieser Arbeit ermöglicht haben.

Herrn Prof. Dr. Ulrich Husemann danke ich für die Möglichkeit eine Promotion am Institut für Experimentelle Teilchenphysik durchzuführen. Von seiner Unterstützung meiner Forschungsprojekte habe ich stark profitiert und seine stets kompetente und schnelle Hilfe hat maßgeblich zum Gelingen dieser Arbeit beigetragen.
Herrn Prof. Dr. Thomas Müller danke ich für seine Unterstützung in den letzten Jahren und für die Übernahme des Korreferats.

Bei Herr Dr. Alexander Dierlamm bedanke ich mich für die ausgezeichnete Betreuung in den letzten Jahren, insbesondere für zahlreiche gewinnbringende Diskussionen über Messaufbauten und -ergebnissen, für ausgezeichnete Vorschläge zur Verbesserung von Präsentationen, sowie für das gewissenhafte Korrekturlesen dieser Arbeit.

Herrn Dr. Stefan Maier und Herrn Dr. Andreas Nürnberg danke ich für die zahlreichen und fruchtbaren Diskussionen über meine Projekte und das Korrekturlesen dieser Arbeit.

Tobias Barvich und Marius Neufeld haben maßgeblichen Anteil am Gelingen dieser Arbeit durch ihre stets zuverlässige, schnelle und geduldige Unterstützung bei mechanischen Konstruktionen und Problemen. Für die zuverlässige Umsetzung elektronischer Schaltungen bedanke ich mich herzlich bei Bernd Berger, Gani Kösker, Julian Stanulla und Pia Steck. Durch eure tatkräftige Unterstützung war es möglich, die Module Test Box Produktion zu einem Erfolg zu bringen. Vielen Dank dafür!
Außerdem gilt mein Dank allen Mitgliedern der mechanischen Werkstatt des ETP für die Fertigung vieler Teile für meine Forschungsprojekte.

Die für die Auslese der Siliziumsensoren nötigen Wire-Bond Verbindungen haben Pia Steck und Dr. Hans Jürgen Simonis stets formvollendet aufgebracht, wofür ich ihnen herzlich danke.

Peichen Chen, Brigitte Gering und Diana Fellner danke ich für die immer kompetente Hilfe bei administrativen Angelegenheiten.

Ich möchte mich bei allen aktuellen und ehemaligen Mitgliedern der CMS-Hardware Abteilung des Instituts für Experimentelle Teilchenphysik bedanken, insbesondere bei Marta Baselga Bacardit, Justus Braach, Alexander Droll, Umut Elicabuk, Ronja Fischer, Christina Klauda, Stefan Maier, Marius Metzler, Jan-Ole Müller-Gosewisch, Daniel Schell, Andreas Nürnberg, Martin Pittermann, Lea Stockmeier und Florian Wittig. Ich habe die angenehme und abwechslungsreiche Arbeitsatmosphäre am Institut sehr genossen und möchte euch allen für die tolle Zeit danken!

Dr. Sarah Seif Nasr-Storey danke ich für ihre wertvolle Hilfe beim Anpassen der Moduleauslesesoftware an die neuesten Komponenten – häufig unter Zeitdruck da der nächste Beam Test vor der Tür stand.

Außerdem gilt ein besonderer Dank meiner ganzen Familie, die mich in allen Phasen meiner Promotion liebevoll unterstützt hat. Ohne euch wäre diese Arbeit nicht möglich gewesen!

Der Landesgraduiertenförderung des Landes Baden-Württemberg und der Karlsruhe School of Elementary Particle and Astroparticle Physics: Science and Technology (KSETA) möchte ich für die Unterstützung während der Promotion danken.

I acknowledge funding by the Federal ministry of Education and Research of Germany in the framework of the project ”Fortführung des CMS-Experiments zum Einsatz am HL-LHC: Verbesserung des Spurdetektors für das Phase-II-Upgrade des CMS-Experiments” under the grants 05H2019VKCC9 and 05H21VKCC9.

The measurements leading to these results have been performed at the Test Beam Facility at DESY Hamburg (Germany), a member of the Helmholtz Association (HGF).

Declaration

I declare that the work in this dissertation was carried out in accordance with the requirements of the University's Regulations and that it has not been submitted for any other academic award. Except where indicated by specific reference in the text, the work is the candidate's own work. Work done in collaboration with, or with the assistance of, others is indicated as such.

Karlsruhe, July 2022

Roland Koppenhöfer